Seismic Design and Testing of Rocking Cross Laminated Timber Walls

Ryan S. Ganey

A thesis
submitted in partial fulfillment of the
requirements for the degree of

Master of Science in Civil Engineering

University of Washington

2015

Committee:
Jeffrey W. Berman
Laura N. Lowes
Richard Wiebe

Program Authorized to Offer Degree:
Department of Civil and Environmental Engineering

©Copyright 2015
Ryan S. Ganey

University of Washington

Abstract

Seismic Design and Testing of Rocking Cross Laminated Timber Walls

Ryan S. Ganey

Chair of the Supervisory Committee:
Professor Jeffrey W. Berman
Civil and Environmental Engineering

Mass timber is an attractive alternative to nonrenewable materials such as concrete and steel. High rise timber buildings have not been built in high seismic areas due to lack of ductile lateral force resisting systems that can have large seismic force reduction factors. Seismically resilient, lateral systems for tall timber buildings can be created by combining cross laminated timber (CLT) panels with post-tensioned (PT) self-centering technology. The concept features a system of stacked CLT walls where particular stories are equipped to rock against the above and below floor diaphragms through PT connections and are supplemented with mild steel U-shaped flexural plate energy dissipation devices (UFPs).

Experiments were conducted to better understand rocking CLT wall behavior and seismic performance. The testing program consisted of five single wall tests with varying PT areas, initial tensioning force, CLT panel composition, and rocking surface and one coupled wall test with UFPs as the coupling devices. The walls were tested with a quasi-static reverse-cyclic load protocol. The experimental results showed a ductile response and good energy dissipation qualities.

To evaluate the feasibility and performance of the rocking CLT wall system, prototype designs were developed for 8 to 14 story buildings in Seattle using a performance-based seismic design procedure. Performance was assessed using numerical simulations performed

in OpenSees for ground motions representing a range of seismic hazards. The results were used to validate the performance-based seismic design procedure for tall timbers buildings with rocking CLT walls.

TABLE OF CONTENTS

Page

List of Figures vi

List of Tables xvii

Chapter 1: Introduction 1
1.1 Overview 1
1.2 Overarching NEES Resilient Timber Building Project 5
1.3 Objectives and Scope of Research 6
1.4 Organization of Thesis 6

Chapter 2: Literature Review 9
2.1 Introduction 9
2.2 Cross Laminated Timber as a Building Material 9
2.3 Previous Tall Timber Research 11
2.3.1 Green and Karsh [2012] 11
2.3.2 Ceccotti et al. [2013] 12
2.3.3 van de Lindt et al. [2013]; Popovski et al. [2010] 14
2.3.4 Pei et al. [2013] 20
2.4 Previous Structural Systems with Base Rocking Research 22
2.4.1 PRESSS 23
2.4.2 Pres-Lam 28
2.4.3 Wiebe et al. [2012a,b] 33
2.4.4 Spieth et al. [2004] 37
2.5 Conclusions and Research Needs 38

Chapter 3: Structural Behavior and Seismic Design of Rocking CLT Walls 41
3.1 Introduction 41

3.2 Rocking CLT Wall Structural Behavior and Considerations for Analysis . . . 41
3.2.1 CLT Panel Behavior and Modeling Considerations . . . 44
3.2.2 Post-Tensioned Connections . . . 47
3.2.3 UFP Energy Dissipating Devices . . . 50
3.2.4 Cyclic Behavior . . . 52
3.2.5 Floor Diaphragm and Shear Transfer . . . 53
3.2.6 Gravity System Interaction . . . 53
3.3 Cross-Sectional Analysis For Design . . . 54
3.4 Performance-Based Design Procedure for Rocking CLT Walls . . . 66
3.4.1 Seismic Hazard Levels . . . 66
3.4.2 Performance Objectives . . . 66
3.4.3 Design Procedure . . . 68
3.5 Archetype Building Design . . . 76
3.5.1 Building Archetypes . . . 76
3.5.2 Prototype Building Designs . . . 79

Chapter 4: Specimen Design and Test Setup . . . 83
4.1 Introduction . . . 83
4.2 Specimen Design . . . 83
4.2.1 Test Matrix . . . 84
4.2.2 Design Parameters . . . 85
4.2.3 Rocking CLT Wall Behavior . . . 85
4.2.4 Specimen 1 . . . 86
4.2.5 Specimen 2 . . . 87
4.2.6 Specimen 3 . . . 87
4.2.7 Specimen 4 . . . 87
4.2.8 Specimen 5 . . . 88
4.2.9 Specimen 6 . . . 88
4.3 Specimen Construction . . . 89
4.4 Test Setup . . . 91
4.4.1 General Experimental Apparatus . . . 91
4.4.2 General Instrumentation . . . 98
4.4.3 Modified Setup 1: Specimen 4 - CLT Base . . . 103

4.4.4 Modified Setup 2: Specimen 6 - Coupled Wall . . . 108
4.4.5 Load Protocol . . . 115

Chapter 5: Experimental Observations . . . 117
5.1 Introduction . . . 117
5.2 Damage States . . . 119
5.3 Specimen 1 . . . 125
5.4 Specimen 2 . . . 135
5.5 Specimen 3a . . . 140
5.6 Specimen 3b . . . 143
5.7 Specimen 3c . . . 151
5.8 Specimen 4 . . . 157
5.9 Specimen 5 . . . 165
5.10 Specimen 6 . . . 173

Chapter 6: Experimental Data Analysis . . . 191
6.1 Introduction . . . 191
6.2 Specimen Summaries . . . 191
6.3 Data Reduction and Corrections . . . 194
6.4 Strength and Ductility . . . 197
6.5 PT Bar Force . . . 202
6.6 Energy Dissipation . . . 206
6.7 System Stiffness . . . 211
6.8 Residual Drift . . . 214
6.9 Elastic and Shear Moduli . . . 216
6.10 Neutral Axis and PT Gap Rotation . . . 222
6.11 Comparison of the Cross-Sectional Analysis Procedure and Experimental Results 225

Chapter 7: Numerical Model Development and Application . . . 233
7.1 Introduction . . . 233
7.2 Description of the Rocking CLT Wall Model . . . 233
7.3 Comparison of the Numerical Model and Experimental Results . . . 236
7.3.1 System Strength . . . 239
7.3.2 System Stiffness . . . 241

7.3.3 PT Force . . . 244
7.3.4 Neutral Axis . . . 247
7.3.5 UFPs . . . 249
7.4 Application of the Numerical Model . . . 250
7.4.1 Description of Building Model . . . 250
7.4.2 Wind and Gravity Loads, Seismic Masses, and Damping . . . 253
7.4.3 Analysis Options . . . 253
7.4.4 Ground Motion Records . . . 254
7.4.5 Nonlinear Dynamic Analysis Results . . . 258
7.5 Evaluation of Design Procedure . . . 279
7.5.1 Evaluation of PO 2 . . . 279
7.5.2 Evaluation of PO 3 . . . 279
7.5.3 Evaluation of PO 4 . . . 280
7.5.4 Placement of the 2nd Rocking Story . . . 281

Chapter 8: Summary and Conclusions . . . 283
8.1 Summary . . . 283
8.1.1 Rocking CLT wall Behavior . . . 283
8.1.2 Performance Based Seismic Design Procedure . . . 284
8.1.3 Experimental Program . . . 285
8.1.4 Numerical Model . . . 286
8.1.5 Results of Dynamic Analyses and Evaluation of Design Procedure . . . 287
8.2 Conclusions . . . 287
8.3 Future Work . . . 288

References . . . 290

Appendix A: Material Tests . . . 297
A.1 CLT Panels . . . 297
A.2 PT Bars . . . 303
A.3 UFPs . . . 304

Appendix B: Example Design Calculations . . . 309
B.1 Introduction . . . 309

B.2 Calculate Demands 309
B.3 Select Design Parameters 310
B.4 Calculate Required Number of Walls 310
B.5 Calculate Required Number of UFPS 311
B.6 Design Hold Downs for Stories 2-7 312
B.7 Check Limit States 312

LIST OF FIGURES

Figure Number — Page

1.1 (a) Typical Construction with CLT Panels and (b) Stadthaus, a 9-Story CLT Building [Karacabeyli and Douglas, 2013] . . . 2
1.2 (a) Elevation of Building with CLT Rocking CLT Walls and (b) Rocking Connection . . . 4
1.3 NEES Reilinet Timber Building Project Overview . . . 5

2.1 CLT Panel Configuration [Karacabeyli and Douglas, 2013] . . . 10
2.2 (a) Plan and (b) Elevation of the 7-Story Specimen [Ceccotti et al., 2013] . 13
2.3 Story Shears for the (a) Long Direction, South Side and (b) Short Direction, East Side [Ceccotti et al., 2013] . . . 14
2.4 Kinematic Model of a CLT Panel [van de Lindt et al., 2013] . . . 15
2.5 Bracket Connectors Used in CLT Experiments [Popovski et al., 2010] . . . 16
2.6 CLT Wall Experimental Setup [Popovski et al., 2010] . . . 17
2.7 Experimental Results [Popovski et al., 2010] . . . 18
2.8 CUREE 10 Parameter Hysteric Model for Wall to Foundation Connections [van de Lindt et al., 2013] . . . 19
2.9 Calibrated CLT Wall Models Compared to Experiments [van de Lindt et al., 2013] . . . 19
2.10 Performance of a Designed CLT Building [Pei et al., 2013] . . . 21
2.11 (a) Hybrid Connection, (b) Rocking Motion and (c) Hysteretic Cehavior of a Beam-Column Joint from the PRESSS program [Palermo et al., 2005] . . . 23
2.12 Behavior States for Unbonded Post-Tensioned Precast Walls [Kurama et al., 1999] . . . 24
2.13 Proposed Seismic Design Approach: (a) Design Objectives and (b) Design Criteria Kurama et al. [1999] . . . 25
2.14 Elevation of PT Shear Wall System [Nakaki et al., 1999] . . . 26
2.15 Wall Base-Moment vs. Roof-Level Displacement Hystersis Response [Priestly et al., 1999] . . . 27

2.16 (a) Wall Analytical Model and (b) Anaytical-Test Comparison [Priestly et al., 1999] . . . 28
2.17 PT Wall Test Setup and Geometry [Palermo et al., 2006] . . . 29
2.18 Lateral Force vs. Drift for the HY1 Specimen [Palermo et al., 2006] . . . 29
2.19 (a) UFP Geometry and (b) UFP Load-Deflection Plot [Iqbal et al., 2007] . . . 30
2.20 Coupled Wall Test Setup [Iqbal et al., 2007] . . . 31
2.21 Force-Displacement Hysteresis of Coupled Wall Test [Iqbal et al., 2007] . . . 31
2.22 In-Plane Shear Transfer Mechanisms [Smith et al., 2008] . . . 32
2.23 Predicted Envelopes for All Configurations During a Record at the 2% in 50 Year Hazard Level: (a) Story Shear and (b) Overturning Moment [Wiebe et al., 2013a] . . . 34
2.24 Results from the experimental and numerical testing with the DBE-3 record [Wiebe et al., 2013a] . . . 35
2.25 (a) Story Shear and (b) Overturning Moment Envelope for INCR Suite of Motions [Wiebe et al., 2013b] . . . 36
2.26 Schematic of Multispring Contact Element [Spieth et al., 2004] . . . 37
2.27 Column Force-Drift of Experiment and Multispring Element with Lobatto Integration [Spieth et al., 2004] . . . 38

3.1 Two Rocking CLT Wall Configurations . . . 42
3.2 Schematic Elevation of Intermediate Story of the SC-CLT Wall System . . . 43
3.3 (a) Sawn Lumber [Wiedenhoeft, 2013] (b) and Wood Fiber Directions [Kretschmann, 2013] . . . 45
3.4 (a) Stress-Strain Behavior of Wood [Buchanan, 1990] (b) and CLT [Horvat, 2013] . . . 46
3.5 Assumed CLT Constitutive Model . . . 47
3.6 Free Body Diagram of Deformed Intermediate Story of the SC-CLT Wall System (Note: small θ_s assumed) . . . 49
3.7 (a) UFP Dimensions and (b) Free Body Diagram [Baird et al., 2014] . . . 51
3.8 UFP Connection: (a) Steel Plate Saddle Bolted and (b) Embedded Plate Site Welded . . . 52
3.9 Cyclic Behavior of Rocking CLT Wall System . . . 53
3.10 (a) Single PT Connection Wall and (b) Dual PT Connection Wall . . . 54
3.11 Section Analysis Flow Chart . . . 55

3.12 Wall Equilibrium at Decompression for (a) Single PT Connection Wall and (b) Dual PT Connection Wall . . . 57
3.13 Aggregate Initial Stiffness of a Rocking CLT Wall . . . 57
3.14 Gap Opening Diagram . . . 58
3.15 Monolithic Wall Analogy for Single PT Connection Wall (a) and Dual PT Connection Wall (b) [Pampanin et al., 2001] . . . 61
3.16 Assumed CLT Constitutive Model Applied to the Cross-Section . . . 62
3.17 Wall Equilibrium for Single PT Connection Wall (a) and Dual PT Connection Wall (b) . . . 63
3.18 Performance Objectives . . . 67
3.19 Proposed Performance-Based Design Procedure . . . 68
3.20 UFP Energy Dissipation Ratio [Seo and Sause, 2005] . . . 71
3.21 Global Tension-Compression Force Couple . . . 73
3.22 Hold Down Wall Free Body Diagram . . . 75
3.23 Residential Archetype Plan . . . 77
3.24 Office Archetype Plan . . . 78

4.1 (a) 5-Ply CLT Panel and (b) CLT Panel with SCL Core . . . 90
4.2 Machine Press . . . 90
4.3 Overview of Single Wall Test Setup - Steel Base . . . 93
4.4 Single Wall Test Setup Schematic - Steel Base . . . 94
4.5 Steel Base Beam Schematic . . . 95
4.6 PT Stressing Apparatus . . . 95
4.7 PT Stressing Apparatus Schematic . . . 96
4.8 East Face Upper Out-of-Plane Restraint . . . 97
4.9 Upper Out-of-Plane Restraint Schematic . . . 98
4.10 General Instrumentation Layout . . . 102
4.11 General Instrumentation Layout Schematic . . . 102
4.12 Overview of the Test Setup for Specimen 4 (CLT Base) . . . 104
4.13 Specimen 4 (CLT Base) Test Setup Schematic . . . 105
4.14 Specimen 4 (CLT Base) Instrumentation Layout . . . 107
4.15 Specimen 4 (CLT Base) Instrumentation Layout Schematic . . . 107
4.16 Overview of Coupled Wall Test Setup . . . 109
4.17 Coupled Wall Test Setup Schematic . . . 110

4.18 Coupled Wall Link Beam Schematic . . . 111
4.19 Coupled Wall UFP Attachment . . . 111
4.20 Coupled Wall Instrumentation Layout . . . 114
4.21 Coupled Wall Instrumentation Layout Schematic . . . 114
5.1 Test Specimen Plan Orientation . . . 117
5.2 Specimen 1 Moment-Drift Response . . . 125
5.3 CLT Yielding (WDS1) at the South End of Specimen 1 During Step 9 (0.5% Drift) . . . 126
5.4 Small Vertical Splits (WDS2) at the Northwest Corner of Specimen 1 During Step 13 (2.8% Drift) . . . 126
5.5 Vertical Splitting (WDS3) at the Northeast Corner of Specimen 1 During Step 14 (3.8% Drift) . . . 127
5.6 Delamination and Splitting (WDS3) at the Northwest Corner of Specimen 1 During Step 14 (3.8% Drift) . . . 128
5.7 Vertical Splitting (WDS3) at the Southeast Corner of Specimen 1 During Step 14 (3.8% Drift) . . . 128
5.8 Vertical Splitting (WDS2) at the Southwest Corner of Specimen 1 During Step 14 (3.8% Drift) . . . 129
5.9 Vertical Splitting (WDS3) at the Northeast Corner of Specimen 1 During Step 15 (4.8% Drift) - Cycle 1 (a) and Cycle 2 (b) . . . 130
5.10 Delamination (WDS3) at the (a) North End and (b) South End of Specimen 1 During Step 15 (4.8% Drift) . . . 130
5.11 Splitting (WDS3) at the (a) Southeast and (b) Southwest Corners of Specimen 1 During Step 15 (4.8% Drift) . . . 131
5.12 (a) Increased Delamination and (b) New Damage of the Second Laminate (WDS4) at the Northwest Corner of Specimen 1 During Step 16 (7.4% Drift) 132
5.13 (Splitting Damage (WDS4) at the Northwest Corner of Specimen 1 During Step 16 (7.4% Drift) . . . 133
5.14 Delamination and Splitting Damage (WDS4) at the South End of Specimen 1 During Step 16 (7.4% Drift) . . . 133
5.15 Wall Damage at the (a) North and (b) South Ends of Specimen 1 During Step 17 (8.0% drift) . . . 134
5.16 Specimen 2 Moment-Drift Response . . . 135
5.17 Wall Decompression of Specimen 2 During Step 7 (0.3% drift) . . . 136

5.18 Horizontal and Vertical Split (WDS3) at the Northeast Corner of Specimen 2 During Step 15 (4.9% Drift) . . . 136
5.19 Horizontal Split (WDS3) of at the Southeast Corner of Specimen 2 During Step 15 (4.9% Drift) . . . 137
5.20 Compression Failure (WDS3) at the Northeast Corner of Specimen 2 During Step 15 (4.9% Drift) - Cycle 2 . . . 137
5.21 Compression Damage (WDS3) at the (a) Southeast and (b) Southwest Corners of Specimen 2 During Step 16 (7.4% Drift) . . . 138
5.22 Compression Damage (WDS3) at the (a) Northeast and (b) Northwest Corners of Specimen 2 During Step 16 (7.4% Drift) . . . 138
5.23 Compression Damage (WDS3) at the (a) Southeast and (b) Southwest Corners of Specimen 2 During Step 17 (9.5% Drift) . . . 139
5.24 Compression Damage (WDS3) at the (a) Northeast and (b) Northwest Corners of Specimen 2 During Step 17 (9.5% Drift) . . . 140
5.25 Specimen 3a Moment-Drift Response . . . 141
5.26 Wall Decompression of Specimen 3a During Step 9 (drift = 0.5%) . . . 141
5.27 Crushing Underneath PT Bearing Plate of Specimen 3a . . . 142
5.28 Specimen 3b Top Plate Retrofit . . . 143
5.29 Specimen 3b Moment-Drift Response . . . 144
5.30 Horizontal Splitting (WDS2) at the Northeast Corner of Specimen 3b During Step 13 (2.9% Drift) . . . 145
5.31 Vertical Split (WDS2) at the Northwest Corner of Specimen 3b During Step 13 (2.9% Drift) . . . 145
5.32 Vertical Splitting and Delamination (WDS3) at the Northeast Corner of Specimen 3b During Step 14 (4.0% Drift) . . . 146
5.33 Compression Damage (WDS3) at Southeast Corner of Specimen 3b During Step 14 (4.0%) Drift . . . 146
5.34 Increased Splitting Damage and Delamination (WDS3) at the Northeast Corner of Specimen 3b during Step 16 (7.8% Drift) . . . 147
5.35 Compression Damage (WDS3) at the Northwest Corner of Specimen 3b During Step 16 (7.8% Drift) . . . 148
5.36 Compression Damage (WDS3) at the (a) Southeast and (b) Southwest Corners of Specimen 3b During Step 16 (7.8% Drift) . . . 148
5.37 Splitting and Delamination (WDS3) at the South End of Specimen 3b During Step 16 (7.8% Drift) . . . 149

5.38 Damage (WDS3) at the Northeast Corner of Specimen 3b During Step 17 (10.0% Drift) . . . 150
5.39 Damage (WDS3) at the Southeast Corner of Specimen 3b During Step 17 (10.0% Drift) . . . 150
5.40 Specimen 3c Moment-Drift Response . . . 151
5.41 Split (WDS2) at the Southwest Corner of Specimen 3c During Step 14 (3.8% Drift) . . . 152
5.42 (a) Vertical Splitting (WDS3) in the Second Ply at the Northeast Corner and (b) Horizontal Splitting (WDS3) of First Ply of the Northwest Corner of Specimen 3c During Step 15 (4.8% Drift) . . . 153
5.43 Splitting Damage (WDS3) at the Southeast Corner of Specimen 3c Specimen 3c Step 15 (4.8% Drift) . . . 153
5.44 Compression Damage (WDS3) at the (a) Northeast and (b) Northwest Corners of Specimen 3c During Step 16 (7.4% Drift) . . . 154
5.45 Compression Damage (WDS3) at the (a) Southeast and (b) Southwest Corners of Specimen 3c During Step 16 (7.4% Drift) . . . 155
5.46 Damage at the (a) Northeast and (b) Northwest Corners of Specimen 3c During Step 17 (9.5% Drift) . . . 156
5.47 Damage of Specimen 3c at the (a) Southeast and (b) Southwest Corners of Specimen 3c During Step 17 (9.5% Drift) . . . 156
5.48 Specimen 4 Moment-Drift Response . . . 157
5.49 Wall Decompression of Specimen 4 During Step 10 (0.8% Drift) . . . 158
5.50 CLT Base Crushing (BDS1) at the (a) North and (b) South Ends of Specimen 4 During Step 10 (0.8% Drift) . . . 158
5.51 CLT Base Crushing (BDS1) at the (a) North and (b) South Ends of Specimen 4 During Step 13 (2.8% Drift) . . . 159
5.52 CLT Base Splitting (BDS4) at the (a) North and (b) South Ends of Specimen 4 During Step 13 (2.8% Drift) . . . 159
5.53 CLT Base Crushing (BDS2) at the (a) North and (b) South Ends of Specimen 4 During Step 14 (3.8% Drift) . . . 160
5.54 CLT Base Splitting (BDS4) at the (a) North and (b) South Ends of Specimen 4 During Step 14 (3.8% Drift) . . . 160
5.55 CLT Base Crushing (BDS2) at the (a) North and (b) South Ends of Specimen 4 During Step 15 (4.8% drift) . . . 161
5.56 CLT Base Crushing (BDS3) at the (a) North and (b) South Ends of Specimen 4 During Step 16 (7.4% Drift) . . . 162

5.57 CLT Base Splitting (BDS4) at the (a) North and (b) South Ends of Specimen 4 During Step 16 (7.4% Drift) . . . 162
5.58 CLT Base Crushing (BDS3) and CLT Base Splitting (BDS4) at the (a) North and (b) South Ends of Specimen 4 During Step 17 (9.4% Drift) . . . 163
5.59 Specimen 4 Wall Post Test . . . 164
5.60 Specimen 4 (a) South and (b) North CLT Base Post Test) . . . 164
5.61 Specimen 5 Moment-Drift Response . . . 165
5.62 Wall Decompression of Specimen 5 During Step 9 (0.5%) . . . 166
5.63 (a) Horizontal Splitting (WDS2) and (b) Vertical Splitting (WDS3) at the Northeast Corner of Specimen 5 During Step 14 (3.8% Drift) . . . 167
5.64 Delamination (WDS3) at the Northwest Corner of Specimen 5 During Step 14 (3.8% Drift) . . . 167
5.65 Small Splits (WDS2) at the Southwest Corner of Specimen 5 During Step 15 (4.8%) . . . 168
5.66 Core Split (WDS3) at the Northeast Corner of Specimen 5 During Step 15 (4.8%) - (a) Cycle 2 and (b) Cycle 3 . . . 169
5.67 Splitting (WDS3) at the Southeast Corner of Specimen 5 During Step 16 (7.3% Drift) - (a) Cycle 1 and (b) Cycle 2 . . . 170
5.68 Splitting (WDS3) at the Southwest Corner of Specimen 5 During Step 16 (7.3% Drift) . . . 171
5.69 (a) Core Splitting (WDS3) and (b) Base Crushing (WDS3) at the Northwest Corner of Specimen 5 During Step 16 (7.3% Drift) . . . 171
5.70 (a) Splitting Failures (WDS3) at the South End and (b) Core Splitting (WDS3) at the Northwest Corner of Specimen 5 During Step 17 (9.4% drift) . . . 172
5.71 Permanent Deformation at the South End of the Wall After Recentering of Specimen 5 Post-Test . . . 173
5.72 Specimen 6 Moment-Drift Response . . . 174
5.73 Wall Decompression of the South Wall of Specimen 6 During Step 10 (0.4% drift) . . . 174
5.74 (a) Delamination (WDS3) at the South End of the South Wall and (b) Vertical Splitting (WDS2) at the Northeast Corner of the North Wall of Specimen 6 During Step 12 (1.6%) . . . 175
5.75 Yielding of the Lower UFP (WDS6) of Specimen 6 During Step 12 (1.6%) . . . 176
5.76 Splitting (WDS3) at the (a) Northeast Corner and (b) the Southwest Corner of the North Wall of Specimen 6 During Step 13 (2.6% drift) . . . 176

5.77 Damage (WDS3) at the (a) Northwest Corner and (b) the South End of the South Wall of Specimen 6 During Step 13 (2.6% drift) 177
5.78 (a) Splitting (WDS3) at the Northeast Corner and (b) Delamination (WDS3) at the North End of the North Wall of Specimen 6 During Step 14 (3.6% drift) 178
5.79 Delamination (WDS3) at the Southeast Corner of the North Wall of Specimen 6 During Step 14 (3.6% drift) 178
5.80 (a) Delamination (WDS3) at the North End and (b) Splitting (WDS3) at the Southwest Corner of the South Wall of Specimen 6 During Step 14 (3.6% Drift) 179
5.81 Lower UFP Deformation (WDS6) of Specimen 6 During Step 14 (3.6%) . . . 180
5.82 (a) Splitting (WDS3) at the Northeast Corner and (b) Delamination (WDS3) at the North End of the North Wall of Specimen 6 During Step 15 (4.6% Drift) 181
5.83 Splitting (WDS3) at the (a) Northeast Corner and (b) Southeast Corner of the South Wall of Specimen 6 During Step 15 (4.6% drift) 182
5.84 Continued Splitting and Delamination (WDS3) of the North Wall of Specimen 6 During Step 16 (7.3% Drift) 183
5.85 (a) Continued Delamination (WDS3) at the Southeast Corner and (b) Splitting Damage (WDS3) at the Southwest Corner of the North Wall of Specimen 6 During Step 16 (7.3% Drift) 183
5.86 (a) Crushing Damage (WDS3) at the Northeast Corner and (b) Delamination (WDS3) at the South End of the South Wall of Specimen 6 During Step 16 (7.3% Drift) 184
5.87 Splitting Damage (WDS3) at the (a) Southeast Corner and (b) the Southwest Corner of the South Wall of Specimen 6 During Step 16 (7.3% Drift) 185
5.88 Lower UFP Damage (UFP1) of Specimen 6 During Step 16 (7.3%) 185
5.89 Damage in the first and Second Plys (WDS3) at the Northeast Corner of the North Wall of Specimen 6 During Step 17 (9.4% Drift) 186
5.90 Splitting Damage (WDS3) at the (a) North End and (b) Northwest Corner of the North Wall of Specimen 6 During Step 17 (9.4% Drift) 187
5.91 Splitting Damage (WDS3) at the (a) Southeast and (b) Southwest Corners of the North Wall of Specimen 6 During Step 17 (9.4% Drift) 187
5.92 Splitting Damage (WDS3) at the (a) North End and (b) Northwest Corner of the South Wall of Specimen 6 During Step 17 (9.4% Drift) 188
5.93 Splitting and Delamination (WDS3) at the South End of the South Wall of Specimen 6 During Step 17 (9.4% Drift) 189
5.94 Lower UFP Deformation (WDS3) of Specimen 6 During Step 17 (9.4% Drift) 189

6.1 Actuator Correction Factor Terms . . . 195
6.2 Specimen 3b PT Load Cell Correction . . . 196
6.3 Specimen 4 Base Deformation Potentiometers . . . 196
6.4 (a) Specimen 1, (b) Specimen 2, (c) Specimen 3b, (d) Specimen 3c, (e) Specimen 4, and (f) Specimen 5 Overturning Moment vs. Drift . . . 199
6.5 Specimen 6 Overturning Moment vs. Drift . . . 200
6.6 (a) Specimen 1, (b) Specimen 2, (c) Specimen 3b, (d) Specimen 3c, (e) Specimen 4, and (f) Specimen 5 PT Force vs. Drift . . . 204
6.7 Specimen 6 (a) North Wall and (b) South Wall PT Force vs. Drift . . . 205
6.8 (a) Single Wall Specimens and (b) Coupled Wall Specimen PT Force Loss . . . 206
6.9 Specimen 6 Lower UFP Force versus Displacement . . . 207
6.10 (a) Specimen 1, (b) Specimen 2 Cumulative, (c) Specimen 3a/3b, (d) Specimen 4, (e) Specimen 5, and (f) Specimen 6 Energy Dissipation . . . 209
6.11 (a) Idealized Flag Shaped Hysteresis and (b) Experimental Overtunring Moment vs. Drift Hysteresis Showing System Stiffness . . . 211
6.12 Elastic Deformation Calculation Schematic . . . 217
6.13 (a) Specimen 2 and (b) Specimen 3c Elastic Deformation . . . 217
6.14 Shear Deformation Calculation Schematic . . . 218
6.15 (a) Specimen 2 and (b) Specimen 3c Shear Deformation . . . 220
6.16 Illustration of NA Location, Depth, and PT Gap Rotation in a CLT Rocking Wall . . . 222
6.17 Specimen 2 (a) Neutral Axis Depth and (b) PT Gap Rotation . . . 224
6.18 Specimen 3c (a) Neutral Axis Depth and (b) PT Gap Rotation . . . 224
6.19 Comparison of the (a) Base Shear vs. Drift, (b) PT Force vs. Drift, (c) Neutral Axis Depth, and (d) Couple Arm Length of Specimen 1 from the Cross-Sectional Analysis and Experiments . . . 227
6.20 Comparison of the (a) Base Shear vs. Drift, (b) PT Force vs. Drift, (c) Neutral Axis Depth, and (d) Couple Arm Length of Specimen 2 from the Cross-Sectional Analysis and Experiments . . . 228
6.21 Comparison of the (a) Base Shear vs. Drift, (b) PT Force vs. Drift, (c) Neutral Axis Depth, and (d) Couple Arm Length of Specimen 3b from the Cross-Sectional Analysis and Experiments . . . 229
6.22 Comparison of the (a) Base Shear vs. Drift, (b) PT Force vs. Drift, (c) Neutral Axis Depth, and (d) Couple Arm Length of Specimen 3c from the Cross-Sectional Analysis and Experiments . . . 230

7.1 Numerical Model for Single Connection Rocking CLT Wall 234
7.2 Material Model for Mulitspring Contact Element 236
7.3 Comparison of UFP Material Test and Numerical Model 238
7.4 Comparison of (a) Specimen 1, (b) Specimen 2, (c) Specimen 3b, (d) Specimen 3c, (e) Specimen 5, and (f) Specimen 6 Overturning Moment vs. Drift from the Numerical Models and Experiments 240
7.5 Comparison of (a) Specimen 1, (b) Specimen 2, (c) Specimen 3b, (d) Specimen 3c, and (e) Specimen 5 PT Force vs. Drift from the Numerical Models and Experiments 245
7.6 Comparison of Specimen 6 (a) North Wall and (b) South Wall PT Force vs. Drift from the Numerical Models and Experiments 246
7.7 Comparison of (a) Specimen 1, (b) Specimen 2, (c) Specimen 3b, (d) Specimen 3c, and (e) Specimen 5 Neutral Axis Depth vs. Drift from the Numerical Models and Experiments 248
7.8 Comparison of Specimen 6 (a) North Wall and (b) South Wall Neutral Axis Depth vs. Drift from the Numerical Models and Experiments 249
7.9 Comparison of Specimen 6 (a) Lower UFP and (b) Upper Displacement vs. Drift from the Numerical Models and Experiments 250
7.10 Numerical Model for the Prototype Buildings 251
7.11 Numerical Model for (a) Dual Connection Rocking CLT Wall and (b) Hold Down Wall (HDW) 252
7.12 Spectral Accelerations for Hazards and Scaled Ground Motions Having a Probability of Exceedence of (a) 50% in 50 Years, (b) 10% in 50 Years, and (c) 2% in 50 Years [USGS, 2015] 257
7.13 (a) Base Shear Response, (b) Overturning Moment Response, (c) Rocking Story Shears, (d) Rocking Story Moments, (e) Roof Displacement History, and (f) Normalized PT Response of Model R8-1.5 Under a 10% in 50 Year Ground Motion (PEER NGA 1148) Representing a DBE 259
7.14 (a) Base Shear Response, (b) Overturning Moment Response, (c) Rocking Story Shears, (d) Rocking Story Moments, (e) Roof Displacement History, and (f) Normalized PT Response of Model R14-1.8 Under a 10% in 50 Year Ground Motion (PEER NGA 752) Representing a DBE 260
7.15 (a) Base Shear Response, (b) Overturning Moment Response, (c) Rocking Story Shears, (d) Rocking Story Moments, (e) Roof Displacement History, and (f) Normalized PT Response of Model R8-1.5 Under a 2% in 50 Year Ground Motion (PEER NGA 1111) Representing the MCE 261

7.16 (a) Base Shear Response, (b) Overturning Moment Response, (c) Rocking Story Shears, (d) Rocking Story Moments, (e) Roof Displacement History, and (f) Normalized PT Response of Model R14-1.8 Under a 2% in 50 Year Ground Motion (PEER NGA 953) Representing the MCE 262
7.17 Peak Story Drift Median ($\mu_{1/2}$) and 84th Percentile Response for 8-Story Model 268
7.18 Peak Story Drift Median ($\mu_{1/2}$) and 84th Percentile Response for 14-Story Models 269
7.19 Maximum Residual Drift Median ($\mu_{1/2}$) and 84th Percentile Response for 8-Story Model 270
7.20 Maximum Residual Drift Median ($\mu_{1/2}$) and 84th Percentile Response for 14-Story Models 271
7.21 Component Criteria Median ($\mu_{1/2}$) and 84th Percentile Response for 8-Story Model 272
7.22 Component Criteria Drift Median ($\mu_{1/2}$) and 84th Percentile Response for 14-Story Models 273
7.23 Number of Analyses Exceeding Yield Criteria for 8-Story Model 277
7.24 Number of Analyses Exceeding Yield Criteria for 14-Story Models 278

A.1 (a) Schematic and (b) Photograph Depicting CLT Orientation 297
A.2 Example of (a) 3 Ply Material Test Setup and (b) Damage (Specimen CLT3.1.3) 298
A.3 Example of (a) 5 Ply Material Test Setup and (b) Damage (Specimen CLT5.1.1) 299
A.4 Stress vs. Strain for CLT Direction 1 300
A.5 Stress vs. Strain for CLT Direction 2 300
A.6 Stress vs. Strain for CLT Direction 3 301
A.7 (a) 1.25 in Diameter and (b) 1.375 in Diameter PT Bar Stress vs. Strain . . 303
A.8 (a) UFP Testing Apparatus Schematic and (b) Photograph 305
A.9 UFP Experimental Force verses Displacement 306
A.10 UFP Coupon Stress verses Strain 307
A.11 Tested UFP Coupon 307

LIST OF TABLES

Table Number Page

3.1 Response Spectra Values (in units of g) for Site Class D for the 5% Dammping Level in Seattle, WA . . . 79
3.2 Design Parameters for R8-1 and R8-1.5 Prototype Building . . . 81
3.3 Design Parameters for R14-1, R14-1.6, R14-1.8, and R14-1.10 Prototype Buildings . . . 81

4.1 Test Matrix . . . 84
4.2 Instrumentation Assignments for General Setup . . . 101
4.3 Instrumentation Assignments for Specimen 4 - CLT Base . . . 106
4.4 Instrumentation Assignments for Specimen 6 - Coupled Wall . . . 112
4.5 Load Protocol . . . 116

5.1 Corrected Drift Readings . . . 118
5.2 CLT Wall Panel Damage States . . . 120
5.3 PT Bar Damage States . . . 121
5.4 CLT Base Damage States . . . 122
5.5 UFP Damage States . . . 123
5.6 Damage State Summary . . . 124

6.1 Specimen Summaries . . . 191
6.2 Experimental Ductility Values . . . 200
6.3 Experimental Strength Values . . . 201
6.4 PT Force at Zero Drift After Third Cycles at Indicated Maximum Drifts . . . 205
6.5 Cumulative Energy Dissipation . . . 210
6.6 System Stiffness . . . 213
6.7 Residual Drifts . . . 215
6.8 Experimental Elastic and Shear Moduli . . . 221
6.9 Moment Arm Length . . . 231
6.10 Experimental-Analytical Overturning Moment Comparison at 2% Drift . . . 231

7.1 Comparison of the Moment Strength from the Numerical Models and Experiments . . . 241
7.2 Comparison of the Initial Stiffness from the Numerical Models and Experiments 242
7.3 Comparison of the Decompression Stiffness from the Numerical Models and Experimentals . . . 243
7.4 Comparison of the Recentering Stiffness from the Numerical Models and Experiments Comparison . . . 243
7.5 Comparison of Drift at PT Yield from the Numerical Models and Experiments 246
7.6 Ground Motion Details ATC [2009b] . . . 256
7.7 Summarized Response Parameters From Nonlinear Analyses for 8-Story Models 265
7.8 Summarized Response Parameters From Nonlinear Analyses for 14-Story Models 266
7.9 Number of Analyses Exceeding Yield Criteria for 8-Story Models . . . 274
7.10 Number of Analyses Exceeding Yield Criteria for 14-Story Models . . . 275

A.1 CLT and SCL Material Test Averages . . . 301
A.2 CLT and SCL Material Test Results . . . 302
A.3 PT Bar Material Test Averages . . . 303
A.4 PT Bar Material Test Results . . . 304
A.5 UFP Material Test Load Protocol . . . 306

ACKNOWLEDGMENT

I would first like to thank my adviser Professor Jeff Berman. Jeff's guidance and support was critical in the completion of this work. He was a joy to work with. I would also like to thank Professors Laura Lowes and Richard Wiebe for taking the time to serve on my reading committee.

I would like to thank the entire project team: Professor Shiling Pei of the Colorado School of Mines; Professor Dan Dolan of Washington State University; Professors Richard Sause and Jim Ricles of Lehigh University; Professor John van de Lindt of Colorado State University; Marjan Popovski of FP Innovations; Hans-Erik Blomgren of Arup; and Douglas Rammer of US Forest Service. I would like to extend a special thank you to Bob Duncan and Scott Lewis, who worked tirelessly to setup and run the experiments at Washington State University and to Tugce Akbas and Sara Loftus, my fellow graduate students on the project.

I would like to thank the George E. Brown Jr. Network for Earthquake Simulation Research under the National Science Foundation for providing the funding for this work (Awards CMMI: 1344617; 1344646; 1344798; 1344590; 1344621). I also would like to thank Weyerhaesuer for donating all the timber material used in the experiments. Some of the numerical analyses presented in this work were done on the Hyak and Ryak super computer clusters of University of Washington.

I would not have been able to get through grad school without the support and company of my fellow grad students. Ryan Ballard, my fellow Wisconsinite with whom I spent many hours laboring over research work; Andrew Winter and Spencer Livermore who provided valuable assistance to my class and research work and of course great company; Ashley Heid and Becky Gilbertson for taking the time to cut and test a coupon for my material tests;

the Marafi-Ganey-Sen lunch club with members Nasser of the illustrious House Marafi and Andy Sen; tea time on Friday afternoons; the Core Crew Extended for all the good times; and finally my parents, family, and friends.

Chapter 1

INTRODUCTION

1.1 Overview

From Japan's Hōryū-ji Temple, one of the oldest timber buildings built in 607, to Russia's Kizhi Pogost church, the tallest wooden building in the world standing at 123 feet tall, timber buildings have been used by humans for over 1,400 years. Currently with the modern urbanization in the United States [Alig et al., 2004], there is a growing need for 8-14 story buildings for residential and light commercial applications and as a sustainable material, timber can meet this need. In 2014 as part of the commitment to mitigate climate change, the U.S. Department of Agriculture announced the U.S. Tall Wood Building Prize Competition to expand the interest in developing tall timber buildings. In seismic applications timber has been considered a less desirable building material than concrete or steel because of it's lack of strength and stiffness and currently cannot be used for the primary structural material for even mid-rise buildings. For instance, in Seattle, Washington timber buildings are limited to five stories because current construction methods are not designed to withstand the high seismic accelerations in the area.

In the early 1990s, a new stronger form of timber was developed called cross-laminated timber (CLT). CLT is an engineered wood product consisting of boards glued in layers perpendicular to each other to form a panel as shown in Figure 1.1a. Because of it's alternating perpendicular layers, CLT has relatively high strength and stiffness in both in-plane directions making it ideal for use in slabs and walls. CLT also lends itself to fast construction by enabling prefabrication of panels off-site and constructing the panels together on-site with mechanical connectors. CLT has been used successfully to construct taller timber buildings. With 10 stories, Melbourne, Australias Forte complex, is the tallest residential timber

building in the world. Located in London, Stadthaus (shown in Figure 1.1b) is a nine story building built with CLT panels. However, the current design methodology for CLT buildings does not provide a ductile response or enough energy dissipation for regions with large seismic hazards.



(a) (b)

Figure 1.1: (a) Typical Construction with CLT Panels and (b) Stadthaus, a 9-Story CLT Building [Karacabeyli and Douglas, 2013]

One of the limiting factors of current CLT design is the low deformation capacity of mechanical connectors used for lateral resistance. In place of mechanical connectors, post-tensioned (PT) connections, which have a ductile response, can be used. PT connections consist of PT bars or strands that run through the height of the wall and are anchored to the diaphragm. This allows the wall to rock about its base when walls experience lateral force. The PT also provides a restoring moment to recenter or bring the building back to it's original configuration. This concept was originally implemented in unbonded PT precast

concrete walls and frames in the early 1990s [Priestly, 1991; Kurama et al., 1999; Nakaki et al., 1999; Priestly et al., 1999] and later extended to laminated veneer lumber walls and frames in the mid 2000s [Palermo et al., 2005, 2006; Iqbal et al., 2007; Smith et al., 2008]. Although the PT supplies recentering capabilities, it is designed to remain elastic in a seismic event so it can supply the restoring moment and thus does not dissipate energy inputted into the system from an earthquake. U-shaped flexural plate energy dissipation devices (UFPs) can be introduced to the system to dissipate energy from the ground motion and reduce accelerations. UFPs are thin mild steel plates that are formed by rolling the plate about a fixed radius to form a semicircular shape with two equally straight sections on either side. The straight portions of the device are attached to two adjacent rocking walls and when rocking action occurs the UFPs deform and dissipate energy.

In this research, a rocking CLT wall seismic force resisting system is proposed for the design of tall wood buildings that combines the self-centering capabilities of the PT connections with the energy dissipation of the UFPs. The concept features certain stories with the rocking CLT walls and other stories with current CLT lateral design consisting of CLT walls with mechanical connectors and hold downs as shown in Figure 1.2. In a seismic event, the building will return to a recentered state, the stories with CLT walls and mechanical connectors are designed to remain elastic such that no repair is required, and the UFPs can easily replaced so the building can quickly return to a fully functional state

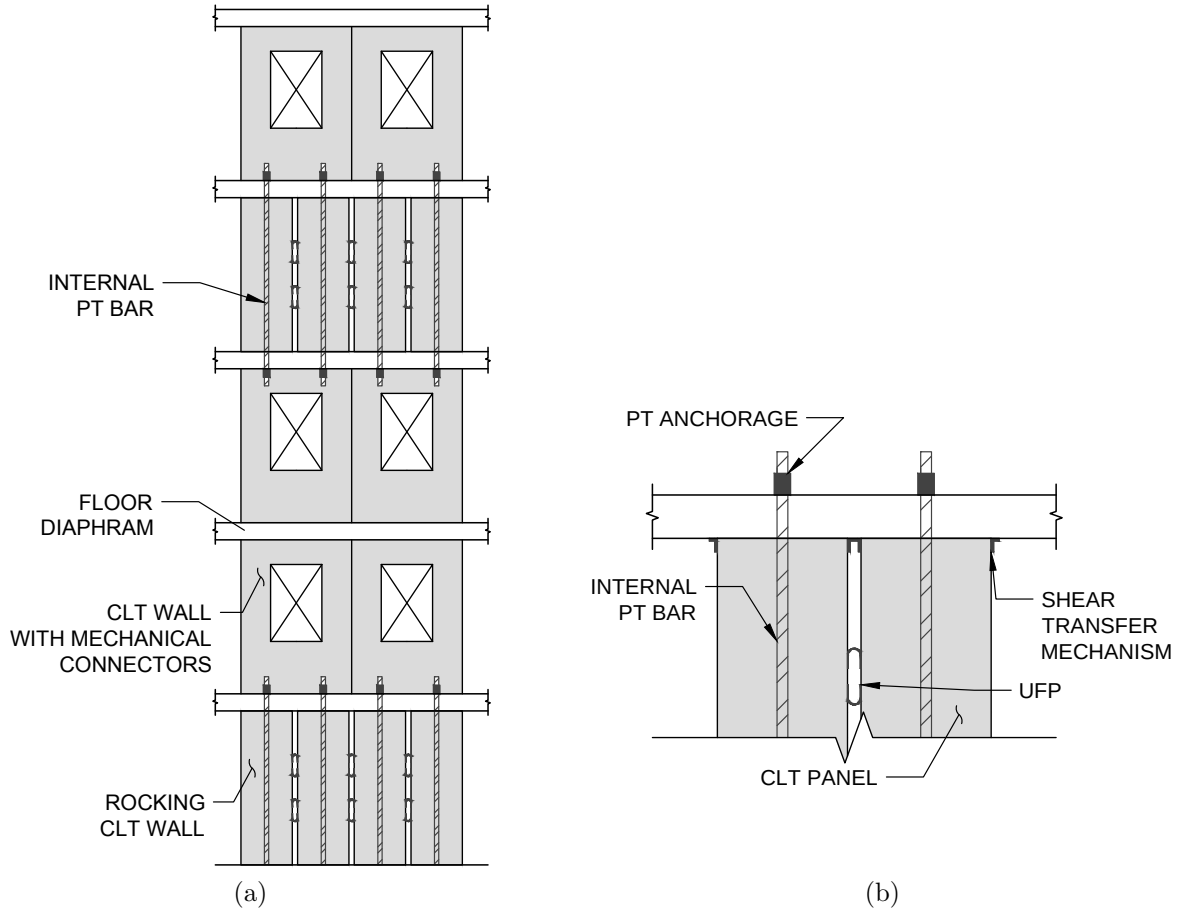

Figure 1.2: (a) Elevation of Building with CLT Rocking CLT Walls and (b) Rocking Connection

1.2 Overarching NEES Resilient Timber Building Project

The research presented in this thesis is part of the Resilient Timber Building Project funded by the National Science Foundation (NSF) under the Network for Earthquake Engineering Simulation (NEES) program (Awards CMMI: 1344617; 1344646; 1344798; 1344590; 1344621). The project focuses on the development, design, and implementation of engineered wood systems for seismically resilient tall buildings. An overview of the entire project is presented in Figure 1.3.

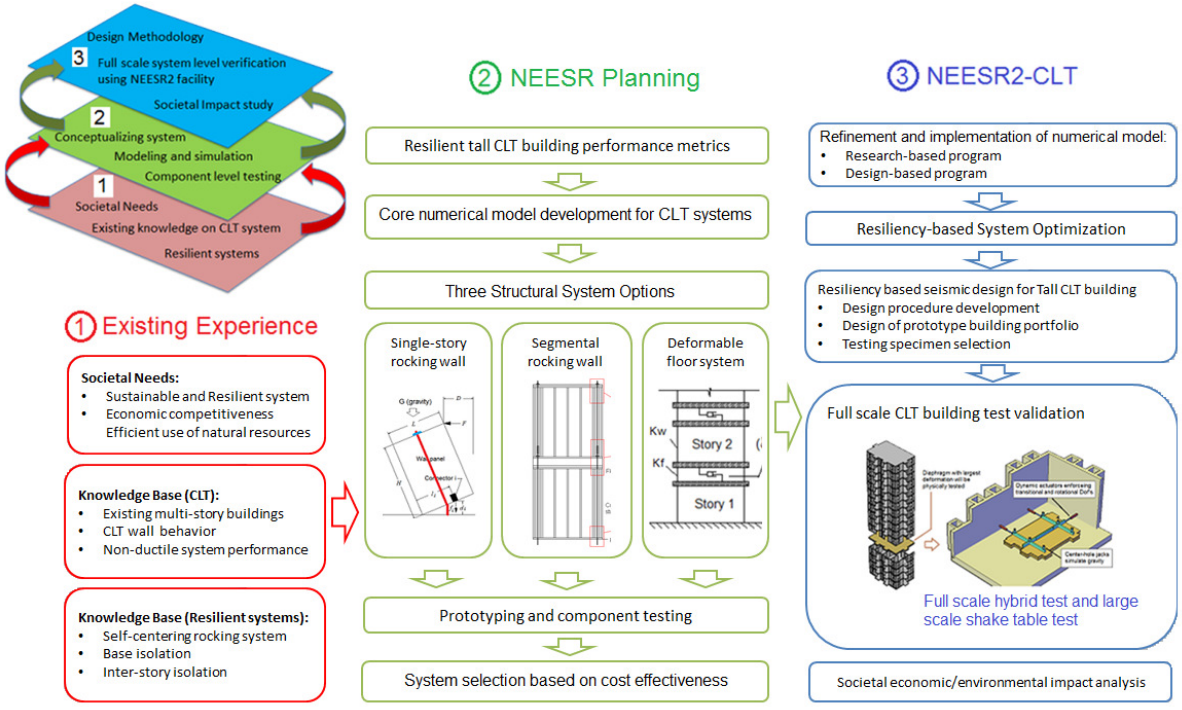

Figure 1.3: NEES Reilinet Timber Building Project Overview

Three resilient seismic systems are being developed: (1) a single story rocking wall configuration, (2) a segmental, multi-story rocking wall configuration, and (3) a deformable floor system. The segmental, multistory rocking wall configuration is being developed by collaborators at Lehigh University and the deformable floor system is being developed by collaborators at Washington State University. The single story rocking wall configuration

will be the focus of this thesis. The component testing, conducted at the Washington State Universtiry Structures Laboratory, presented in this thesis is valuable to both rocking wall configurations.

1.3 Objectives and Scope of Research

The objectives of this research are outlined below:

- Develop an understanding of the behavior of the proposed rocking CLT wall system.
- Develop a design procedure to achieve performance objectives during seismic events for tall timber buildings with rocking CLT walls.
- Develop a relatively simple numerical model to simulate the behavior of rocking CLT walls.
- Perform an experimental investigation into rocking CLT walls.
- Calibrate the numerical model with the experimental results.
- Evaluate the proposed design procedure by assessing the performance objectives using the results of nonlinear dynamic analyses.
- Propose additional research needed to further the development and implementation of rocking CLT walls and tall timber buildings.

1.4 Organization of Thesis

The remaining chapters of this thesis are organized as follows:

- *Chapter 2* contains an overview of previous related research pertaining to CLT, tall timber buildings, and buildings with walls allowed to rock at their base.

- *Chapter 3* contains an introduction into the behavior of rocking CLT walls and outlines a performance-based design approach for tall timber buildings with rocking CLT walls. This chapter also proposes performance objectives and a design procedure. The proposed design procedure is used to design a series of prototype buildings with the rocking CLT wall system.

- *Chapter 4* contains an overview of the six rocking CLT wall experimental specimens and the test setup used for the experiments. The six specimens consisted of five single wall specimens and one coupled wall specimen where a series of parameters were changed for each specimen.

- *Chapter 5* contains observations of the six experiments. Damage states were created to help monitor the damage throughout each test.

- *Chapter 6* contains an overview of the data analysis of the experiments. Data analysis includes, but is not limited to, investigation of strength, stiffness, energy dissipation, and residual drifts.

- *Chapter 7* details the development of a simplified rocking CLT wall numerical model that was validated by comparison to the experimental results presented in Chapter 6. This chapter also describes the results of nonlinear dynamic analyses of the prototype buildings using the simplified numerical model and comparing the results to the performance objectives presented in Chapter 3.

- *Chapter 8* provides a summary of the key findings from this research and recommendations for future study.

Chapter 2

LITERATURE REVIEW

2.1 Introduction

The proposed seismic force resisting system for tall timber buildings presented in this thesis builds upon research on cross laminated timber (CLT) as a structural material and research on the seismic behavior of systems allowed to rock at their base. This chapter will review previous studies in these areas that are relevant to the current study.

2.2 Cross Laminated Timber as a Building Material

Cross laminated timber (CLT) is an engineered wood product consisting of laminated boards glued in layers perpendicular to each other forming a panel. Typically the number of layers ranges from three to seven with thickness of each layer varying from 5/8 to 2 inches. Figure 2.1 shows the configuration of a CLT panel. The boards are sawn, visually graded or machine stress-rated, and kiln dried [Karacabeyli and Douglas, 2013]. Typical panel dimensions have widths ranging from 2 feet to 10 feet, lengths up to 60 feet, and thickness up to 20 inches [Mohammad et al., 2012]. CLT wall outer layers are generally oriented parallel to vertical loads to maximize the force resistance. For diaphragm applications, the outer layers run parallel to the major span direction.

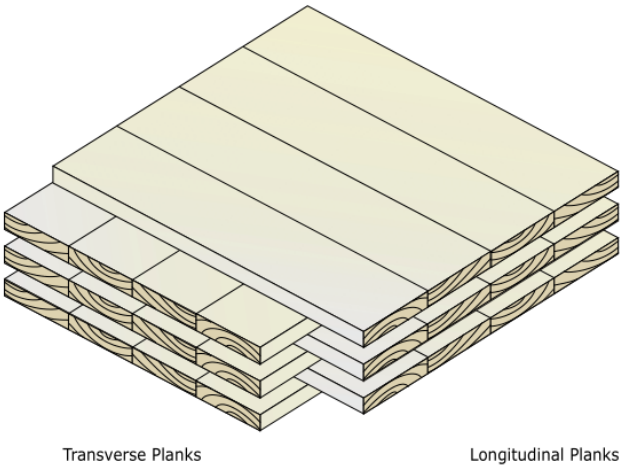

Figure 2.1: CLT Panel Configuration [Karacabeyli and Douglas, 2013]

CLT is a strong, versatile building material. Because of the alternating perpendicular layers, CLT has relatively high strength and stiffness in both in-plane directions which gives it two-way action capabilities similar to reinforced concrete slabs and makes CLT ideal for use in floor and wall applications. The cross lamination also increases the splitting resistance for certain types of connection systems. This differs from other engineered wood products, such as glulam and laminated veneer lumber (LVL), which have high strength in only one direction. Because CLT panels are light and prefabricated, they create ideal components for construction. CLT lends itself to fast construction speeds because panels can be lifted and maneuvered easily into place with cranes.

CLT was first developed in the 1990s in Austria and Germany and is now is being used in residential and non-residential buildings throughout Europe. CLT is gaining interest in the construction industry in the United States and Canada. A CLT product standard was developed and published by the ANSI/APA CLT Standard Committee [APA, 2012]. FPInnovations, a non-profit research institution for the Canadian forest industry, has published a handbook that summarizes design and construction procedures for CLT in U.S. and Canadian markets [Karacabeyli and Douglas, 2013].

2.3 Previous Tall Timber Research

2.3.1 Green and Karsh [2012]

Green and Karsh [2012] prepared a report focused on the feasibility and benefits of tall wood buildings. The study finds that the world's urban population is growing and will need more large buildings to accommodate the population growth. However concrete buildings, which are currently used to meet much of this demand, are not environmentally sustainable because of the large emissions resulting from the manufacturing of cement. Since the building industry is responsible for one third of all greenhouse gas emissions, Green and Karsh [2012] proposed tall wood buildings as a means to reduce the industry's environmental impact and potentially store carbon and other greenhouse gases.

Green and Karsh [2012] presented a series of tall wood buildings that are already built or in the process of being built. Highlighted examples included: (i) The Stadthaus, currently the second tallest timber residential building in the world, a 9-story CLT building that was successfully completed in London in 2008; (ii) Life Cycle One Tower, an 8-story mixed use tower consisting of CLT walls, glulam beams, and reinforced concrete slabs that was built in Austria and; (iii) A 16-17 story timber cultural center being planned for construction in Norway.

A series of case studies focused in Vancouver, BC were also presented in the research. Green and Karsh [2012] designed a group of concrete buildings and a group of replacement wood buildings. The concrete buildings all had the same floor plan and all had building heights of 10, 20 and 30 stories. The wood buildings, in the case study, were designed using the Finding the Forest Through the Tress (FFTT) system, a tilt up construction system using engineered wood panels. The panels, used for walls and floors, were integrated with engineered wood columns and steel beams and ledgers. Green and Karsh [2012] found that it is possible to design tall timber buildings using the FFTT system that are equivalent to the concrete reference buildings.

2.3.2 Ceccotti et al. [2013]

Ceccotti et al. [2013] performed an experimental investigation to assess the feasibility of building 7-story CLT buildings in seismic regions. CLT was chosen because of its lower weight to strength ratio in comparison with other materials such as masonry and concrete and its ductility obtained through proper design of joints with mechanical fasteners. Using the results from previous monotonic and reversed cyclic tests of CLT panels, pseudodynamic tests on a one-story CLT specimen, and a 1D shake table test on a full-scale 3-story specimen, a 3D shake table test on a full-scale 7-story building was designed and conducted.

The 3-story specimen was designed according to the simplified lateral force method in Eurocode 8 with a design peak ground acceleration (PGA_{design}) of 0.35 g which corresponded to a high seismic region in Italy. The building had a 10 meter story height and 7x7 meter floor area. To calculate seismic design forces, Eurocode 8 uses an initial behavior factor, (q), to reduce the buildings seismic acceleration response spectrum. The initial behavior factor, (q), is analogous to the response modification factor, (R), used in the United State's ASCE [2010]. The authors defined q as $PGA_{near-collapse}/PGA_{design}$ where $PGA_{near-collapse}$ is the peak ground acceleration recorded at a defined near-collapse state. Since overstrength and energy dissipation are unknown for CLT, they were not considered and thus the three-story specimen was designed with a q of 1.0 to be purely elastic. A $PGA_{near-collapse}$ of 1.20 g was recorded during the test. Using the defined equation for q, a value of 3.4 was calculated for the three-story specimen.

Ceccotti et al. [2013] designed the 7-story building with the force-based simplified lateral force method in Eurocode 8, using an initial behavior factor of $q = 3$ derived from the three story building test. The building had a total height of 23.5 meters and a 7.5x13.5 meter floor area. Plan and elevation views are shown in Figure 2.2. The floors and walls were constructed out of CLT. The wall to floor joint connections consisted of hold-downs, angle brackets, and self-drilling screws and were designed for the calculated story shears. The building was subjected to three different earthquake records. The first six motions applied

were in one direction with two different intensities and used 3D shaking.

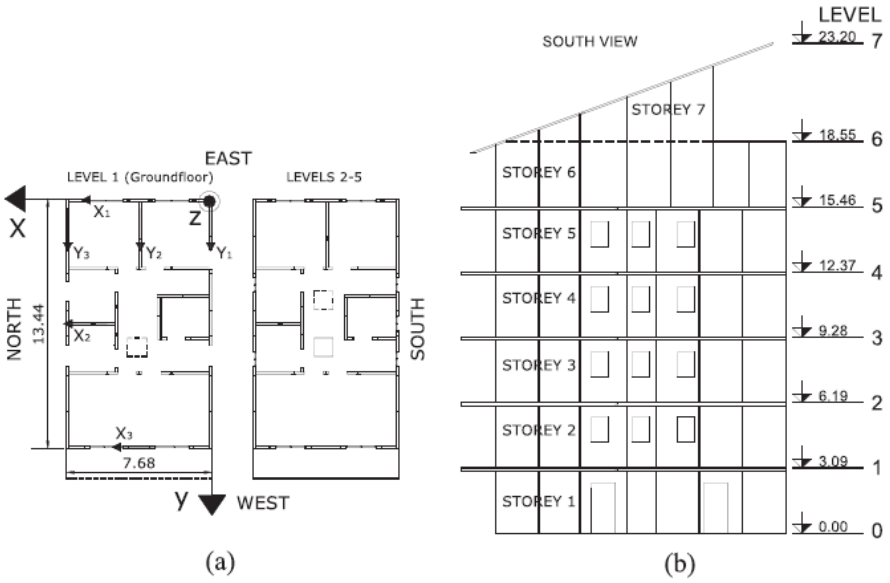

Figure 2.2: (a) Plan and (b) Elevation of the 7-Story Specimen [Ceccotti et al., 2013]

For all shake table tests, the building remained upright. The repair consisted mainly of tightening loose hold-down bolts and replacing bent and sheared screws. The CLT walls remained mostly elastic for all tests. The building had an average fundamental period of 0.37 seconds in the short direction and 0.53 seconds in the long direction. Because of damage throughout the test the periods were reduced to 0.28 seconds in the short direction and 0.47 in the short direction. Design forces could be reduced if the stiffness of the building was reduced. Ceccotti et al. [2013] determined the forced-based design in Eurocode 8 was a valid design procedure for CLT buildings. Figure 2.3 shows the design and test story shears. The error in the design story shears and the experimental story shears was 20% and 29% for the long and short direction respectively. Since the structure was designed to remain essentially elastic, high accelerations were experienced in the upper stories with a maximum acceleration of 3.8 g. While the test demonstrated sufficient structural strength and stiffness of CLT panels, the lack of reliable energy dissipation mechanisms and the elastic behavior

design method make implementation in high seismic zones in the U.S. difficult.

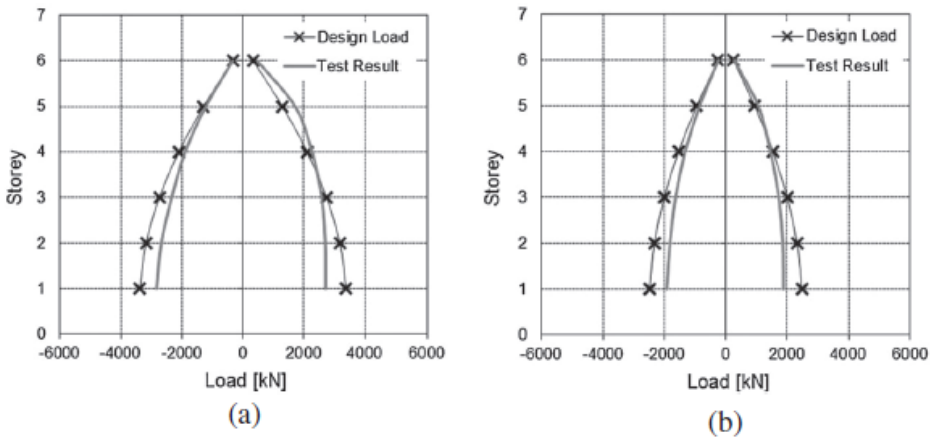

Figure 2.3: Story Shears for the (a) Long Direction, South Side and (b) Short Direction, East Side [Ceccotti et al., 2013]

2.3.3 van de Lindt et al. [2013]; Popovski et al. [2010]

van de Lindt et al. [2013] created a numerical model for the response of a CLT building. Figure 2.4 shows a simple kinematic model used to calculate the lateral force resistance of a single CLT panel. The panel is assumed to remain rigid and rotate about a lower corner. The lateral force resistance is calculated by summing the resistance to overturning from the weight (G) and the resisting connection force ($f_i(d_i)$).

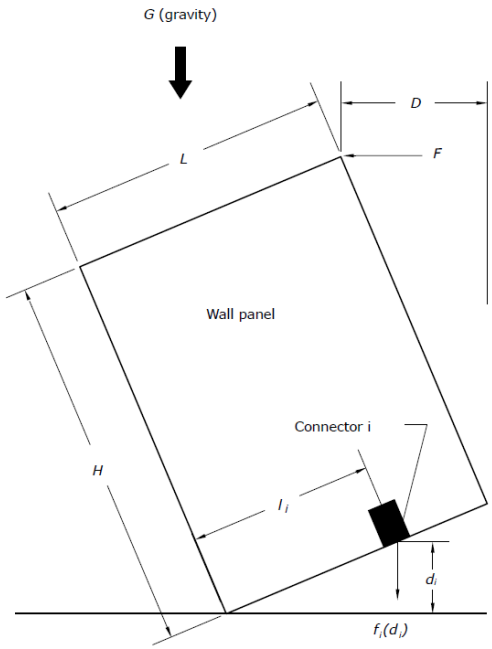

Figure 2.4: Kinematic Model of a CLT Panel [van de Lindt et al., 2013]

A force deformation relationship for the connection force was developed and calibrated from CLT wall experimental tests performed by FPInnovations [Popovski et al., 2010]. The test program consisted of 32 monotonic and cyclic tests of 3-ply, or 3 layers thick, CLT panels with a total thickness of 3.7 inches. Four different wall-to-foundation bracket connectors were used in 12 different wall configurations. One story specimens had aspect ratios (H:W) of 1:1 or 1.5:1 and two story specimens had an aspect ratio of 2:1. The CLT panels were connected to the foundations with bracket connectors shown in Figure 2.5. Screws, spiral nails, and timber rivets were used to connect the brackets to the CLT panels. Bracket A was a Simpson Strong-Tie AE116, 3.5x1.9x4.6 inch (WxDxH), Bracket B was a Simpson Strong tie ABR105, 3.5x4.1x4.1 inch. Both Bracket A and B were off-the-shelf products commonly used in CLT construction in Europe. Brackets C and D were custom made out of 0.25 inch thick steel plates and were connected with timber rivets.

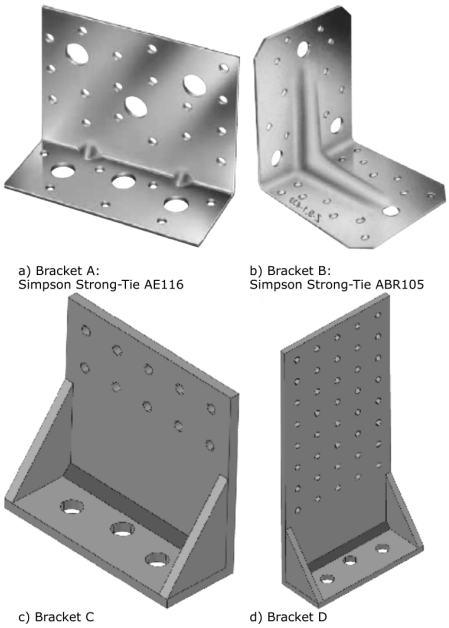

Figure 2.5: Bracket Connectors Used in CLT Experiments [Popovski et al., 2010]

The test setup is shown in Figure 2.6. The specimens were bolted to the foundation which consisted of steel I beams reinforced with stiffeners. Another steel I beam was bolted to the top of the CLT panels to distribute the lateral load. Lateral guides with rollers were used to ensure in-plane movement of the wall. Vertical load was applied with one or two 3 kip hydraulic actuators. The walls were subjected to either monotonic or cyclic lateral loading from a 24.7 kips hydraulic actuator.

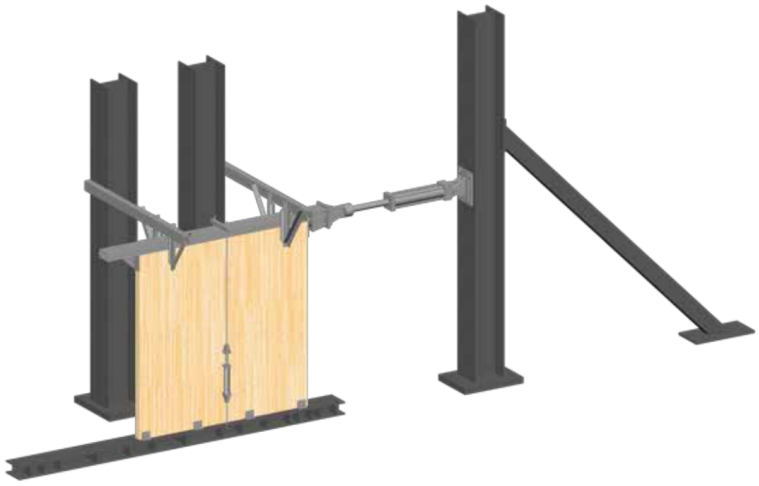

Figure 2.6: CLT Wall Experimental Setup [Popovski et al., 2010]

During testing, the walls behaved almost as rigid bodies with slight shear deformations in the panels, though most of the displacement was a result of the deformation in the braces connecting the wall to the foundation. A typical hysteretic force-displacement curve from a cyclic test and a monotonic pushover curve is shown in Figure 2.7. The walls with screws had similar capacity but lost strength faster when compared to the walls with nails. The specimens with hold downs showed the highest stiffness and ductility capacity. The walls with timber rivets showed higher capacity and stiffness than walls with nails or screws.

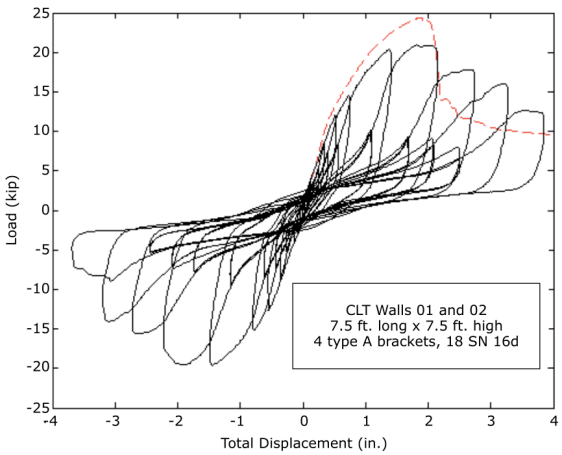

Figure 2.7: Experimental Results [Popovski et al., 2010]

van de Lindt et al. [2013] modeled the the connection hysteretic behavior using the Consortium of Universities for Research in Earthquake Engineering (CUREE) 10-parameter hysteretic model developed by Folz and Filiatrauult [2001] as shown in Figure 2.8. The CUREE 10-parameter hysteretic model has been widely adopted for wood frame shear walls and wood connection modeling. The 10 parameters are the initial stiffness (K_0), the four stiffness factors ($r_1 - r_4$), the peak displacement (X), the backbone tangent intersection (F_0), the loading path intersection (F_1), and the uploading stiffness (K_p). The model parameters were adjusted to match the numerical hysteresis with the experimental hysteresis for a series of connections. van de Lindt et al. [2013] developed a series of connection configurations and used the numerical model to develop corresponding CLT wall resistances for each configuration and connection type. Two of the calibrated models compared to the experiments are shown in Figure 2.9.

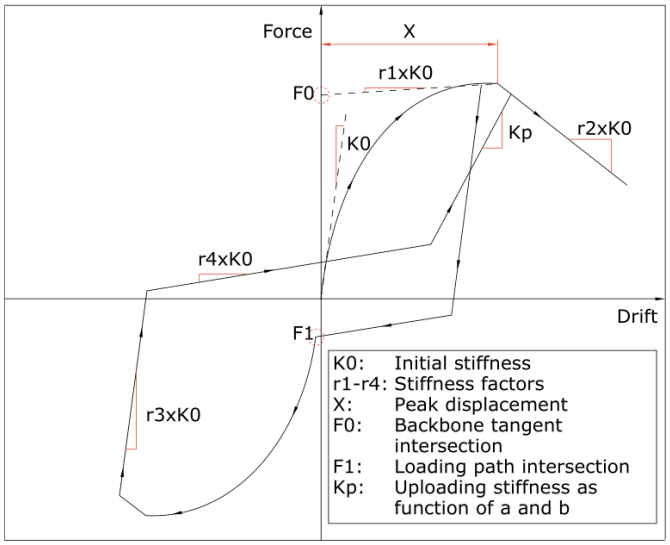

Figure 2.8: CUREE 10 Parameter Hysteric Model for Wall to Foundation Connections [van de Lindt et al., 2013]

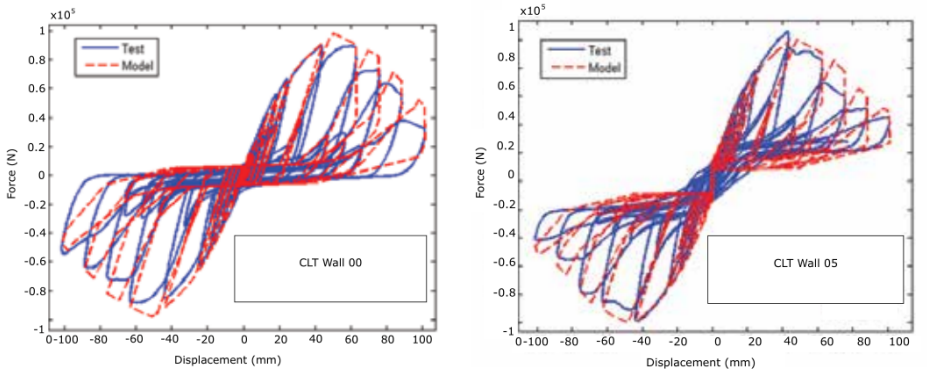

Figure 2.9: Calibrated CLT Wall Models Compared to Experiments [van de Lindt et al., 2013]

van de Lindt et al. [2013] used the numerical model to design a 6-story CLT building using the force-based Equivalent Lateral Force Procedure in ASCE 7-10 [ASCE, 2010]. The design strength of the walls was equal to ultimate load as determined from the numerical model divided by a factor of 2.5. Four different designs were completed using four different R-factors of 2, 3, 4 and 6. The performance of the structure was assessed numerically with a

suite of ground motions scaled to 2/3 and 1.0 of the maximum considered earthquake (MCE). The building was determined to remain stable up to a 3.5% drift ratio. The building showed adequate performance under 2/3 of the MCE with an R less than 4 and under the MCE with an R equal to 2. It should be noted that the building is assumed to collapse at 3.5% drift, but a collapse mechanism were not specifically modeled.

2.3.4 Pei et al. [2013]

Pei et al. [2013] expanded on research done by van de Lindt et al. [2013] by calculating an approximate seismic force reduction factor, R, for CLT walls with bracket connections. An estimation of R was calculated from computed inter-story drifts from a designed 6-story CLT apartment building located in a region with high seismic accelerations.

A performance-based seismic design (PBSD) was carried out for a 6-story CLT building located in Los Angeles, CA. The PBSD procedure used was based on a procedure developed by Pang et al. [2010] for mid rise, wood-frame buildings. Three performance objectives, taken from Pang et al. [2010], were used to design the building. The performance objectives were: (Level 1) a 50% nonexceedence probability of 1% drift when subjected to an earthquake representing the 50% in 50 year hazard level; (Level 2) a 50% nonexceedence probability of 2% drift when subjected to an earthquake representing the 10% in 50 year hazard level; and (Level 3) a 50% nonexceedence probability of 4% drift when subjected to an earthquake representing the 2% in 50 year hazard level. The total wall resistance per story was designed by using direct displacement design (DDD). Given the performance target and the story weight and height, story lateral resistance requirements at specific inter-story drift levels were calculated based on DDD. Three wall designs were used with three types of connections. The connection force resistances were calculated using the experimental results and hysteretic model from van de Lindt et al. [2013] by summing the computed backbone curves of each wall in a story to meet the target lateral resistances. The design was validated through nonlinear, time history analyses of the model subjected to a suite of 22 ground motions representing the three seismic hazards. During each analysis, the maximum inter-story drift

value at any story in any direction was recorded. These values were then used to create empirical cumulative distribution functions (CDF). The CDF values were then compared with the performance objectives. As shown in Figure 2.10, the building met the probability of non-exceedance values for the designated PBSD drift targets for Level 2 and Level 3. The Level 1 performance was approximately met and would not affect the overall performance of the building because the damage would be insignificant.

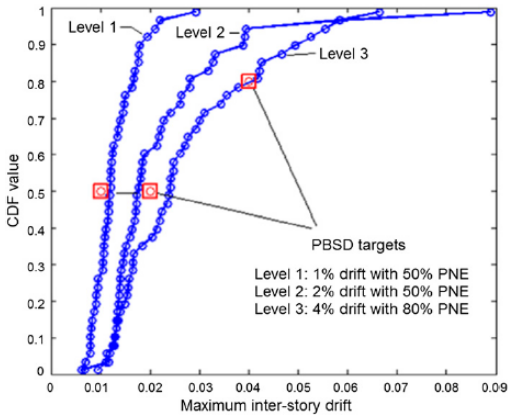

Figure 2.10: Performance of a Designed CLT Building [Pei et al., 2013]

Pei et al. [2013] calculated R for use in the ASCE 7-10 Equivalent Lateral Force Procedure (ELFP) [ASCE, 2010]. The building importance factor was set equal to 1.0 and the calculated building period, using the ASCE 7-10 simplified formula, was 0.4 seconds. The seismic hazard design values for a location in Los Angeles were obtained from the USGS design maps with a short-period design response spectra equal to 1.62 g and a design long-period response spectra equal to 0.57 g. The target story shears were obtained by adding the force resistance of all the walls at a story based on the wall resistances calculated from the PBSD. R was adjusted so that the forces computed from the ELFP were the same or higher than the target story shears. The R factors were computed for all three wall designs. Pei et al. [2013] determined an R of approximately 4.5 is appropriate for CLT wall components. This research provides a starting point for design of CLT buildings that needs to be expanded on.

2.4 Previous Structural Systems with Base Rocking Research

The first research project to introduce post-tensioned connections to reduce seismic component damage and provide recentering was the PREcast Structural Seismic Systems (PRESSS) program in the 1990s [Priestly, 1991; Kurama et al., 1999; Nakaki et al., 1999; Priestly et al., 1999]. PRESSS, discussed below, developed seismic resisting systems with post-tensioned precast beam-to-column connections and precast walls with post-tensioned base rocking connections. During the early 2000s, steel beams-to-column post-tensioned connections were developed by Ricles et al. [2001] and Christopoulos et al. [2001]. Eatherton et al. [2008] conducted experiments on braced frames allowed to rock about their base. Sause et al. [2010] conducted a series of large scale experimental studies on post-tensioned base rocking concentrically braced frames. Hasan et al. [2013] discussed how the the rocking effect of self-centering concentrically braced frame systems tends to cause more of a higher mode response than an equivalent fixed-base structure. Pollino and Bruneau [2008] developed a controlled base rocking pier for steel truss bridges and observed more of a higher mode effect due to the rocking action. An extensive research program at the University of Canterbury, New Zealand, discussed below, developed and tested post-tensioned connections for timber seismic systems referred to as Pres-Lam systems [Palermo et al., 2005, 2006; Iqbal et al., 2007; Smith et al., 2008]. This literature review will focus on post-tensioned base rocking connections and the mitigation of higher mode effects from these connections as these are the self-centering components used in this research.

2.4.1 PRESSS

Priestly [1991] coordinated research on seismically resilient systems under the PRESSS program. The PRESSS program developed a hybrid system consisting of unbonded post-tensioned (PT) concrete frame and wall systems combined with mild steel energy dissipation devices as shown in Figure 2.11a. The rocking motion (shown in Figure 2.11b), from unbonded PT connections, provided self-centering and the mild steel provided energy dissipation, resulting in flag-shape hysteretic behavior as shown in Figure 2.11c. The PRESSS program developed comprehensive design procedures and through a series of experiments showed the hybrid system had good ductility and minimal damage at large drifts.

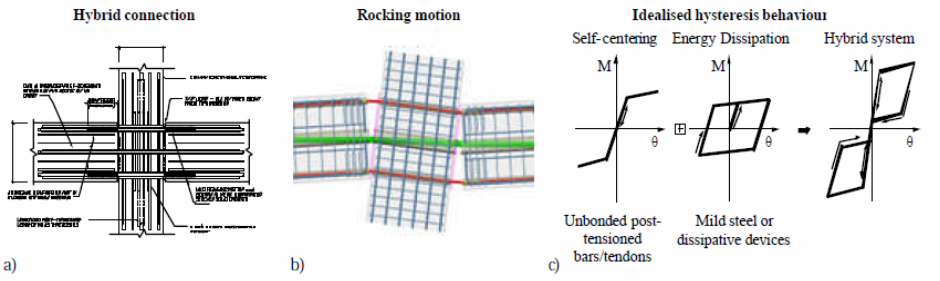

Figure 2.11: (a) Hybrid Connection, (b) Rocking Motion and (c) Hysteretic Cehavior of a Beam-Column Joint from the PRESSS program [Palermo et al., 2005]

Kurama et al. [1999] developed design equations for unbonded post-tensioned precast concrete walls that could lift off and rock at their base. Four states, shown in Figure 2.12 were created to define the behavior of the walls: (1) decompression state, defined as the initiation of a gap opening at the base; (2) softening state, defined as the beginning of significant reduction in lateral stiffness due to the gap opening; (3) yielding state, defined as the point at which the PT reaches its yield strain; and (4) failure state, defined as a axial-flexural failure in the wall as a result of concrete crushing.

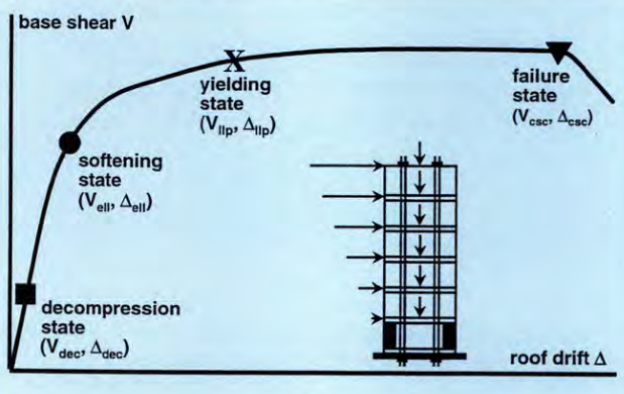

Figure 2.12: Behavior States for Unbonded Post-Tensioned Precast Walls [Kurama et al., 1999]

Kurama et al. [1999] used the behavior states to create a seismic design approach based on design objectives (Figure 2.13a) and design criteria (Figure 2.13b). The two objectives were: (1) to achieve the immediate occupancy performance level under the design level ground motion; and (2) to achieve the collapse prevention performance level under the survival level ground motion. The immediate occupancy performance level focused on keeping the wall linear elastic, and the collapse prevention performance level focused on preventing axial-flexural failure in the concrete and yielding in the PT. The design criteria consisted of computing force and displacement capacities of the wall that exceeded estimated demands.

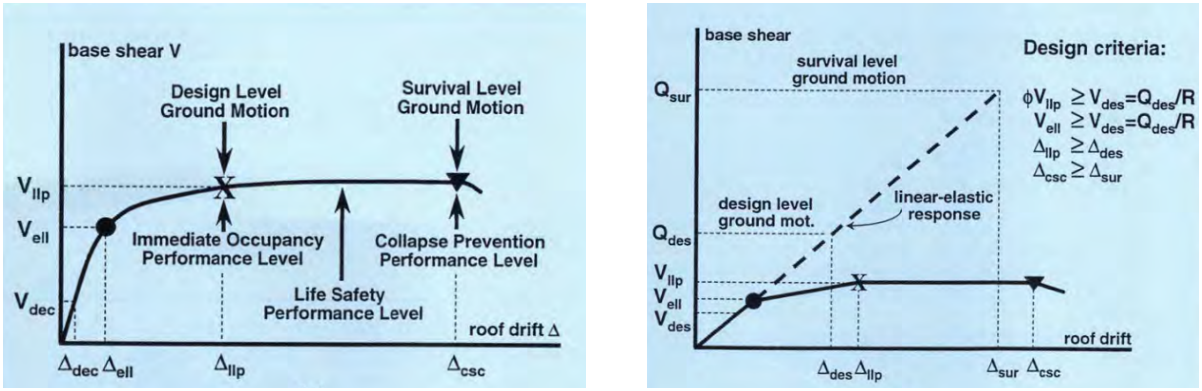

(a) (b)

Figure 2.13: Proposed Seismic Design Approach: (a) Design Objectives and (b) Design Criteria Kurama et al. [1999]

To validate the design procedure, Kurama et al. [1999] designed a series of prototype walls that were subjected to a series of nonlinear dynamic time-history analyses. The walls showed the desired flag shaped hysteretic behavior with large energy dissipation and self-centering capabilities. Kurama et al. [1999] concluded the unbonded PT precast walls provide more desirable behavior compared to conventional monolithic cast-in-place concrete walls in seismic regions.

Nakaki et al. [1999] designed a 60 percent scaled 5-story precast/prestressed concrete building that was tested under simulated seismic loading. The building was designed with the direct displacement based approach. The building had four different seismic rocking frame systems in one direction and a PT rocking shear wall system in the perpendicular direction. The shear walls were designed following the procedure laid out by Kurama et al. [1999]. U-Shaped flexural plates (UFP) were used to couple the shear walls and provide energy dissipation and damping by means of flexural yielding of the plates. UFPs, first developed by Kelly et al. [1972], are thin mild steel plates that are rolled into a U-shape and connect two structurally separated walls. When the coupled walls move laterally, the UFPs deform and yield dissipating energy. An elevation of the shear walls in provided in

Figure 2.14.

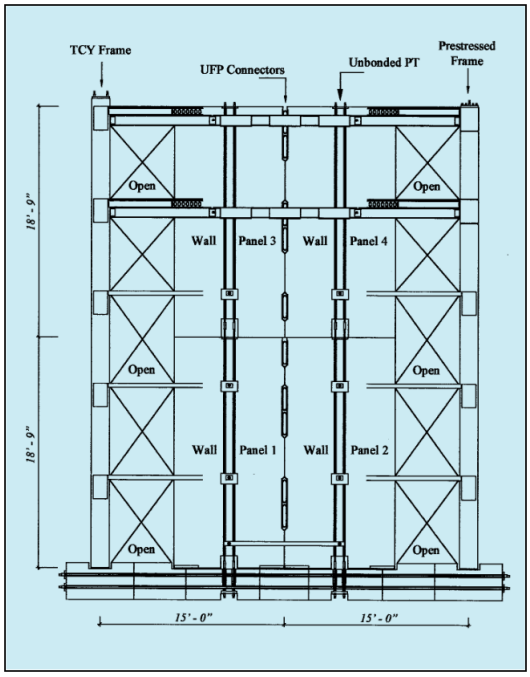

Figure 2.14: Elevation of PT Shear Wall System [Nakaki et al., 1999]

Priestly et al. [1999] tested the five story structure by loading it with a series of actuators mounted to each floor and to a reaction wall. The structure was tested under a displacement controlled pseudo-dynamic loading procedure that represented four different earthquake levels corresponding to 33, 50, 100 and 150 percent of a design level earthquake. After the test, the damage to the walls was minimal with cracking only developing at the base connection to the foundation. Minor crushing occurred at each end of the wall base at a height of about 6 inches above the foundation. This damage was considered cosmetic and could be easily repaired. The walls had considerable energy dissipation and strength as shown in the base moment versus roof displacement hysteresis for the highest level shaking (Figure 2.15).

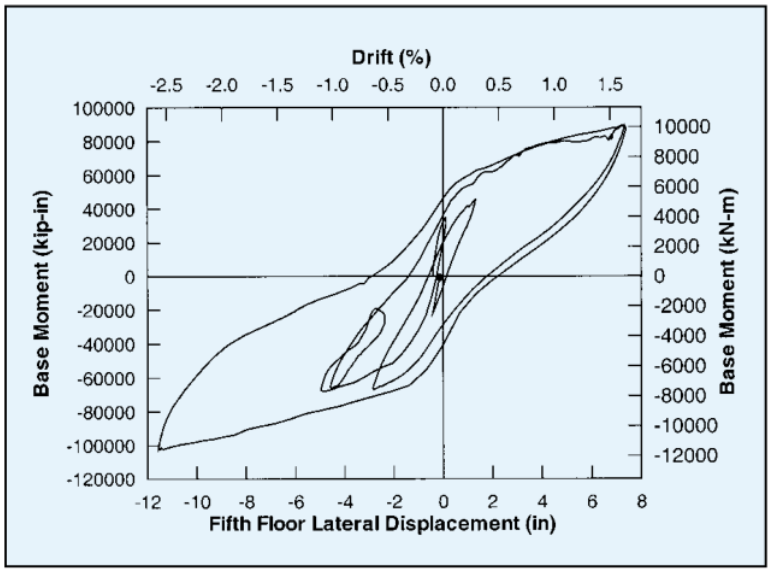

Figure 2.15: Wall Base-Moment vs. Roof-Level Displacement Hystersis Response [Priestly et al., 1999]

Priestly et al. [1999] developed analytical models to predict the experimental response of the 5-story test structure. The wall analytical model is shown in Figure 2.16a. The walls were represented by elements at their respective center lines and given structural properties based on the uncracked section of the concrete. The base of the walls was connected to the top of rigid horizontal links that were supported at each end by compression-only springs that were located at the calculated center of compression at each wall end under a rocking response. The compression springs were preloaded with an equivalent force representing the sum of the weight and the unbonded PT force. To simulate the elongation of the PT threaded bars, a spring with the appropriate properties was placed underneath each wall and was activated once the wall started to decompress. Each UFP was modeled with a vertical spring with the assigned UFP material properties. The vertical spring was connected to the wall elements through horizontal rigid links. Prior to testing, predictions were made by running an inelastic time-history analysis with the analytical model using the Ruaumokko computer program. Overall the analytical model had a fairly good prediction of the experiment. The overturning

moment comparison is shown in Figure 2.16b.

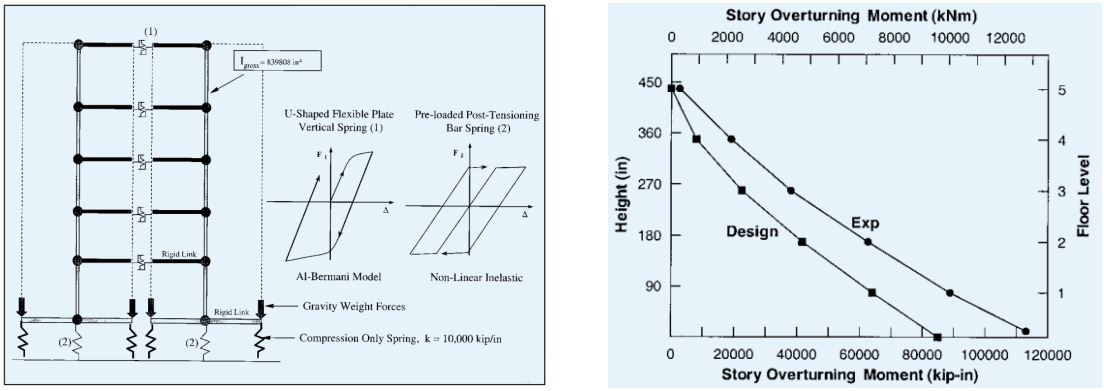

(a) (b)

Figure 2.16: (a) Wall Analytical Model and (b) Anaytical-Test Comparison [Priestly et al., 1999]

2.4.2 Pres-Lam

The seismic timber research program at the University of Canterbury developed and tested ductile post-tensioned beam-to-column, wall-to-foundation, and column-to-foundation connections for laminated veneer lumber (LVL) systems under seismic loading. These systems were named Pres-Lam systems. LVL was chosen over glulam and sawn lumber because it consists of 3 mm thick veneers that are staggered during processing such that the wood is thoroughly mixed and thus defects, such as knots, are randomized to a point where their influence on the material properties are negligible. The design of the timber rocking connections was an extension of the PRESSS program from concrete to timber.

Palermo et al. [2005, 2006] conducted cyclic quasi-static and pseudo-dynamic tests on PT only and hybrid rocking laminated veneer lumber (LVL) frames and walls. The single base rocking wall assembly was stressed vertically with two unbonded PT strands, and an actuator applied lateral load. The hybrid tests used internal and external mild steel bar dissipators that were fixed in the concrete base and epoxied to the LVL wall. A total of three hybrid

tests were performed (HY1, HY2, and HY3). The test setup for the wall assembly is shown in Figure 2.17. From the tests, Palermo et al. [2005, 2006] found good recentering and energy dissipation capabilities with minimal damage to the LVL walls. Figure 2.18 shows the force versus drift of the hybrid specimen with internal dissipaters (HY1). No visible wall damage occurred up to 3.5% drift for HY1 and HY2 and 4.4% drift for HY3. HY1 and HY2 were both stopped at 3.5% drift because of buckling failures of the energy dissipation devices. The PT strands did not yield in any of the tests.

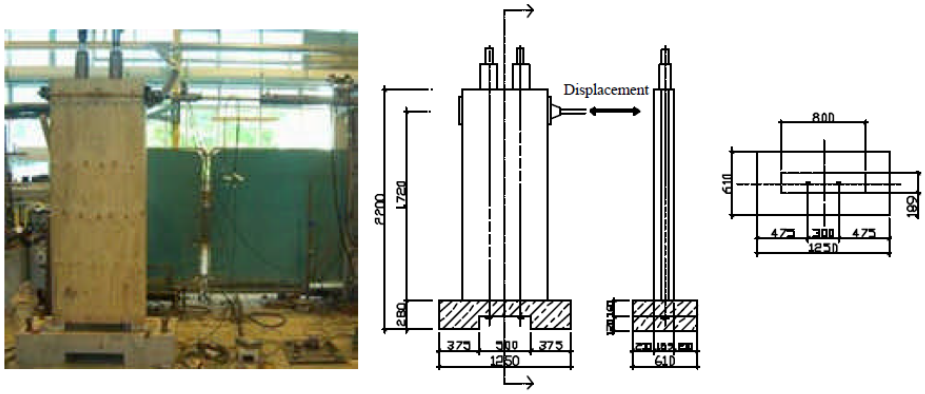

Figure 2.17: PT Wall Test Setup and Geometry [Palermo et al., 2006]

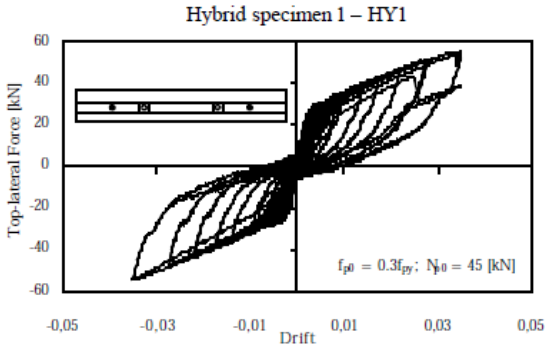

Figure 2.18: Lateral Force vs. Drift for the HY1 Specimen [Palermo et al., 2006]

Iqbal et al. [2007] expanded on the hybrid concept by Palermo et al. [2005, 2006] by conducting cyclic quasi-static and pseudo-dynamic tests on PT base rocking walls that used UFP devices instead of mild steel bars for energy dissipation. For the experiments, Iqbal et al. [2007] used two different sizes of UFPs. One of the UFP sizes and the corresponding energy dissipating hysteresis is shown in Figure 2.19 a and b.

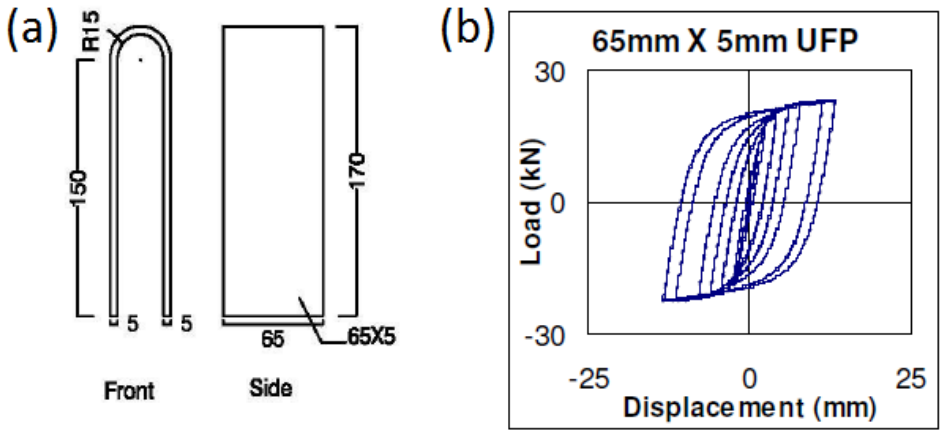

Figure 2.19: (a) UFP Geometry and (b) UFP Load-Deflection Plot [Iqbal et al., 2007]

The walls were tested in two configurations, a PT only system and a hybrid system. The hybrid system used the UFPs to couple the walls together. The test setup was similar to that used in Palermo et al. [2006] except with two walls coupled with UFP devices instead of one wall as shown in Figure 2.20. All walls were 2.5 meters tall, 0.78 meters long, and 0.195 meters thick. The wall aspect ratio (H:W) was 3.2:1. Figure 2.21 shows the lateral force verses top displacement hysteresis of a post-tensioned only and two hybrid tests. The quasi-static tests resulted in the desired flag shape hysteresis. Iqbal et al. [2007] discovered by combining different UFP arrangements with different PT forces, a comparable level of peak lateral force was reached with different overall values of dissipation. From the pseudo-dynamic tests, Iqbal et al. [2007] observed that the hybrid system had smaller peak displacements compared to the PT only system due to the additional energy dissipation from the UFPs. There were no

residual displacements and minimal damage was observed after the pseudo-dynamic tests.

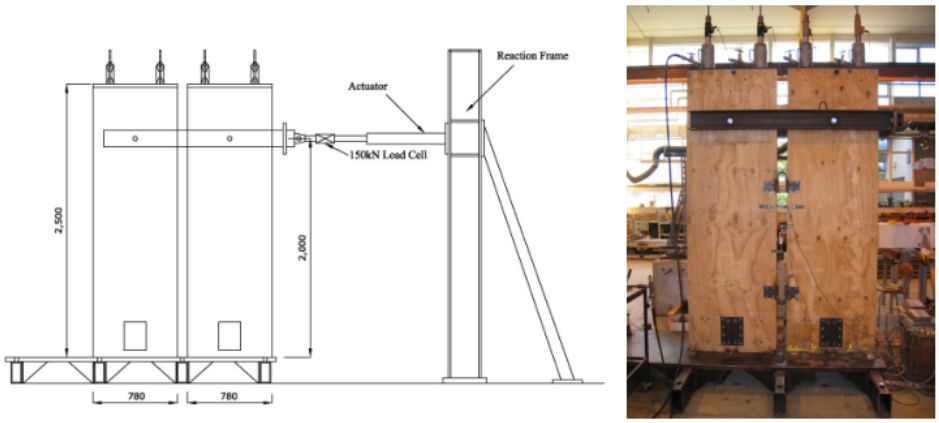

Figure 2.20: Coupled Wall Test Setup [Iqbal et al., 2007]

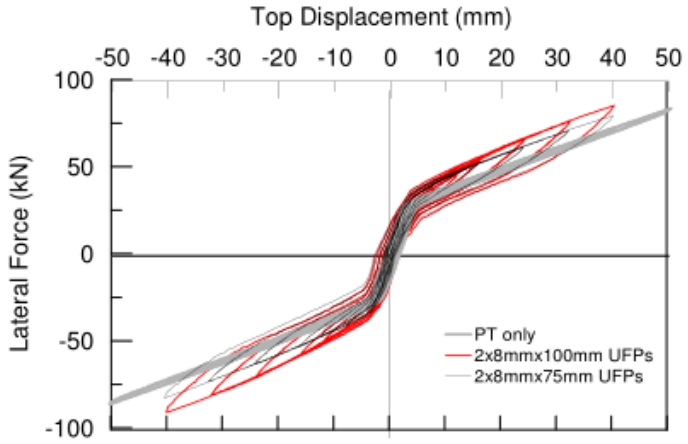

Figure 2.21: Force-Displacement Hysteresis of Coupled Wall Test [Iqbal et al., 2007]

Smith et al. [2008] redesigned a 6-story reinforced concrete building located in New Zealand with the Pres-Lam system. The seismic systems consisted of LVL frames with PT beam-to-column connections in one direction and walls with PT base connections in the perpendicular direction. Both lateral systems were designed using direct displacement design

with an inter-story drift limit of 2% for the frames and 1% for the walls.

The floor system was a timber composite deck consisting of LVL timber panels prefabricated off-site with a 65 millimeter cast-in-place concrete topping. The deck was supported by LVL floor joists supported on steel joist hangers. The floor joists framed into LVL beams which transferred the gravity load into the columns through corbels. In a seismic event, the in-plane shear force from the diaphragm was designed to be transferred into the lateral resisting system by either coach screws cast into the concrete topping and inserted into the side face of the beams (Figure 2.22a) or reinforcing bars connected to the solid wall through fixed bolts with threaded couplers (Figure 2.22b). To reach the desired moment capacity at the base of the columns and wall, steel dissipating bars were fixed into the foundation and epoxied into the walls or columns. A preliminary cost estimate was performed and it was found that the timber design was comparable to a structurally equivalent mixed concrete and steel design. Because of the prefabrication of many of the timber elements, it was estimated that the timber design construction would be faster than the mixed concrete and steel design.

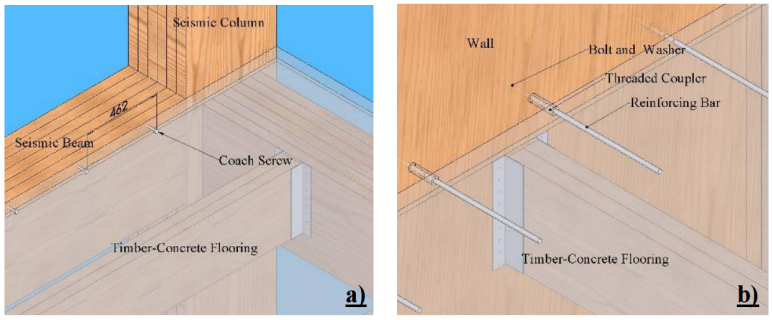

Figure 2.22: In-Plane Shear Transfer Mechanisms [Smith et al., 2008]

2.4.3 Wiebe et al. [2012a,b]

Wiebe et al. [2013a,b] studied the effect of adding a second rocking joint to a controlled rocking seismic system to mitigate higher mode effects. Base rocking systems tend to have long first mode periods and greater ductility demands and thus higher mode effects may significantly impact the higher mode response. The research focused on creating a numerical model to determine the effectiveness of a second rocking joint at mid-height of a building in reducing higher mode effects and validating the numerical model through experiments.

The multiple rocking joint design was implemented in a prototype steel braced frame 8-story office building placed in Vancouver, BC. A reference building with a buckling restrained braced frame (BRBF) seismic resisting system was analyzed to determine a design base moment for the controlled rocking building. The rocking frame was designed for the base moment taken from a pushover of the BRBF to 2.0% roof drift. Each rocking joint was designed for the rocking moment which was calculated as the sum of the moments from the weight of the frame, the post-tensioning, and the energy dissipation. The gravity moment was determined to be 10% of the base overturning moment; the PT moment was designed to carry 50% of the overturning moment; and the energy dissipation moment was designed to carry 40% of the overturning moment. The second rocking joint was assigned half the energy dissipation of the base rocking joint.

To assess structural performance Wiebe et al. [2013a] modeled the rocking system in OpenSees [Mazzoni et al., 2009]. The predicted results showed the base shear and overturning moment are reduced with the implementation of a second rocking joint as shown in Figure 2.23. To validate the numerical model, Wiebe et al. [2013a] carried out an experimental investigation on the prototype building. The experimental setup was scaled to 30% of the prototype building and subjected to a suite of ground motions though shake table tests. Because of the available PT tendon sizes the PT force could not exactly replicate the prototype building. Instead the PT provided 58% of the base overturning moment at 2.0% roof drift, and the energy dissipation provided 32%.

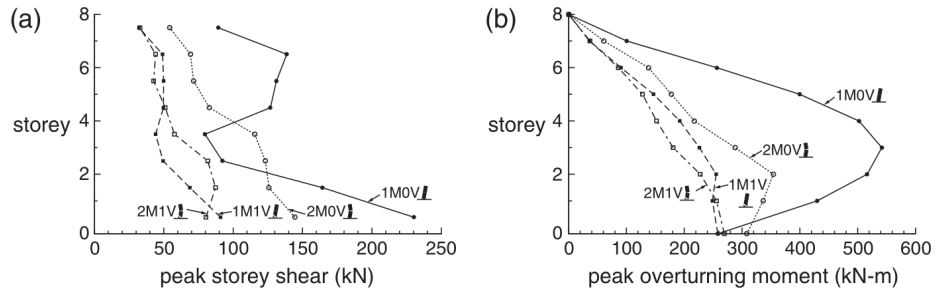

Figure 2.23: Predicted Envelopes for All Configurations During a Record at the 2% in 50 Year Hazard Level: (a) Story Shear and (b) Overturning Moment [Wiebe et al., 2013a]

The first part of the experimental program was a series of small amplitude tests that focused on a suite of ground motions consisting of two Service Level Earthquakes (SLE) and three Design Based Earthquakes (DBE), which corresponded to 50% and 10% in 50-year events respectively. Figure 2.24 shows the story shear force and overturning moment envelopes from the experimental and numerical results for the DBE-3 record. 1M0V and 2M0V signify one and two rocking joints respectively. The other markers are for a nonlinear brace addition which is beyond the scope of this thesis. Figure 2.24 shows that the story shears and overturning moments were reduced by adding a second rocking joint. Wiebe et al. [2013a] did not observe a sizable increase in peak story drift when the second rocking joint was added. Overall Wiebe et al. [2013a] observed good agreement between the numerical model and experimental results.

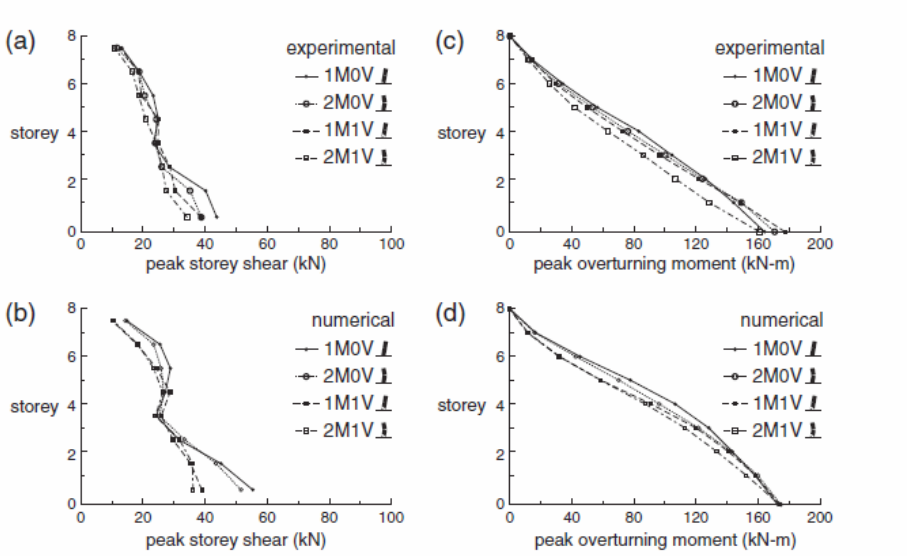

Figure 2.24: Results from the experimental and numerical testing with the DBE-3 record [Wiebe et al., 2013a]

To verify the influence of higher modes on rocking systems and determine if a second rocking joint will mitigate those effects, Wiebe et al. [2013b] conducted further experiments using large amplitude ground motions that included two simulated Cascadia Subduction Zone (CAS) motions that had relatively small spectral accelerations at short periods, two Eastern North America (ENA) motions that had relatively small spectral accelerations at long periods and large spectral accelerations at short periods that are associated with higher modes of response, two Maximum Considered Earthquake (MCE) motions that corresponded to a 2% in 50-year event, and a series of incremental (INC) motions that were based on a MCE-level event scaled from 25% to 200%.

Fifty-six large amplitude shake table tests were performed on the test frame with no apparent damage. Like the small amplitude tests, Wiebe et al. [2013b] did not see a large increase in the peak story drift when the second rocking joint was added. The moment-rotation behavior of the rocking joints followed the desired flag-shape hysteresis. There was little deviation in the story shears of the configurations for the CAS-1 motion, which did

not excite higher modes. The ENA-1 motion, which did excite higher modes, showed a large variation in the story shears for the different configurations. When the second rocking joint was added to the structure, the base shear was reduced by 18% and the story shears throughout the height were greatly reduced by up to 54%. Similar reductions were observed in the INC suite of ground motions as shown in Figure 2.25a. The upper stories of the single rocking configuration were influenced by the second mode. When a second rocking joint was added at mid-height, the story shears in the upper stories were greatly reduced. Like the story shears, the overturning moments from the CAS-1 record did not deviate for the two configurations. The base overturning moments from the ENA-1 motion were similar for both configurations, but there was a reduction of 58% in the overturning moments at the fourth story. Similar results are shown for the INCR suite of motions in Figure 2.25b. As the INCR ground motions were scaled up, the moments increased more rapidly for the single rocking joint structure compared to the double rocking joint structure. Wiebe et al. [2013b,b] concluded that by adding a second rocking joint to a controlled rocking structure, force demands can be reduced when higher mode effects are present.

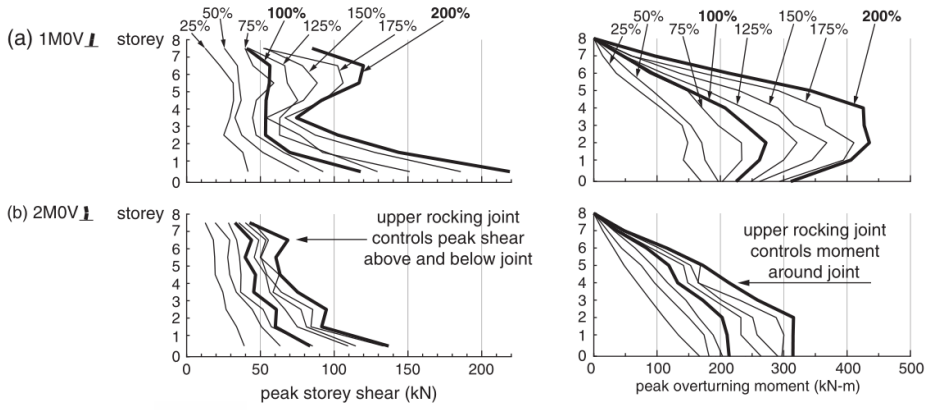

Figure 2.25: (a) Story Shear and (b) Overturning Moment Envelope for INCR Suite of Motions [Wiebe et al., 2013b]

2.4.4 Spieth et al. [2004]

Spieth et al. [2004] developed and compared a series of modeling methods to simulate the behavior of a precast prestressed concrete frame rocking joint. One of the methods that particularly lends itself to base rocking connections was the multispring modeling approach. The multispring element model consisted of a series of zero tension, compression only springs that were distributed along the length of the contact area as shown in Figure 2.26. A overall contact stiffness was determined and weighted or distributed to the springs. Spieth et al. [2004] determined rocking joints have highest local stiffness and strength at the center of the section, and the local stiffness and strength decreases as the point of contact moves towards the edge. Spieth et al. [2004] looked at two methods to distribute and weight the springs along the contact surface: Gauss Quadrature Integration and Labatto Integration. Gauss Integration had the disadvantage that no spring was ever positioned at the edge of the contact area, while Labatto Integration placed a spring at the each edge of the contact area. This model was similar to the PRESSS wall analytical model [Priestly et al., 1999] except instead of only two compression only springs positioned at the edges of the contact surface, the multispring model has additional springs along the base.

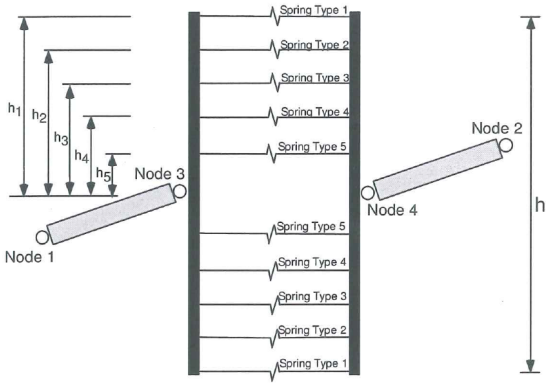

Figure 2.26: Schematic of Multispring Contact Element [Spieth et al., 2004]

Spieth et al. [2004] conducted an experimental test of a concrete beam-to-column con-

nection with a post-tensioned bar. Spieth et al. [2004] compared the multispring model to the experimental model. Spieth et al. concluded that as more springs were used in the multispring model, it converged the experimental results as shown in Figure 2.27. Overall Spieth et al. [2004] found the model was accurate in modeling rocking joint behavior and had low computational cost.

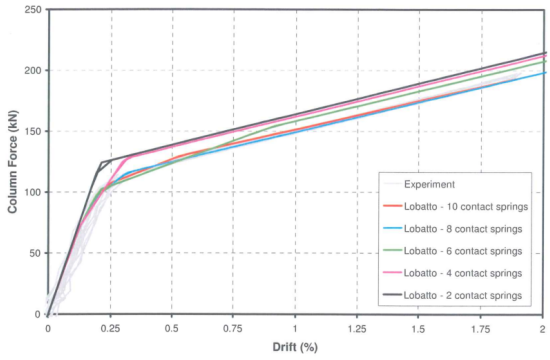

Figure 2.27: Column Force-Drift of Experiment and Multispring Element with Lobatto Integration [Spieth et al., 2004]

2.5 Conclusions and Research Needs

The research presented in this chapter has addressed the following conclusions:

- CLT is a strong, versatile building material. CLT is a renewable resource and the production has a low environmental impact.

- Research has been conducted on the feasibility of using CLT walls with mechanical connectors for seismic resisting systems. While CLT panels showed sufficient structural strength and stiffness, they essentially remained elastic which is not feasible for regions with high seismicity. The mechanical connectors used for lateral resistance do not have the ductility required for the resistance of forces due to high seismic accelerations.

- Design methodologies and experiments of concrete and timber rocking walls with post-tensioned base connections and mild steel dissipation devices have shown ductile behavior, good energy dissipation, and self-centering characteristics that are important for designing seismic systems for regions with high seismic accelerations.

- Research has shown that rocking systems have considerable contribution to the total response from higher modes when compared to equivalent fixed base systems. A way to reduce these higher mode effects is to add a second rocking joint at a location above the base rocking joint.

- Modeling rocking joints with a series of compression only springs that are distributed along the contact area and have weighted strength and stiffness relative to a defined contact stiffness has shown good correlation to experimental results.

Because of the world's growing population there is a need for new construction of tall buildings. Building materials used must have a low impact on the environment. CLT has the capabilities to meet this need, however there currently is not a structural system for CLT construction that would be feasible for regions with high seismic accelerations and that exhibits resilient seismic performance (i.e. little damage in frequent earthquakes and collapse prevention at the MCE). By using CLT walls with post-tensioned base connections, a resilient, ductile system can be developed that under high seismic accelerations remains damage-free, exhibits high energy dissipation, and has self-centering characteristics.

Chapter 3

STRUCTURAL BEHAVIOR AND SEISMIC DESIGN OF ROCKING CLT WALLS

3.1 Introduction

In this chapter, the structural behavior of the rocking CLT wall system is explained and a simple cross-sectional analytical model is presented for the estimation of the lateral load capacity. A set of performance objectives is presented along with a design procedure to meet these performance objectives. The design procedure is used to design a series of prototype wood buildings.

3.2 Rocking CLT Wall Structural Behavior and Considerations for Analysis

This section describes the structural behavior of rocking CLT walls and discusses the considerations and constitutive models used to estimate moment-rotation behavior in the cross-sectional analysis for use in design.

Two possible building configurations for the rocking CLT wall system, shown in Figure 3.1, are: (1) certain stories with rocking CLT walls, while other stories would be constructed more conventional lateral resisting CLT walls with mechanical connectors and (2) a core system with segmental rocking walls. The single rocking story configuration is the focus of this work.

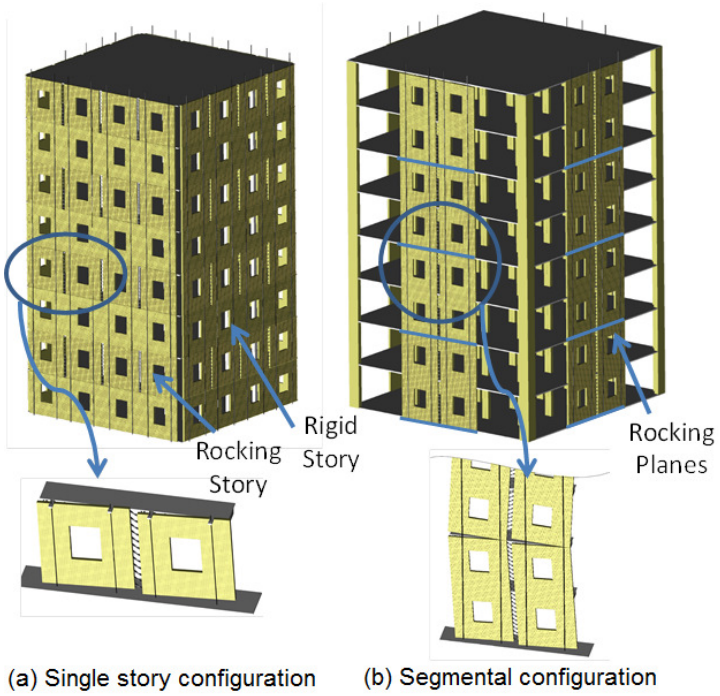

Figure 3.1: Two Rocking CLT Wall Configurations

The single story rocking CLT wall system, shown in Figure 3.2, consists of post-tensioned (PT) CLT panels supplemented with U-shaped flexural plates (UFP) for energy dissipation. The placement of the rocking stories is elaborated on later in this chapter. To resist lateral load, the conventional CLT walls use hold down connections from the wall to the floor diaphragm such as those used in previous CLT wall studies such as Popovski et al. [2010] and Ceccotti et al. [2013]. Because of the use of hold down connections, the conventional CLT walls will be refereed to as hold down walls (HDWs).

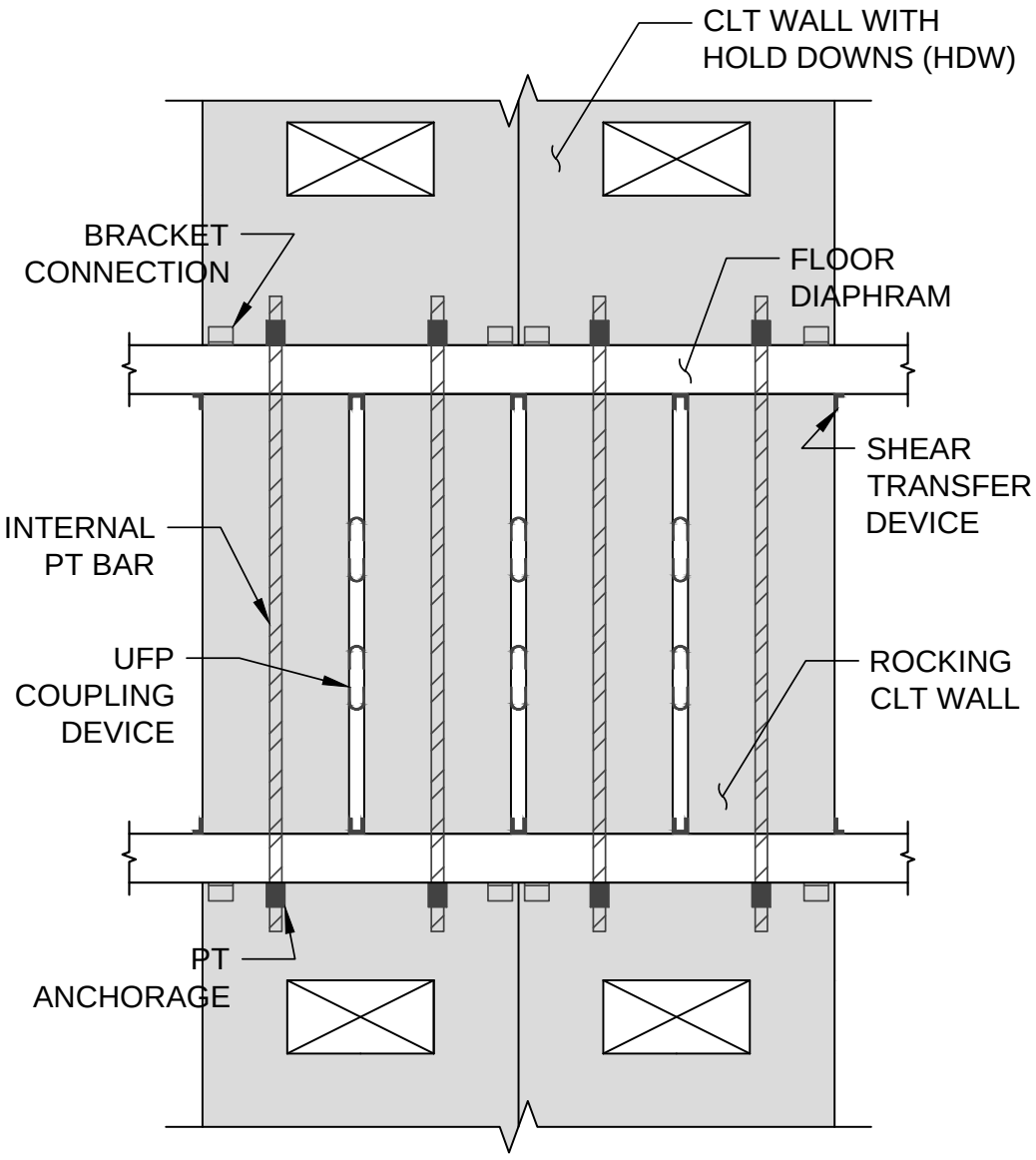

Figure 3.2: Schematic Elevation of Intermediate Story of the SC-CLT Wall System

3.2.1 CLT Panel Behavior and Modeling Considerations

This section discusses the stress-strain behavior of CLT and a simplified constitutive model that was used in the cross-sectional analysis procedure in Section 3.3 and the numerical model in Chapter 7.

Because it once was a living organism, wood is a very unique building material. Material properties of individual timber boards can vary based on factors in the parent tree's environment such as soil conditions, moisture, and growing space [Kretschmann, 2013]. The primary strength of wood comes from tubular cells or fibers that during the tree's life are used to transport water and nutrients throughout the tree. Sawn lumber is cut from a tree trunk such that the length of the board is along the height of the tree or length of fibers as shown in Figure 3.3a [Wiedenhoeft, 2013]. Because of the varying directions of the wood cells, wood is an anisotropic material and has different material properties in three perpendicular directions as shown in Figure 3.3b [Kretschmann, 2013]. The strongest direction (longitudinal direction) is parallel to the fiber direction and the two weaker directions, tangential direction (which is tangent to the growth rings) and radial direction (which is perpendicular to the growth rings), are perpendicular to the fiber direction. A knot causes an interruption of continuity and change in the direction of the wood fiber [Kretschmann, 2013]. A knot is caused by a branch that extruded from the tree trunk at that point. Knots reduce the local strength and increase the chances of splitting at their location.

The material properties of CLT are a conglomerate of the material properties of the individual perpendicular boards that make up the wood product. Like the wood boards that make up CLT, CLT has has three principal directions with three different sets of material properties. For CLT the direction of grain refers to the direction of grain of the outer boards.

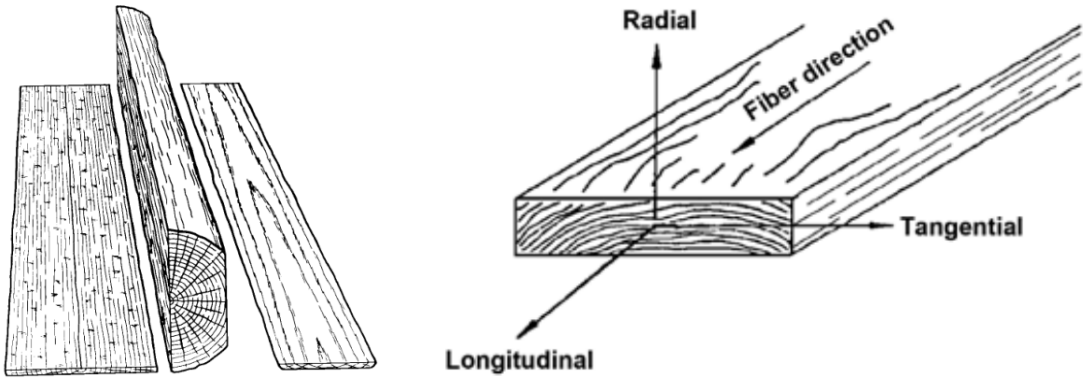

(a) (b)

Figure 3.3: (a) Sawn Lumber [Wiedenhoeft, 2013] (b) and Wood Fiber Directions [Kretschmann, 2013]

Generally, when subjected to axial tension, timber exhibits linear elastic behavior and fails in a brittle manner. When subjected to axial compression, timber exhibits nonlinear, ductile behavior by reaching a yield strength and then showing a slight decreasing yield plateau. This typical stress-strain relationship is shown in Figure 3.4a [Buchanan, 1990]. As discussed earlier, it should be noted that the strength and stiffness in the parallel to grain direction is much higher than in the perpendicular grain direction.

The CLT panels in the rocking CLT wall system experience compression and shear. Since the walls uplift at the base, they do not experience tensile stress and thus for the stress-strain relationship compression is only considered. CLT exhibits the same nonlinear, ductile behavior in compression as discussed previously. An example of experimental stress-strain behavoir of CLT, calculated from a series of $19\frac{1}{2}$ inch long CLT Columns tested by Horvat [2013], is shown in Figure 3.4b.

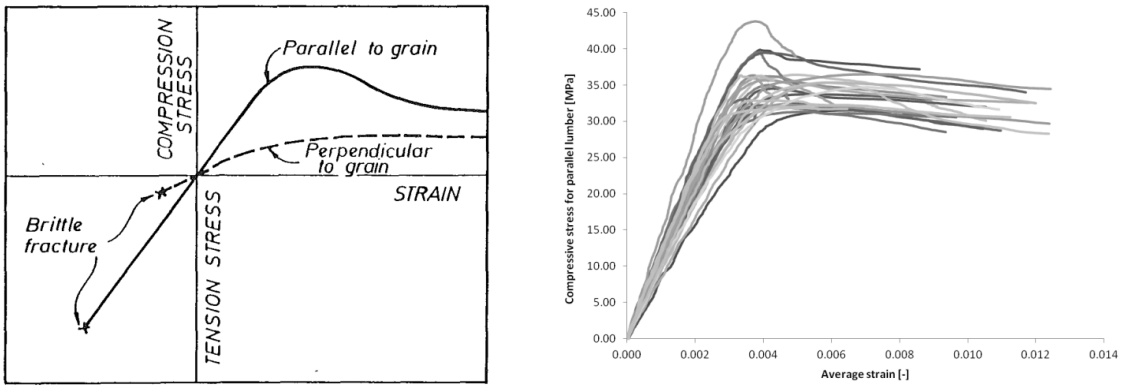

(a) (b)

Figure 3.4: (a) Stress-Strain Behavior of Wood [Buchanan, 1990] (b) and CLT [Horvat, 2013]

In the cross-sectional analysis procedure described in Section 3.3, an elastic-perfectly plastic material model is assumed to model the stress-strain behavior of CLT. Even though the CLT behavior in Figure 3.4b has a slight decrease in strength after yield, a perfectly plastic yield plateau is assumed for simplicity. The approximate elastic-perfectly plastic stress-strain behavior is shown in Figure 3.5. Material properties for the constitutive model of the CLT used in analysis of the walls were chosen from experimental results presented in Chapter 6 and material tests on short column specimens presented in Appendix A. The material properties for the longitudinal direction or parallel to grain in the outer plys or boards of CLT walls were used because the rocking CLT walls experience compression stress in that direction.

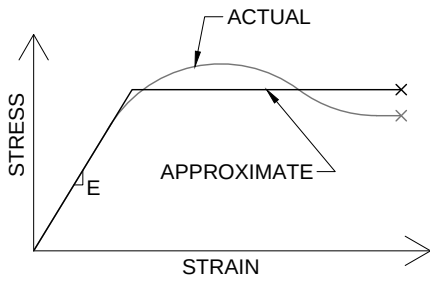

Figure 3.5: Assumed CLT Constitutive Model

3.2.2 Post-Tensioned Connections

Instead of a traditional fixed bracket connection to connect the walls to the floor diaphragm, the rocking walls use PT connections, which are created by tensioning a PT bar placed in a cavity of a CLT panel and anchored to the floor diaphragm above and below the wall, thus initially putting the CLT panel in compression. Before decompression, or the point when a gap opens at the connection interface, the wall behaves as a fixed CLT wall and the lateral load is resisted by the wall causing elastic deformations.

At a certain lateral load, the moment due to the the lateral load, M_{dec}, will overcome the moment due to the gravity load, W, and the initial PT force, T_0, causing a gap, θ_{gap}, to form at the interface between the wall and the floor diaphragms as illustrated in Figure 3.6. The decompression moment is then calculated as follows:

$$M_{dec} = (W + T_0)\, d \tag{3.1}$$

where d is the moment arm length between the PT tension force and weight at the top of the wall and the resulting CLT panel compression force at the base of the wall. Note that as the wall rocks, the PT tension force and the weight are transferred through the portion of the

wall that is still in contact with the floor diaphragm. At the onset of decompression, the shear force due to the UFPs, V_{UFP} is essentially zero and does not contribute to the decompression moment because the UFPs have not yet deformed substantially. A formulation for d at decompression is presented in the following section analysis procedure.

Once the connection has decompressed the moment due to the lateral load is balanced by a resisting moment, M_i, due to the force couple between the the gravity load, the PT force, T, and the wall compression force, C. As the story drift, θ_s, increases, the gap opening increases, the PT elongates, and the PT force increases causing the resisting moment to increase. As the story drift decreases, the gap opening closes and the PT tension force supplies a restoring moment causing the wall to recenter. Also as the story drift increases, the shearing force due to UFP deformation, V_{UFP}, contributes to the moment resistance. However the additional moment due to the UFP is small in comparison to the PT moment couple. A free body diagram of a intermediate SC-CLT wall story showing the external lateral forces and the internal restoring forces is shown in Figure 3.6. The total moment resistance of a rocking story can be calculated by summing the individual resisting moments of each wall in that story as follows:

$$M_i = \sum_{1}^{n_w} (T + W)\, d + \sum_{1}^{n_{UFP}} V_{UFP} L_w \tag{3.2}$$

where n_w is the number of walls in the rocking story, n_{UFP} is the number of UFPs coupling two walls together, L_w is the length of an individual panel, and V_w is the shear resistance for each wall. A section analysis procedure for calculating the moment resistance for an individual wall was developed and explained below. A calculation for the UFP shearing force is also explained below. The shear force is transferred from the upper floor diaphragm to the CLT panels through a shear transfer mechanism that is beyond the scope of this thesis. It should be noted that small values of θ_s and θ_{gap} are assumed and thus the horizontal component of T can be ignored and T is resolved into the vertical component.

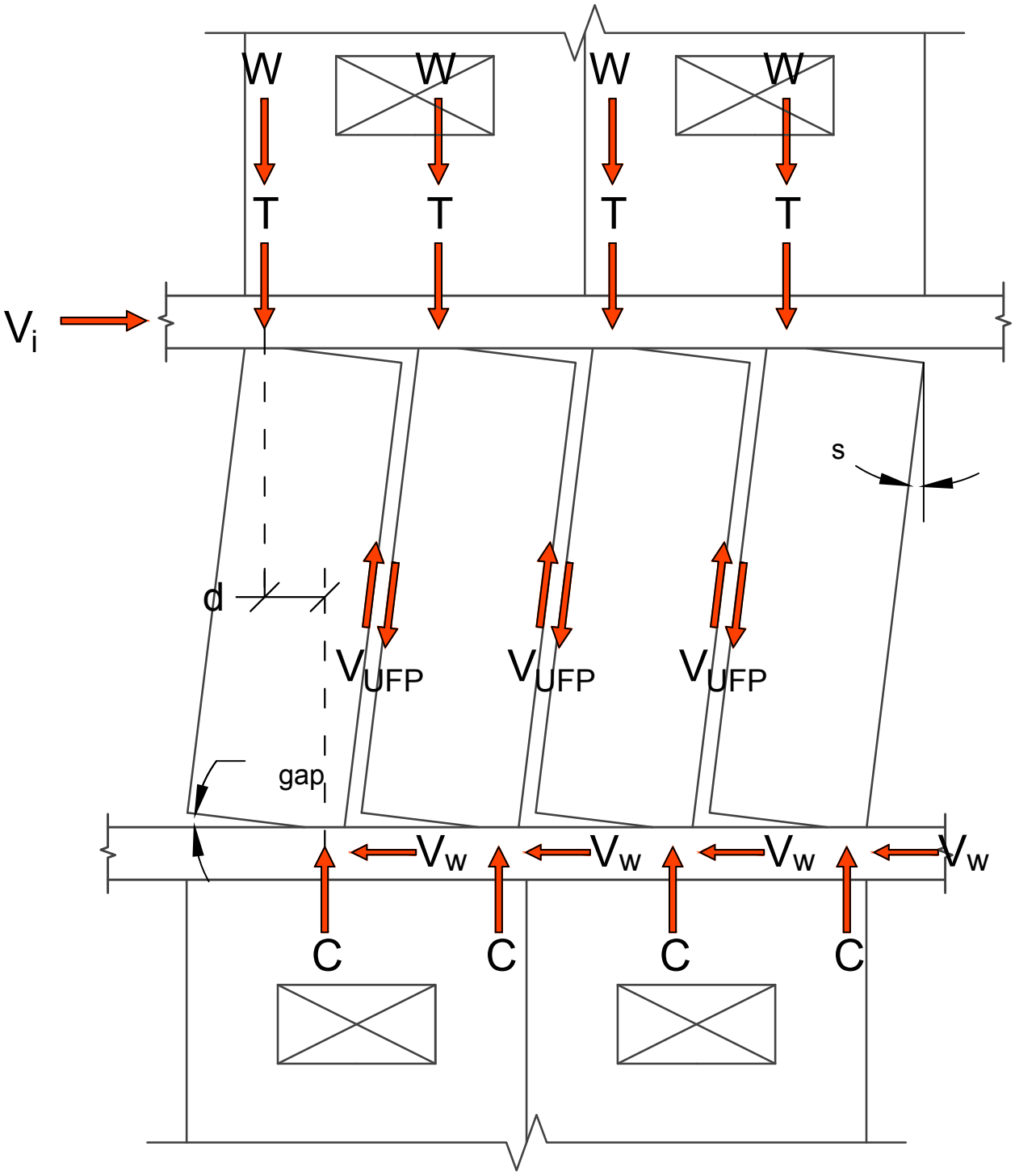

Figure 3.6: Free Body Diagram of Deformed Intermediate Story of the SC-CLT Wall System (Note: small θ_s assumed)

3.2.3 UFP Energy Dissipating Devices

For the rocking CLT wall system studied here, U-shaped flexural plates (UFPs) are used as the primary energy dissipation mechanism. UFPs are made by rolling a thin mild steel plate about a fixed radius to form a semicircular shape with two equally straight sections on either side. A schematic of a UFP with the dimensions is shown in Figure 3.7a. When one side of a UFP is displaced vertically relative to the opposite side, work is done as the radius of curvature changes at the two points where the straight and semicircular sections meet. As the UFP is cycled, yielding will occur at the two points, which will move along the plate. Once the entire surface of the UFP has yielded, the maximum UFP force, F_p, can be estimated by equating the shear couple to the sum of the plastic moments, M_p, as shown in Figure 3.7b Kelly et al. [1972]:

$$M_p = f_y Z = \frac{1}{4} f_y b_u t_u^2 \tag{3.3}$$

$$F_p = \frac{2M_p}{D_u} = \frac{f_y b_u t_u^2}{2D_u} \tag{3.4}$$

where, f_y is the yield stress of the mild steel, Z is the plastic section, b_u is the width, t_u is the thickness, and D_u is the bend diameter.

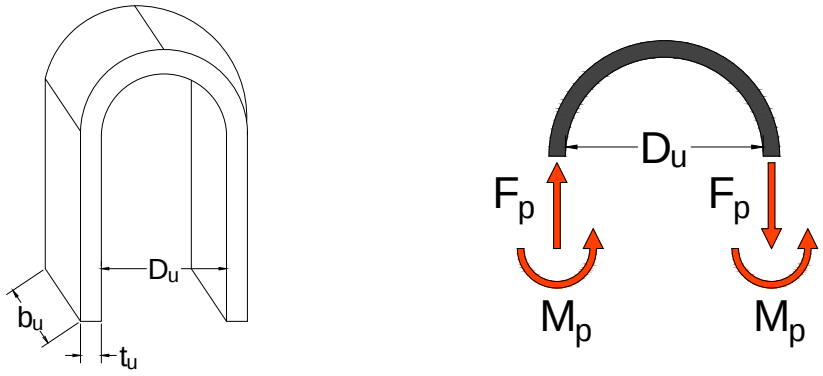

(a) (b)

Figure 3.7: (a) UFP Dimensions and (b) Free Body Diagram [Baird et al., 2014]

For modeling purposes it is important to be able to estimate the initial stiffness of the UFP. By calculating the yield displacement through energy methods, the initial stiffness can be calculated as [Baird et al., 2014]:

$$k_0 = \frac{16Eb_u}{27\pi}\left(\frac{t_u}{D_u}\right)^3 \tag{3.5}$$

where, E is the modulus of elasticity of the mild steel.

In the rocking CLT wall system, UFP devices are mounted in between the rocking CLT panels to couple them together. The UFP is attached to a steel saddle or an embedded plate with either bolts or a site weld as shown in Figure 3.8. This provides easy UFP replacement after an event. During an earthquake, once the story experiences lateral drift and the walls decompress, the UFPs deform and yield thus dissipating energy. In compression the CLT panel shows inelastic, ductile behavior at high drifts and also contributes to the energy dissipation in the system, however for design, the desired energy dissipation will be calculated considering only the UFP deformation.

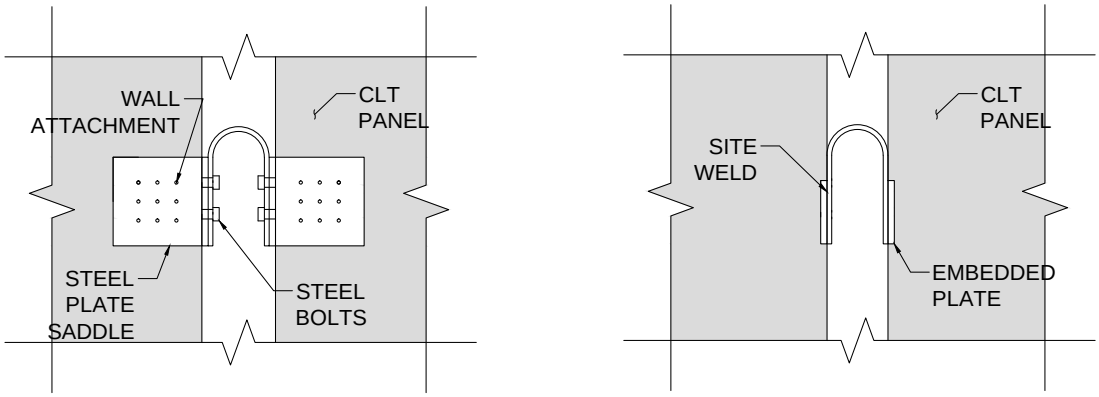

(a) (b)

Figure 3.8: UFP Connection: (a) Steel Plate Saddle Bolted and (b) Embedded Plate Site Welded

3.2.4 Cyclic Behavior

For seismic design, it is important to understand the typical cyclic behavior of the system. Because of the rocking behavior and the inelastic UFPs and CLT panel components, the overall moment-drift behavior is nonlinear as shown in Figure 3.9. The wall will be linear elastic and have the elastic stiffness of the CLT panels until the decompression point when the stiffness will change to a smaller decompression stiffness. The building period will decrease because of the smaller decompression stiffness.

As the wall experiences more lateral drift, the UFPs will reach their maximum force and the stiffness will continue to decrease. Next, the CLT walls will reach their compressive yield stress at the corner of the panel and CLT yielding will progress inward. This will cause another decrease in stiffness. At high drifts when the PT bar yields, all components will have yielded, the stiffness will approach zero, and the system will reach it's maximum capacity.

If the PT has not yielded or lost it's tension force for other reasons, as the lateral drift starts to decrease and approach zero, the PT bar force will cause the wall to recenter. If the CLT has yielded, the CLT panel will permanently compress at its corner and in the

next cycle the wall will reach decompression sooner because more CLT wall length will be required to balance the PT tension force and gravity load, thus decreasing the moment arm length.

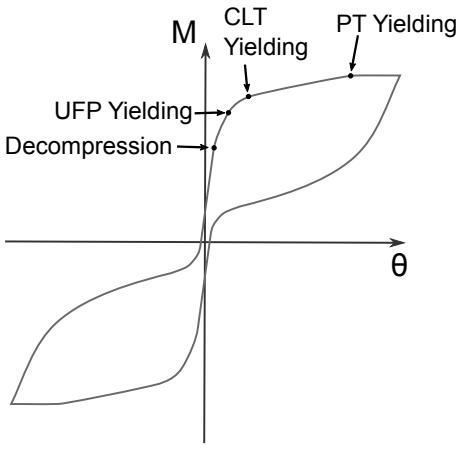

Figure 3.9: Cyclic Behavior of Rocking CLT Wall System

3.2.5 Floor Diaphragm and Shear Transfer

Two options for the floor diaphragm are a rigid concrete slab or a flexible CLT slab. Both designs would span between wood joists or glulam beams. A device needs to be used to transfer the shear force from the diaphragm to the rocking walls. One option would be a steel angle mounted to the floor diaphragm and butted up against each end of the rocking CLT wall. The design and implementation of the shear transfer devices is beyond the scope of the work presented here.

3.2.6 Gravity System Interaction

The assumed gravity system of a building with rocking CLT walls consists of CLT walls, glulam columns and beams, and CLT slabs or concrete floors. On the rocking floors, the

gravity system has to be allowed to deform with the rocking walls. The design of these gravity connections is beyond the scope of this thesis.

3.3 Cross-Sectional Analysis For Design

A simplified analytical model was developed for single rocking CLT walls to estimate moment capacity and aid the design procedure. The analytical procedure is a modified version of an iterative trial and error cross-sectional analysis procedure developed by Pampanin et al. [2001] for rocking concrete connections and expanded on by Newcombe et al. [2008] for rocking laminated veneer lumber (LVL) timber connections. The procedure is laid out for a single PT connection wall (Figure 3.10a) and a dual connection PT wall (Figure 3.10b) in a flowchart in Figure 3.11 and explained in more detail below. The single connection PT wall, which has one PT connection at the base, was used for the experimental tests presented in Chapter 4 and the dual connection PT wall, which has a PT connection at the base and at the top, was used in the design procedure presented below.

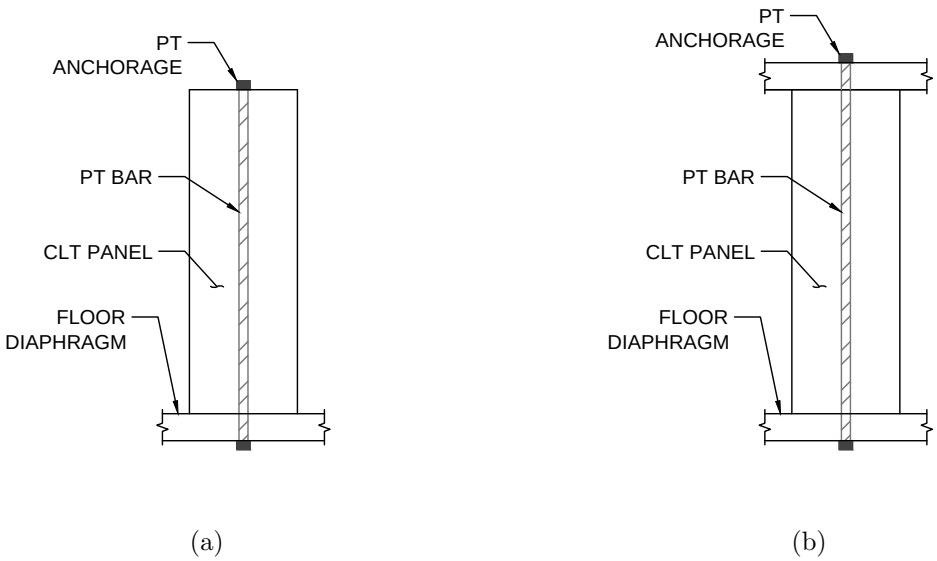

(a) (b)

Figure 3.10: (a) Single PT Connection Wall and (b) Dual PT Connection Wall

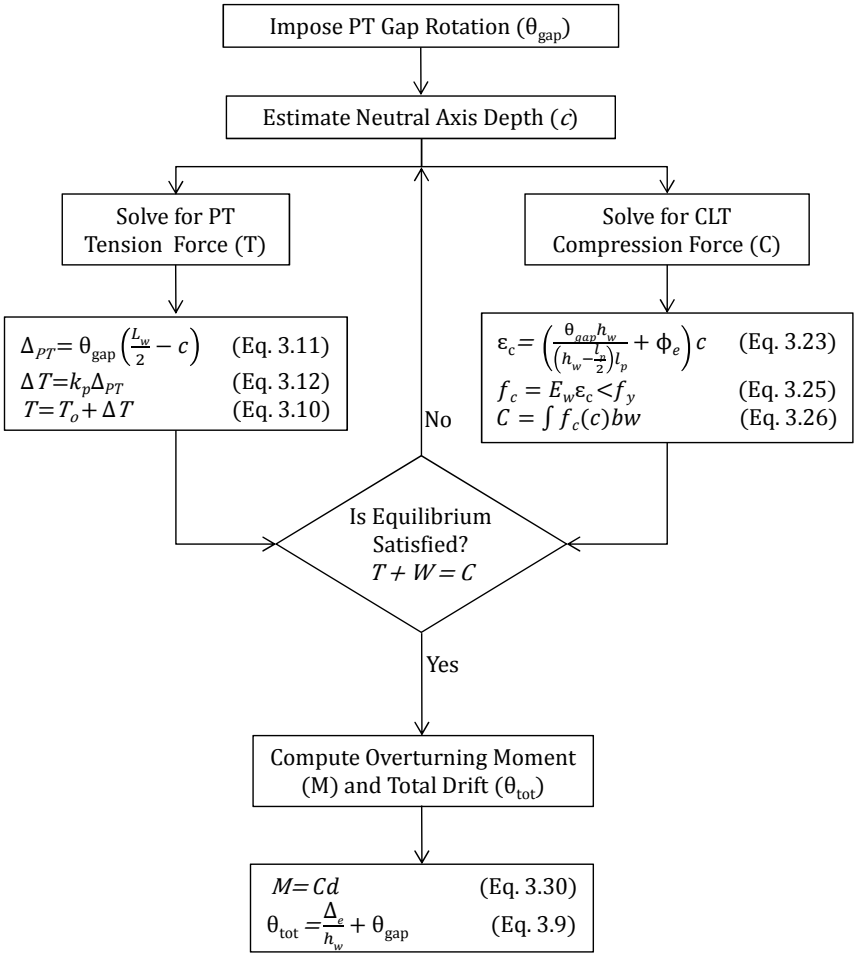

Figure 3.11: Section Analysis Flow Chart

Calculate the Decompression Moment

First the decompression moment is calculated. From the experimental results presented in Chapter 6, the CLT walls decompress when the depth of the neutral axis, c, is equal to $\frac{3}{8}$ of the base length of the wall, L_w. While this likely depends on the initial PT, gravity load, and panel stiffness, decompression when c is equal to $\frac{3}{8}L_w$ will be used here in lieu of additional data. Since the CLT panel has not yet yielded, a linear stress distribution is assumed and the location of the compression force, $\overline{c}$, is assumed to be $\frac{1}{3}$ of the neutral axis depth. The decompression moment can then be calculated using Equation 3.1. For the single PT connection wall, there is one connection at the base of the wall, making the couple arm length, d, equal to $\frac{L_w}{2}$ minus $\overline{c}$ (Figure 3.12a). For the dual PT connection wall, there is a connection at the base and top of the wall, making the moment arm length double that of the single connection wall and equal to L_w minus $\overline{c}$ (3.12b).

The wall is elastic before uplift and the initial stiffness can be calculated as an aggregate of the flexural and shear stiffnesses of the CLT panel as shown in Figure 3.13:

$$k_w = \left(\frac{h_w^3}{3E_wI_w} + \frac{h_w}{G_wA_w}\right)^{-1} \quad (for\ single\ PT\ connection) \tag{3.6}$$

$$k_w = \left(\frac{h_w^3}{12E_wI_w} + \frac{h_w}{G_wA_w}\right)^{-1} \quad (for\ dual\ PT\ connection) \tag{3.7}$$

where E_w is the modulus of elasticity of the CLT panel, I_w is the second moment of inertia of the CLT panel, h_w is the height of the wall, G_w is the shear modulus of the wall, and A_w is the cross-sectional area of the wall. The elastic displacement of the wall at the location of the lateral load is calculated as:

$$\Delta_e = \frac{M}{k_w h_w} \tag{3.8}$$

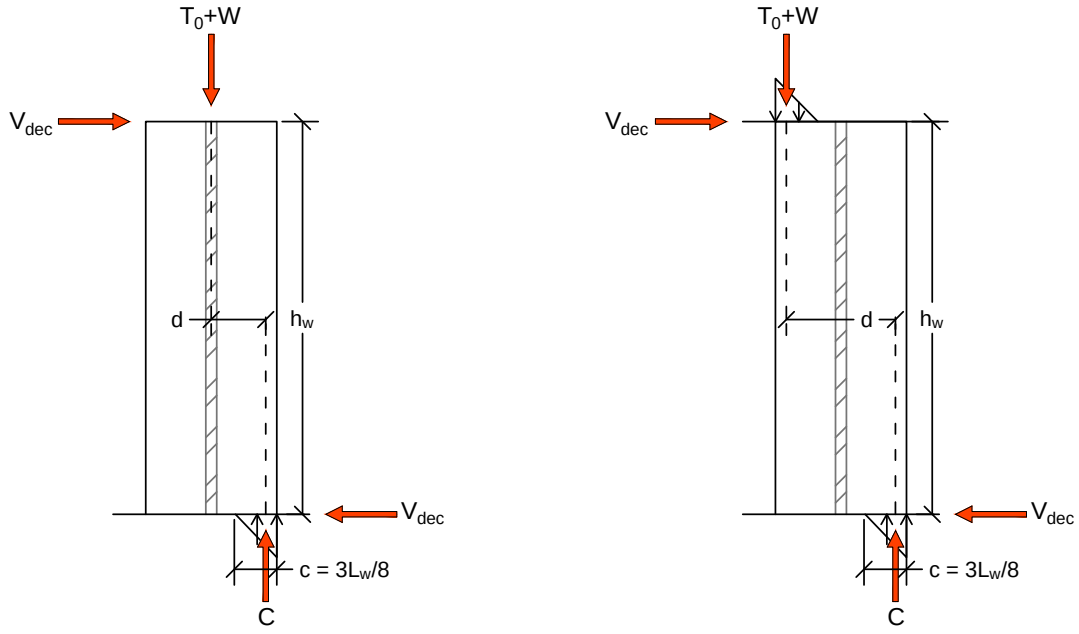

(a) (b)

Figure 3.12: Wall Equilibrium at Decompression for (a) Single PT Connection Wall and (b) Dual PT Connection Wall

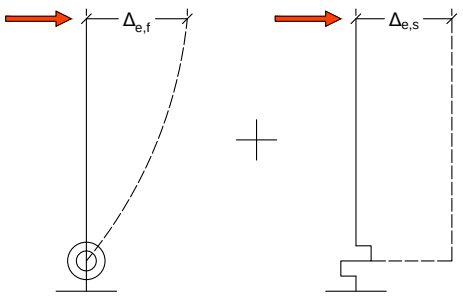

Figure 3.13: Aggregate Initial Stiffness of a Rocking CLT Wall

Impose Gap Rotation

A fixed value for the gap rotation, θ_{gap}, shown in Figure 3.14 must be chosen. The gap rotation quantifies the gap opening after the wall has decompressed. Along with the elastic displacement, Δ_e, the gap rotation can be used to compute the story drift, θ_s, as:

$$\theta_s = \frac{\Delta_e}{h_w} + \theta_{gap} \tag{3.9}$$

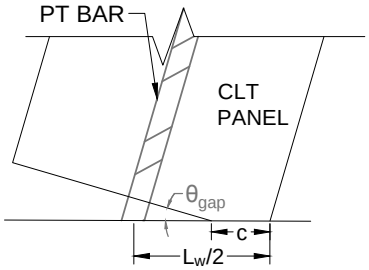

Figure 3.14: Gap Opening Diagram

Estimate Neutral Axis Depth

The next step is to estimate the neutral axis depth, c, which is the length of wall that is in compression as shown previously in Figure 3.14. The neutral axis depth is the iterative value in the procedure.

Solve for the PT Tension Force

The PT tension force, T, is defined by the initial PT force, T_0, plus the change in PT force, ΔT, due to PT elongation, Δ_{PT} (Equation 3.10). Δ_{PT} at each connection is calculated by multiplying θ_{gap} by the distance from the PT bar to the decompression point via the small angle theorem (Equation 3.11). For wall with two rocking connections (top and bottom), the PT bar is assumed to elongate at both connections. ΔT is then calculated by multiplying Δ_{PT} by the PT bar axial stiffness, k_p (Equation 3.12).

$$T = T_0 + \Delta T \tag{3.10}$$

$$\Delta_{PT} = \theta_{gap}\left(\frac{L_w}{2} - c\right) \tag{3.11}$$

$$\Delta T = k_p \Delta_{PT} \tag{3.12}$$

Solve for the CLT Compression Force

The basic strain compatibility assumptions used in a classical cross-sectional analysis cannot be used because the curvature at the decompression point is infinite, and therefore the strain must be defined in terms of the rotation. The monolithic beam analogy, developed by Pampanin et al. [2001], provides a member compatibility condition for predicting the strain for a given level of connection opening and can be applied to the rocking CLT wall system. The analogy defines a relationship between the neutral axis depth, c, and the compression strain in the CLT, ϵ_c. An equal lateral displacement is imposed on two walls (shown in Figure 3.15), one rocking and one monolithic, both with the same geometric and material properties. The analogy holds true for walls with single connections and dual connections. Since the eometry and material properties are equal for both the rocking wall and monolithic wall, the elastic displacements, Δ_e, are equal and therefore the rocking wall displacement due to gap opening, Δ_{gap}, and the monolithic wall displacement due to plastic deformation, Δ_p, must be equal (Equations 3.13-3.15).

$$\Delta_{tot(rocking)} = \Delta_{tot(monolithic)} \tag{3.13}$$

$$\Delta_{gap} + \Delta_e = \Delta_p + \Delta_e \tag{3.14}$$

$$\Delta_{gap} = \Delta_p \tag{3.15}$$

For the rocking wall, Δ_{gap} can be quantified by multiplying θ_{gap} by the height of the wall, h_w (Equation 3.16).

$$\Delta_{gap} = \theta_{gap} h_w \tag{3.16}$$

For the monolithic wall, the concept of a plastic hinge is utilized to calculate the plastic deformation and a plastic hinge length must be determined. Here, the plastic hinge length is determined by comparing the cross-sectional analysis results to the experimental results presented in Chapter 6. The displacement due to plastic deformation, Δ_p, can be quantified by multiplying the plastic hinge rotation, θ_p, by the distance from the top of the wall to the midpoint of the plastic hinge (Equation 3.17). θ_p is calculated by multiplying the plastic curvature, ϕ_p, by the length of the plastic hinge, l_p, (Equation 3.18). ϕ_p is equal to the total curvature, ϕ_{tot} minus the elastic curvature,ϕ_e (Equation 3.19). ϕ_{tot} is equal to the compression strain at the extreme fiber, $\epsilon_{c,ext}$, divided by the depth of the neutral axis (Equation 3.20). ϕ_e is equal to the moment on the section, M_r, divided by EI of the CLT panel (Equation 3.21). Since the moment is unknown, the value from the previous step should be used for the first iteration. By combining the previous five equations, the displacement due to plastic deformation, Δ_p, can be solved for in terms of the compression strain, ϵ_c (Equation 3.22).

$$\Delta_p = \theta_p \left(h_w - \frac{l_p}{2} \right) \tag{3.17}$$

$$\theta_p = \phi_p l_p \tag{3.18}$$

$$\phi_p = \phi_{tot} - \phi_e \tag{3.19}$$

$$\phi_{tot} = \frac{\epsilon_c}{c} \tag{3.20}$$

$$\phi_e = \frac{M}{EI} \tag{3.21}$$

$$\Delta_p = \left(\frac{\epsilon_c}{c} - \phi_e \right) l_p \left(h_w - \frac{l_p}{2} \right) \tag{3.22}$$

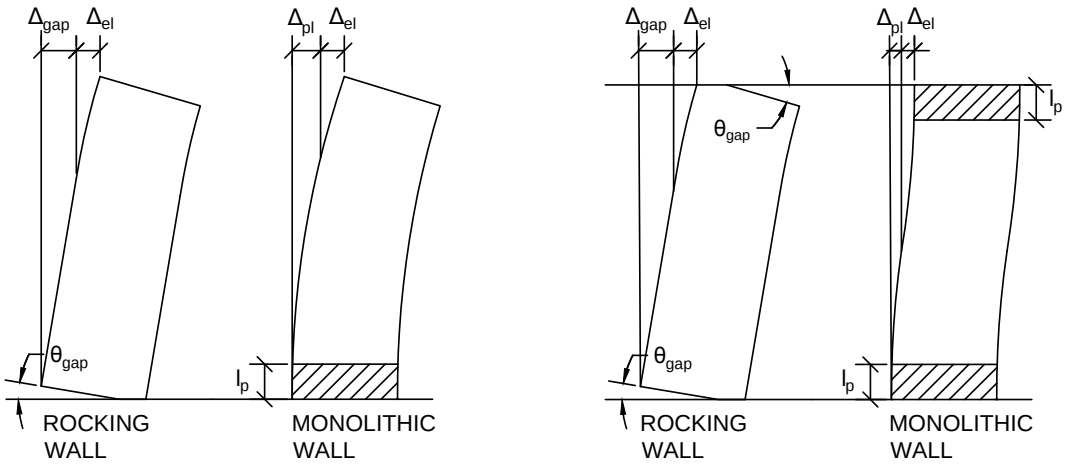

(a) (b)

Figure 3.15: Monolithic Wall Analogy for Single PT Connection Wall (a) and Dual PT Connection Wall (b) [Pampanin et al., 2001]

By combining Equation 3.16 and Equation 3.22 with Equation 3.15 the compression strain, ϵ_c, can be solved for in terms of the gap rotation, θ_{gap}, and the neutral axis depth, c, which were both estimated in the first steps of the cross-sectional analysis procedure (Equation 3.23).

$$\epsilon_c = \left(\frac{\theta_{gap} h_w}{l_p (h_w - \frac{l_p}{2})} - \phi_e \right) c \tag{3.23}$$

The compression strain is assumed to be zero at the decompression point and to have a linear distribution from there on. The CLT yield strain, ϵ_y, is assumed to be equal to the CLT yield stress, f_y, divided by the CLT modulus of elasticity, E_w (Equation 3.24). The CLT stress-strain relationship is assumed to be elastic-perfectly plastic. If at any point along the neutral axis depth, the compression strain is greater than the yield strain the CLT is assumed to have yielded at that point. The assumed constitutive relationship is shown in

Equation 3.25 and Figure 3.16.

$$\epsilon_y = \frac{f_y}{E_w} \tag{3.24}$$

$$f_c = E_w \epsilon_c \leq f_y \tag{3.25}$$

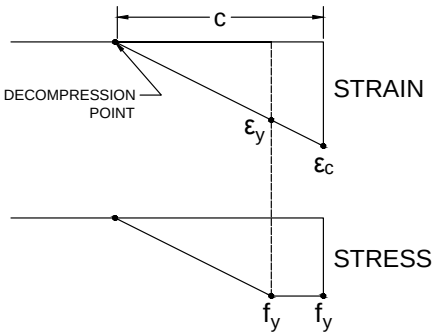

Figure 3.16: Assumed CLT Constitutive Model Applied to the Cross-Section

The CLT compression force, C, can be calculated by integrating the stress distribution, f_c, over the compressed area of the neutral axis depth, c, multiplied by the wall thickness, b_w:

$$C = \int_0^c f_c(c)(b_w)dx \tag{3.26}$$

Check Equilibrium

The wall free body diagram (Figure 3.17) shows equilibrium in the y-direction is governed by Equation 3.27 where W is the gravity load. If the calculated PT tension force, T, and CLT compression force, C, satisfy y-direction equilibrium then the estimated neutral axis, c, is correct for the chosen gap rotation, θ_{gap}. If the calculated PT tension force, T, and CLT compression force, C, do not satisfy y-direction equilibrium then a new value for the neutral axis, c, must be chosen and the cross-sectional analysis process repeated until equilibrium is satisfied.

$$T + W = C \tag{3.27}$$

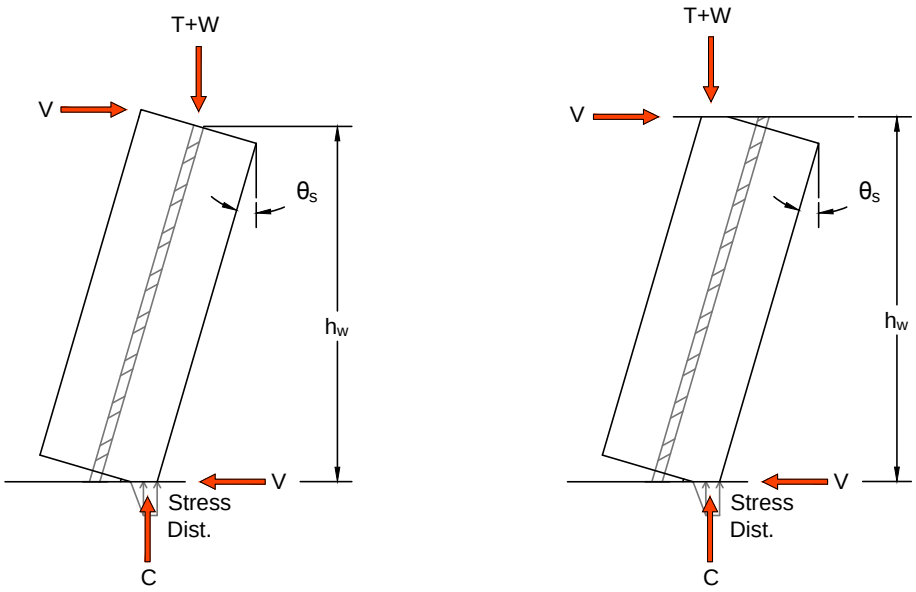

(a) (b)

Figure 3.17: Wall Equilibrium for Single PT Connection Wall (a) and Dual PT Connection Wall (b)

Solve for the Moment and Shear Capacity

Once the tension and compression forces are verified through equilibrium, the wall moment, M, and shear, V, can be solved for. M is equal to the tension-compression couple between the PT tension force, T, plus the gravity force, W, and the CLT compression force, C, (Equation 3.30). For the single connection wall, the moment arm length, d, is equal to the distance between the location of the PT bar, $\frac{L_w}{2}$, and the centroid of the compression force, $\bar{c}$, which is determined by the CLT compressive stress distribution (Equation 3.28). For the dual connection wall, the moment arm is twice as long as a single connection wall (Equation 3.29) since gaps form at the top and bottom of the wall. The wall shear, V, is determined by dividing the moment, M, by the wall height, h_w (Equation 3.31).

$$d = \frac{L_w}{2} - \bar{c} \quad (for\ single\ connection) \tag{3.28}$$

$$d = L_w - 2\bar{c} \quad (for\ dual\ connection) \tag{3.29}$$

$$M_o = Cd \tag{3.30}$$

$$V = \frac{M_o}{h_w} \tag{3.31}$$

Decompression Stiffness

An approximate expression for the decompression stiffness can be determined by using the relationships defined above. An expression for the overturning moment in terms of the gap rotation is created by combining Equations 3.30 and 3.27, then expanding the the PT tension force, T, into the initial tension force, T_0, and the change in PT force, ΔT, and then defining the change in PT force, ΔT, in terms of the gap rotation, θ_{gap}. At high story drifts the drift due to the elastic displacement is small and the story drift, θ_s, approaches the gap rotation ,θ_{gap}, as shown in Equation 3.9. Therefore the recentering moment can be determined in terms of the story drift as:

$$M_o = (T_0 + W)d + k_p d\left(\frac{L_w}{2} - c\right)\theta_s \tag{3.32}$$

From Equation 3.32, the decompression stiffness can be calculated as:

$$k_{dec} = k_p d\left(\frac{L_w}{2} - c\right) \tag{3.33}$$

This stiffness equation is dependent on the couple arm length, d, and the neutral axis location, c, and thus the stiffness changes as the gap rotation increases.

3.4 Performance-Based Design Procedure for Rocking CLT Walls

The components of the rocking CLT wall system include CLT panels, PT connections, and UFP coupling devices. Each component is designed such that certain limit states occur for seismic demands associated with a given hazard level. This design approach is a simplification of the performance-based seismic design (PBSD) procedure laid out by ATC [2012] and does not include the probabilistic framework and correlation of damage with economic impact.

3.4.1 Seismic Hazard Levels

The rocking CLT wall system is designed to reach certain structural performance objectives for three seismic hazard levels. The seismic hazard levels consist of earthquakes with a 50%, 10%, and 2% probability of exceedance in 50 years (referred to 50% in 50 year, 10% in 50 year, and 2% in 50 year). These hazards represent earthquakes with return periods of 72, 475, and 2475 years, respectively. For this design, the 10% in 50 year event is assumed to approximate a design basis earthquake (DBE).

3.4.2 Performance Objectives

The proposed design method has four performance objectives which are listed below and shown in Figure 3.18.

PO 1: *No wall decompression under wind loading.*

PO 2: *Immediate Occupancy: No repair of the system is required after an earthquake representing the 50% in 50 year hazard level.* To have no repair required for the system, the UFPs must not reach their yield strength and the system must recenter. To achieve recentering the system should have residual drifts no greater than 0.2%, which corresponds to out-of-plumb limits in construction [ATC, 2012].

PO 3: *Limited Repair: System recenters and only UFP replacement is required after an*

earthquake representing the 10% in 50 year hazard level. Since they can easily be replaced after an event, significant yielding is allowed to occur in the UFPs, but the PT bars should not yield, the CLT walls should not crush, and the hold down connections should remain elastic. Story drifts should be limited to the 2% code-based drift limit [ASCE, 2010].

PO 4: *Collapse Prevention: System damage is limited to prevent building collapse after an earthquake representing the 2% in 50 year hazard level.* To prevent sudden loss of stiffness and strength the PT elements should not yield at high drifts, the CLT walls should not crush excessively, and the hold downs should not fail. Based on engineering judgment and the drift at which the system sees significant PT bar yielding and CLT crushing in the experimental data presented in Chapter 6, a target drift limit for this PO is set at 4% drift.

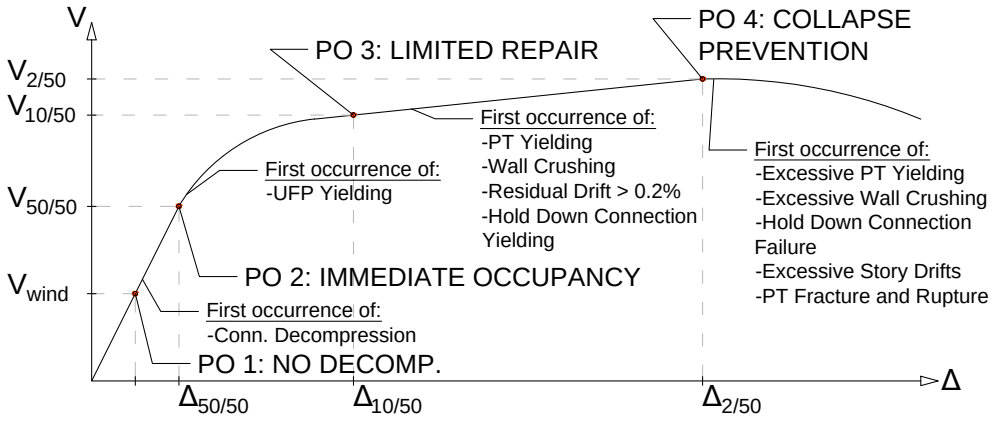

Figure 3.18: Performance Objectives

3.4.3 Design Procedure

The proposed design procedure for the rocking CLT wall system to achieve the above performance objectives is outlined in the following sections and shown in Figure 3.19.

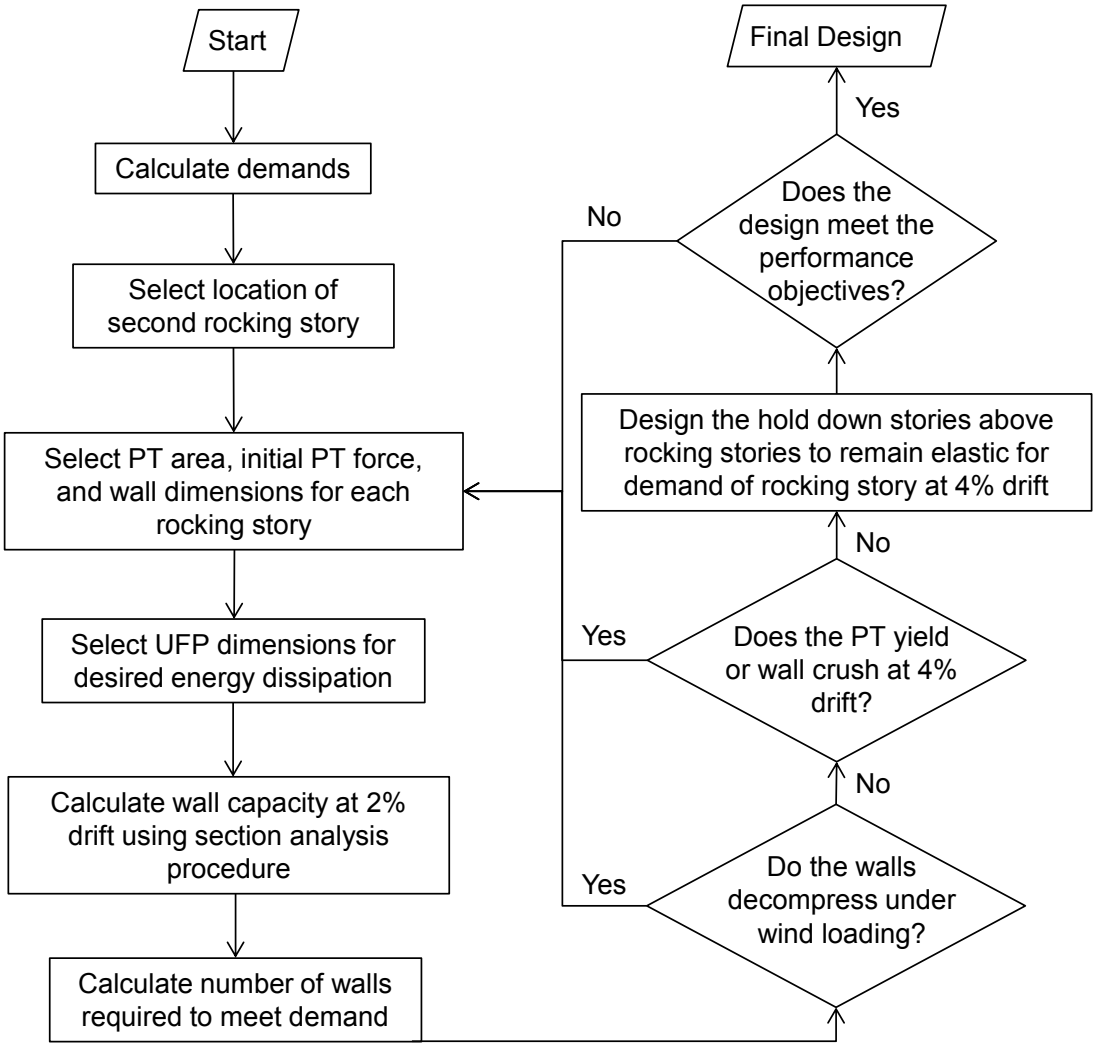

Figure 3.19: Proposed Performance-Based Design Procedure

Calculate Demands

The first step to the design procedure is to estimate a preliminary seismic base shear for the structure. The building's period is calculated from the approximate period, T_a, in ASCE [2010]. The spectral acceleration for 5% damping associated with the 10% in 50 year seismic hazard level is selected since this is considered the level near the DBE. The base shear is then calculated by multiplying the seismic mass by the spectral response acceleration and dividing by a assumed response modification factor, R. Since R is unknown for rocking CLT walls, based on engineering judgment, an R of 6 was assumed. Pei et al. [2013] estimated an R-factor of 4.5 for conventional CLT walls with mechanical connectors. The assumed R is larger because the rocking CLT wall system is expected to have higher ductility than conventional CLT walls. Next, the vertical distribution of seismic forces is estimated using the ASCE 7-10 equivalent lateral force (ELF) distribution [ASCE, 2010]. Once the seismic base shear and the lateral load distribution is determined, the story shears and overturning moments can be calculated from statics.

Selection of Second Rocking Story

To reduce demands due to higher mode effects in buildings eight stories and taller a second rocking story of CLT walls should be utilized in addition to a rocking story at the first story of the building. To accomplish this Wiebe et al. [2013a,b] placed a second rocking story at mid-height of an eight story building. By performing multiple numerical analyses presented in Chapter 7 it was determined that the optimal location for a second rocking story is somewhere around the middle story for buildings eight and fourteen stories tall. A procedure for determining the optimal location for a second or third rocking story in tall CLT buildings was not developed and is included in the research needs.

Selection of Design Parameters for Rocking Stories

The parameters used for the design of the rocking CLT walls should be chosen based on the performance objectives. The parameters of interest are:

- PT bar area and length, A_p and L_p
- Initial PT bar force, T_0,
- CLT panel base length and thickness, L_w and b_w
- UFP dimensions, D_u, b_u, and t_u

PT Bar Area and Length, A_p and L_p

The PT bar cross-sectional area increases the maximum strength of the system by increasing the yield strength of the PT bar and the moment capacity in Equation 3.2. This will result in a larger compression force in the CLT and could cause CLT damage at lower drifts because of the higher PT bar axial stiffness, k_p. However by increasing the PT bar length (L_p), k_p can be reduced and cause the PT bar to yield at higher drifts, which is important for PO 4. Since k_p is also proportional to the decompression stiffness, k_{dec}, (Equation 3.33), the decompression stiffness increases as A_p increases and decreases as L_p increases, which is important for PO 3.

Initial PT Bar Force, T_0

Increasing the initial PT bar force, T_0, will increase the decompression moment, M_{dec}, as shown in Equation 3.1 which is important for PO 1. By increasing T_0, the PT bar will be closer to its yield strength and therefore yield at lower drifts. Also by having a higher force in the PT bar the CLT will likely damage earlier impacting PO 4.

CLT Panel Base Length and Thickness, L_w and b_w

By increasing the CLT panel base length, L_w, the moment arm length, d, increases and the maximum moment capacity increases per Equation 3.2. The gap opening will be further from the PT bar, increasing the PT force. PT yielding and CLT damage will then occur lower drifts effecting PO 4. By increasing the panel thickness, the neutral axis, c, will decrease for

the same CLT compression force as shown in Equation 3.26. If the neutral axis decreases the gap opening will also be further from the PT bar.

UFP Dimensions, D_u, b_u, and t_u

The primary use of the UFPs for design is to supply energy dissipation for the system. The expected percent of energy dissipation from the UFPs is calculated from Equation 3.4, where V_{UFP} is the shear force supplied by the UFP. Note that increasing t_u or b_u will increase V_{UFP}, though t_u will have a greater effect because it is a squared term and increasing D_u will decrease V_{UFP}. The energy dissipated by the UFPs, is represented by the ratio of the area of the flag-shaped hysteresis to the area of the full elastic-plastic hysteresis as shown in Figure 3.20 [Seo and Sause, 2005]. This ratio, β can be calculated as [Seo and Sause, 2005]:

$$\beta = \frac{M_{UFP}}{2M_{dec}} \tag{3.34}$$

where M_{UFP} is the moment due to the UFP and M_{dec} is the decompression moment as calculated in Equation 3.1. The moment due to each UFP can be calculated by multiplying the panel length, L_w, by V_{UFP}.

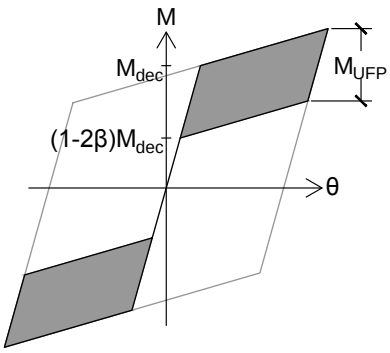

Figure 3.20: UFP Energy Dissipation Ratio [Seo and Sause, 2005]

Calculate Number of Walls Required for Each Rocking Story

Once the trial values for the design parameters are chosen, the required number of walls per rocking story can be calculated. There must be enough walls such that the total story moment capacity is greater than the overturning moment from the applied lateral earthquake loads. The moment capacity of each rocking story can be calculated using Equation 3.2. The section analysis procedure should be used to calculate the moments due to PT moment couple at a story drift, θ_s, of 2% (PO 3). This method is conservative because it assumes the floor will only move laterally such that the gap openings at each wall will be equal. This is not the true nature of a series of base rocking walls because it does not account for any overturning resistance provided by a global tension-compression force couple of the entire rocking story as shown in Figure 3.21. The resultant of the lateral earthquake loads acts at an effective height, h_{eff}, around two-thirds of the total building height. Since there are multiple HDW stories above each rocking story, the overturning moment due to the story shears will cause a floor rotation, θ_{floor}. This overturning moment will be resisted by the sum of the individual wall moments and the global tension-compression moment couple due to the unequal PT tension and CLT compression resultant wall forces. On one end of the story the resultant force will be in tension and on the other side the resultant will be in compression, thus creating a global tension-compression moment couple.

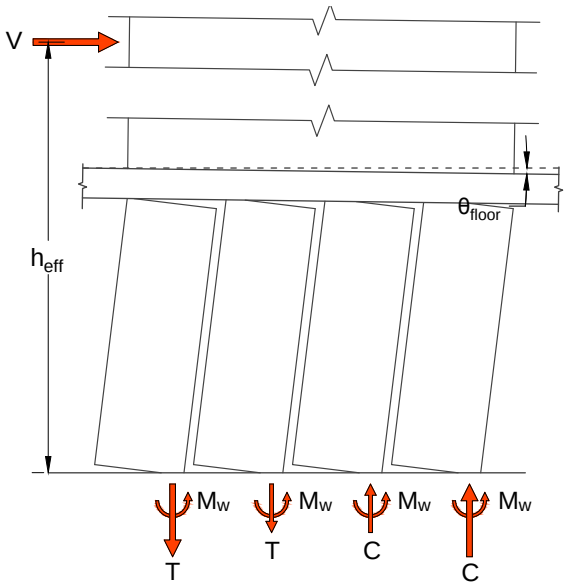

Figure 3.21: Global Tension-Compression Force Couple

Design of HDW Stories

To meet PO 4 the hold down wall (HDW) stories should be designed to remain elastic for the demand of the rocking wall story below up to 4% story drift. The demand for the HDW stories should be calculated from the moment capacity in Equation 3.2.

The CLT Handbook [van de Lindt et al., 2013] is used to calculate the lateral resistance of each HDW story. Hold downs should be used as lateral resistance for the HDWs. The lateral resistance of a single HDW is calculated by summing the resisting moments due to the hold downs at the bottom and top of the wall and the resisting moment due to gravity loads as follows and illustrated in Figure 3.22:

$$V = \frac{W\frac{L_w}{2} + \sum F_{conn} d_{conn}}{h_w} \tag{3.35}$$

where V is the lateral resistance, W is the gravity load, F_{conn} is the resisting tension force of the hold down connector, d_{conn} is the distance from the wall pivot point to a connector, and h_w is the height of the wall. F_{conn} can be calculated as:

$$F_{conn} = k_{conn}\Delta_{conn} = k_{conn}\theta_s d_{conn} \tag{3.36}$$

where k_{conn} is the hold down stiffness, Δ_{conn} is the hold down displacement, and θ_s is the story drift. Because the walls experience small displacements, they are assumed to be rigid and the linear relationship between Δ_{conn} and θ_s is assumed. To keep the connectors elastic, F_{conn} for the connectors at the ends of the wall should be held to $\frac{2}{3}$ of F_0 as shown on the connector hysteretic diagram in Figure 2.8. Assuming the connectors have equal stiffness, using the limiting connector force, F_{limit}, and Equation 3.36 the forces for the other connectors can be calculated as:

$$F_{conn,n} = F_{limit}\frac{d_{conn,n}}{L_w} \tag{3.37}$$

The total lateral resistance of an entire HDW story is calculated by taking the sum of the lateral resistance of each the wall on that story.

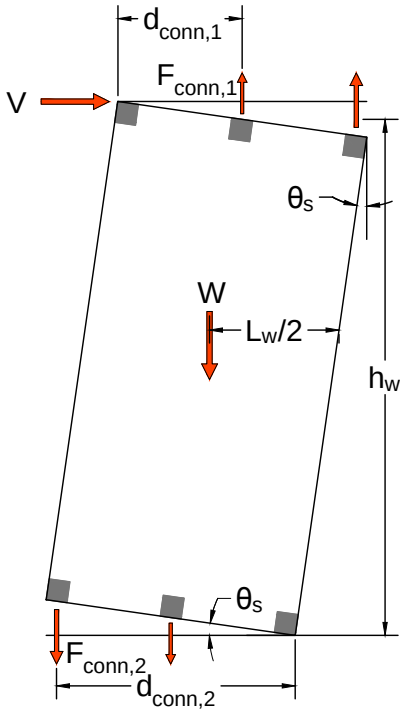

Figure 3.22: Hold Down Wall Free Body Diagram

Check Limit States

The last step in the design procedure for the PT bars and CLT panels are to check the limit states. To satisfy PO 1, the walls must not decompress under wind loading. This can be checked by making sure the decompression moment, M_{dec}, from Equation 3.1 is greater than the overturning moment from wind loading. The wind story shears can be calculated from ASCE [2010]. To satisfy PO 4, the PT must not yield and the CLT must not reach it's crushing strain. These limit states can be checked by calculating the wall capacities at 4% drift with the cross-sectional analysis procedure. In the previous step the HDW stories were capacity designed such that they will remain elastic for the demand of the rocking story below up to 4% story drift. If any of the performance objective are not achieved, the design parameters should be modified and design iterations should be carried out.

3.5 Archetype Building Design

To evaluate the proposed design procedure, buildings were designed with the rocking CLT wall system, and the seismic performance was assessed through numerical simulations discussed in Chapter 7. One building consisted of eight stories and the other two consisted of 14 stories. All buildings were designed with one rocking story at the first story and another at mid-story or above. The buildings were modeled after a residential building archetype discussed below. The design details and prototype buildings are presented below.

3.5.1 Building Archetypes

A workshop, held in Seattle, Washington and attended by industry professionals, focused on societal needs and implementation of tall timber structures in areas of high seismicity [Pei et al., 2014]. Two building archetypes, a residential building and an office building, were developed based on the input from the workshop. Plans for each archetype are shown in Figures 3.23 and 3.24.

For the residential archetype, the first story clear height was 14 feet and total height was 16 feet. All other clear story heights were 8 feet and total heights were 10 feet. The floor dimensions were 100 feet by 55 feet with a total area of 5500 square feet. The two options for the floor slab were: (1) a rigid 2.5 inch deep concrete slab and (2) a series of more flexible CLT panels. The floors were supported by 11 inch deep TJI joists spaced at 16 inches on center. The TJI joists were supported by walls on the north-south grid lines. In the north-south direction the rocking CLT walls would be located between units on grid lines A through E and in the east-west direction they would be located on the edge of the main corridor along grid lines 1 and 2. HDWs were placed on all grid lines on the stories without rocking walls.

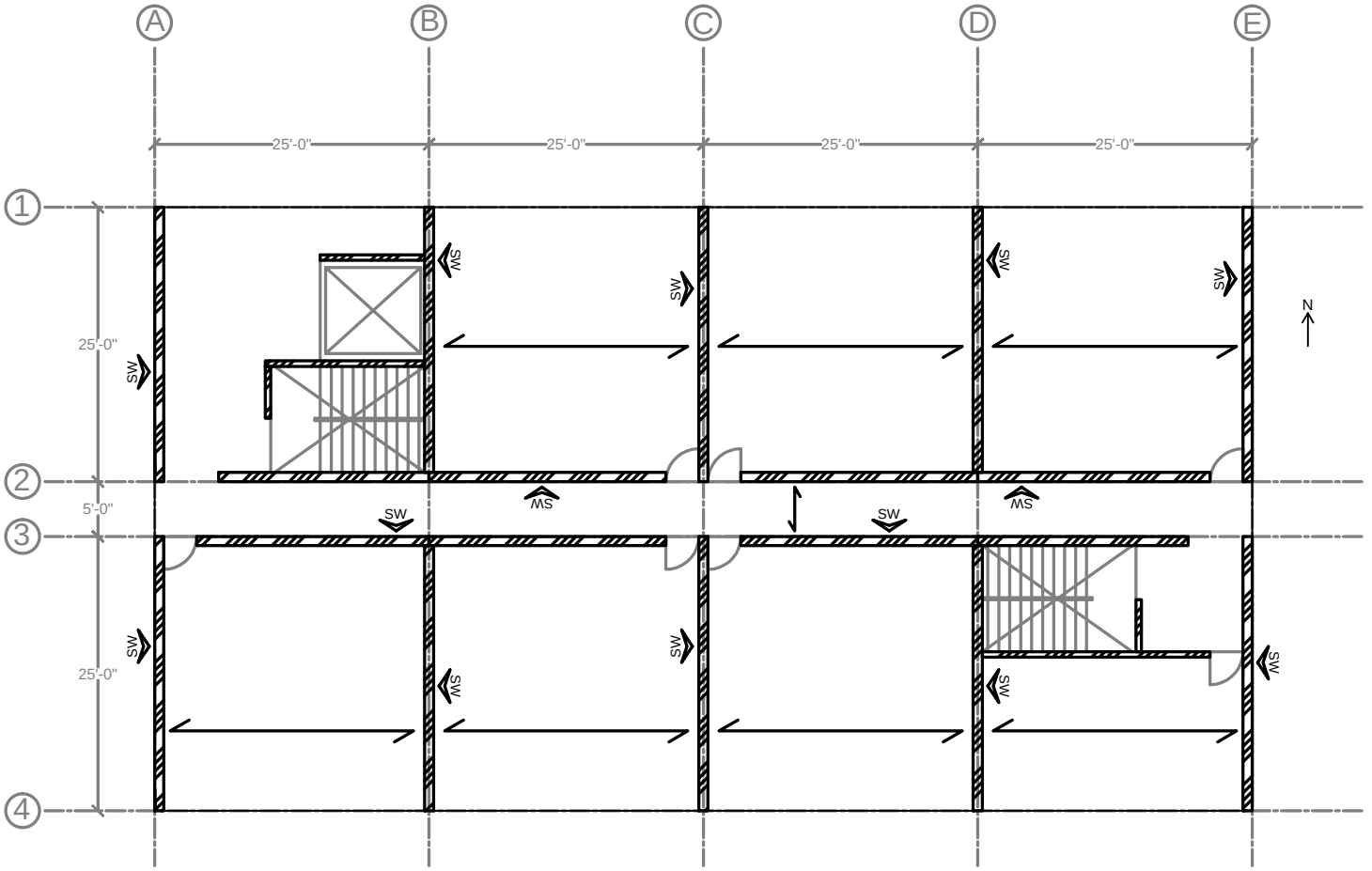

Figure 3.23: Residential Archetype Plan

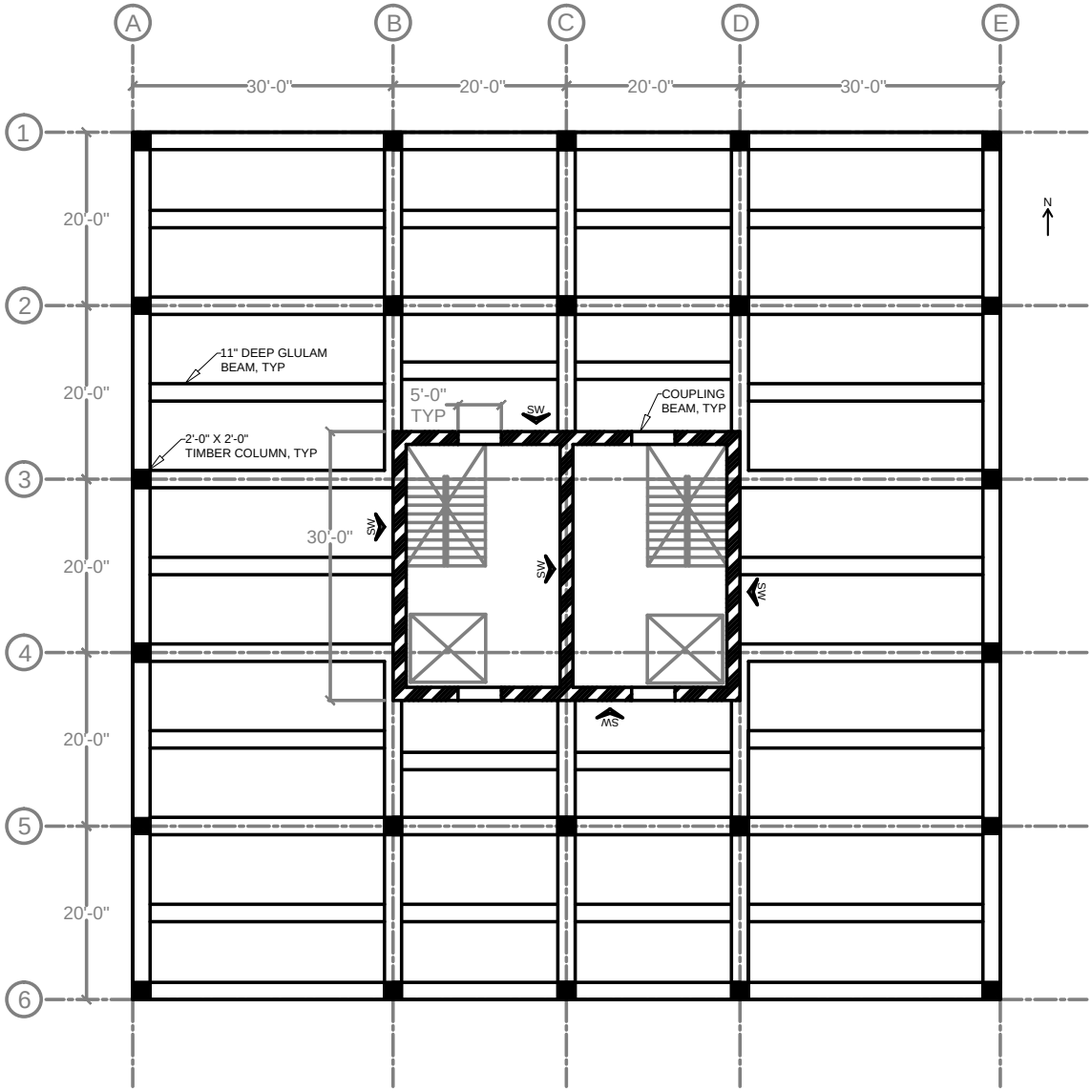

Figure 3.24: Office Archetype Plan

For the office archetype, the first story clear height was 16 feet and the total height was 18 feet. All other clear story heights were 10 feet and total heights were 12 feet. The floor dimensions were 100 feet by 100 feet with a total area of 10,000 square feet. Like the residential archetype, the floors were either a concrete slab or a series of CLT panels. The floors were supported by 11 inch deep glulam beams spaced at 10 feet on center. The glulam beams were supported by glulam columns. To resist seismic loads, CLT walls were placed around the stair and elevator core in the center of the building.

For the residential archetype, in addition to the structure's self-weight, the dead load consisted of a 3 psf ceiling/floor load, a 7 psf mechanical/electrical load, and a 10 psf partition load. The office archetype had the same dead loads except for a 15 psf partition load. The residential archetype had a 40 psf live load and the office archetype had a 50 psf live load.

Both archetypes were assigned an importance factor, I, of 1.0. The archetypes were chosen to be located in the South Lake Union Neighborhood in Seattle, Washington. Table 3.1 lists the spectral response parameters for the seismic design. The parameters were adjusted for Site Class D soil.

Table 3.1: Response Spectra Values (in units of g) for Site Class D for the 5% Dammping Level in Seattle, WA

	Period (Sec)	
Hazard Level	0.3	1.0
50% in 50 year	0.387	0.136
10% in 50 year	0.967	0.428
2% in 50 year	1.83	0.855

3.5.2 Prototype Building Designs

Three prototype buildings, two 8-story and four 14-story, were designed with the design procedure presented above. All prototypes used the residential archetype and had a rocking

stories at the first story of the building. One design for each building did not have a second rocking story. For second 8-story prototype, the rocking story was placed at story 5. For other 14-story buildings, the second rocking story was at either the 6th, 8th, or 10th story. The effects of moving the second rocking story are discussed in Chapter 7. The prototype buildings were designed for a seismic event in the north-south direction and walls were placed on grid lines A through F. For optimal resistance of the overturning moment, the walls were placed at the north and south ends of the building.

Table 3.2 lists the key design parameters for the 8 story prototype buildings. Table 3.3 lists the key design parameters for the 14-story prototype buildings with the single rocking story at the base and the buildings with the second rocking story at story 6, 8, and 10. The naming scheme for the prototypes is the archetype used followed by the number of stories followed by the stories with rocking walls (e.g. R8-1.5 is the eight story archetype building with rocking wall stories at the first and fifth stories). All three prototypes were designed with the rigid concrete floor diaphragm. The CLT panels used for the rocking CLT walls had either a 4 foot or a 4 foot 6 inch long base length. All panels had a 5-ply thickness (6.75 inches in thickness). The PT bar areas varied from 0.85 in^2 to 2.52 in^2. All PT bars were designed to be stressed to $0.4f_{pu}$ where f_{pu} is the ultimate stress of the bar. In most cases the PT bar had to be extended into the story above and below to reduce the bar stiffness so the bar would not yield at low drift levels. The UFPs were designed to supply roughly 30% energy dissipation relative to the full elastic-plastic hysteresis. The HDWs were designed to be 5 feet long and 10 feet tall. Hold downs were required at the corners on both sides, top and bottom of the walls. Actual hold downs were not chosen, instead a required hold down capacity was calculated for the HDWs based on the design procedure above. The stiffnesses of the hold downs were determined by using a limiting displacement of 0.24 inches which corresponds to the elastic limit for a Simpson Strong-Tie HTT 16 [van de Lindt et al., 2013]. A detailed design example is presented in Appendix B.

Table 3.2: Design Parameters for R8-1 and R8-1.5 Prototype Building

Rocking Story Number	1	5
Number of Rocking Walls	30	20
h_w (ft)	16	10
L_w (ft)	4.5	4
CLT Plys	5	5
Ap (in^2)	1.58	0.85
f_{p0} (ksi)	$0.4fp_u$	$0.4fp_u$
L_p (ft)	36	50
Number of UFPs	80	20
$F_{UFP,P}$ (kips)	10.4	10.4
β (%)	30	32
F_{conn} Req. Above (kips)	14	9.5

Table 3.3: Design Parameters for R14-1, R14-1.6, R14-1.8, and R14-1.10 Prototype Buildings

Rocking Story Number	1	6	8	10
Number of Rocking Walls	40	30	20	
h_w (ft)	16	10	10	10
L_w (ft)	4.5	4	4	4
CLT Plys	5	5	5	5
Ap (in^2)	2.52	1.58	1.25	0.85
f_{p0} (ksi)	$0.4fp_u$	$0.4fp_u$	$0.4fp_u$	$0.4fp_u$
L_p (ft)	20	40	40	40
Number of UFPs	150	100	80	60
$F_{UFP,P}$ (kips)	10.4	10.4	10.4	10.4
β (%)	31	36	37	30
F_{conn} Req. Above (kips)	21	17	14	9.5

Chapter 4

SPECIMEN DESIGN AND TEST SETUP

4.1 Introduction

To better understand the performance of rocking CLT walls, experiments for single story rocking CLT walls were conducted at the Washington State University Composite Materials & Engineering Center. Using a quasi-static reverse-cyclic loading procedure, a total of six tests were performed, including five single wall tests and one coupled wall test. The specimen design, construction, and test setup are presented in this chapter.

4.2 Specimen Design

The goal of the experimental program was to better understand the structural behavior of the rocking CLT wall system. Experimental data was collected on single story rocking walls to be used for calibration of numerical models presented in Chapter 7. The wall specimens represented a full scale wall located at the first story of a building. Each specimen was designed to explore different potential damage progressions and limit states by varying the PT bar size, initial PT force, CLT panel composition, and wall configuration. The effects of these parameters on wall performance relative to the performance objectives discussed in Chapter 3 was also important. To design the test specimens, design parameters were manipulated and preliminary numerical models were used to estimate the desired structural behavior. These models are not discussed here, however they were revised using the test results and are described in detail in Chapter 7.

4.2.1 Test Matrix

Table 4.1 shows a summary of all specimens and their key parameters. The rationale for the specimen designs is discussed below.

Table 4.1: Test Matrix

Test Specimen	Test Description	A_p (in^2)	f_{p0} (ksi)	T_0 $(kips)$	Base Material
Specimen 1	Low Decompression Moment, Low Decompression Stiffness	1.25	$0.32f_{pu}$	60	Steel
Specimen 2	Low Decompression Moment, High Decompression Stiffness	1.58	$0.10f_{pu}$	22.5	Steel
Specimen 3a	High Decompression Moment, Low Decompression Stiffness	1.25	$0.40f_{pu}$	75	Steel
Specimen 3b	High Decompression Moment, Low Decompression Stiffness	1.25	$0.40f_{pu}$	75	Steel
Specimen 3c	High Decompression Moment, Low Decompression Stiffness	1.25	$0.40f_{pu}$	75	Steel
Specimen 4	CLT Base	1.25	$0.40f_{pu}$	75	CLT
Specimen 5	Stronger CLT Core	1.58	$0.32f_{pu}$	75	Steel
Specimen 6	Coupled Wall	1.25	$0.4f_{pu}$	150	Steel

4.2.2 Design Parameters

The design parameters held constant throughout all specimen designs were the wall thickness, wall length, and loading height. The parameters that varied between specimens were PT bar area, PT bar initial stress, wall type, base type, and wall configuration. Two sizes of PT bar (1.25 in^2 and 1.58 in^2 cross-sectional area), three initial stresses of the PT bar, two wall types (5-ply CLT and Structural Composite Lumber (SCL) Core), two bases (steel and 5-ply CLT), and two wall configurations (single wall panel and coupled wall panels) were used. These parameters were selected to provide a range of behaviors and also fit within the constraints of the experimental setup available.

4.2.3 Rocking CLT Wall Behavior

Wall Decompression

Wall decompression is the point when there is no compression force at the uplifted toe of the wall and the wall begins to decompress and uplift. At decompression the stiffness changes from the larger elastic stiffness to the smaller decompression rocking stiffness. The overturning decompression moment is directly related to the PT bar initial prestress force as shown in Equation 3.1. A larger initial PT force results in a larger overturning decompression moment.

Post Decompression Stiffness

The post decompression stiffness or rocking stiffness is the stiffness after the wall has decompressed. The post decompression stiffness is largely dependent on the PT bar stiffness which is controlled by the PT bar area and length as shown in Equation 3.33. A wall with a lower decompression stiffness will have a lower strength capacity and less CLT damage compared to a wall with a higher decompression stiffness at the same drift ratio assuming the same decompression force.

Rocking Surface

As discussed in Chapter 3, two floor diaphragm designs were considered: a rigid concrete floor and a flexible CLT floor. It was unknown how the wall stiffness would change depending on the rocking surface. A steel base was used to represent the rigid concrete floor and a CLT base was used to represent the flexible CLT floor.

CLT Panel Strength

The composition of the panel may change the progression of CLT damage among other behavior. The strength of the CLT could be changed by using a modified CLT panel. A structural composite lumber (SCL) core panel was used in one specimen design to examine the differences between a CLT and a modified CLT panel.

Panel Configuration

The number of CLT panels used may change the wall behavior. All specimens except one were designed as a single wall. The exception was a specimen with two panels coupled together with UFP devices.

4.2.4 Specimen 1

Specimen 1 was designed to have a low decompression moment and a low decompression stiffness. The low decompression moment would cause the wall to uplift at a low drift level and applied lateral force. It was also assumed that the design would also result in large drifts prior to CLT panel damage and PT bar yielding. Specimen 1 was designed to simulate rocking on a stiff foundation or floor system by using the steel base. To achieve these objectives, a PT bar with an area of 1.25 in^2 was used and was stressed initially to $0.25f_{pu}$, which resulted in an initial PT bar force of 47.5 kips.

4.2.5 Specimen 2

Specimen 2 was designed to have a low decompression moment and a high decompression stiffness, and used a stiff steel base. The low decompression moment would cause the wall to uplift at a low drift and applied lateral force. For Specimen 2 the larger bar (1.58 in^2 area) was stressed initially to $0.10f_{pu}$ which resulted in an initial PT bar force of 24.5 kips. Because of the higher stiffness of the PT bar the compression force in the CLT wall toe would increase at a higher rate than Specimen 2. Because of the combination of a lower initial PT force and a larger PT stiffness relative to Specimen 1, a comparison for the progression of CLT damage can be made. At PT yield the moment at the wall base will be larger for Specimen 2 and more CLT damage would be expected, however the damage progression is unclear.

4.2.6 Specimen 3

Specimen 3 was designed with a high decompression moment and a low decompression stiffness. The high decompression moment would cause the wall to uplift at a higher drift level and applied lateral force compared to Specimens 1 and 2. The compression force in the CLT wall toe would initially be higher than Specimens 1 and 2, potentially causing more damage in the CLT wall and yielding the PT bar at a lower drift. Specimen 3 used the rigid steel base. To achieve these objectives, the smaller bar (1.25 in^2 area) was stressed initially to $0.40f_{pu}$ which resulted in an initial PT bar force of 75 kips.

4.2.7 Specimen 4

Specimen 4 was designed to study the effects of having a flexible rocking surface. The base material used for this test was 5 ply CLT laid such that the wall compression force would be perpendicular to grain. The smaller bar (1.25 in^2) was used and stressed initially to $0.40f_{pu}$ which resulted in an initial PT bar force of 75 kips. This is the same PT bar and initial stress as Specimen 3.

4.2.8 Specimen 5

Specimen 5 was designed to asses the performance of a CLT panel with a structural composite lumber (SCL) core that increased the panel compressive strength. A CLT panel with a SCL core as the inner three plys was used as the lower part of the wall. A 5-ply CLT wall was used as the upper part of the wall. By using the SCL core, the specimen was expected to exhibit higher strength and stiffness than the 5-ply CLT specimens. The larger bar (1.58 in^2 area) was used and stressed initially to $0.32f_{pu}$ which resulted in an initial PT bar force of 75 kips.

4.2.9 Specimen 6

Specimen 6 was the only specimen to have two walls coupled with UFP devices. Both walls used the smaller bar (1.25 in^2 area) and were stressed initially to $0.40f_{pu}$ which resulted in an initial PT bar force of 75 kips. This was the same PT bar and initial stress as Specimen 3. From preliminary numerical modeling of the coupled wall. The UFP dimensions were chosen to supply 10% damping. The UFP dimensions (shown in Figure 3.7a) were as follows:

- Diameter (D_u) = $4\frac{1}{16}$ inches
- Width (b_u) = 4 inches
- Thickness (t_u) = $\frac{3}{8}$ inches

4.3 Specimen Construction

This section discusses the various materials used in the specimen construction. Each specimen consisted of a CLT wall resting on a base. A PT bar was placed through a cavity in the CLT wall and anchored at the base and the top of the wall. For nomenclature purposes, a ply is a single board in a layer thickness and a laminate is a single board is the layer length (see Figure 4.1a). Material tests for the CLT panels and PT bars can be found in Appendix A.

The two types of CLT walls used during testing were a 5-ply CLT wall and a CLT wall with a structural composite lumber (SCL) core for inner 3 layers. A 5-ply CLT panel is shown in Figure 4.1a and a CLT panel with an inner SCL core is shown in Figure 4.1b. SCL is an engineered wood product created by gluing dried and graded wood veneers and strands together with adhesive. The CLT panel with the SCL core was manufactured with the same process as the 5-ply CLT panel. Both wall types were manufactured in a press at the Washington State University Composite Materials & Engineering Center. All the wood material was donated by Weyerhaeuser. The lumber used to create the CLT panels was Douglas Fir - Larch No. 2 & Better.

To manufacture the CLT panels, the plys were first laid up in a single layer and planned to provide a uniform surface, and adhesive glue was poured on top of the layer. The adhesive glue used was Isoset SX 1050 Adhesive. Another layer was then placed perpendicular on top of the the glued layer. This was repeated until the panel had five layers. The two outer plys and the center inner ply were cut to 8 feet. These plys would run longitudinally and would bare perpendicular to grain on the base beam during the tests. The other two inner plys were cut to 4 feet. These plys would run laterally and would bare parallel to grain on the base beam during the tests. When laying the panel, a cavity for the PT was created by not placing the middle laminate of the middle ply. To complete the construction of the panels, the glued panel was inserted into a pressing machine, shown in Figure 4.2, and pressed at 70 psi for 90 minutes. The panel was removed, and the panel sides were sawn square. The resulting panels were roughly 8 feet long by 4 feet wide by $6\frac{3}{4}$ inches thick.

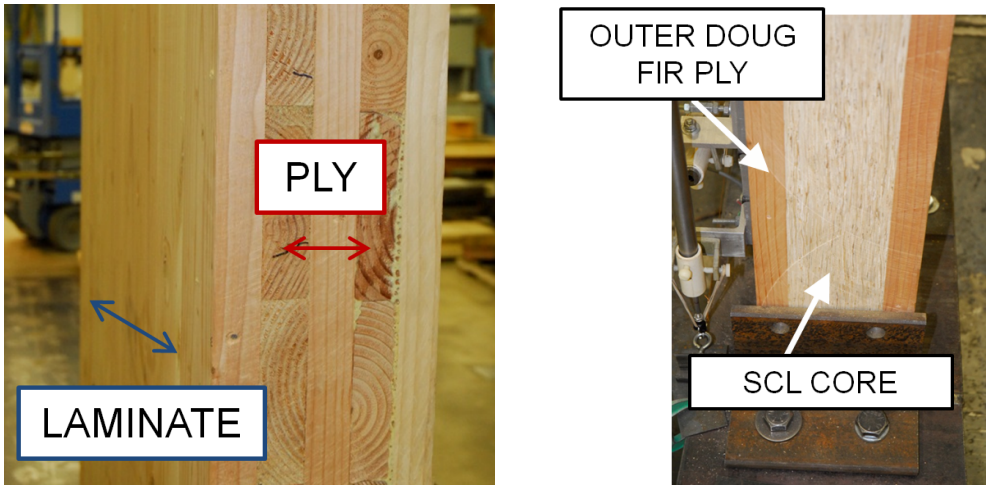

(a) (b)

Figure 4.1: (a) 5-Ply CLT Panel and (b) CLT Panel with SCL Core



Figure 4.2: Machine Press

To create a CLT wall for the test specimen, two panels were connected to form a 16 foot tall specimen. To connect the panels four 48x12x$\frac{1}{4}$ inch steel splice plates were mounted, two on each side, to the panels. The splice plates were connected to the panels with Simpson Strong-Drive SDS $\frac{1}{4}$x2 screws.

The two sizes of PT bars used in the test were manufactured by DYWIDAG Systems International. The smaller bar size had a nominal diameter of 1.25 in^2 and a nominal cross-sectional area of 1.25 square inches. The larger bar size had a nominal diameter of 1.375 inches and a nominal cross-sectional area of 1.58 in^2. Both bars had a listed yield stress of 127.5 ksi and a listed ultimate stress of 150 ksi. Tension pull tests on bar coupons were conducted at Lehigh University, and the results from the tests were used in the analysis of the experimental data. Results can be found in Appendix A.

4.4 Test Setup

4.4.1 General Experimental Apparatus

Specimens 1, 2, 3a, 3b, 3c, and 5 were tested using the same general setup. Specimen 4 used a modified setup that used a CLT base instead of a steel base. Specimen 6 used a modified setup that integrated another base beam to accommodate the coupled wall. Figure 4.3 shows an annotated photograph of the general test setup and Figure 4.4 shows an annotated schematic. The general setup consisted of a steel base beam, a PT stressing apparatus, a 30-kip actuator connected to a W14x90 reaction column and to the CLT wall specimen via two channels, and several out-of-plane restraints.

The CLT wall rested on a W12x72 base beam used to simulate a rigid surface for the wall to rock against and a bottom restraint for the PT. A schematic of the base beam is shown in Figure 4.5. The base beam was modified with stiffeners to resist the maximum PT tension and CLT compression loads during testing. To construct the beam, a rectangular hole was cut in the top middle center of the W12x72 base beam flange, and the web below the hole was removed. A 1$\frac{3}{4}$ inch thick plate with a circular hole cutout was welded in the web cutout

against two $\frac{1}{2}$ inch thick compression plates that transferred load to the top flange. The PT bar was placed in a cavity in the CLT wall and beared against the $1\frac{3}{4}$ inch plate with a $5\frac{1}{2}$x$5\frac{1}{2}$x$\frac{3}{4}$ steel anchor plate and nut. The beam was designed for the maximum compression load from the CLT wall by welding four $\frac{1}{2}$ inch thick stiffener plates at each end of the base beam. Two more $\frac{1}{2}$ inch stiffener plates were welded $8\frac{3}{4}$ inches from the center of the beam to stop the web from buckling. Six $1\frac{1}{4}$ inch diameter grade 8 steel bolts were used to mount the base beam to the strong floor.

To apply the initial stress to the PT, a stressing apparatus, provided by collaborators at Lehigh University, was used. A photograph of the PT stressing apparatus is provided in Figure 4.6 and a schematic is provided in Figure 4.7. The internal PT bar was coupled to an external PT bar that was placed in a steel stressing box. The stressing box was placed on top of a load cell which measured the change in the PT force. The load cell was placed on a bearing box that transferred the compression load into the CLT wall. The bearing box was built after the first specimens, Specimens 3a and 3b, were tested. Specimens 3a and 3b used a one inch thick bearing plate which bowed during the testing. The bearing box was constructed out of a 22 inch long, 1 inch steel base plate that had two $\frac{1}{2}$ inch edge plates welded longitudinally along the base plate and four $\frac{1}{2}$ inch stiffener plates welded transversely across the base plate. The PT load cell rested on a 2 inch thick plate that was placed in the middle of the bearing box. A Simplex 100 ton capacity hydraulic ram was placed on top of the stressing box and enclosed by four rods and a steel top plate. To restrain the PT at the top, an anchor plate and nut was threaded on the external PT bar against the hydraulic ram top plate.

To stress the PT and apply an initial compression force to the CLT wall, the hydraulic ram's internal cylinder would elongate against the top plate of the PT box. The load would transfer through the PT box, through the load cell, and through the bearing box into the CLT wall. The load cell was monitored during stressing to ensure the desired initial force was achieved. After Specimens 3a and 3b were tested, strain gauges were added at the top of the internal PT bar to add redundancy in the PT load data collection.

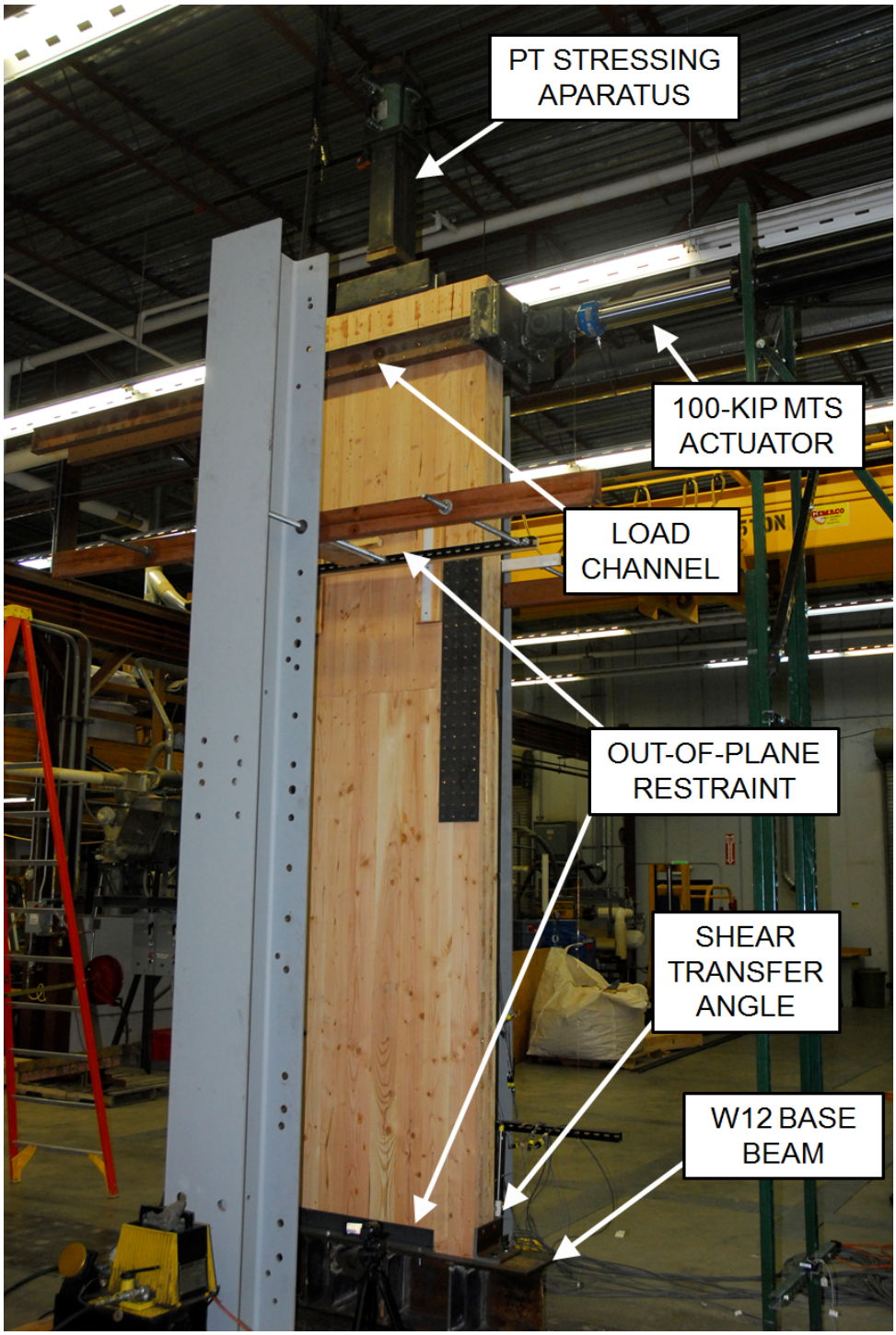

Figure 4.3: Overview of Single Wall Test Setup - Steel Base

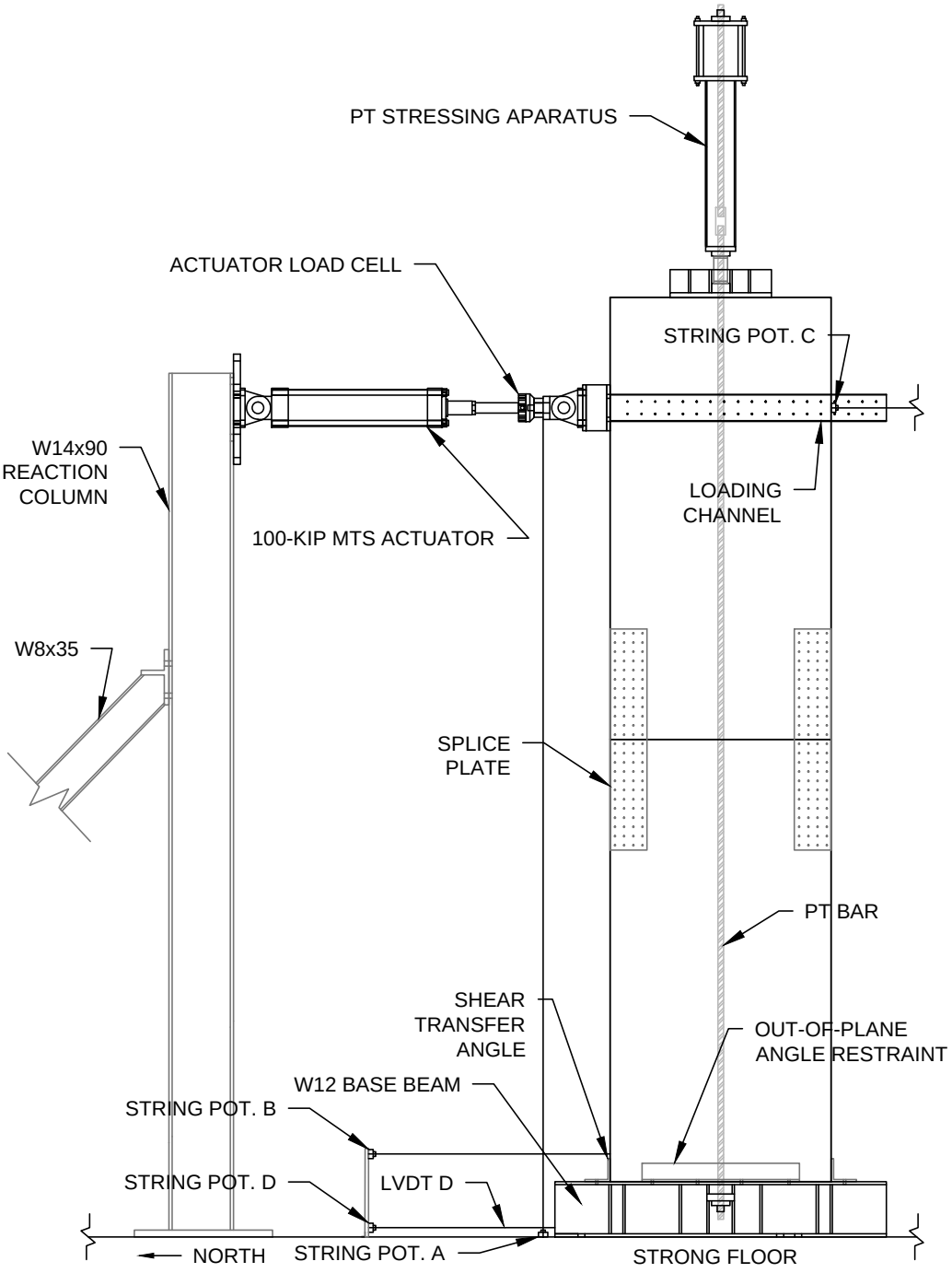

Figure 4.4: Single Wall Test Setup Schematic - Steel Base

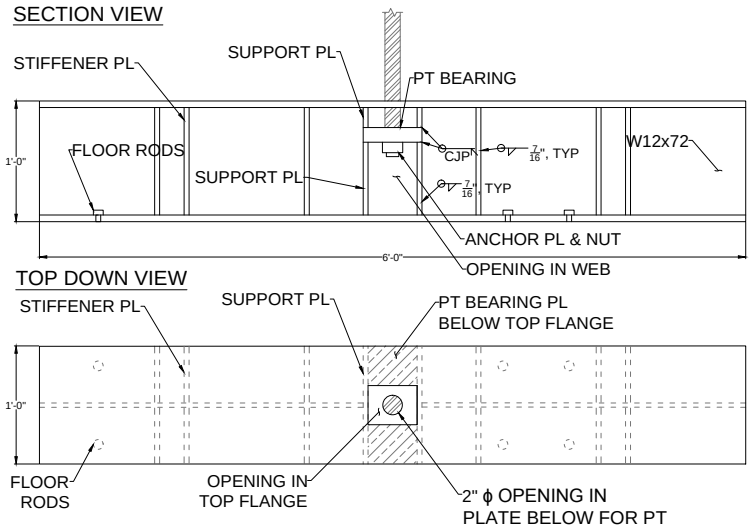

Figure 4.5: Steel Base Beam Schematic

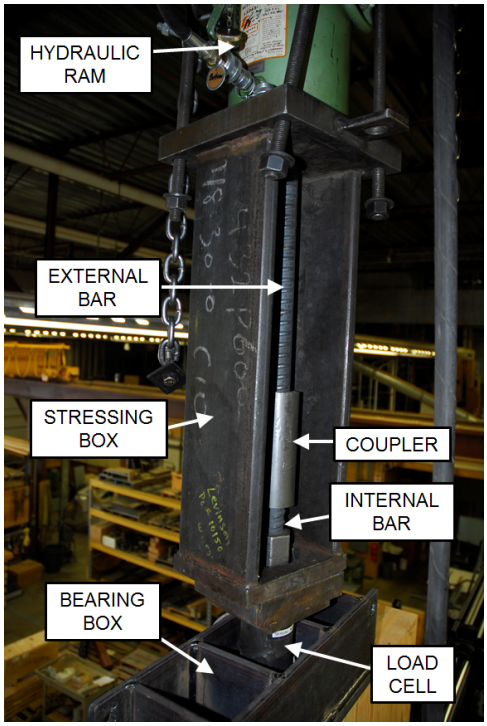

Figure 4.6: PT Stressing Apparatus

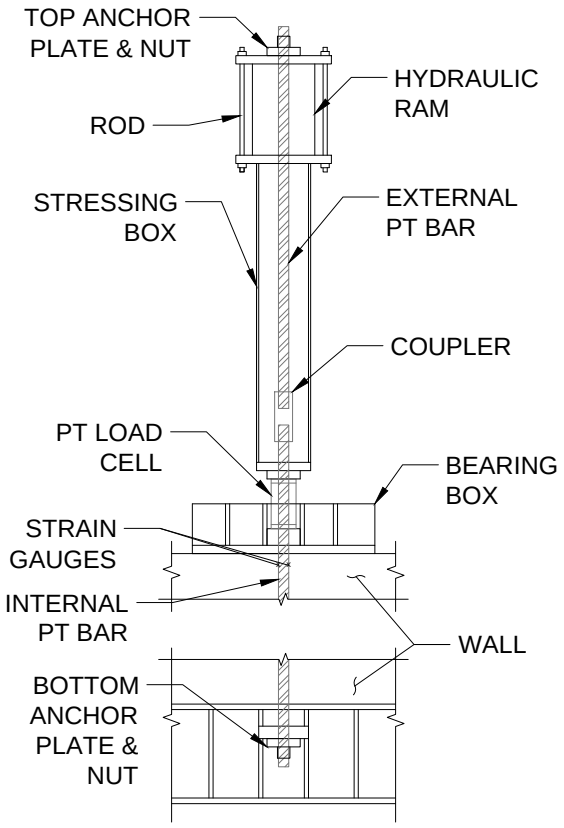

Figure 4.7: PT Stressing Apparatus Schematic

During testing, lateral load was applied to the wall through a 100-kip MTS actuator. As shown in Figure 4.4, the actuator was mounted at a height of 13 feet and 6 inches from the top of the base beam to a W14x90 column braced by a W8x35 to transfer the lateral reaction into the strong floor. The actuator was mounted to the CLT wall specimen with a steel box that was fixed to two MC6 channels. The channels, one on each side of the wall, were fixed to the CLT wall with Simpson Strong-Drive SDS $\frac{1}{4}$x2 screws. The two clevises at each end of the actuator ensured the actuator would only apply load in its axial direction. A load cell was attached between the actuator and clevis on the CLT wall side to measure the load in the actuator. Away from the W14x90 column the actuator rested on a steel channel

support. During testing when the CLT wall rocked, the shear force from the actuator was transferred into the base beam through two 8 inch long L5x5x1 steel angles that were bolted transversely east to west on the north and south sides of the base beam. The shear transfer angles are shown in Figure 4.3 and Figure 4.4.

To restrict out-of-plane movement of the CLT wall, upper and lower out-of-plane restraints were added to the testing apparatus. The lower out-of-plane restraint consisted of two 32 inch long L5x5x1 steel angles each bolted longitudinally north to south to the base beam restricting movement in the east and west directions. The lower restraint is shown in Figure 4.3 and Figure 4.4. The upper out-of-plane restraint was provided at a height of 10 feet on both the east and west sides of the wall. A photograph of the upper restraint is shown in Figure 4.8 and a schematic is shown in Figure 4.9. To keep the wall in-plane each upper restraint had a $1\frac{5}{8}$x$1\frac{5}{8}$ inch steel channel lined with plytetrafluoroethylene (PTFE) and connected with a threaded rod to a HSS 5x2x$\frac{3}{16}$. The HSS was in turn connected to a W14x90 column. To eliminate friction resistance, two strips of PTFE were connected to the east and west faces of the wall so the wall would run against the steel channel.

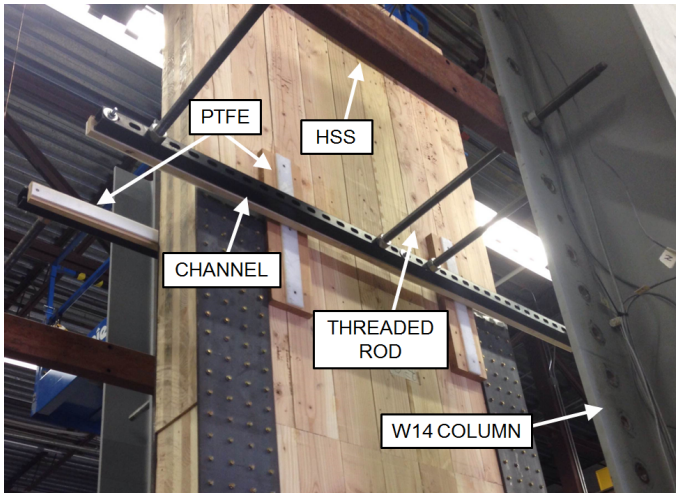

Figure 4.8: East Face Upper Out-of-Plane Restraint

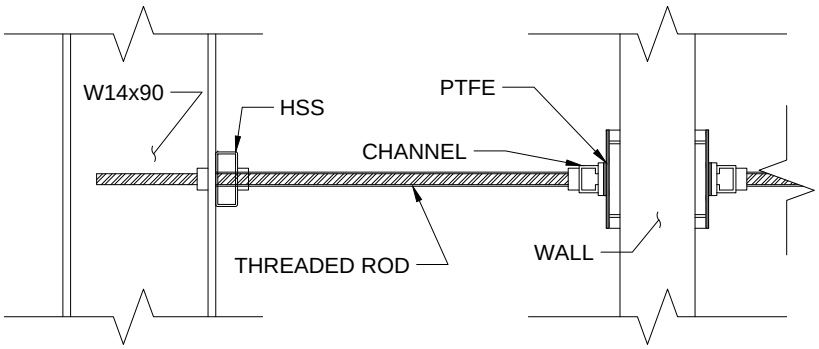

Figure 4.9: Upper Out-of-Plane Restraint Schematic

4.4.2 General Instrumentation

This section describes the instrumentation for Specimens 1, 2, 3a, 3b, 3c, and 5. The instrumentation for Specimen 4 and Specimen 6 is described in the following sections. A total of twenty-four instruments were used for data collection. Table 4.2 lists the instruments used during the tests. The first part of the section lists the instrument specifications and the second part of this section lists the quantities measured by the instruments.

StrainSmart System 5000 by Micro Measurements was used for all instrument data acquisition. Instrument calibration factors were calculated and inputted in StrainSmart to convert measured voltages to displacements or strains. A Vishay Model S100B scanner was used to record instrument measurements at 10 hertz (10 times per second) and to store the measurements in delimited output files. The conductive plastic potentiometers used were Duncan 9600 Series Linear Position Sensor Modules made by Regal Components AB. The LVDTs used were either the Macro Sensor DC 750 Series or the SE 750 Series. The inclinometers used were Accustar Electronic Inclinometers made by Sherborne Sensors.The string potentiometers used were Celesco-SM Series Linear Potentiometers. The strain gauge model used was the Tokyo Sokki Kenkyuho CO. Ltd. YFLA-05-5LT model. The gauges acted uniaxially with a 5 mm gauge length and a 2.11 nominal gauge factor. The accuracy

was reported to be 2% strain.

The conductive plastic potentiometers (Duncan potentiometers), inclinometers, and LVDTs were used to measure wall gap openings, CLT panel base deformation, and CLT panel rotations, and shear deformation of the CLT panel. Figure 4.10 shows a photograph of the Duncan potentiometers, LVDTs, and inclinometers on a specimen and Figure 4.11 shows a schematic for the same instruments.

The Duncan potentiometers were placed on the east wall face to measure vertical compression deformations and gap openings. The Duncan potentiometers were placed equally 8 inches apart at the base of the wall. The Duncan potentiometers had a stroke of $1\frac{1}{2}$ inches and were initially set at $\frac{3}{4}$ inch of displacement.

Inclinometers were used to measure the rotation of the CLT wall which was used in the calculation of the elastic modulus of the CLT panels. The inclinometers were placed horizontally in the middle of the east face and vertically at 9 inches and 35 inches from the base beam.

Two Linear variable differential transformers (LVDTs) were connected to a mount which was connected to the wall with a single screw. A total of eight LVDTs and four mounts were used. The four lower LVDTs were used to measure gap opening and wall compression. Two 3.0 inch total stroke (long stroke) LVDTs were set on the east face to measure vertical displacement at the north and south corners. Two 1.5 inch (short stroke) total stroke LVDTs were mounted 9 inches vertically from the base beam and oriented diagonally at either the north or south corner of the east face to measure gap opening of the opposite corner. The four upper LVDTs were used to measure the shear deformation of the CLT panels and were placed higher up on the wall in a similar manner to the lower LVDTs. Two 1.5 inch total stroke LVDTs were mounted 35 inches vertically from the base beam and oriented vertically to measure vertical displacement of the CLT wall panel. Two 3.0 inch total stroke LVDTs were mounted 35 inches vertically from the base beam and oriented diagonally to measure diagonal displacement of the CLT wall panel.

String potentiometers were used to measure large displacements of the system. Figure 4.4

shows the string pot locations. String Pot. A measured the vertical displacement of the actuator to be used in for correction of String Pot C's readings and the actuator LVDT readings. String Pot. B measured the lateral displacement of the wall at the lower north side and String Pot. C measured the lateral displacement of the wall at the upper south side. These measurements were compared to the actuator LVDT measurement.

An actuator load cell was used to measure the actuator force used for calculation of the base shear and overturning moment. A PT load cell and strain gauges were used to measure the PT Force. For all tests except Specimen 3a and 3b, two strain gauges were attached to the upper part of the PT bar. Figure 4.7 shows the locations of the strain gauges.

Table 4.2: Instrumentation Assignments for General Setup

Instrument	Instrument Type	Channel	Measurement
LVDT-ACT	Actuator LVDT	1	Actuator disp.
String Pot. A	String Pot.	2	Vertical disp. of actuator
String Pot. B	String Pot.	3	Lateral disp. of wall
String Pot. C	String Pot.	4	Lateral disp. of wall
String Pot. D	String Pot.	5	Steel base beam slip
DP-1	Duncan Pot.	6	Gap opening/ Wall deformation
DP-2	Duncan Pot.	7	Gap opening/ Wall deformation
DP-3	Duncan Pot.	8	Gap opening/ Wall deformation
DP-4	Duncan Pot.	9	Gap opening/ Wall deformation
DP-5	Duncan Pot.	10	Gap opening/ Wall deformation
LVDT-1	Long Stroke LVDT	15	Gap opening/ Wall deformation
LVDT-2	Short Stroke LVDT	11	Gap opening/ Wall deformation
LVDT-3	Long Stroke LVDT	17	Gap opening/ Wall deformation
LVDT-4	Short Stroke LVDT	12	Gap opening/ Wall deformation
LVDT-5	Short Stroke LVDT	13	Shear deformation
LVDT-6	Long Stroke LVDT	18	Shear deformation
LVDT-7	Short Stroke LVDT	14	Shear deformation
LVDT-8	Long Stroke LVDT	16	Shear deformation
RM-1	Inclinometer	19	Wall rotation
RM-2	Inclinometer	20	Wall rotation
LC-ACT	Load Cell	21	Actuator load
LC-PT	Load Cell	22	PT bar load
SG-1	Strain Gauge	23	PT bar strain
SG-2	Strain Gauge	24	PT bar strain

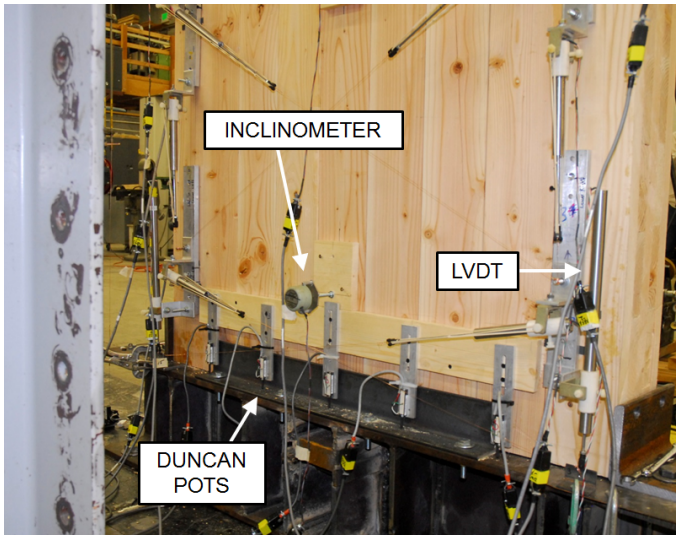

Figure 4.10: General Instrumentation Layout

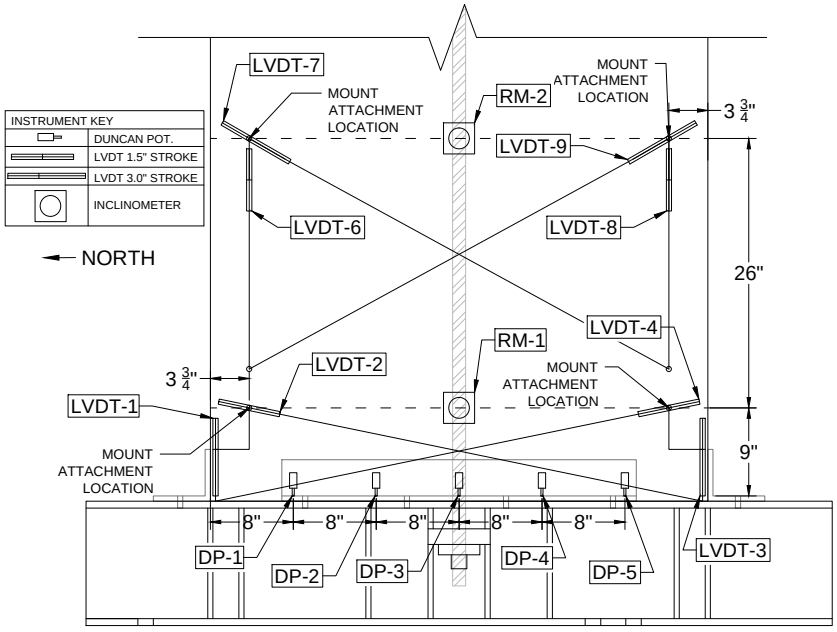

Figure 4.11: General Instrumentation Layout Schematic

4.4.3 Modified Setup 1: Specimen 4 - CLT Base

Specimen 4 was tested on a CLT base requiring modifications to the setup as shown in Figure 4.12 and Figure 4.13. A 5 ply CLT base with a $5\frac{1}{2}$ inch diameter PT hole cutout was mounted on top of the steel base beam. The CLT wall specimen was placed on top of the CLT base. The PT bar was placed and stressed in the same manner as in the general setup. The same shear transfer angles were used. New out-of-plane angles were added in between the Duncan potentiometers so the Duncan potentiometers could bear against the CLT base. Holes for the angle mounting were drilled through the CLT base to the mounting locations in the steel base beam. The upper out-of-plane restraint was the same as in the general setup.

For Specimen 4, the instrumentation scheme was modified to measure the CLT base deformation and the CLT wall deformation. The instrumentation layout can be seen in Figure 4.14 and Figure 4.15. Table 4.3 lists the instruments used in the CLT base test. The Duncan potentiometers and two vertical LVDTs on the ends were left in the same locations as the general setup to measure wall deformation. A string potentiometer was placed on a fixed channel above Duncan potentiometers and connected to the Duncan potentiometers and LVDT mounting locations. The string potentiometers measured the total deformation of the wall and the base. However, the instrumentation setup did not work as planned since the CLT base only deformed directly underneath the wall so the Duncan potentiometers and LVDTs did not measure the correct deformation. A LVDT was used to measure the steel base beam slip. String Pot. B was connected to the CLT base to measure slip. String Pot. A and C were kept in the same locations.

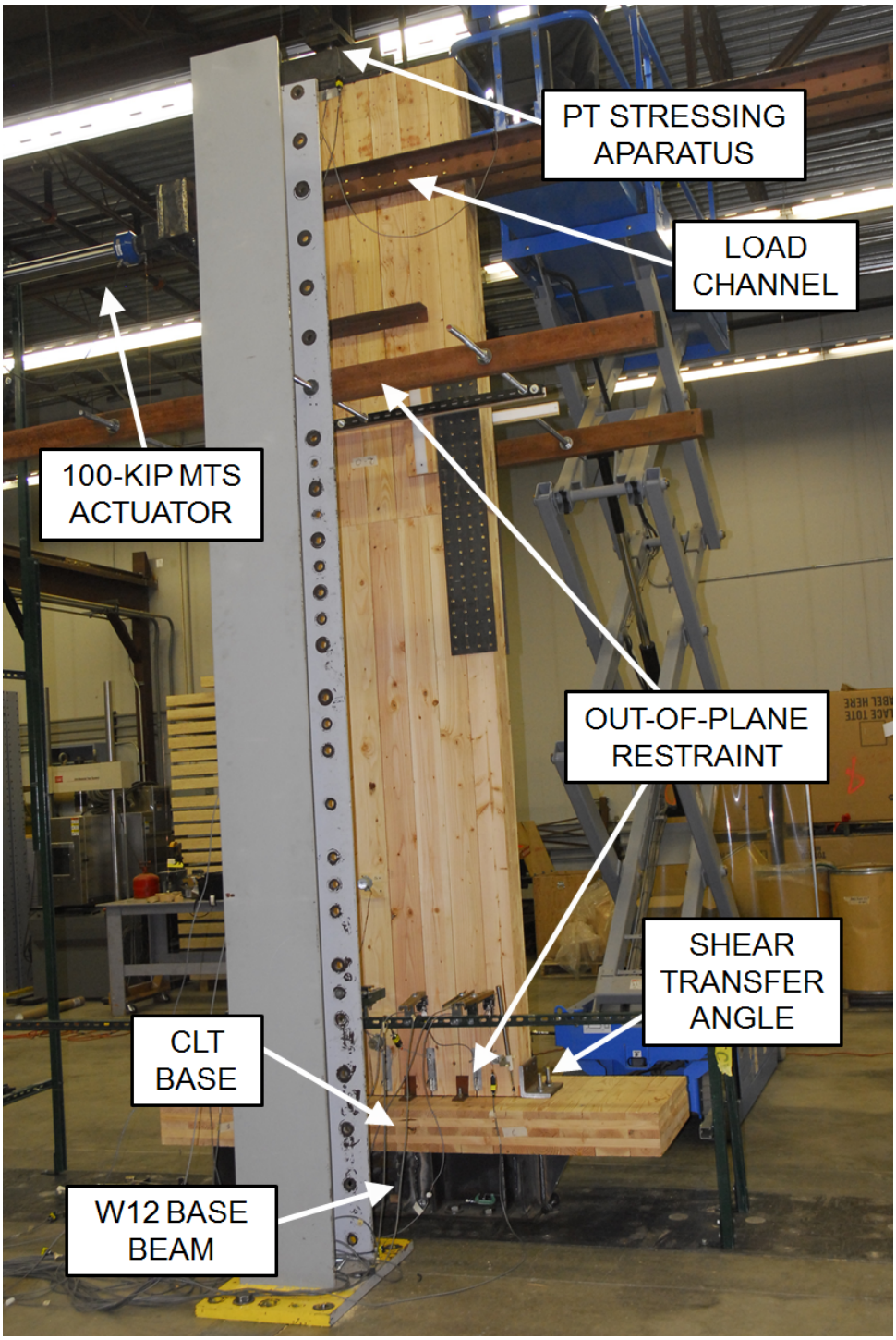

Figure 4.12: Overview of the Test Setup for Specimen 4 (CLT Base)

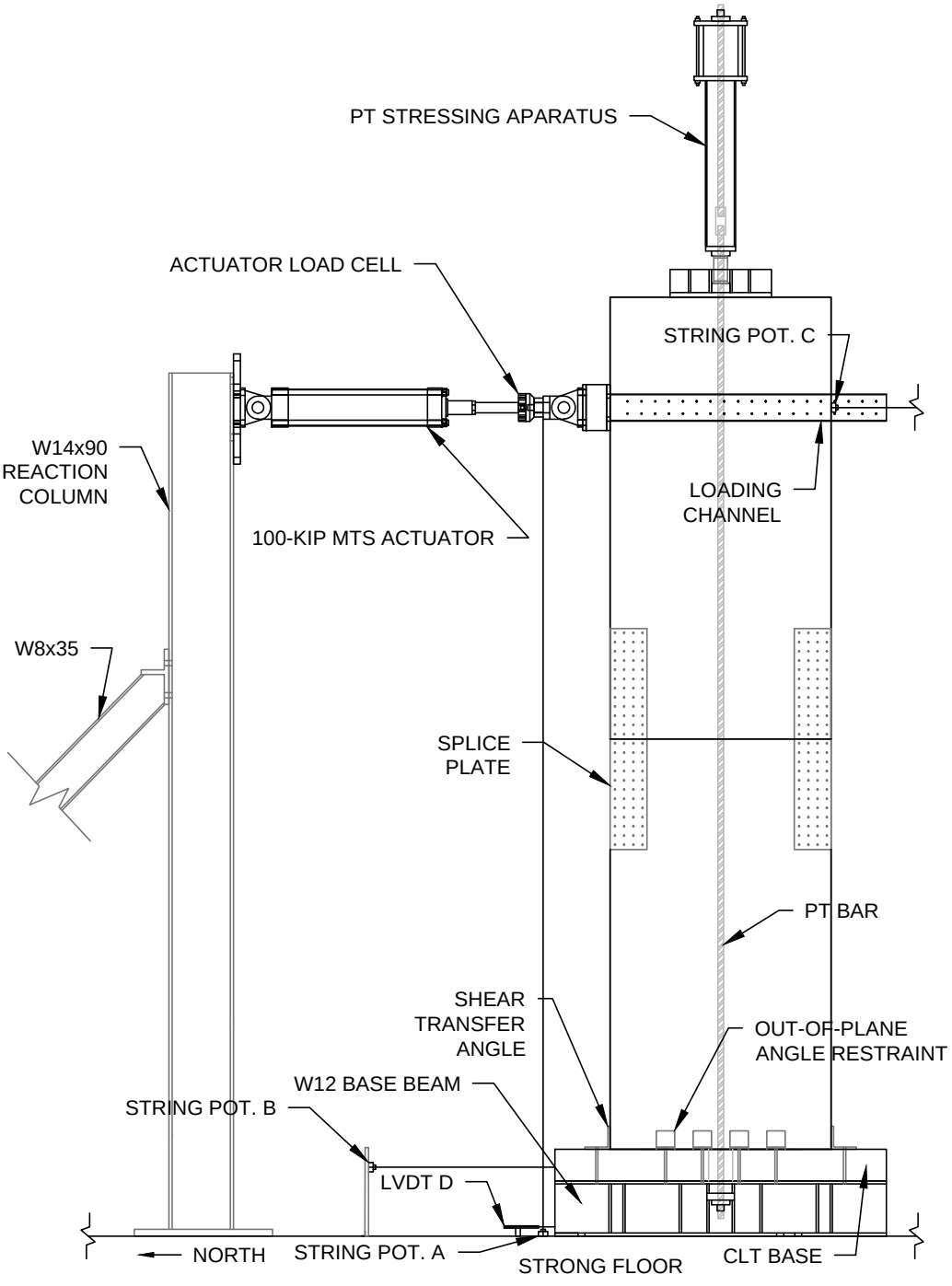

Figure 4.13: Specimen 4 (CLT Base) Test Setup Schematic

Table 4.3: Instrumentation Assignments for Specimen 4 - CLT Base

Instrument	Instrument Type	Channel	Measurement
LVDT-ACT	Actuator LVDT	1	Actuator disp.
String Pot. A	String Pot.	2	Vertical disp. of actuator
String Pot. B	String Pot.	3	Lateral disp. of wall
String Pot. C	String Pot.	4	Lateral disp. of wall
LVDT D	Long Stroke LVDT	16	Steel base beam slip
DP-1	Duncan Pot.	6	Gap opening/ Wall deformation
DP-2	Duncan Pot.	7	Gap opening/ Wall deformation
DP-3	Duncan Pot.	8	Gap opening/ Wall deformation
DP-4	Duncan Pot.	9	Gap opening/ Wall deformation
DP-5	Duncan Pot.	10	Gap opening/ Wall deformation
LVDT-1	Long Stroke LVDT	18	Gap opening/ Wall deformation
LVDT-2	Long Stroke LVDT	17	Gap opening/ Wall deformation
SP-1	String Pot.	9	Gap opening/ Total deformation
SP-2	String Pot.	11	Gap opening/ Total deformation
SP-3	String Pot.	12	Gap opening/ Total deformation
SP-4	String Pot.	13	Gap opening/ Total deformation
SP-5	String Pot.	14	Gap opening/ Total deformation
SP-6	String Pot.	15	Gap opening/ Total deformation
RM-1	Inclinometer	19	Wall rotation
RM-2	Inclinometer	20	Wall rotation
LC-ACT	Load Cell	21	Actuator load
LC-PT	Load Cell	22	PT bar load
SG-1	Strain Gauge	23	PT bar strain
SG-2	Strain Gauge	24	PT bar strain

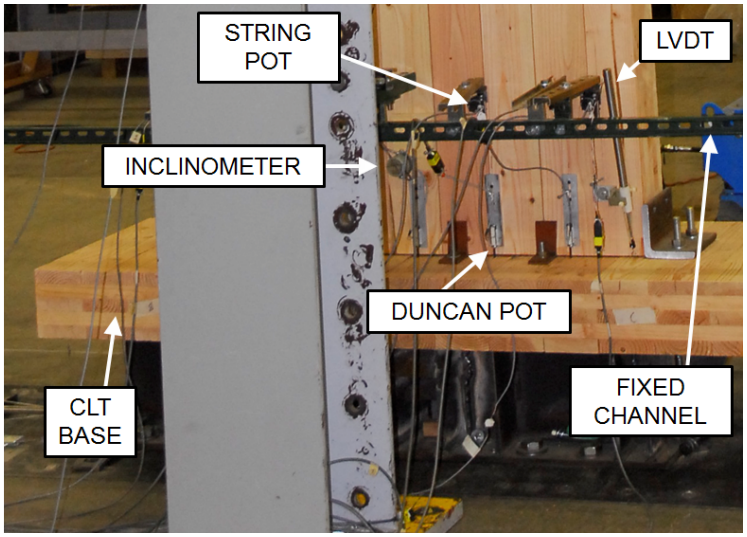

Figure 4.14: Specimen 4 (CLT Base) Instrumentation Layout

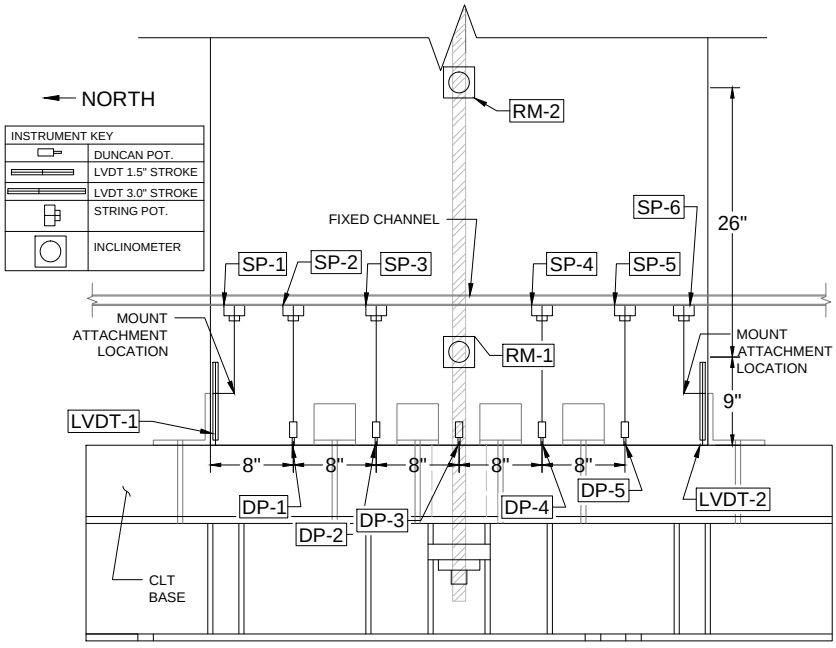

Figure 4.15: Specimen 4 (CLT Base) Instrumentation Layout Schematic

4.4.4 Modified Setup 2: Specimen 6 - Coupled Wall

Specimen 6 consisted of two 5-ply CLT walls coupled together with two UFP devices. The setup was similar to the general setup referenced in Section 4.4.1. The two walls rocked on two adjacent steel base beams. The PT bars were placed and stressed in the same manner as for the other specimens. Steel angles were mounted on either side of the walls and an HSS was mounted in between the walls to transfer the applied shear force. The same out-of-plane restraints used for Speicimens 1-5 were used for Specimen 6. An overview photograph of the setup is shown in Figure 4.16 and and a schematic is shown in Figure 4.17.

To apply the actuator lateral load to the walls a link beam was constructed as shown in Figure 4.18. Fixed MC6x12s were mounted on both sides of the north and south walls. Similar to the general setup, the actuator was connected to the MC6x12s on the north wall. An HSS 5x2x$\frac{3}{16}$ was used to link the walls together through the MC6x12s. A $1\frac{1}{2}$ inch diameter hardened steel pin was placed at the middle of each wall through a $\frac{1}{4}$ inch thick steel plate welded to the fixed MC6x12 and through a $\frac{1}{2}$ inch thick steel plate bolted to the HSS 5x2x$\frac{3}{16}$ link. The $\frac{1}{2}$ inch thick steel plate was placed against another steel plate covered in grease to make a frictionless surface which allowed the link beam to rotate freely about the pin.

The walls were coupled with two UFPs whose details are shown in Figure 4.19. The lower UFP was mounted at $\frac{1}{3}$ of the total wall height (5 feet and 4 inches above the base beam) and the upper UFP was mounted at $\frac{2}{3}$ of the total wall height (10 feet 8 inches above the base beam). To attach each UFP to the wall, a saddle was created by welding two $\frac{1}{4}$ inch plates perpendicular to each edge of a $\frac{1}{2}$ inch plate. The $\frac{1}{4}$ inch plates were mounted to the CLT walls with timber rivets. A saddle was attached to each wall at each mounting location. The UFP was attached to the $\frac{1}{2}$ inch plate on each saddle with $\frac{3}{4}$ inch steel bolts.

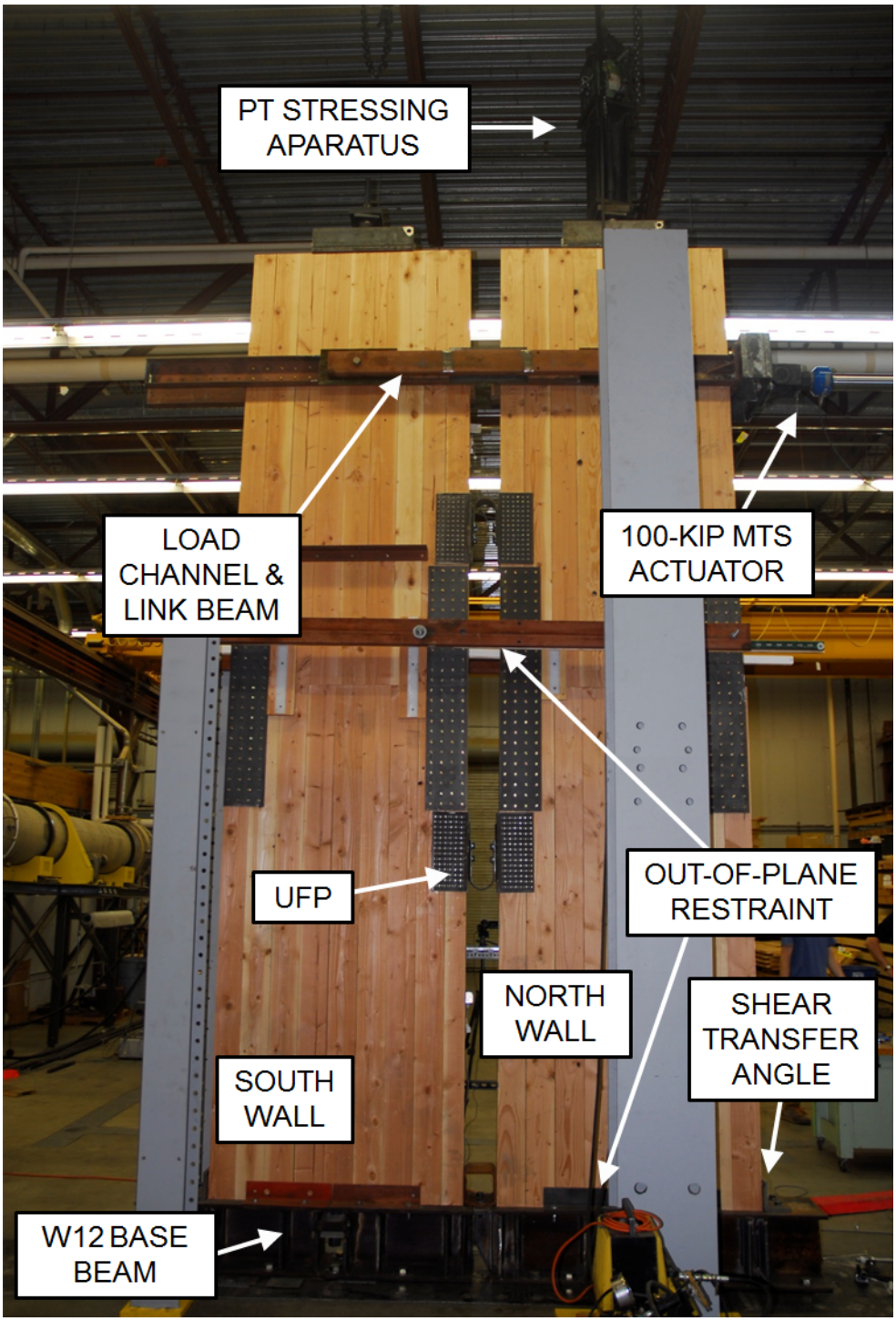

Figure 4.16: Overview of Coupled Wall Test Setup

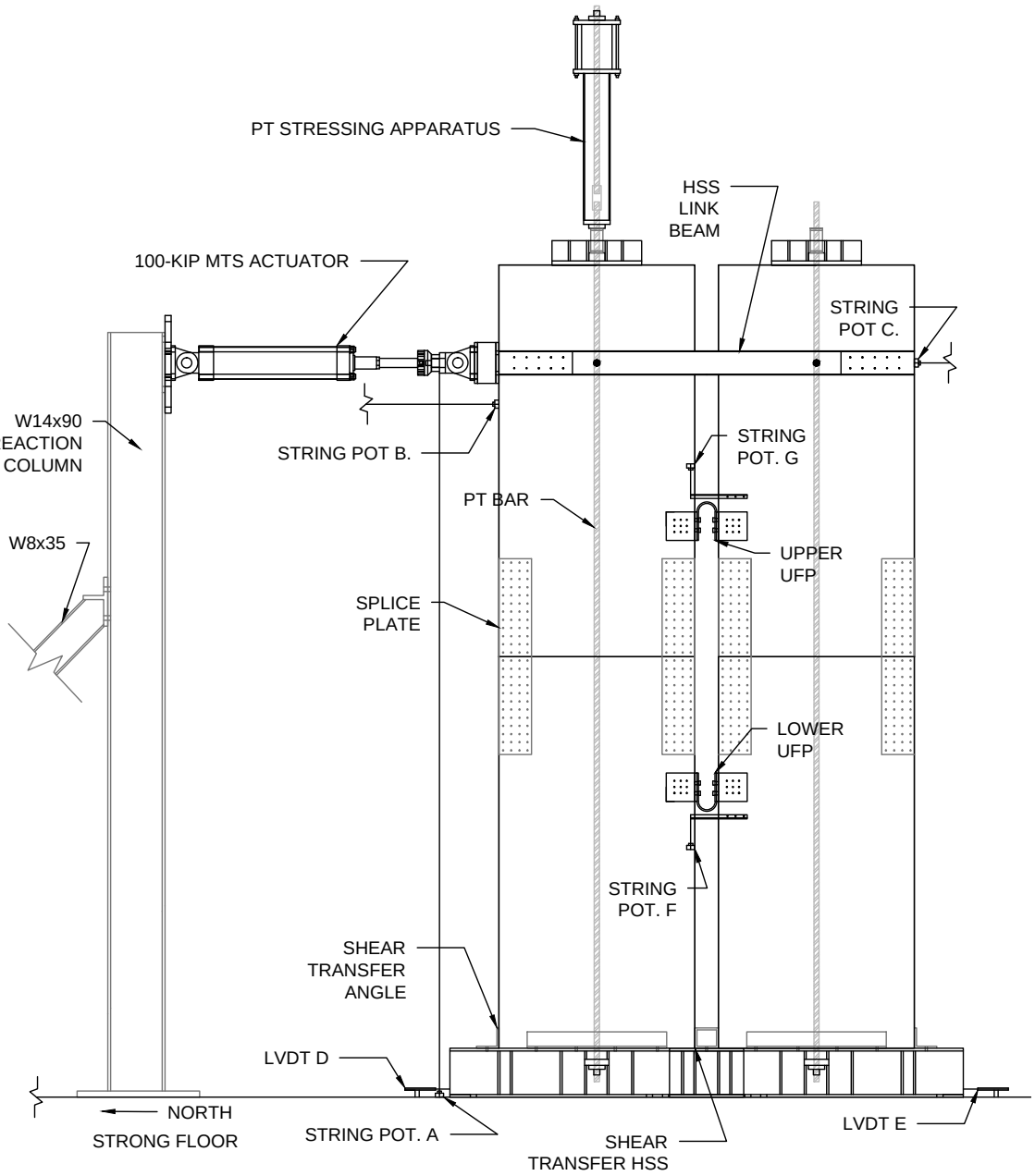

Figure 4.17: Coupled Wall Test Setup Schematic

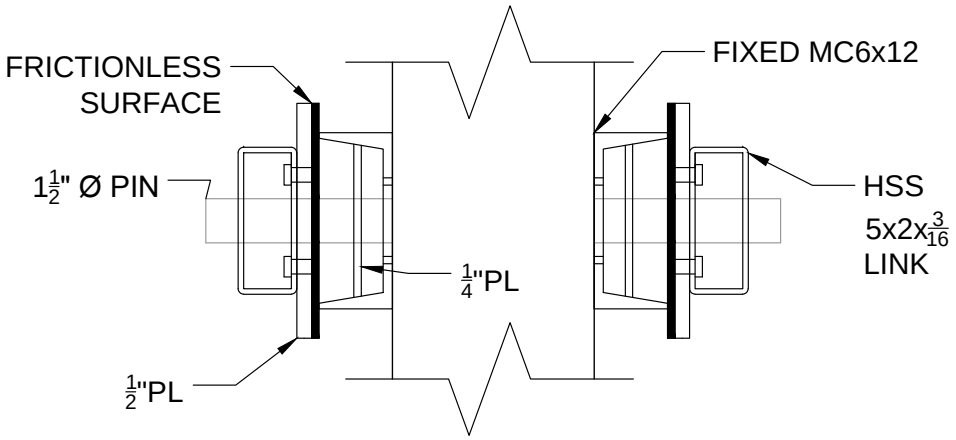

Figure 4.18: Coupled Wall Link Beam Schematic

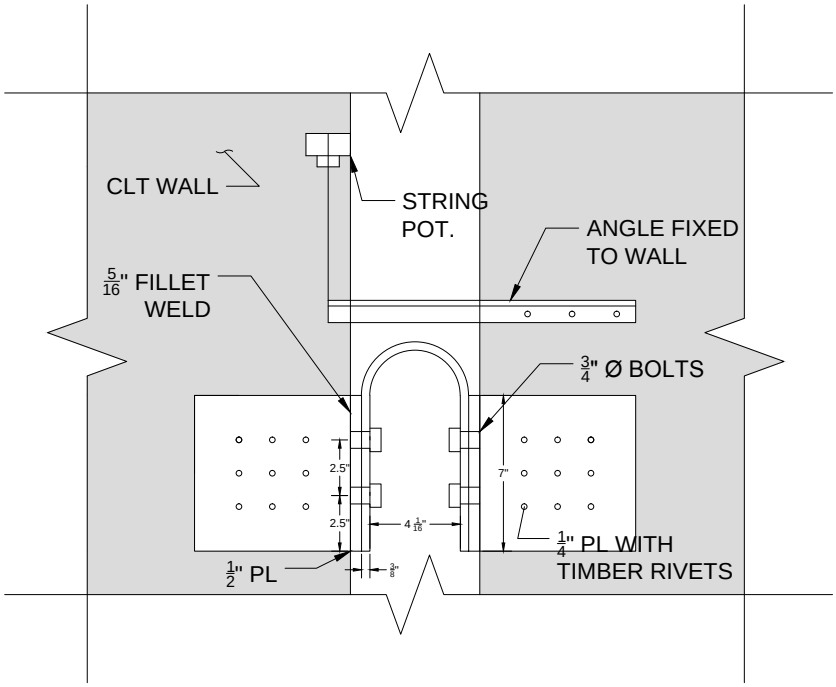

Figure 4.19: Coupled Wall UFP Attachment

Since the data acquisition system was limited to 20 channels, the instrumentation scheme was modified, as shown in Figure 4.16 and Figure 4.21, so data could be collected from both walls. To measure lateral wall displacement, a string potentiometer was connected to the top of each wall. As with the general setup, a string pot was connected from the strong floor to the actuator to measure vertical displacement of the actuator. LVDTs were mounted to the strong floor and connected to each base beam to measure base beam slip. To measure the UFP deformation, at each UFP location, a string potentiometer was mounted to one wall and attached to a aluminum angle mounted to the other wall. Inclinometers were placed 24 inches above the base beam in the center of each wall. String potentiometers were placed at the base edges to measure base deformation and uplift. Duncan potentiometers were placed at every 12 inches from the edge of the wall to also measure base deformation and uplift. On the south wall, an LVDT was used instead of a Duncan potentiometer due to the channel constraints. At the top of each PT bar a load cell was used. Two strain gauges were attached at the top of each PT bar as well. Table 4.4 lists the instruments used in the coupled wall test.

Table 4.4: Instrumentation Assignments for Specimen 6 - Coupled Wall

Instrument	Instrument Type	Channel	Measurement
LVDT-ACT	Actuator LVDT	1	Actuator disp.
String Pot. A	String Pot.	2	Vertical disp. of actuator
String Pot. B	String Pot.	11	Lateral disp. of north wall
String Pot. C	String Pot.	4	Lateral disp. of south wall
LVDT D	Long Stroke LVDT	18	North steel base beam slip
LVDT E	Long Stroke LVDT	17	South steel base beam slip
String Pot. F	String Pot.	14	Lower UFP disp.
String Pot. G	String Pot.	14	Upper UFP disp.
DP-1	Duncan Pot.	5	North Wall gap/ deformation

Continued on next page

Table 4.4 – Continued from previous page

Instrument	Instrument Type	Channel	Measurement
DP-2	Duncan Pot.	6	North Wall gap/ deformation
DP-3	Duncan Pot.	7	North Wall gap/ deformation
DP-4	Duncan Pot.	8	South Wall gap/ deformation
DP-5	Duncan Pot.	10	South Wall gap/ deformation
LVDT-1	Long Stroke LVDT	18	South Wall gap/ deformation
SP-1	String Pot.	3	Gap opening/ Total deformation
SP-2	String Pot.	9	Gap opening/ Total deformation
SP-3	String Pot.	12	Gap opening/ Total deformation
SP-4	String Pot.	13	Gap opening/ Total deformation
RM-1	Inclinometer	19	North wall rotation
RM-2	Inclinometer	20	South wall rotation
LC-ACT	Load Cell	21	Actuator load
LC-PTN	Load Cell	22	North PT bar load
LC-PTS	Load Cell	27	South PT bar load
NSG-1	Strain Gauge	23	North PT bar strain
NSG-2	Strain Gauge	24	North PT bar strain
SSG-1	Strain Gauge	25	South PT bar strain
SSG-2	Strain Gauge	26	South PT bar strain

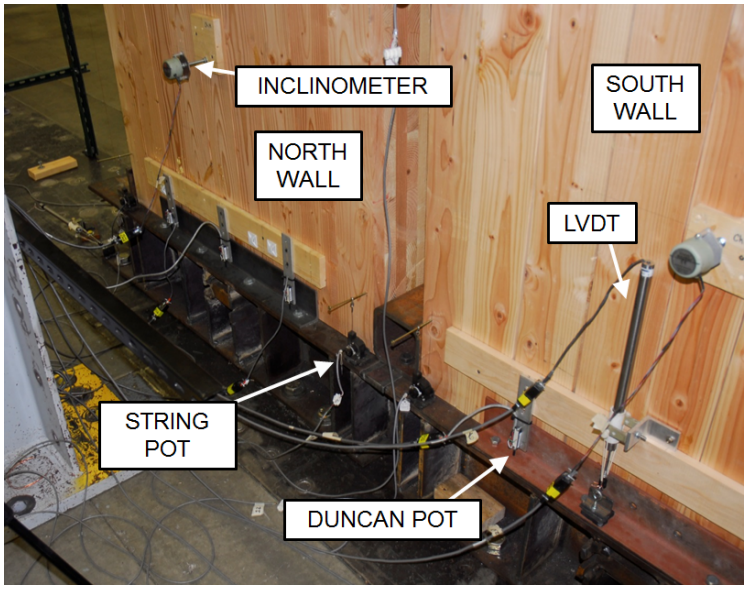

Figure 4.20: Coupled Wall Instrumentation Layout

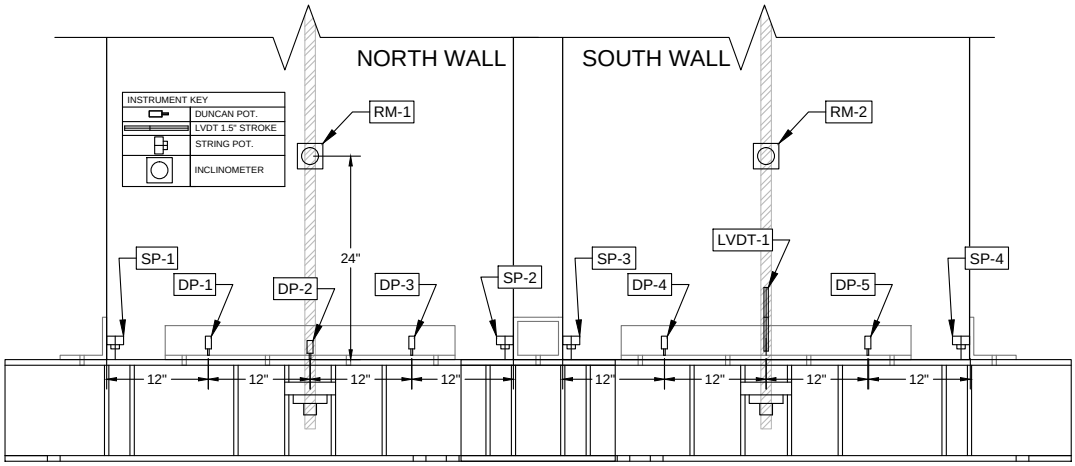

Figure 4.21: Coupled Wall Instrumentation Layout Schematic

4.4.5 Load Protocol

All specimens were subjected to the same quasi-static reverse-cyclic loading procedure. The procedure consisted of a monotonically increasing, cyclic displacement history applied by the actuator LVDT. The actuator displacements were controlled from a personal computer using MTS FlexTest software. At points of interest, which were generally at peak displacements, the actuator loading was paused allowing time to record observations and take photographs of the specimens. The displacement history was then resumed. A load rate of 0.15 inches per second was used throughout the tests, except for Specimen 1 which used a load rate of 0.30 inches per second.

Due to the system's similarity to post-tensioned precast concrete walls, the displacement protocol was constructed according to *ACI ITG-5.1-07 Acceptance Criteria for Special Unbonded Post-Tensioned Precast Structural Walls Based on Validation Testing*. The protocol consisted of 18 steps which corresponded to target drift ratios. Table 4.5 lists the full drift ratio history used for the tests. Specimens 2, 3a, 3b, and 3c were subjected to steps 1 through 17. Specimens 1, 4, 5, and 6 were subjected to steps 1 through 18. The actuator input displacements were calculated by multiplying the target drift ratios by the height from the top of the base beam to the actuator pin location. To incorporate the effect of cyclic fatigue, three fully reversed cycles were run for each drift ratio.

Table 4.5: Load Protocol

Step No.	Target Drift Ratio (%)
1	0.035
2	0.050
3	0.075
4	0.10
5	0.15
6	0.20
7	0.30
8	0.40
9	0.60
10	0.90
11	1.35
12	2.00
13	3.00
14	4.00
15	5.00
16	7.50
17	9.50
18	11.0

Chapter 5

EXPERIMENTAL OBSERVATIONS

;

5.1 Introduction

This chapter documents the experimental observations on the 6 rocking CLT wall specimens. Damage states, described in the next section, were tracked and recorded throughout each test. To help with the damage descriptions the orientation of each test specimen is shown in Figure 5.1. A description of CLT construction (plys vs. laminates) was shown in Figure 4.1a. The actuator load history was described in Section 4.4.5. During testing the actuator reaction column flexed which resulted in slightly different drifts for each specimen. The corrected drift readings (corrected in Chapter 6) are shown in Table 5.1. Positive displacement corresponded to the actuator retracting and the wall being pulled to the north, and negative displacement corresponded to the actuator extending and the wall being pushed to the south. In the test photographs the CLT damage is highlighted in red.

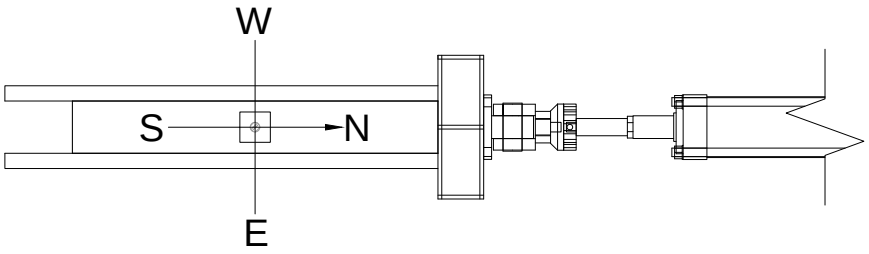

Figure 5.1: Test Specimen Plan Orientation

Table 5.1: Corrected Drift Readings

Step	Target	Specimen Actual Peak Drift (%)							
No.	Drift (%)	1	2	3a	3b	3c	4	5	6
1	0.035	0.020	0.030	0.015	N/A	0.010	0.010	0.020	0.010
2	0.050	0.030	0.040	0.025	N/A	0.020	0.020	0.030	0.020
3	0.075	0.050	0.070	0.040	N/A	0.030	0.040	0.045	0.040
4	0.10	0.07	0.09	0.06	N/A	0.05	0.07	0.06	0.05
5	0.15	0.12	0.13	0.11	N/A	0.10	0.11	0.10	0.09
6	0.20	0.16	0.17	0.14	N/A	0.13	0.16	0.13	0.12
7	0.30	0.23	0.27	0.21	N/A	0.21	0.25	0.19	0.19
8	0.40	0.31	0.36	0.29	N/A	0.29	0.34	0.28	0.26
9	0.60	0.47	0.55	0.49	0.51	0.46	0.47	0.46	0.40
10	0.90	0.76	0.85	0.79	0.81	0.75	0.75	0.75	0.64
11	1.35	1.19	1.29	1.25	1.26	1.17	1.18	1.17	1.05
12	2.00	1.84	1.91	1.96	1.91	1.80	1.83	1.79	1.64
13	3.00	2.81	2.88	N/A	2.94	2.77	2.82	2.77	2.60
14	4.00	3.81	3.86	N/A	3.99	3.76	3.82	3.75	3.61
15	5.00	4.82	4.86	N/A	5.07	4.76	4.84	4.76	4.63
16	7.50	7.42	7.42	N/A	7.78	7.35	7.35	7.34	7.26
17	9.50	9.50	9.50	N/A	9.96	9.45	9.41	9.40	9.40
18	11.0	N/A	N/A	N/A	N/A	N/A	11.0	11.0	11.0

5.2 Damage States

Throughout each test damage states were tracked to help communicate the progression of damage and the behavior of each test specimen and inform performance-based design procedures in the future. An abbreviation was assigned to each damage state for reference throughout the chapter. The CLT wall panel damage states recorded in each test are described in Table 5.2. The PT bar damage states were recorded in each test and are described in Table 5.3. The CLT base damage states were recorded for Specimen 4 and are described in Table 5.4. The UFP damage states were recorded for Specimen 6 and are described in Table 5.5. Table 5.6 lists at which step and drift each damage state was reached by each test specimen.

Table 5.2: CLT Wall Panel Damage States

Abb.	Damage State	Description	Picture
WDS1	CLT Yielding	Creaking noise is heard and small deformations are visible at the base of the wall. No repair necessary.	
WDS2	Initial CLT Damage	Compression splits and delamination measuring 1 inch or less in length. No repair necessary.	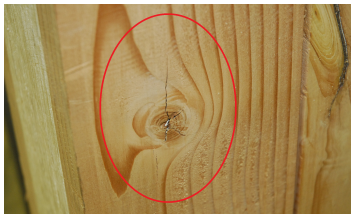
WDS3	Moderate CLT Damage	Compression splits and delamination measuring more than 1 inch in length. System maintains majority of strength capacity. Repair maybe required.	
WDS4	Significant CLT Damage	Large drop in system strength capacity due to CLT crushing damage. Repair maybe required.	

Table 5.3: PT Bar Damage States

Abb.	Damage State	Description	Picture
PT1	PT Bar Yielding	The PT bar reaches its yield stress. Repair maybe required.	
PT2	PT Bar Fracture	The PT bar reaches its ultimate stress and fractures. Repair maybe required.	

Table 5.4: CLT Base Damage States

Abb.	Damage State	Description	Picture
BDS1	Inital CLT Crushing Damage	Crushing depth is less than $\frac{1}{4}$ inch. Repair maybe required.	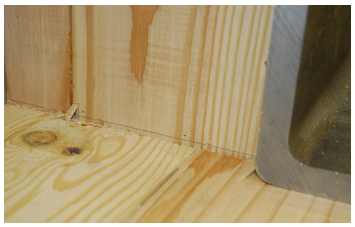
BDS2	Moderate CLT Crushing Damage	Crushing depth is greater than $\frac{1}{4}$ inch and less than $\frac{3}{4}$inch. Repair maybe required.	
BDS3	Significant CLT Crushing Damage	Crushing depth is greater than $\frac{3}{4}$ inch. Repair maybe required.	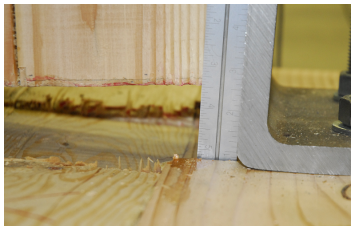
BDS4	CLT Splitting Damage	Splitting caused in outer plys of CLT base. Repair maybe required.	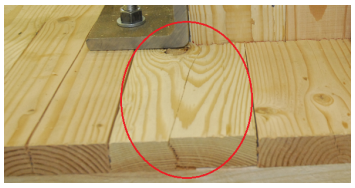

Table 5.5: UFP Damage States

Abb.	Damage State	Description	Picture
UFP1	UFP Yielding	A UFP reaches its yield stress. Repair maybe required.	
UFP2	UFP Fracture	A UFP reaches its ultimate stress and fractures. Repair maybe required.	

Table 5.6: Damage State Summary

Step	Drift	Specimen								
No.	Ratio (%)	1	2	3a	3b	3c	4	5	6-NW	6-SW
1	0.035				N/A					
2	0.050				N/A					
3	0.075				N/A					
4	0.10				N/A					
5	0.15				N/A					
6	0.20				N/A					
7	0.30				N/A					
8	0.40				N/A					WDS1
9	0.60	WDS1								WDS1
10	0.90	WDS1	WDS1	WDS1			BDS1		WDS1	WDS1
11	1.35	WDS1	WDS1	WDS1			BDS1	WDS1	WDS1	WDS1
12	2.00	WDS1	WDS1	WDS1			BDS1	WDS1	WDS2/UFP1	WDS3/UFP1
13	3.00	WDS2	WDS1	N/A	WDS2	WDS2	BDS1/4	WDS1	WDS3/UFP1	WDS3/UFP1
14	4.00	WDS3	WDS1	N/A	WDS3	WDS3	BDS2/4	WDS3	WDS3/UFP1	WDS3/UFP1
15	5.00	WDS3	WDS3	N/A	WDS3	WDS3/PT1	BDS2/4	WDS3	WDS3/UFP1	WDS3/UFP1/PT1
16	7.50	WDS4	WDS3	N/A	WDS3/PT1	WDS3/PT1	BDS3/4	WDS3/PT1	WDS3/UFP1/PT1	WDS3/UFP1/PT1
17	9.50	WDS4	WDS3/PT1	N/A	WDS3/PT1	WDS3/PT1	BDS3/4	WDS3/PT1	WDS4/UFP1/PT1	WDS4/UFP1/PT1
18	11.0	N/A	N/A	N/A	N/A	WDS3/PT1	BDS3/4	WDS3/PT1	WDS4/UFP1/PT1	WDS4/UFP1/PT1

5.3 Specimen 1

Specimen 1 was tested on April 14th, 2015. The test was open to the public to show the capabilities of rocking CLT wall system. Practitioners from around the Pacific Northwest traveled to Pullman, WA to view the test live. The objective for Specimen 1 and was to investigate the performance of a rocking CLT wall with a low decompression force and a low decompression stiffness. The CLT wall panels and PT bar were reused from Specimen 4, which was tested previously, as they were visibly undamaged. The lower 5-ply CLT panel was 4 feet long and 8 feet tall. The upper 5-ply CLT panel was 4 feet long and 6 feet $6\frac{3}{8}$ inches tall. The total wall height was 14 feet $6\frac{5}{16}$ inches and the actuator loading height was 13 feet $6\frac{1}{16}$ inches. Specimen 1 used a 1.25 inch diameter (1.25 in^2 area) PT bar. The PT bar was stressed to 59 kips ($0.37T_y$) prior to actuator loading. The first direction of loading was to the north (positive drift). The overturning moment versus drift response is shown in Figure 5.2 with major events indicated and described below.

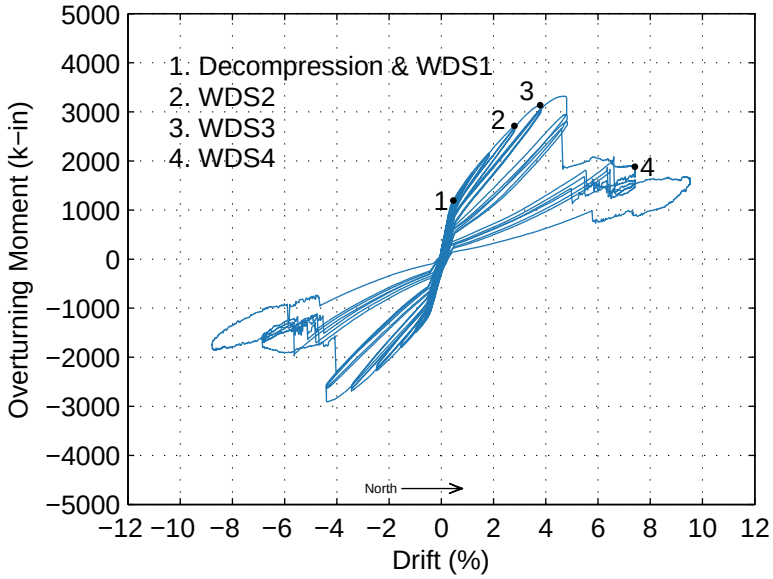

Figure 5.2: Specimen 1 Moment-Drift Response

During step 9 (0.5% drift) decompression and uplift were first observed. Also during Step 9, CLT yielding was first observed at the base of the wall at both the north and south ends (WDS1, Figure 5.3).



Figure 5.3: CLT Yielding (WDS1) at the South End of Specimen 1 During Step 9 (0.5% Drift)

At Step 13 (2.8% drift) creaking sounds were heard at the peak displacements which indicated yielding of the CLT (WDS1). Small vertical splits measuring $\frac{3}{4}$ inch were observed at the northwest corner (WDS2, Figure 5.4).

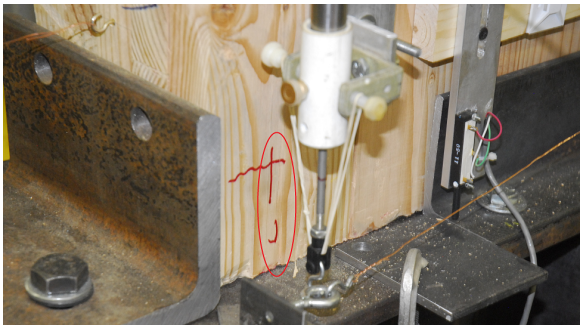

Figure 5.4: Small Vertical Splits (WDS2) at the Northwest Corner of Specimen 1 During Step 13 (2.8% Drift)

Substantial damage occurred during the first cycle of Step 14 (3.8% drift). Vertical splits were observed at two separate wood knots on the first laminate of the outer ply at the northeast corner (WDS3, Figure 5.5). These splits propagated from existing splits in the wood prior to testing. There was a large delamination of 40 inches in length and $\frac{1}{8}$ inch in width between the outer ply and adjacent inner ply at the northwest corner (WDS3, Figure 5.6a). The delamination damage led to a large failure and drop in capacity later in the test. More wood splitting around a wood knot was observed at the northwest face of the wall (WDS3, Figure 5.6b). During the negative (south) part of cycle 1 of Step 14, wood splitting was observed at the southeast corner (WDS3, Figure 5.7). Small vertical splits were observed at the southeast corner (WDS2, Figure 5.8). During Step 14, the PT bar reached a force of 140 kips in the north direction ($0.88T_y$. The PT bar force was 15 kips higher in the positive (north) part of the cycles when compared to the negative (south) part of the cycles. This unsymmetrical behavior was most likely due to a difference in bearing area causing more PT elongation in the north direction.

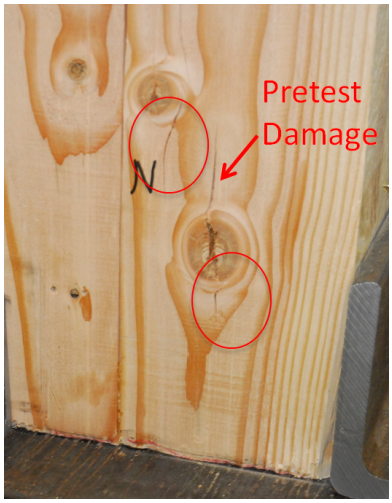

Figure 5.5: Vertical Splitting (WDS3) at the Northeast Corner of Specimen 1 During Step 14 (3.8% Drift)

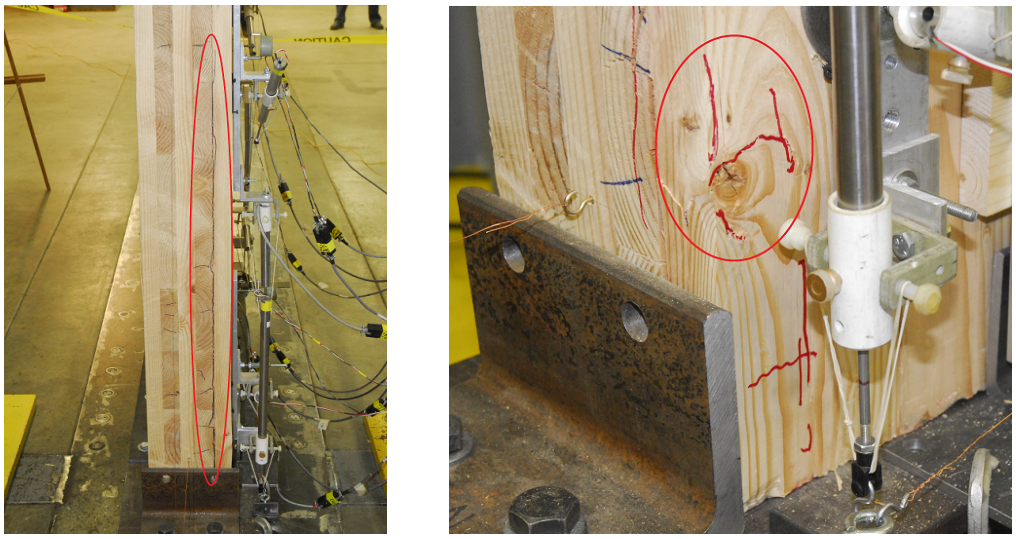

(a) (b)

Figure 5.6: Delamination and Splitting (WDS3) at the Northwest Corner of Specimen 1 During Step 14 (3.8% Drift)



(a) (b)

Figure 5.7: Vertical Splitting (WDS3) at the Southeast Corner of Specimen 1 During Step 14 (3.8% Drift)



Figure 5.8: Vertical Splitting (WDS2) at the Southwest Corner of Specimen 1 During Step 14 (3.8% Drift)

The CLT damage increased during Step 15 (4.8% drift). During Cycle 1 the splits at the northeast corner expanded (WDS3, Figure 5.9a). During Cycle 2 a new vertical split measuring 15 inches in length formed from the crushing of the wall (WDS3, Figure 5.9b). The damage did not increase during Cycle 3. During Cycle 1, a delamination of 7 inches of the outer northeast ply was observed (WDS3, Figure 5.10a). The existing delamination at the northwest corner widened to $1\frac{3}{4}$ inches after Cycle 1 and to $1\frac{7}{8}$ after during Cycle 3. The delamination did not increase in length. When the wall was cycled to the south, a delamination of 24 inches in length and $\frac{1}{8}$ inches in width occurred at the outer southeast ply from the inner plys (WDS3, Figure 5.10b). A new horizontal split was observed and existing damage increased at the southeast corner (WDS3, Figure 5.11a). Numerous splits due to wall crushing occurred at the southwest corner (WDS3, Figure 5.11b). During Step 15, the difference in PT bar force still existed. The PT bar reached a peak force of 155 kips ($0.97T_y$) when the wall was pulled to the north (positive drift) and 142 kips ($0.9T_y$) when the wall was pushed to the south (negative drift).



(a) (b)

Figure 5.9: Vertical Splitting (WDS3) at the Northeast Corner of Specimen 1 During Step 15 (4.8% Drift) - Cycle 1 (a) and Cycle 2 (b)

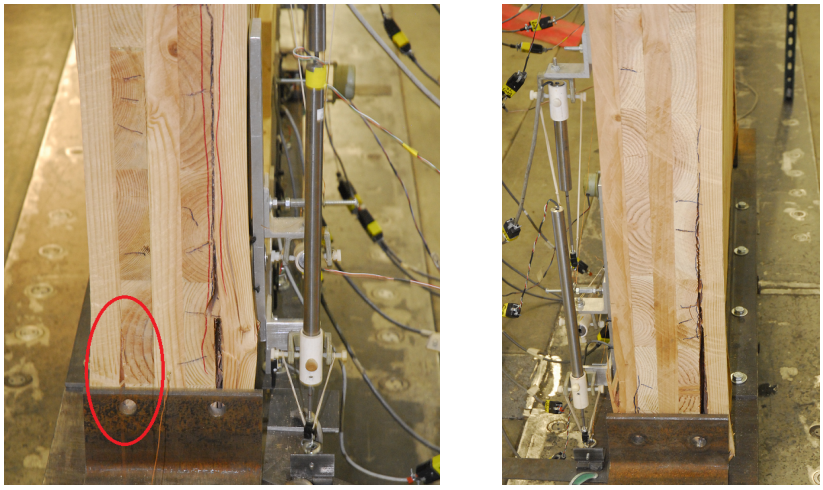

(a) (b)

Figure 5.10: Delamination (WDS3) at the (a) North End and (b) South End of Specimen 1 During Step 15 (4.8% Drift)

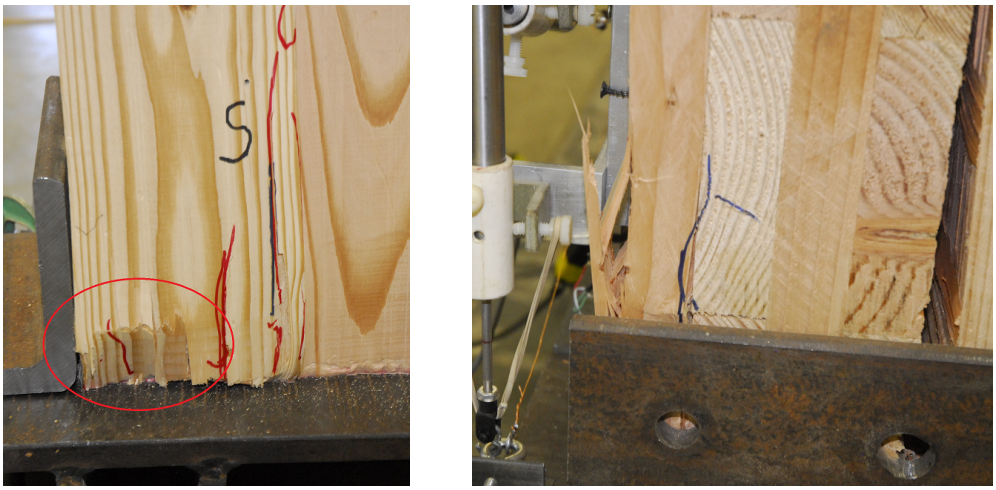

(a) (b)

Figure 5.11: Splitting (WDS3) at the (a) Southeast and (b) Southwest Corners of Specimen 1 During Step 15 (4.8% Drift)

Additional delamination and significant reduction in strength occurred during Step 16 (7.4% drift). During the first cycle, at positive 5.0% drift, the system load capacity dropped from 20 kips (3240 k-in) to 12 kips (1940 k-in) and the previously noted delamination increased in length to 70 inches and extended to the splice plate (WDS4, Figure 5.12a). The second laminate on the northwest side split out from the adjacent ply to a length of 30 inches (WDS4, Figure 5.12a). The existing delamination at the northeast corner extended to 20 inches. The splitting damage on the northeast side increased and propagated to the second laminate (WDS4, Figure 5.13). During the half cycle to the south the system capacity dropped from 18 kips (2920 k-in) to 10 kips (1620 k-in). The delamination at the southeast corner widened to $\frac{7}{8}$ inch and did not extend in length, and the damage at the southeast corner increased (WDS4, Figure 5.14). The PT bar reached a peak force of 140 kips ($0.88T_y$) to the north and 125 ($0..78T_y$) kips to the south. All gap opening instruments were removed after the first cycle of Step 16 so they would not be damaged.



(a) (b)

Figure 5.12: (a) Increased Delamination and (b) New Damage of the Second Laminate (WDS4) at the Northwest Corner of Specimen 1 During Step 16 (7.4% Drift)



Figure 5.13: (Splitting Damage (WDS4) at the Northwest Corner of Specimen 1 During Step 16 (7.4% Drift)

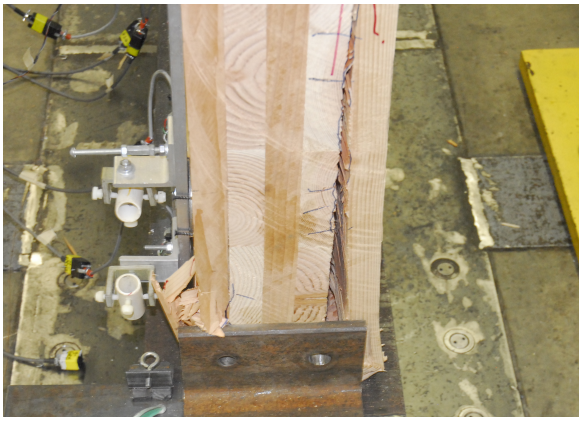

Figure 5.14: Delamination and Splitting Damage (WDS4) at the South End of Specimen 1 During Step 16 (7.4% Drift)

To complete the test, one cycle was run for Step 17 (9.5% drift). Because of the failure during the previous step the wall never reached 9.5% drift, instead reaching a maximum of 8.0% drift. At the northwest corner, the second laminate delmaminated further up the wall and the third laminate started to delaminate. At the northeast corner the wall continued to split and delaminate (WDS4, Figure 5.15a). The existing delamination and crushing at

the southeast corner continued to worsen. The outer ply at the southwest corner started to delaminate and split from the inner ply and the crushing damage increased (WDS4, Figure 5.15b). Because of the damage to the CLT panel before and during Step 16, the PT bar never reached its yield stress.



(a) (b)

Figure 5.15: Wall Damage at the (a) North and (b) South Ends of Specimen 1 During Step 17 (8.0% drift)

5.4 Specimen 2

Specimen 2 was tested on March 26, 2015. The objective for Specimen 2 was to investigate the performance of a rocking CLT wall with a low decompression force and a high decompression stiffness. The lower 5-ply CLT panel was 4 feet long and 8 feet tall. The upper 5-ply CLT panel was 4 feet long and 6 feet $6\frac{3}{8}$ inches tall. The total height of the specimen was 14 feet $6\frac{3}{8}$ inches and the actuator height was 13 feet $4\frac{1}{4}$ inches. Specimen 2 used the 1.375 inch diameter (1.58 in^2 area) PT bar. The PT bar was stressed to 25.5 kips ($0.37T_y$ prior to actuator loading. The first direction of loading was to the south (negative drift). The overturning moment versus drift response is shown in Figure 5.16.

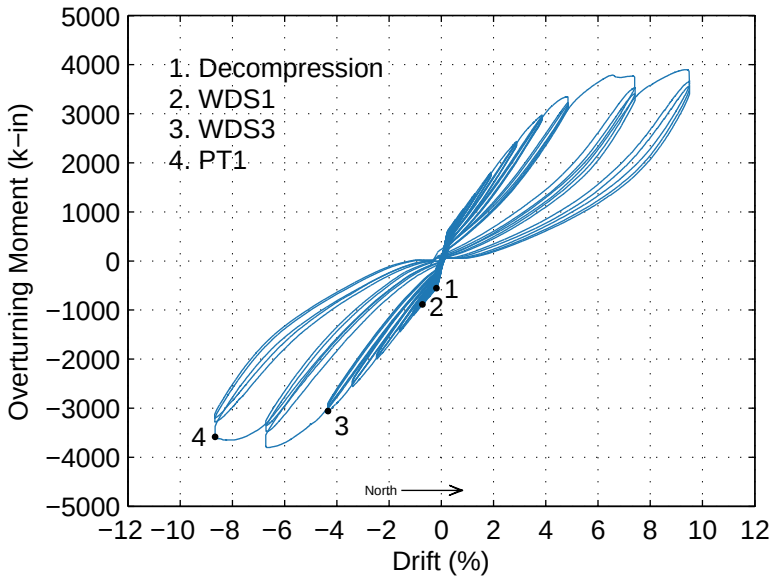

Figure 5.16: Specimen 2 Moment-Drift Response

Decompression and uplift were first observed at Step 7 (.3% drift) as shown in Figure 5.17. Creaking noises were heard during Step 10 (0.9% drift) indicating CLT yielding had occurred (WDS1).



Figure 5.17: Wall Decompression of Specimen 2 During Step 7 (0.3% drift)

The first visible CLT damage was observed at Step 15 (4.9% drift). During the first cycle, no damage was visible at the south end and a compression failure consisting of a horizontal split measuring $2\frac{1}{2}$ inches in length and a vertical split measuring $2\frac{1}{4}$ inches in length occurred at the northeast corner (WDS3, see Figure 5.18). During the second negative drift cycle, a horizontal split measuring 3 inches in length occurred at a wood knot at the southeast corner (WDS3, Figure 5.19). During the second positive drift cycle, a small compression split occurred on the first outside ply at the northeast corner (see Figure 5.20). During Step 15, the PT bar reached a maximum force of 150 kips ($0.74T_y$).

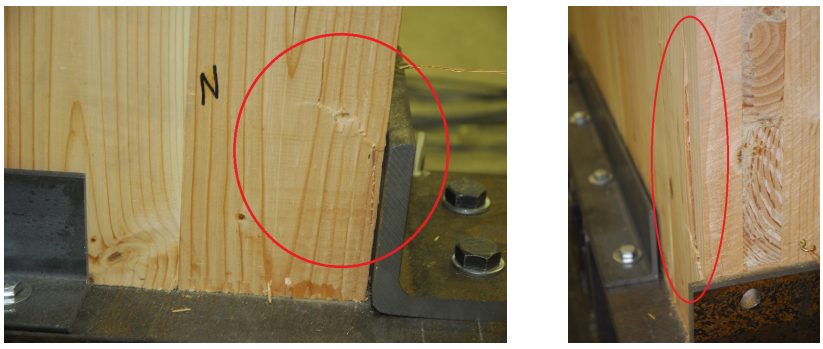

(a) (b)

Figure 5.18: Horizontal and Vertical Split (WDS3) at the Northeast Corner of Specimen 2 During Step 15 (4.9% Drift)

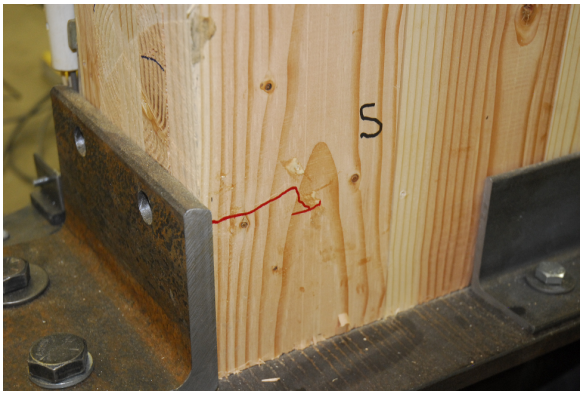

Figure 5.19: Horizontal Split (WDS3) of at the Southeast Corner of Specimen 2 During Step 15 (4.9% Drift)

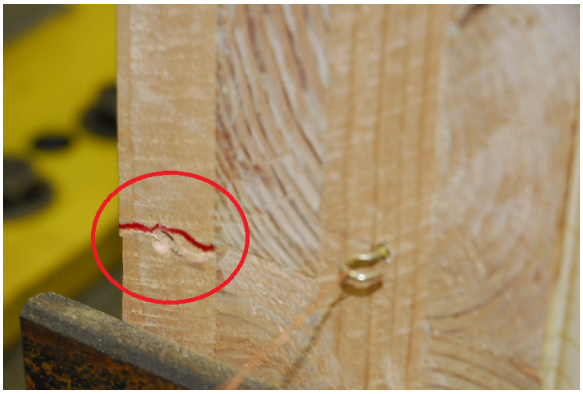

Figure 5.20: Compression Failure (WDS3) at the Northeast Corner of Specimen 2 During Step 15 (4.9% Drift) - Cycle 2

The CLT damage continued to progress throughout Step 16 (7.4% drift). At the southeast corner, CLT damage propagated into larger horizontal and vertical splits from the horizontal split(WDS3, Figure 5.21a). At the southwest corner, wood splitting due to compression failures were observed for the first time (WDS3, Figure 5.21b). The damage at the northeast corner progressed vertically and new damage was observed in the second laminate on the east side (see Figure 5.22a). CLT Damage due to wood crushing was first observed at the northwest corner (WDS3, Figure 5.22b). The PT bar reached a maximum force of 180 kips

$(0.89T_y)$ in both directions.

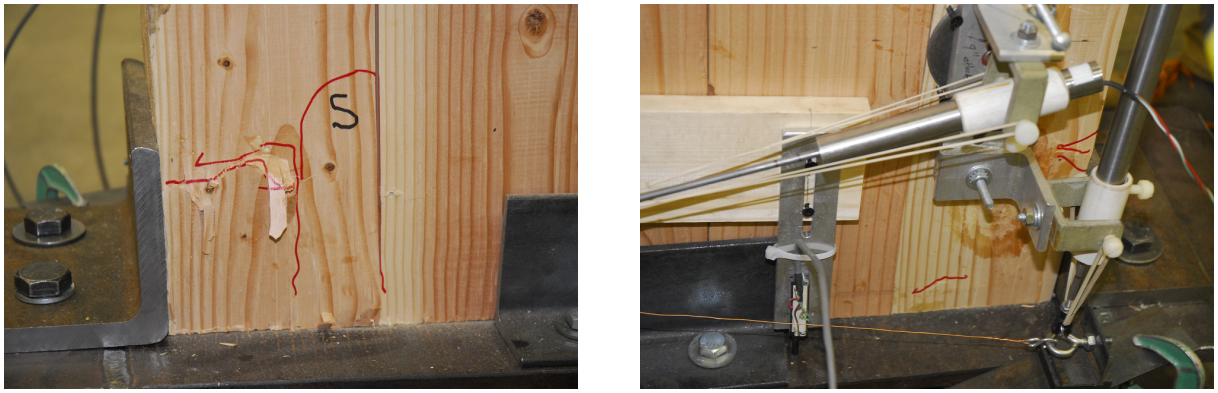

(a) (b)

Figure 5.21: Compression Damage (WDS3) at the (a) Southeast and (b) Southwest Corners of Specimen 2 During Step 16 (7.4% Drift)

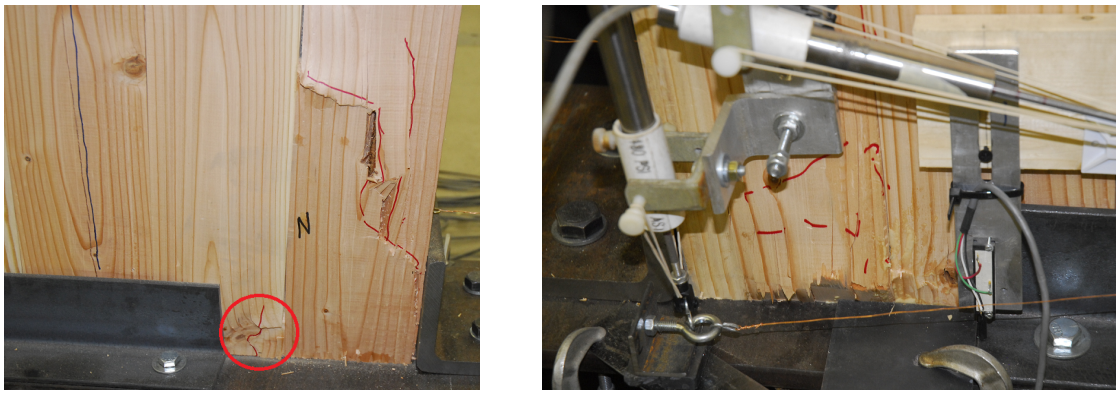

(a) (b)

Figure 5.22: Compression Damage (WDS3) at the (a) Northeast and (b) Northwest Corners of Specimen 2 During Step 16 (7.4% Drift)

Wall damage continued to increase throughout Step 17 (9.5% drift). At the southeast corner, damage increased in the first laminate and occurred for the first time in the second laminate (WDS3, Figure 5.23a). The outside ply at the southwest corner completely split open from the compression failures experienced earlier in the test (WDS3, Figure 5.23b). Damage in the first and second laminates at the northeast corner continued to propagate vertically up the specimen (WDS3, Figure 5.24a). At the northwest corner, the wall continued to crush against the steel base and damage progressed into the second laminate (WDS3, Figure 5.24b). During the first cycle to the north (positive drift) the PT bar reached its yield stress (PT1). The wall never saw a substantial drop in force capacity and thus never reached WDS4. The test was stopped because the actuator did not have enough stroke to move the wall out to further drifts.

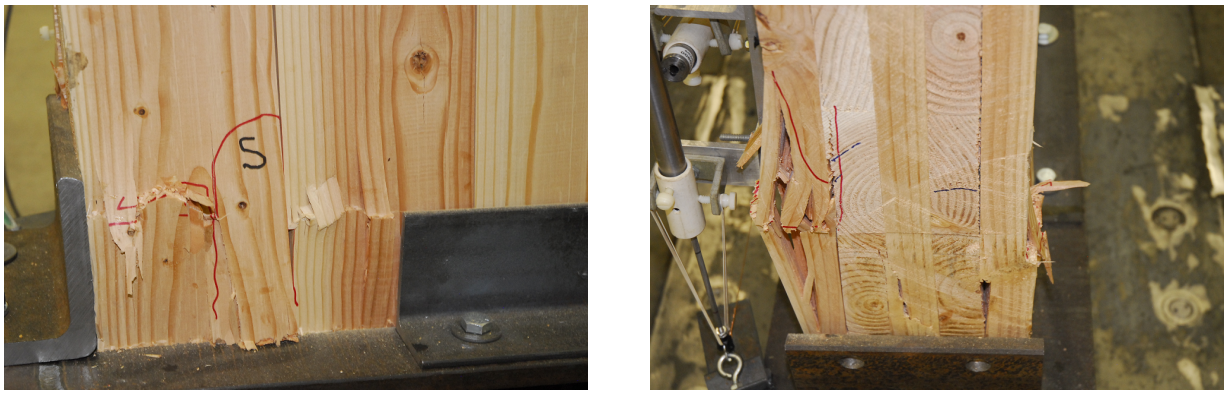

(a) (b)

Figure 5.23: Compression Damage (WDS3) at the (a) Southeast and (b) Southwest Corners of Specimen 2 During Step 17 (9.5% Drift)

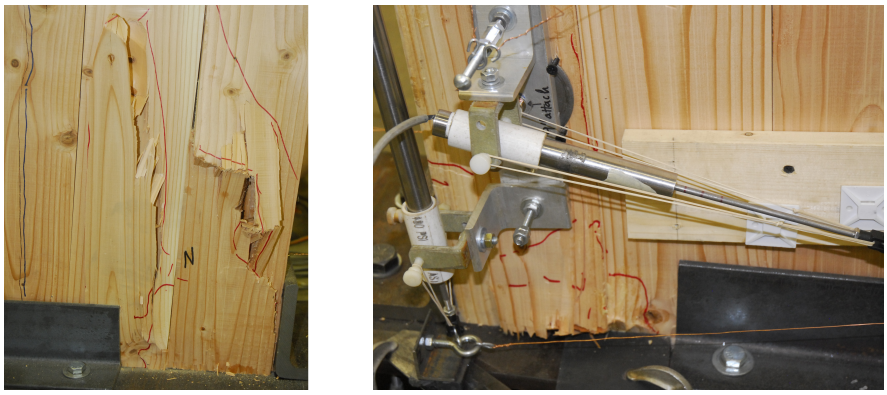

(a) (b)

Figure 5.24: Compression Damage (WDS3) at the (a) Northeast and (b) Northwest Corners of Specimen 2 During Step 17 (9.5% Drift)

5.5 Specimen 3a

Specimen 3a was the first test performed and was tested on March 3, 2015. Specimen 3a was designed to investigate the behavior of a wall with a high decompression force and low decompression stiffness. The CLT wall consisted of two 4 feet long and 8 feet tall 5 ply CLT panels, making a total height of 16 feet. The actuator height was 13 feet $5\frac{1}{8}$ inches. Specimen 3a used the 1.25 inch diameter (1.25 in^2 area) PT bar. The PT bar was stressed to 79 kips ($0.50T_y$) prior to actuator loading. The first direction of loading was to the north (positive drift). The displacements used for the actuator control were based on a 14 foot loading height, but the actual loading height was $6\frac{7}{8}$ inches lower. This specimen did not use the PT load box. Instead a small 1 inch thick steel bearing plate was placed underneath the PT load cell. The small bearing plate failed at Step 12 (2.0% drift) and the specimen was retested as Specimen 3b. The overturning moment versus drift response is shown in Figure 5.25.

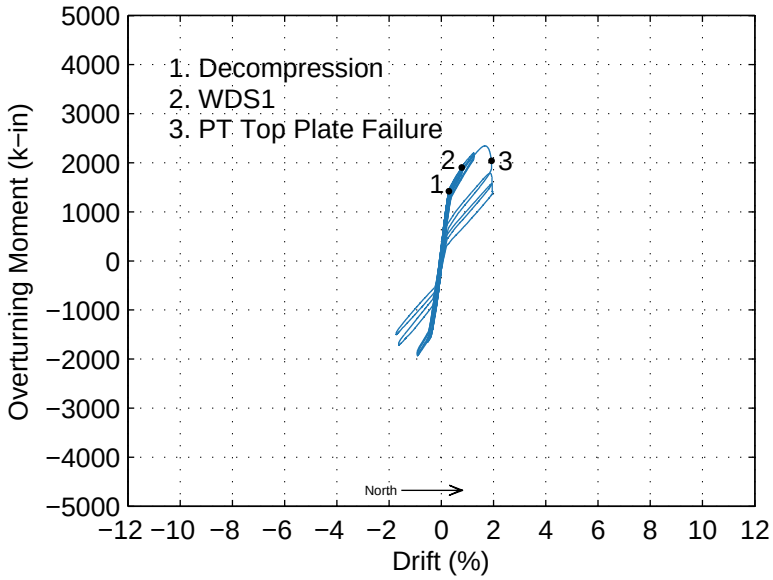

Figure 5.25: Specimen 3a Moment-Drift Response

Decompression was first observed at Step 9 (0.5% drift) as shown in Figure 5.26. Creaking noises were heard at Step 10 (0.8% drift) indicating CLT yielding (WDS1).



Figure 5.26: Wall Decompression of Specimen 3a During Step 9 (drift = 0.5%)

At Step 12 (2.0% drift) there was a sudden drop in PT force due to the wall crushing underneath the PT bearing plate. The test was paused at Step 12 after the 3rd cycle and wall crushing was observed on the east side underneath the PT bearing plate as shown in Figure 5.27a. The test was stopped because of fear of the PT bar pulling out of the wall. The PT bearing plate crushed the top of the wall as shown in Figure 5.27b. The specimen was retrofitted and retested as Specimen 3b.



(a) (b)

Figure 5.27: Crushing Underneath PT Bearing Plate of Specimen 3a

5.6 Specimen 3b

Specimen 3a was retrofitted and retested as Specimen 3b on the same day as the Specimen 3a test. The crushed area shown in Figure 5.27b was filled with plaster. Two splice plates were added at the top of the wall on the east and west faces to confine the CLT. To help distribute the load out across the top of the CLT wall, a 22 inch long 1 inch thick plate was used as the PT bearing plate. The PT bar was stressed to 80 kips ($0.5T_y$) before the actuator force was applied. The final retrofit is shown in Figure 5.28.



Figure 5.28: Specimen 3b Top Plate Retrofit

Specimen 3b's load protocol was the same as Specimen 3a's except for Specimen 3b was started at Step 9 (0.45% drift) instead of Step 1 (0.1% drift). Bowing of the new longer PT bearing plate was observed as soon as the loading was started. This caused errors in the PT load cell data that were later corrected. Like Specimen 3a, the specimen was loaded to the north for every first half cycle. The overturning moment verses drift response is shown in Figure 5.29.

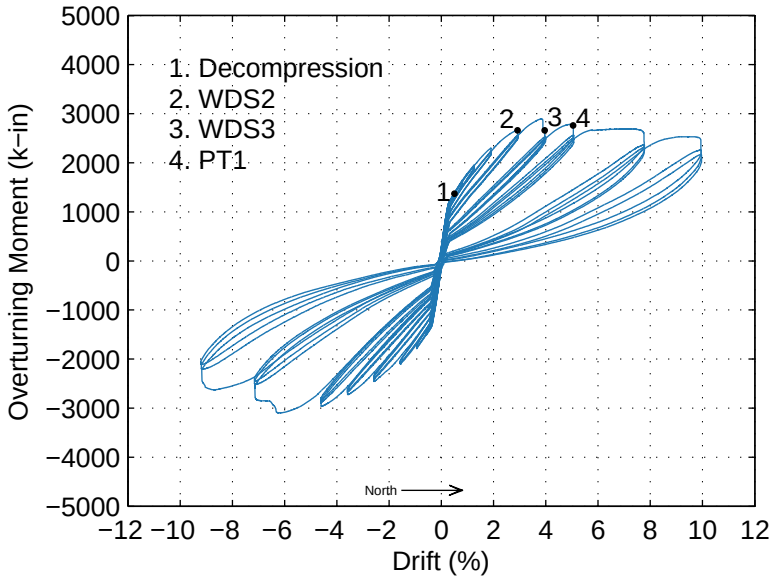

Figure 5.29: Specimen 3b Moment-Drift Response

Like Specimen 3a, decompression was first observed at Step 9 (0.5% drift). Damage was first observed at Step 13 (2.9% drift). Horizontal splitting of the first ply measuring $\frac{7}{8}$ inch in length was observed at the northeast corner (WDS2, Figure 5.30). At the northwest corner, there was slight vertical splitting of the outside ply due to wood crushing that measured $\frac{3}{4}$ inch in length (WDS2, Figure 5.31). No damage was observed at the south end of the wall. During Step 13, the PT bar reached a peak force of 120 kips ($0.75T_y$).

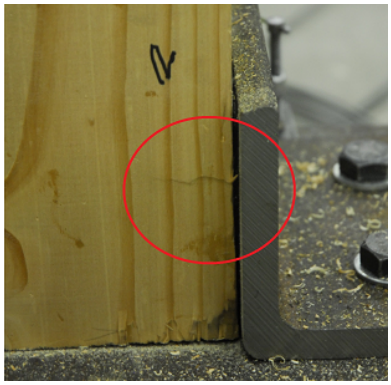

Figure 5.30: Horizontal Splitting (WDS2) at the Northeast Corner of Specimen 3b During Step 13 (2.9% Drift)



Figure 5.31: Vertical Split (WDS2) at the Northwest Corner of Specimen 3b During Step 13 (2.9% Drift)

More CLT damage occurred at Step 14 (4.0% drift). A loud cracking noise was heard towards the north side during the first cycle at positive drift. The northeast corner crushed outward from the horizontal split observed during the previous step. The crushing caused a split of 28 $\frac{1}{2}$ inches to run up the middle of the outer ply on the north east face (WDS3, Figure 5.32). At the northwest corner, delamination of the outer ply from the inner ply was observed (WDS3). During the second cycle towards the south, damage was observed at wood knot located at the southeast corner (WDS3, Figure 5.33). During Step 13, the PT bar reached a peak force of 135 kips ($0.85T_y$).



Figure 5.32: Vertical Splitting and Delamination (WDS3) at the Northeast Corner of Specimen 3b During Step 14 (4.0% Drift)

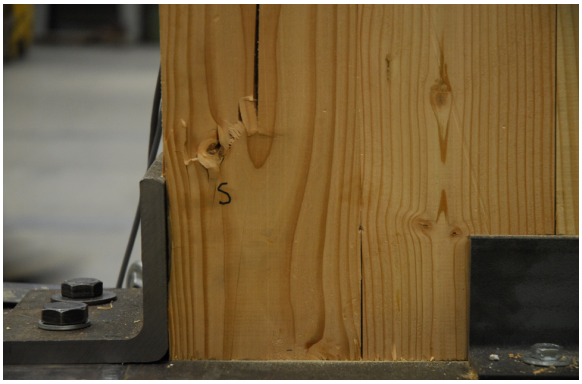

Figure 5.33: Compression Damage (WDS3) at Southeast Corner of Specimen 3b During Step 14 (4.0%) Drift

The northeast corner continued to crush during Step 15 (5.1% drift). The damage stayed within the outer ply and first laminate. No new damage was observed at the south end.

There was a significant increase in damage at Step 16 (7.8% drift). The splitting at the northeast corner increased and moved into the second lam (WDS3, Figure 5.34a). The existing splitting at the northeast corner extended to 34 inches in length and $1\frac{3}{4}$ inches in width (WDS3, Figure 5.34b). At the northwest corner, wood splitting caused by compression was observed (WDS3, Figure 5.35). During this step, damage was first observed at the southwest corner (WDS3, Figure 5.36a). At the southeast corner, vertical splitting and wall crushing was observed, stemming from the initial splitting at the wood knot (WDS3, Figure 5.36b). At the southwest and south east corners, delamination of the outer plys and vertical splitting was observed (WDS4, Figure 5.37). During the first half cycle to the north (positive drift), the PT bar force reached its yield strength of 160 kips ($1.0T_y$) (PT1).



(a) (b)

Figure 5.34: Increased Splitting Damage and Delamination (WDS3) at the Northeast Corner of Specimen 3b during Step 16 (7.8% Drift)

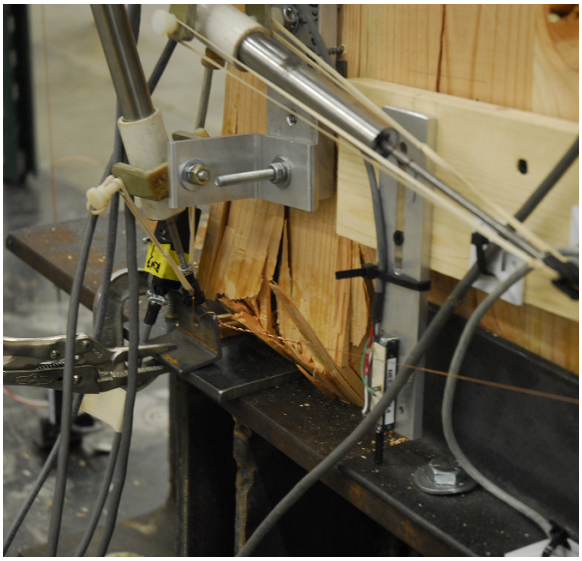

Figure 5.35: Compression Damage (WDS3) at the Northwest Corner of Specimen 3b During Step 16 (7.8% Drift)

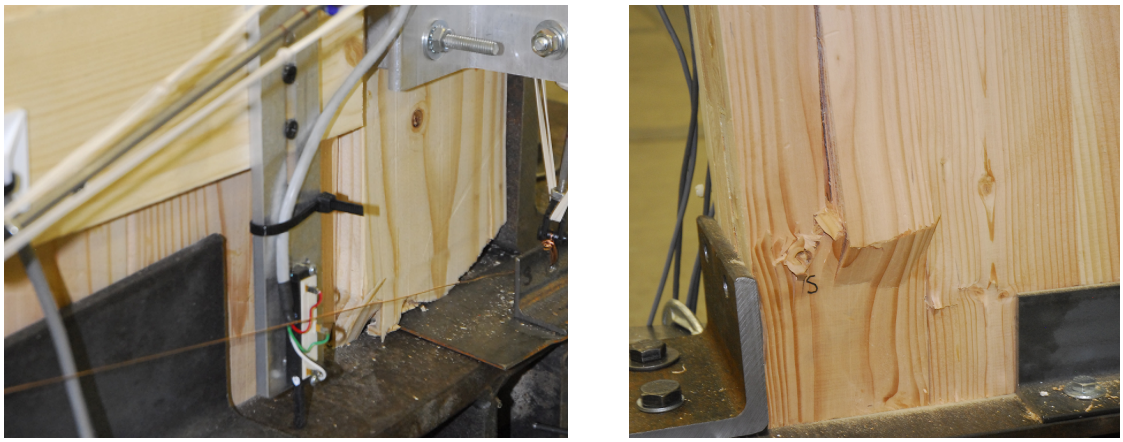

(a) (b)

Figure 5.36: Compression Damage (WDS3) at the (a) Southeast and (b) Southwest Corners of Specimen 3b During Step 16 (7.8% Drift)

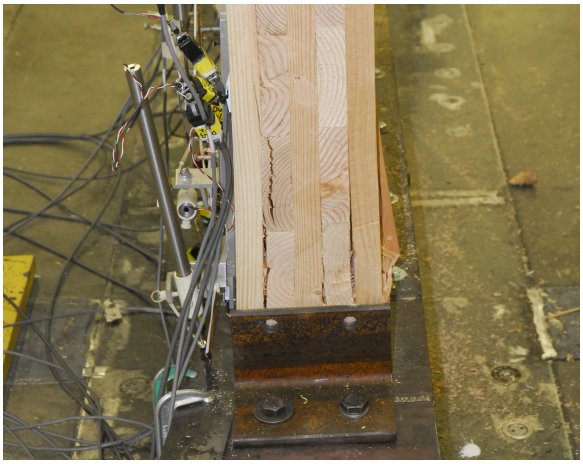

Figure 5.37: Splitting and Delamination (WDS3) at the South End of Specimen 3b During Step 16 (7.8% Drift)

The damage continued to increase at all corners during Step 17 (10.0% drift). At the northeast corner, vertical splitting continued to move up the specimen. Crushing was observed in the second lam of the northeast corner (D3, Figure 4.30). Delamination was observed in the outer ply of the northwest corner. Crushing was observed in the second lam of the southeast corner (WDS3, Figure 4.29). After the test, noticeable permanent deformations were observed at the bottom of both wall toes. The PT bar bent at the base beam connection. Throughout the test, the wall did not lose a significant amount of capacity and thus did not reach WDS4.



Figure 5.38: Damage (WDS3) at the Northeast Corner of Specimen 3b During Step 17 (10.0% Drift)



Figure 5.39: Damage (WDS3) at the Southeast Corner of Specimen 3b During Step 17 (10.0% Drift)

5.7 Specimen 3c

Specimen 3c was tested on March 14, 2015. It was a retest of Specimens 3a and b. The CLT panels used for Specimens 3a and b were cut down to remove the permanent wall deformation due to crushing and reused for Specimen 3c. This decreased the total wall height and PT bar height from 16 feet to 14 feet $5\frac{11}{16}$ inches. The actuator height was 13 feet $5\frac{7}{8}$ inches. The actuator displacements were corrected using the drifts and the actual actuator height. Specimen 3c was the first test to use the PT bearing box instead of the PT bearing plate (see Chapter 4) to transfer the PT load into the wall and to have strain gauges on the PT bar. Before the actuator load was applied, the new 1.25 inch diameter (1.25 in^2 area) PT bar was initially stressed to 80 kips ($0.50T_y$). The first cycle for each step was to the north (positive drift). The overturning moment verses drift response for Specimen 3c is shown in Figure 5.40.

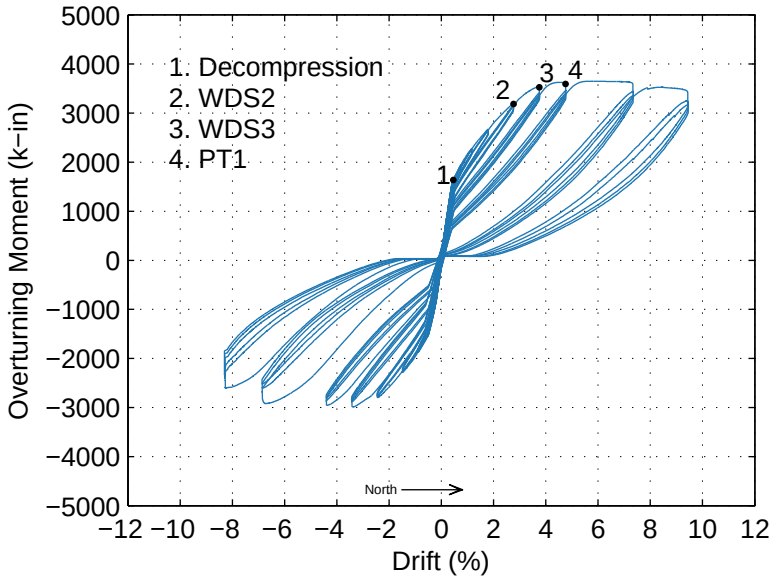

Figure 5.40: Specimen 3c Moment-Drift Response

Decompression was first observed at Step 9 (0.5% drift). The first observed damage occurred during Step 14 (3.8% drift). At the southwest corner, a small wood split measuring $\frac{1}{2}$ inch in length was observed in the second ply (WDS2, Figure 5.41). There was no observable damage at the north end of the wall. During Step 14, the PT bar reached a peak force of 155 kips ($0.97T_y$.

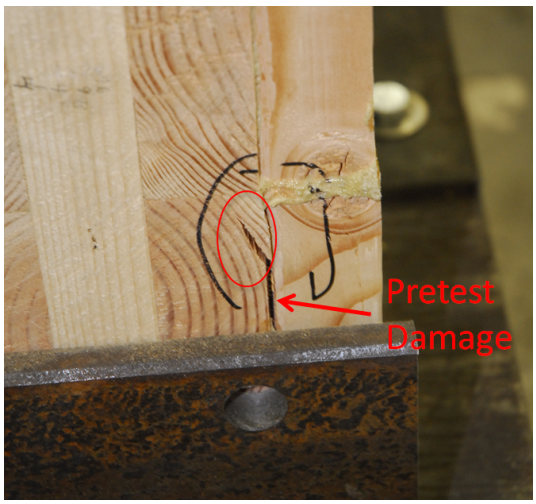

Figure 5.41: Split (WDS2) at the Southwest Corner of Specimen 3c During Step 14 (3.8% Drift)

CLT Damage occurred at the north and south ends of the wall during Step 15 (4.8% drift). On the northeast side, a vertical split measuring 3 inches in length was observed in the second ply (WDS3, Figure 5.42a). At the northwest corner, a horizontal split measuring $1\frac{1}{4}$ inches occurred (WDS3, Figure 5.42b). The split at the southwest end progressed across into the outer ply (WDS3, Figure 5.43a). At the southwest end, new horizontal and vertical splits occurred in the second ply (WDS3, Figure 5.43b). During the first cycle of Step 15, the PT bar reach its yield strength of 160 kips (PT1) ($1.0T_y$.



(a) (b)

Figure 5.42: (a) Vertical Splitting (WDS3) in the Second Ply at the Northeast Corner and (b) Horizontal Splitting (WDS3) of First Ply of the Northwest Corner of Specimen 3c During Step 15 (4.8% Drift)

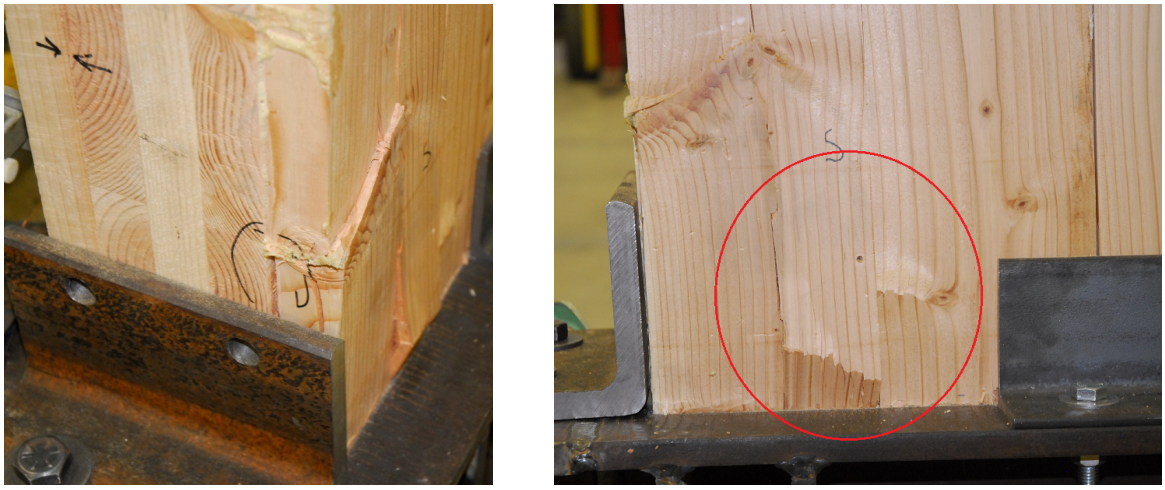

(a) (b)

Figure 5.43: Splitting Damage (WDS3) at the Southeast Corner of Specimen 3c Specimen 3c Step 15 (4.8% Drift)

Wall damage continued to progress during Step 16 (7.4% drift). At the northeast corner, new horizontal and vertical splits were observed in the first ply (WDS3, Figure 5.44a). At the northwest corner, the existing damage increased from the horizontal split noticed from the previous step and a new horizontal split was observed about 6 inches above the base beam (WDS3, Figure 5.44b). The splitting at the southeast corner continued to progress into the 3rd laminate (WDS3, Figure 5.45a). At the southwest corner, splitting due to wood compression was first observed (WDS3, Figure 5.45b).

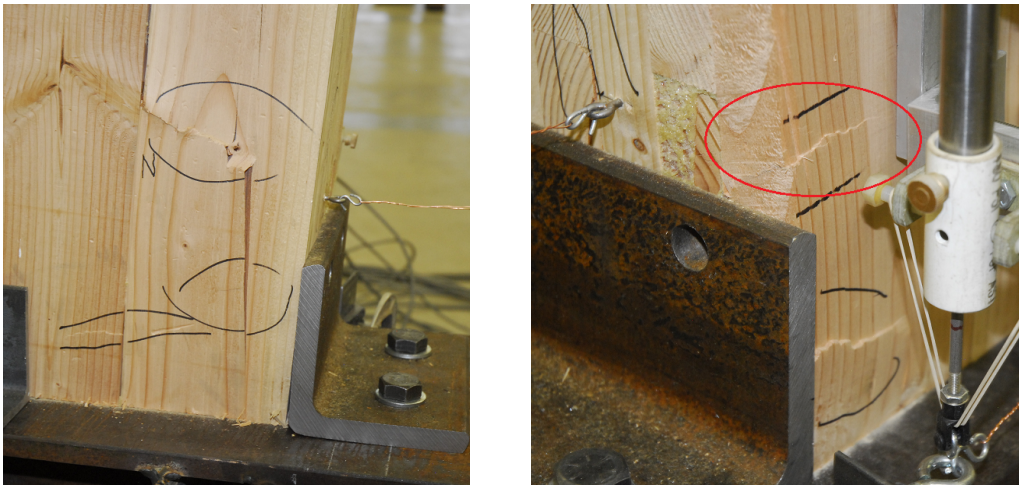

(a) (b)

Figure 5.44: Compression Damage (WDS3) at the (a) Northeast and (b) Northwest Corners of Specimen 3c During Step 16 (7.4% Drift)



(a) (b)

Figure 5.45: Compression Damage (WDS3) at the (a) Southeast and (b) Southwest Corners of Specimen 3c During Step 16 (7.4% Drift)

More damage occurred during the final loading at Step 17 (9.5% drift). The damage in the northeast corner propagated into the second laminate (WDS3, Figure 5.46a). The split in the northwest corner propagated 8 inches up the wall (WDS4, Figure 5.46b). On the southeast face, wall crushing progressed to the third laminate (WDS3, Figure 5.47a). At the southwest corner, the splitting continued to worsen (see Figure 5.47b). After the test, noticeable permanent deformations were observed at the bottom of both toes. Similar to Specimen 3b, the PT bar bent at the base beam connection. Throughout the test, the wall did not lose a significant amount of capacity and thus did not reach WDS4.

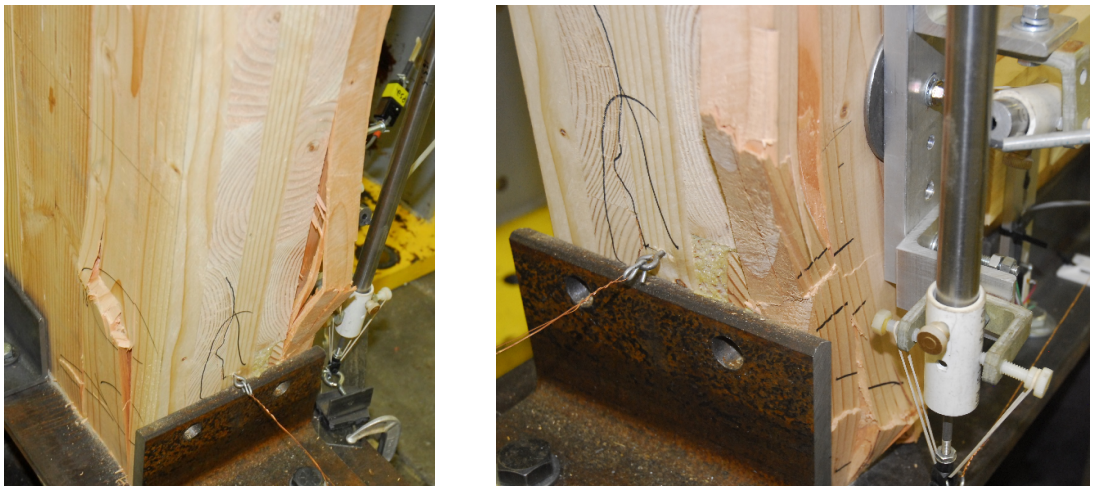

(a) (b)

Figure 5.46: Damage at the (a) Northeast and (b) Northwest Corners of Specimen 3c During Step 17 (9.5% Drift)

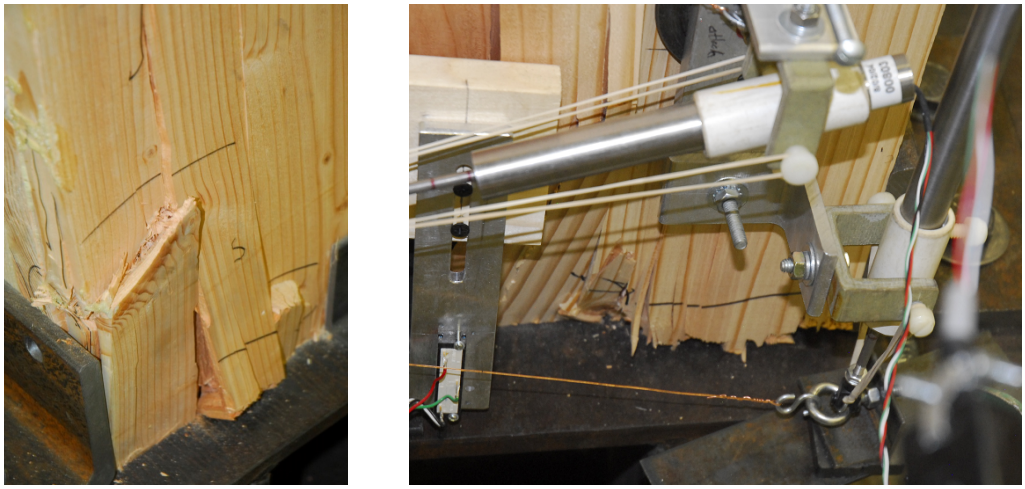

(a) (b)

Figure 5.47: Damage of Specimen 3c at the (a) Southeast and (b) Southwest Corners of Specimen 3c During Step 17 (9.5% Drift)

5.8 Specimen 4

Specimen 4 was tested on April 14, 2015. Specimen 4 was the only specimen to rock on the CLT base. The lower panel was 4 feet long and 8 feet tall and $6\frac{9}{16}$ inches wide. The top 5-ply CLT panel was 4 feet long and 6 feet $6\frac{3}{8}$ inches tall. The total height of the specimen was 14 feet $6\frac{3}{8}$ inches. The actuator loading height from the CLT base was 12 feet $11\frac{1}{16}$ inches. The CLT base had a height of $6\frac{13}{16}$ inches. Specimen 3a used the 1.25 inch diameter (1.25 in^2 area) PT bar. The PT bar was stressed to 76 kips ($0.48T_y$) prior to actuator loading. The first direction of loading was to the north (positive drift). Specimen 4 was the second test with the added Step 18 (11.0% drift). At the end of the test, the wall remained visibly undamaged, and the CLT base was the only part of the specimen damaged. Because the CLT base was crushed directly underneath the wall, the instrumentation setup could not correctly measure the crushing depth of the CLT base. The test was paused at peak displacements and the crushing depth was measured with a ruler. The overturning moment versus drift response is shown in Figure 5.48.

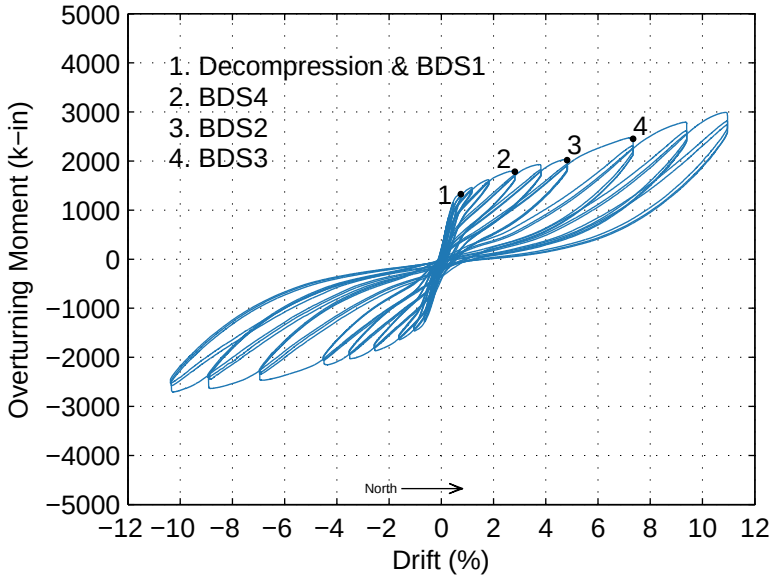

Figure 5.48: Specimen 4 Moment-Drift Response

Decompression was first observed at Step 10 (0.8% drift) as shown in Figure 5.49. During Step 10, small magnitude and localized CLT base crushing was observed at the north and south ends (BDS1, Figure 5.50).



Figure 5.49: Wall Decompression of Specimen 4 During Step 10 (0.8% Drift)

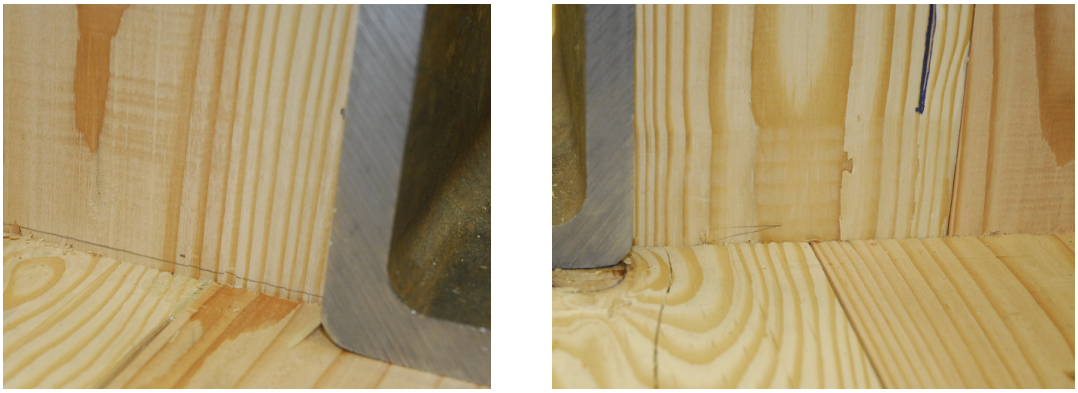

(a) (b)

Figure 5.50: CLT Base Crushing (BDS1) at the (a) North and (b) South Ends of Specimen 4 During Step 10 (0.8% Drift)

The CLT base crushing depth at both ends of the wall was less than $\frac{1}{8}$ inch throughout Step 11 (1.2% drift) and Step 12 (1.8% drift). During Step 13 (2.8% drift) the crushing depth of the CLT base reached $\frac{1}{8}$ inch on both the north and south ends (BDS1, Figure 5.51). When the wall was pushed to the north (positive drift), the CLT base laminate in the outer ply

underneath the north end of the wall split (BDS4, Figure 5.52a). A CLT base ply also split underneath the south end of the wall when the wall was pushed to the south (negative drift) (BDS4, Figure 5.52b). During Step 12 the PT bar reached a peak force of 105 kips ($0.67T_y$).

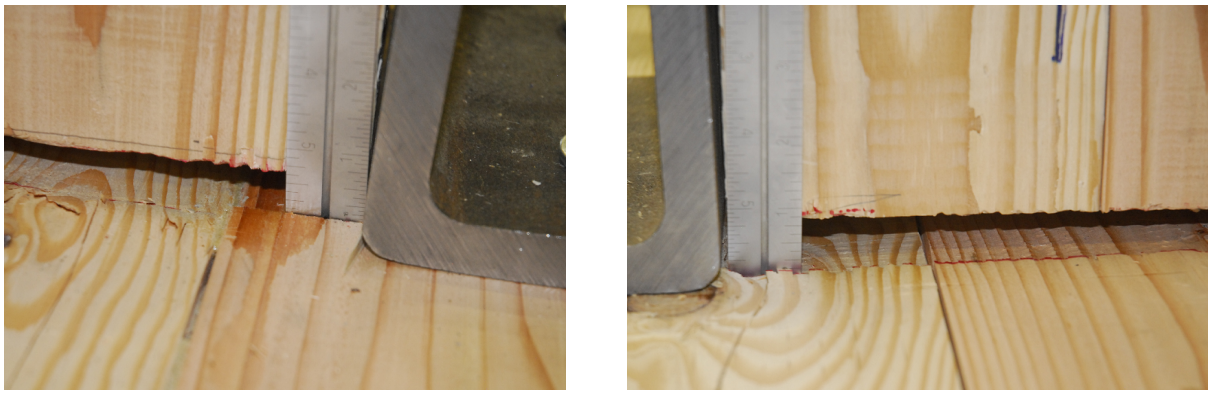

(a) (b)

Figure 5.51: CLT Base Crushing (BDS1) at the (a) North and (b) South Ends of Specimen 4 During Step 13 (2.8% Drift)

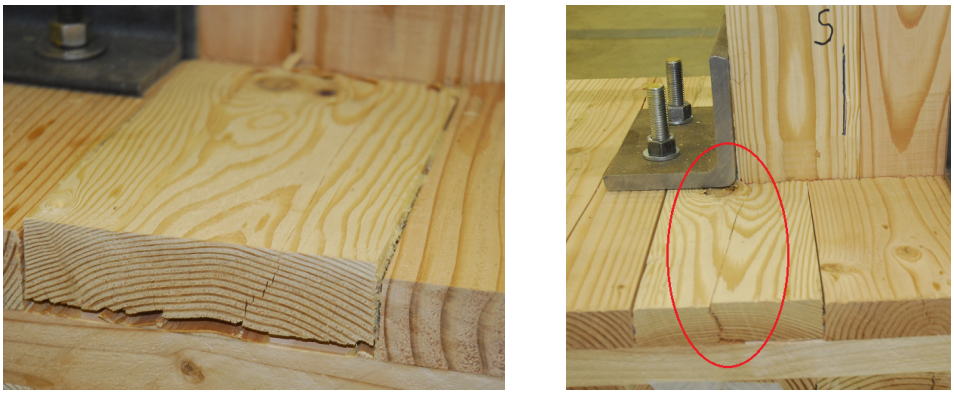

(a) (b)

Figure 5.52: CLT Base Splitting (BDS4) at the (a) North and (b) South Ends of Specimen 4 During Step 13 (2.8% Drift)

During Step 14 (3.8% drift) the CLT base crushing depth increased to $\frac{1}{4}$ inch at both the north and south ends of the wall (BDS2, Figure 5.53). In the outer ply at the north end of the CLT base, splitting damage was observed in the laminate south of the previous damage (BDS4, Figure 5.54a). At the south end, splitting damage, similar to the north end damage, was observed in the laminate north of the previous damage (BDS4, Figure 5.54b). During Step 14 the PT bar reached a peak force of 112 kips ($0.70T_y$).

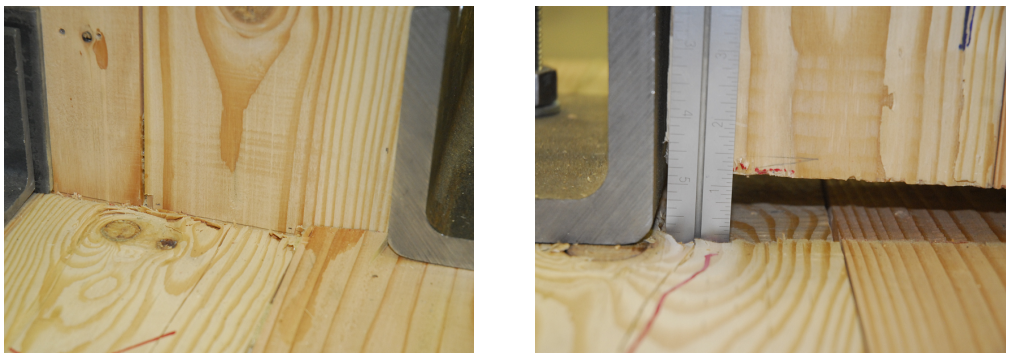

(a) (b)

Figure 5.53: CLT Base Crushing (BDS2) at the (a) North and (b) South Ends of Specimen 4 During Step 14 (3.8% Drift)

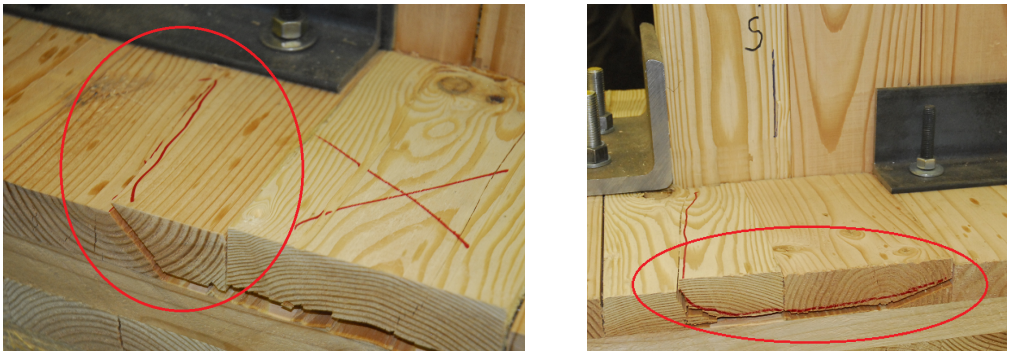

(a) (b)

Figure 5.54: CLT Base Splitting (BDS4) at the (a) North and (b) South Ends of Specimen 4 During Step 14 (3.8% Drift)

During Step 15 (4.8% drift) the CLT base crushing depth increased to $\frac{1}{2}$ inch on the north end and to $\frac{3}{8}$ inch on the south end (BDS2, Figure 5.55). During Step 15, there was no new CLT base splitting and the PT bar reached a peak force of 119 kips ($0.75T_y$).

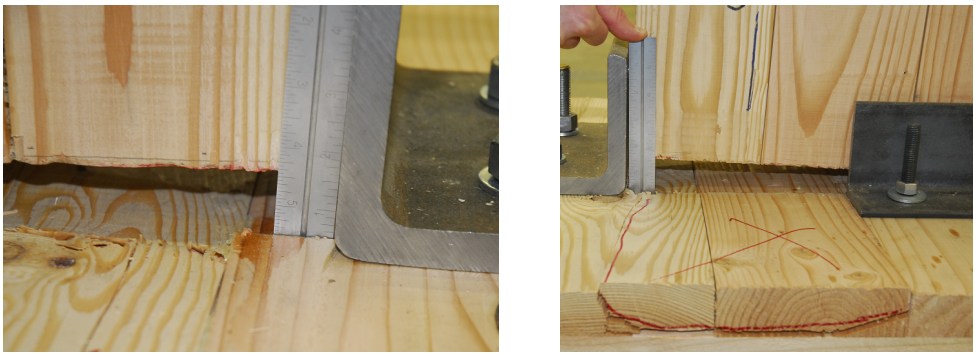

(a) (b)

Figure 5.55: CLT Base Crushing (BDS2) at the (a) North and (b) South Ends of Specimen 4 During Step 15 (4.8% drift)

During Step 16 (7.4% drift) the CLT base crushing depth increased to $\frac{7}{8}$ inch on the north side and to $\frac{3}{4}$ inch on the south side (BDS3, Figure 5.56). The existing CLT base splitting damage at the north and south ends continued to increase in length, however no new splits were observed (BDS4, Figure 5.57). The PT bar reached a peak force of 140 kips ($0.88T_y$).

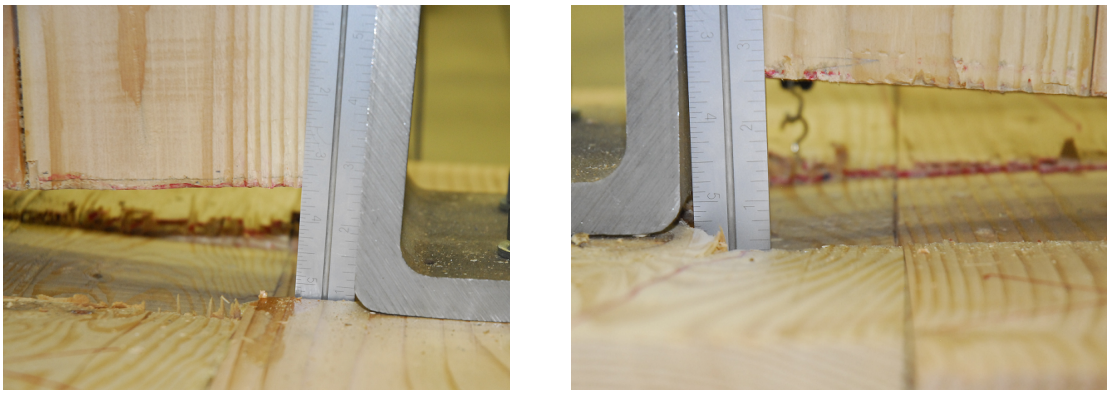

(a) (b)

Figure 5.56: CLT Base Crushing (BDS3) at the (a) North and (b) South Ends of Specimen 4 During Step 16 (7.4% Drift)

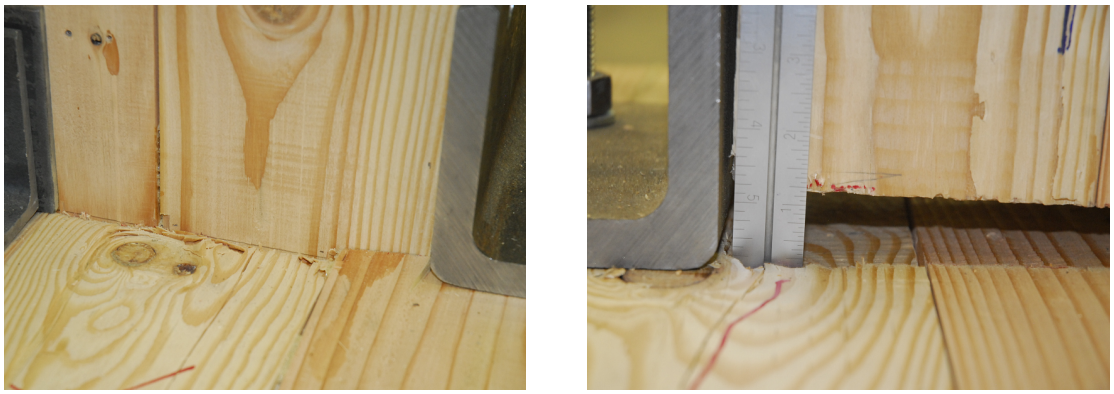

(a) (b)

Figure 5.57: CLT Base Splitting (BDS4) at the (a) North and (b) South Ends of Specimen 4 During Step 16 (7.4% Drift)

During Step 17 (9.4% drift) the CLT base crushing depth increased to 1 inch on both sides (BDS3, Figure 5.58). The existing CLT base splitting damage at the north and south ends continued to increase and no new splits were observed (BDS4). The PT bar reached a peak force of 145 kips ($0.91T_y$). During Step 18 (11.0% drift) the CLT base crushing depth increased to $1\frac{1}{4}$ inches on the north side and to $1\frac{1}{8}$ inches (BDS3, Figure 5.56). The existing CLT base splitting damage at the north and south ends continued to increase and no new splits were observed (BDS4). The PT bar reached a peak force of 155 kips ($0.97T_y$).



(a) (b)

Figure 5.58: CLT Base Crushing (BDS3) and CLT Base Splitting (BDS4) at the (a) North and (b) South Ends of Specimen 4 During Step 17 (9.4% Drift)

The wall remained visibly undamaged throughout the test and the wall base corners were square post test as shown in Figure 5.59. Since the wall was visibly undamaged, it would be reused for Specimen 1. The CLT base showed increased crushing damage at the north and south ends and reduced crushing towards the center as shown in Figure 5.60. The PT bar did not yield and thus PT1 was not reached.



Figure 5.59: Specimen 4 Wall Post Test



(a) (b)

Figure 5.60: Specimen 4 (a) South and (b) North CLT Base Post Test)

5.9 Specimen 5

Specimen 5 was tested on April 2, 2015. Specimen 5 was the only specimen with a CLT panel with a structural composite lumber (SCL) core. The panel with the SCL core was used as the lower panel of the wall assembly and was 4 feet long and 8 feet tall and $6\frac{9}{16}$ inches wide. The top 5-ply CLT panel was 4 feet long and 6 feet $6\frac{3}{8}$ inches tall. The global height of the specimen was 14 feet $6\frac{3}{8}$ inches tall. The actuator loading height was 13 feet $5\frac{1}{8}$ inches. Specimen 5 used the 1.375 inch diameter (1.58 in^2 area) PT bar. The PT bar was stressed to 75 ($0.47T_y$) kips prior to actuator loading. The first direction of loading was to the south (negative drift). Specimen 5 was the first test with the added Step 18 (11.0% drift). The overturning moment versus drift response is shown in Figure 5.61.

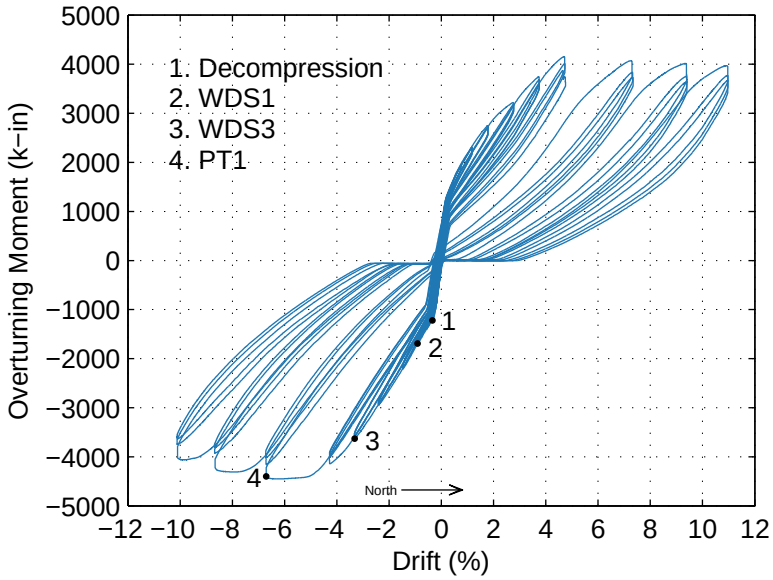

Figure 5.61: Specimen 5 Moment-Drift Response

Decompression was first observed at Step 9 (0.5% drift) as shown in Figure 5.62. Creaking noise was heard during Step 11 (1.2% drift) indicating yielding of the CLT (WDS1).

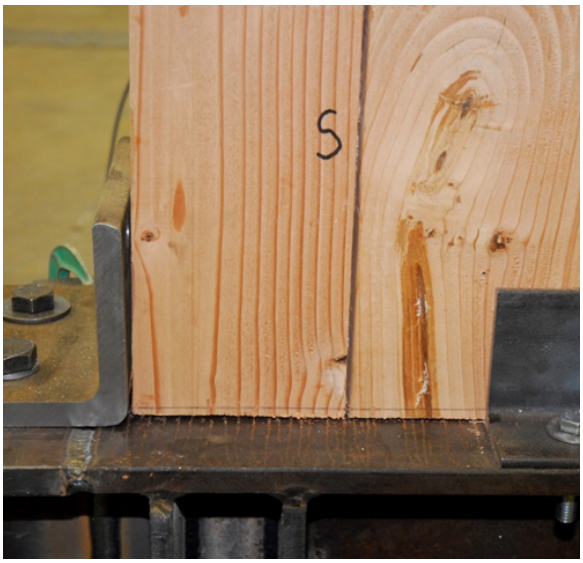

Figure 5.62: Wall Decompression of Specimen 5 During Step 9 (0.5%)

During the first cycle towards the south of Step 14 (3.8% drift) creaking that signified the CLT was yielding was heard, though no damage was visible (WDS1). The first visible wall damage occurred on the second cycle at the north end of the wall. At the northeast corner, a small horizontal split measuring $\frac{7}{8}$ inches long occurred in the outer ply (WDS2, Figure 5.63a). On the north end, east side, the SCL core and part of the outer ply split vertically 6 inches in length (WDS3, Figure 5.63b). At the northwest corner, delamination, measuring 9 inches in length, of the outer ply from the inner SCL core occurred (WDS3, Figure 5.64). The PT force reached a peak value of 160 kips ($0.79T_y$) to the south and 175 kips ($0.87T_y$) to the north. The difference in PT force is reflected by the damage to the north and the nonexistent damage to the south.



(a) (b)

Figure 5.63: (a) Horizontal Splitting (WDS2) and (b) Vertical Splitting (WDS3) at the Northeast Corner of Specimen 5 During Step 14 (3.8% Drift)

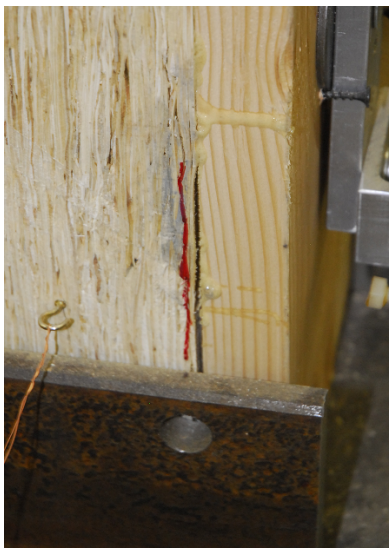

Figure 5.64: Delamination (WDS3) at the Northwest Corner of Specimen 5 During Step 14 (3.8% Drift)

Specimen 5 saw increased damage at the north end and a small amount of new damage at the south end during Step 15 (4.8% drift). During the first half cycle to the south, at the southwest corner, small splits at a wood knot were observed (WDS2, Figure 5.65). During the first cycle to the north, the core split that occurred during the previous step extended vertically up the wall to a total length of 24 inches. During the second cycle, the split increased to a length of 34 inches (see Figure 5.66a). During the final third cycle, the outer ply split off of the wall and the split in the core increased to a total length of 70 inches (see Figure 5.66b). The splice plate connecting the two panels stopped the split in the core from increasing for the duration of the test. The PT force reached a peak value of 180 kips ($0.89T_y$) to the south and 190 kips ($0.94T_y$) to the north.



Figure 5.65: Small Splits (WDS2) at the Southwest Corner of Specimen 5 During Step 15 (4.8%)

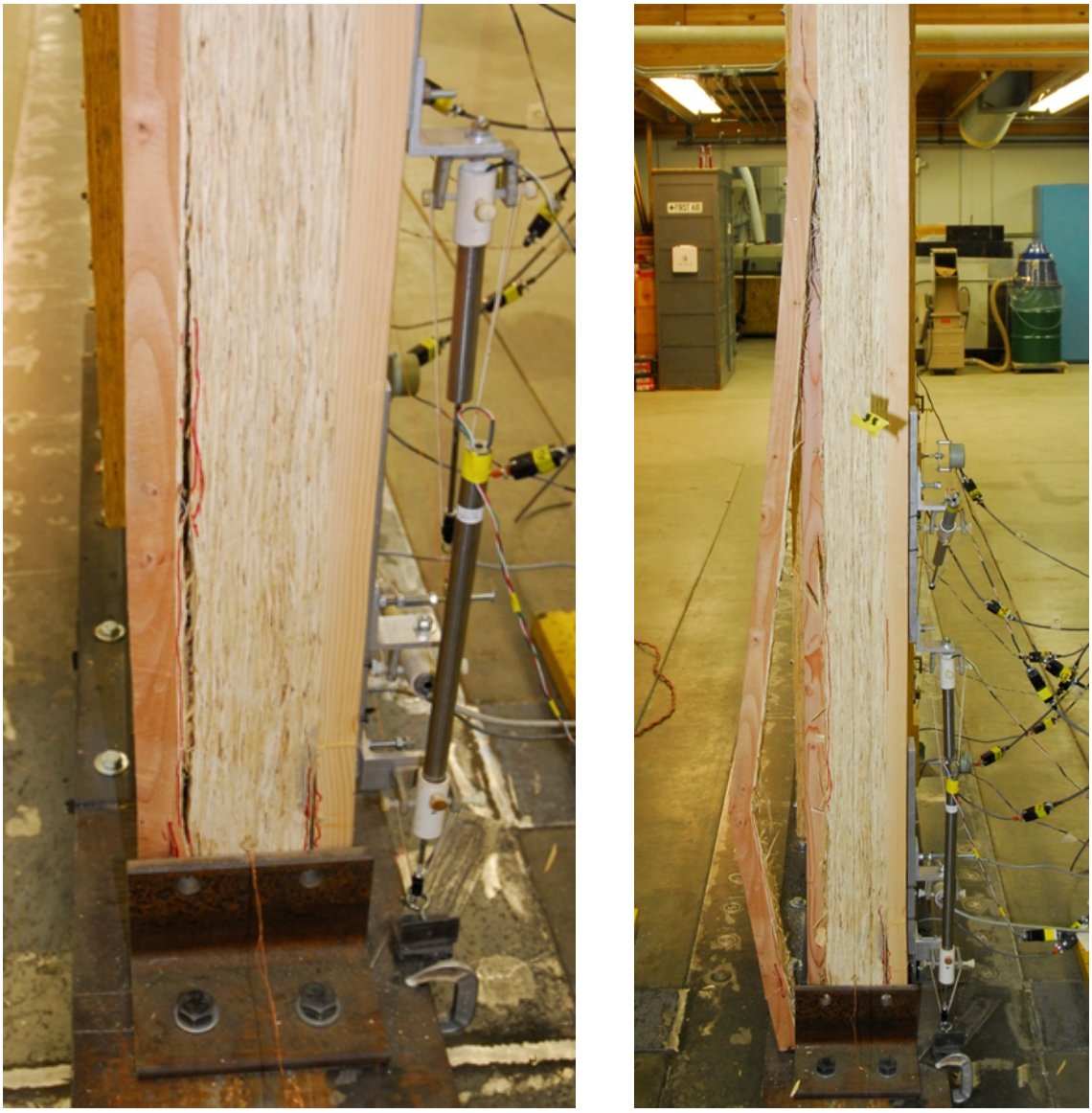

(a) (b)

Figure 5.66: Core Split (WDS3) at the Northeast Corner of Specimen 5 During Step 15 (4.8%) - (a) Cycle 2 and (b) Cycle 3

The wall damage increased during Step 16 (7.3% drift). During cycle 1, a horizontal split measuring $2\frac{1}{2}$ inches occurred at the southeast corner (WDS3, Figure 5.67a). The vertical splitting increased during cycle 2 (WDS3, Figure 5.67b). The splitting at the southwest corner increased to over 1 inch in length (WDS3, Figure 5.68c). At the northwest corner, the SCL core started to split next to the delamination that occurred in the previous step (see Figure 5.69d) and new splits near the base beam were observed (see Figure 5.69e). During the first half cycle (to the south) of Step 16 the PT bar reached yield (PT1).

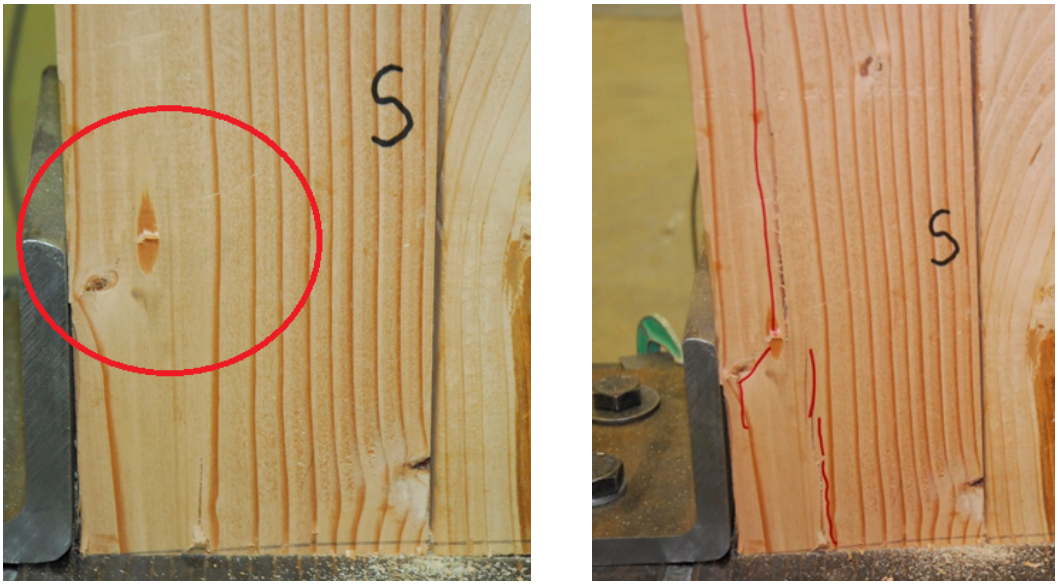

(a) (b)

Figure 5.67: Splitting (WDS3) at the Southeast Corner of Specimen 5 During Step 16 (7.3% Drift) - (a) Cycle 1 and (b) Cycle 2



Figure 5.68: Splitting (WDS3) at the Southwest Corner of Specimen 5 During Step 16 (7.3% Drift)

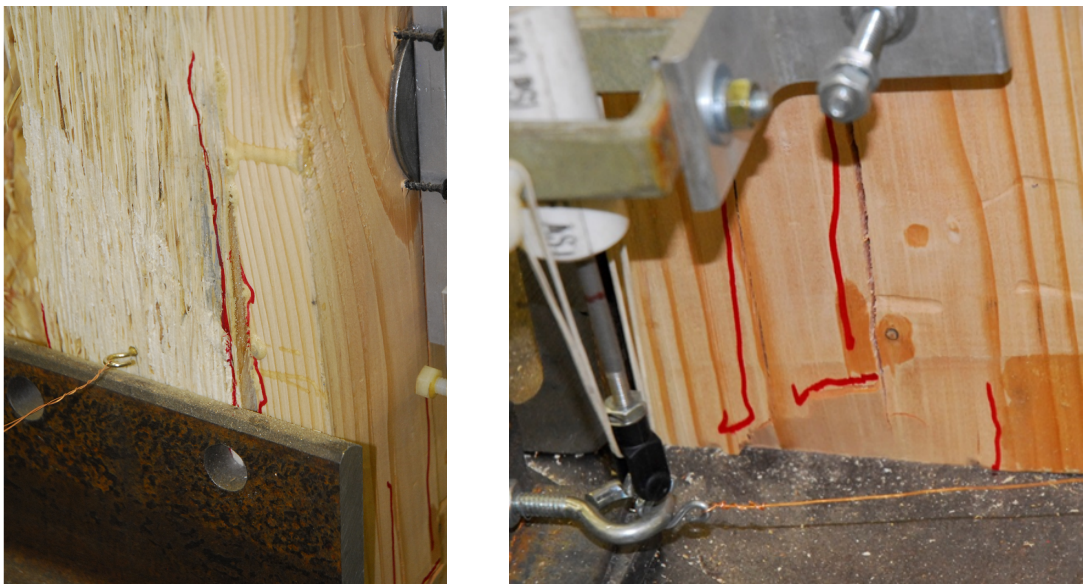

(a) (b)

Figure 5.69: (a) Core Splitting (WDS3) and (b) Base Crushing (WDS3) at the Northwest Corner of Specimen 5 During Step 16 (7.3% Drift)

The CLT damage continued to progress during Step 17 (9.4% drift). The southeast side of the core and both outer plys at the south end split vertically (WDS3, Figure 5.70a). The SCL core split at the northeast corner continued to increase (WDS3, Figure 5.70b).



(a) (b)

Figure 5.70: (a) Splitting Failures (WDS3) at the South End and (b) Core Splitting (WDS3) at the Northwest Corner of Specimen 5 During Step 17 (9.4% drift)

All existing damage increased during Step 18 (11.0% drift). After the test when the wall was recentered, there was about $\frac{3}{4}$ inch of vertical permanent deformation at the north and south toes. Figure 5.71 shows the deformation at the southeast end of the wall. Throughout the test, the wall did not lose a significant amount of capacity and thus did not reach WDS4.

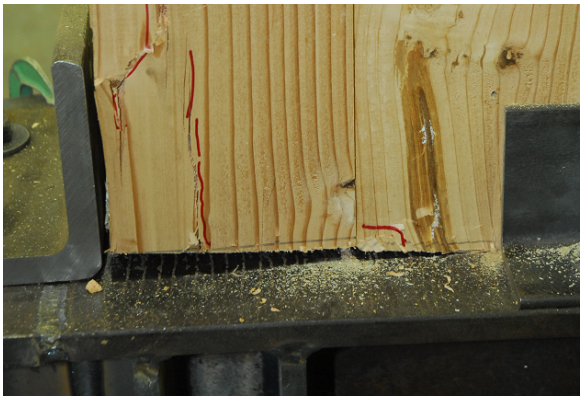

Figure 5.71: Permanent Deformation at the South End of the Wall After Recentering of Specimen 5 Post-Test

5.10 Specimen 6

Specimen 6 was tested on June 16, 2015. The primary objective for Specimen 6 was to understand the behavior of a coupled wall with U-shaped energy dissipators. The panels used for the wall were 5-ply CLT. In the following observations and descriptions, the north wall is the northern most wall (closest to the actuator) and the south wall is the southern most wall. The north wall lower CLT panel was 3 feet and $11\frac{7}{8}$ inches long and 8 feet tall, and the upper panel was 4 feet long and 7 feet and $11\frac{1}{2}$ inches tall. The total height of the north wall was 15 feet and $11\frac{1}{2}$ inches. The south wall lower CLT panel was 3 feet and 11 inches long and 7 feet and $11\frac{1}{2}$ inches tall, and the upper panel was 4 feet long and 7 feet and $11\frac{1}{2}$ inches tall. The total height of the south wall was 15 feet and 11 inches. The actuator height was 13 feet $5\frac{7}{8}$ inches. Both the north and south walls used a 1.25 inch diameter (1.25 in^2 area) PT bar. The north wall PT bar were stressed to 75 kips ($0.47T_y$) prior to actuator loading. Due to an offset in the load cell that was not accounted for, the south wall PT bar was stressed to 85 kips ($0.53T_y$) instead of 75 kips prior to loading. The first direction of loading was to the north (positive drift). The overturning moment versus drift response is shown in Figure 5.72.

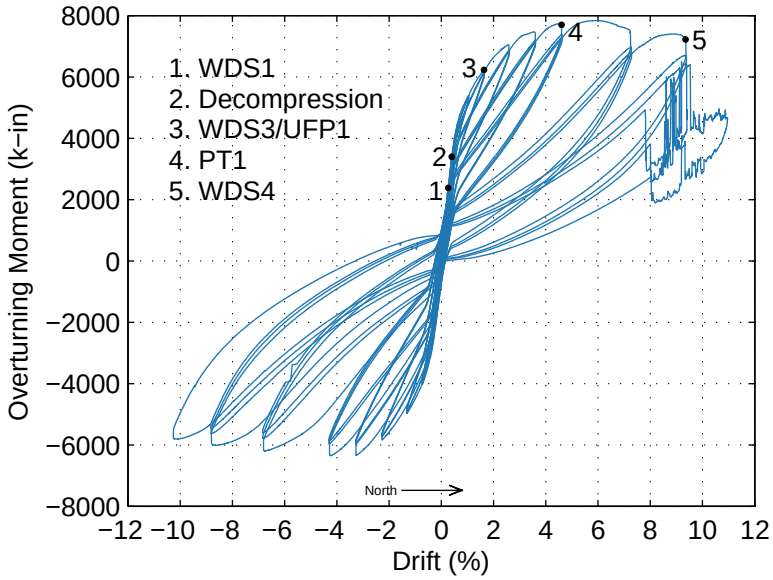

Figure 5.72: Specimen 6 Moment-Drift Response

During Step 8 (0.3% drift) creaking was heard in the south wall indicating initial CLT yielding (WDS1). During Step 9 (0.4% drift) decompression was observed at both ends of each wall. Decompression of the north end of the south wall as shown in Figure 5.73. During Step 9 (0.4% drift) creaking was heard in the north wall indicating CLT yielding (WDS1). During Step 11 (1.0% drift) UFP bending was observed.



Figure 5.73: Wall Decompression of the South Wall of Specimen 6 During Step 10 (0.4% drift)

The first splitting damage was observed during Step 12 (1.6% drift). At the northeast corner of the north wall, a vertical compression split of 1 inch was observed (WDS2, Figure 5.74a). At the south end of the south wall, there was vertical delamination of the west outer ply of $1\frac{1}{2}$ inches that lead into a horizontal split of 1 inch of the inner ply (WDS3, Figure 5.74b). During Cycle 2 yielding was observed in the lower UFP (WDS6, Figure 5.75.



(a) (b)

Figure 5.74: (a) Delamination (WDS3) at the South End of the South Wall and (b) Vertical Splitting (WDS2) at the Northeast Corner of the North Wall of Specimen 6 During Step 12 (1.6%)



Figure 5.75: Yielding of the Lower UFP (WDS6) of Specimen 6 During Step 12 (1.6%)

During Step 13 (2.6% drift) the wall damage increased. The vertical split on the north wall at the northeast corner grew to $1\frac{1}{8}$ inches (WDS3, Figure 5.76a). At the northeast corner of the north wall, a small vertical split measuring $1\frac{1}{2}$ inches in length started at a knot and an additional horizontal split of $1\frac{1}{4}$ inches occurred away from the knot (WDS2, Figure 5.76b). At the southeast corner of the north wall, a part of the wall split off measuring 8 inches in length (WDS3, Figure 5.76b).

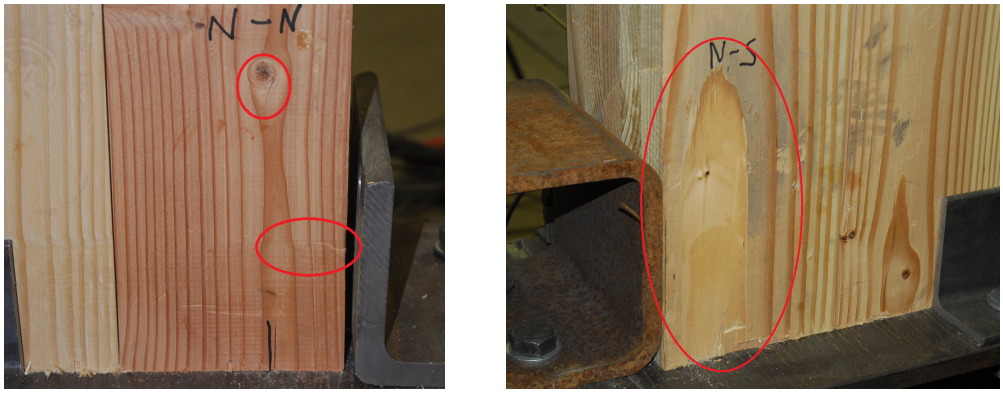

(a) (b)

Figure 5.76: Splitting (WDS3) at the (a) Northeast Corner and (b) the Southwest Corner of the North Wall of Specimen 6 During Step 13 (2.6% drift)

During Step 13 (2.6% drift) at the northwest corner of the south wall, a compression split measuring 4 inches in length was observed (WDS3, Figure 5.77a). The delamination and splitting at the south end of the south wall extended 4 inches up the wall (WDS3, Figure 5.77b). There was no observable damage at the south end of the south wall.



(a) (b)

Figure 5.77: Damage (WDS3) at the (a) Northwest Corner and (b) the South End of the South Wall of Specimen 6 During Step 13 (2.6% drift)

There was increased damage during Step 14 (3.6% drift). At the northeast corner of the north wall, the existing split at the knot extended to 2 inches below and $3\frac{1}{4}$ inches horizontally from the knot. Two new vertical splits measuring $5\frac{1}{2}$ inches and $2\frac{1}{2}$ inches occurred above the existing damage (WDS3, Figure 5.78a). At the north end of the north wall, the east outer ply delaminated from the inner ply a length of $14\frac{1}{2}$ inches (WDS3, Figure 5.78a). During the first cycle to the south (negative direction), at the southeast corner of the north wall, a large delamination measuring 29 inches and splitting at the knot at the top of the delamination occurred (WDS3, Figure 5.79).



(a) (b)

Figure 5.78: (a) Splitting (WDS3) at the Northeast Corner and (b) Delamination (WDS3) at the North End of the North Wall of Specimen 6 During Step 14 (3.6% drift)



Figure 5.79: Delamination (WDS3) at the Southeast Corner of the North Wall of Specimen 6 During Step 14 (3.6% drift)

During Step 14 (3.6% drift) the damage continued to increase in the south wall. The splitting by the knot at the northwest corner continued to expand by increasing to $1\frac{1}{2}$ inches in length (WDS3). A new delamination measuring 16 inches in length occurred at the north side between the center inner ply and the adjacent eastern ply (WDS3, Figure 5.80a). At the southwest corner of the south wall, new horizontal splits measuring $2\frac{1}{2}$ inches occurred (WDS3, Figure 5.80b). Both the upper and lower UFPs had noticeable deformations over 1 inch (WDS 6, Figure 5.81).



(a) (b)

Figure 5.80: (a) Delamination (WDS3) at the North End and (b) Splitting (WDS3) at the Southwest Corner of the South Wall of Specimen 6 During Step 14 (3.6% Drift)

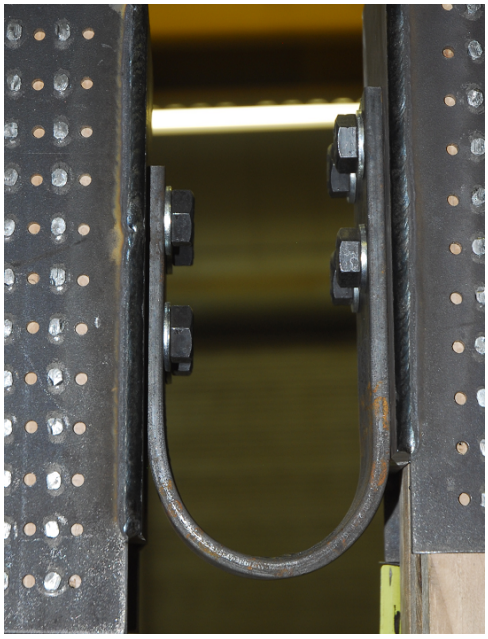

Figure 5.81: Lower UFP Deformation (WDS6) of Specimen 6 During Step 14 (3.6%)

During Step 15 (4.6% drift) damage continued to increase in both walls. At the northeast corner of the north wall, all splits continued to increase (WDS3, Figure 5.82a). At the north end of the north wall, the delamination extended 2 inches to a total length of 16 inches and new splits were observed in the second ply from the west face (WDS3, Figure 5.82b). The delamination at the southeast corner opened to a width of a $1\frac{1}{4}$ inches (WDS3).



(a) (b)

Figure 5.82: (a) Splitting (WDS3) at the Northeast Corner and (b) Delamination (WDS3) at the North End of the North Wall of Specimen 6 During Step 15 (4.6% Drift)

During Step 15 (4.6% drift), at the northwest corner of the south wall, the existing vertical splitting extended to 2 inches in length and new splitting damage occurred against the shear transfer HSS (WDS3, Figure 5.83a). At the southeast corner of the south wall, a vertical split measuring 17 inches long was observed (WDS3, Figure 5.83b). During the first cycle to the north (positive direction) the PT bar in the south wall yielded (PT1).

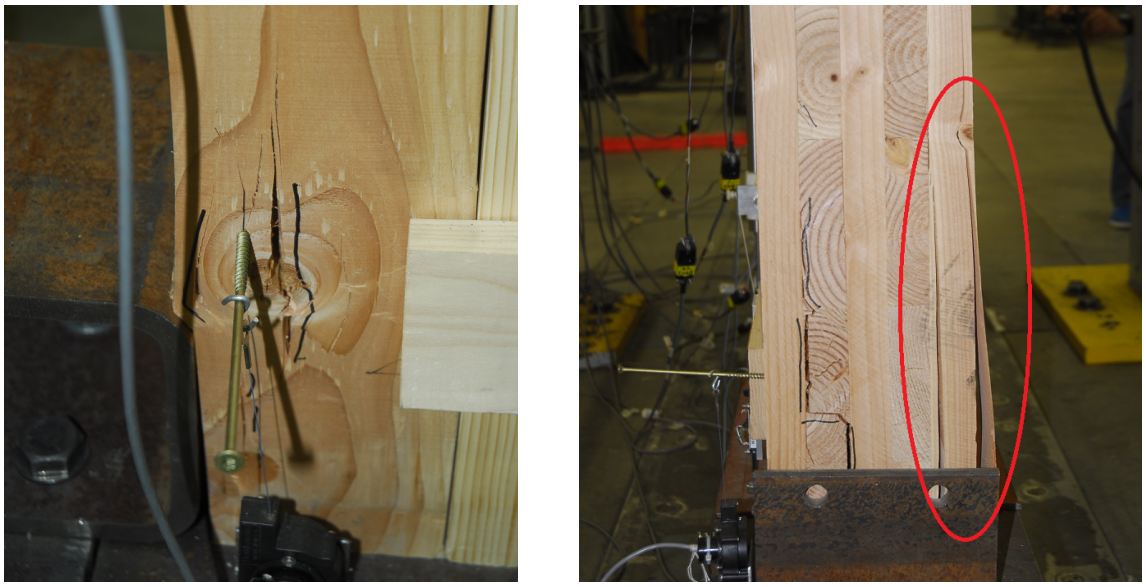

(a) (b)

Figure 5.83: Splitting (WDS3) at the (a) Northeast Corner and (b) Southeast Corner of the South Wall of Specimen 6 During Step 15 (4.6% drift)

During Step 16 (7.3% drift) the delamination at the northeast end of the north wall increased in length by 6.5 inches to a total length of $22\frac{1}{2}$ inches (WDS3, Figure 5.84. At the northwest corner of the north wall, two splits measuring 2 inches and 4 inches occurred (WDS3). The delamination at the southeast end of the north wall opened from a width of $1\frac{1}{4}$ inch to 1 inch (WDS3, Figure 5.85a). At the southwest corner of the north wall, crushing damage, consisting of vertical splits, was observed for the first time (WDS3, Figure 5.85b). During the first cycle to the north (positive direction) the PT bar in the north wall yielded (PT1).



Figure 5.84: Continued Splitting and Delamination (WDS3) of the North Wall of Specimen 6 During Step 16 (7.3% Drift)

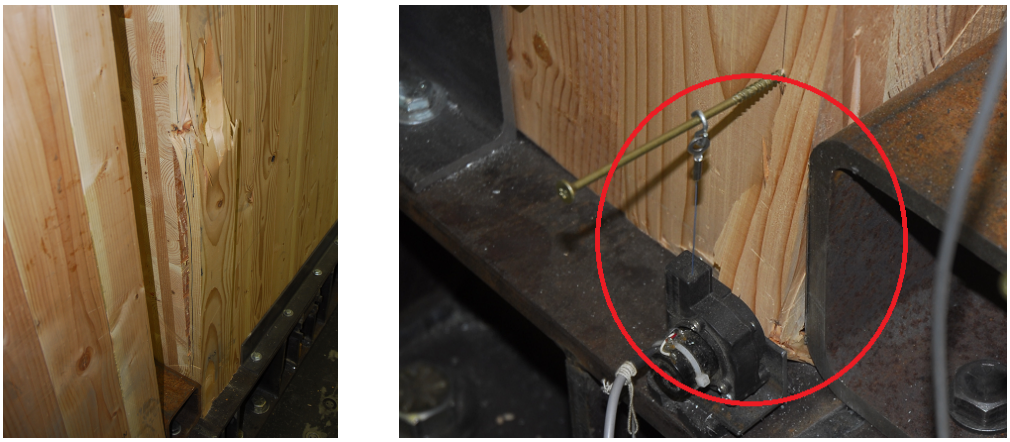

(a) (b)

Figure 5.85: (a) Continued Delamination (WDS3) at the Southeast Corner and (b) Splitting Damage (WDS3) at the Southwest Corner of the North Wall of Specimen 6 During Step 16 (7.3% Drift)

During Step 16 (7.3% drift), at the northeast corner of the south wall, crushing damage was first observed in the first and second plys (WDS3, Figure 5.86a). The delamination at the south end of the south wall continued to grow (WDS3, Figure 5.86b). At the southeast corner of the south wall, the damage continued to grow in the first ply (WDS3, Figure 5.87a). At the southwest corner of the south wall, splitting damage continued in the first ply and new splitting damage was observed in the second ply (WDS3, Figure 5.87b). Throughout Step 16, both UFPs continued to deform (UFP1, Figure 5.88).



(a) (b)

Figure 5.86: (a) Crushing Damage (WDS3) at the Northeast Corner and (b) Delamination (WDS3) at the South End of the South Wall of Specimen 6 During Step 16 (7.3% Drift)

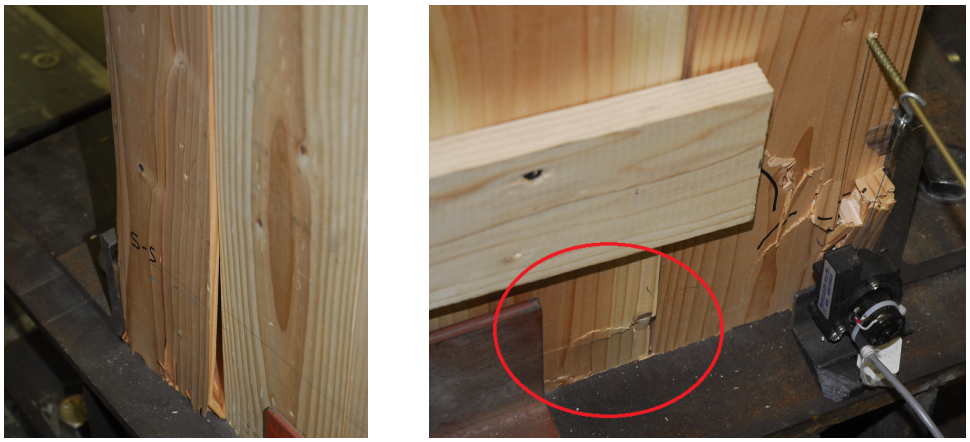

(a) (b)

Figure 5.87: Splitting Damage (WDS3) at the (a) Southeast Corner and (b) the Southwest Corner of the South Wall of Specimen 6 During Step 16 (7.3% Drift)

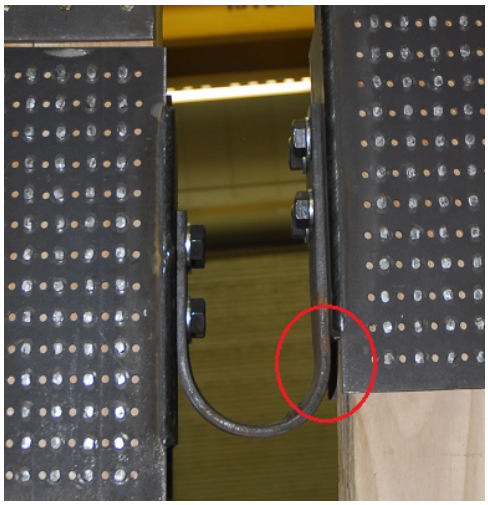

Figure 5.88: Lower UFP Damage (UFP1) of Specimen 6 During Step 16 (7.3%)

During Step 17 (9.4% drift) damage continued for both north and south walls. At the northeast corner of north wall, damage was observed in the second ply (WDS3, Figure 5.84). The splits and delamination at the north end of the north wall continued to grow and a new split measuring 3 inches was observed (WDS3, Figure 5.90a). The splitting damage at the northwest corner continued to worsen in the first ply and a new split measuring $1\frac{3}{4}$ inches was observed in the second ply (WDS3, Figure 5.90b). At the southeast corner of the north wall, the delamination and splitting continued to grow (WDS3, Figure 5.86a). At the southwest corner, new splitting damage measuring $1\frac{1}{2}$ inches in length was observed in the second ply (WDS3, Figure 5.91b).



Figure 5.89: Damage in the first and Second Plys (WDS3) at the Northeast Corner of the North Wall of Specimen 6 During Step 17 (9.4% Drift)



(a) (b)

Figure 5.90: Splitting Damage (WDS3) at the (a) North End and (b) Northwest Corner of the North Wall of Specimen 6 During Step 17 (9.4% Drift)

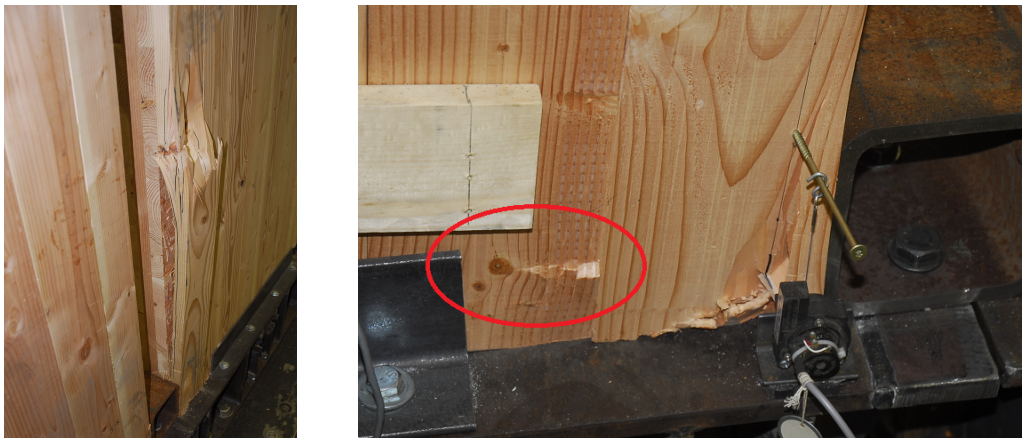

(a) (b)

Figure 5.91: Splitting Damage (WDS3) at the (a) Southeast and (b) Southwest Corners of the North Wall of Specimen 6 During Step 17 (9.4% Drift)

During Step 17 (9.4% drift), at the north end of the south wall, the delamination continued to propagate up the height of the wall (WDS3, Figure 5.92a). There damage continued to worsen at the northwest corner of the south wall around the knot and against the shear transfer HSS in between the north and south walls (WDS3, Figure 5.92b). At the south end of the south wall, splitting damage and delamination continued to worsen (WDS3, Figure 5.93). Both the upper and lower UFPs deformed well over 3 inches (WDS 6, Figure 5.94). During the third cycle of Step 17, Specimen 6 experienced a sudden loss in strength (WDS4).

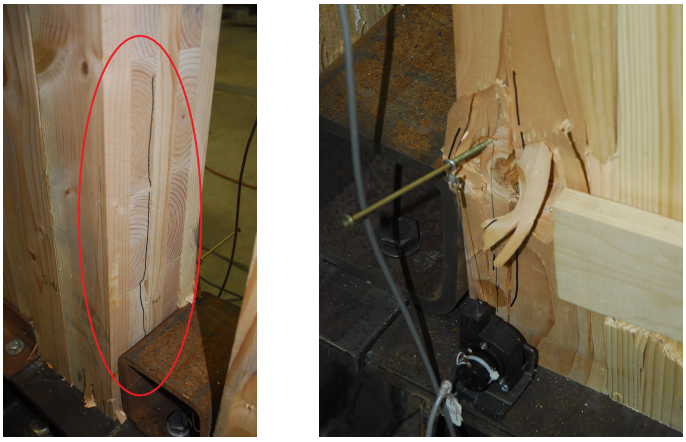

(a) (b)

Figure 5.92: Splitting Damage (WDS3) at the (a) North End and (b) Northwest Corner of the South Wall of Specimen 6 During Step 17 (9.4% Drift)

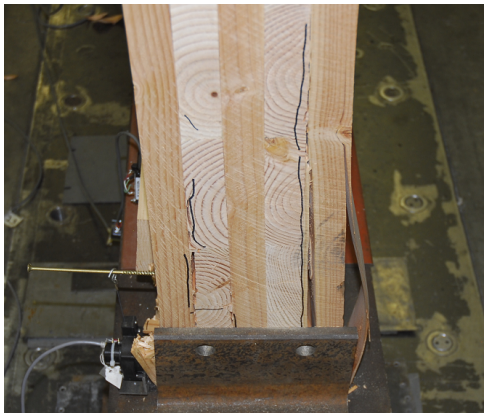

Figure 5.93: Splitting and Delamination (WDS3) at the South End of the South Wall of Specimen 6 During Step 17 (9.4% Drift)

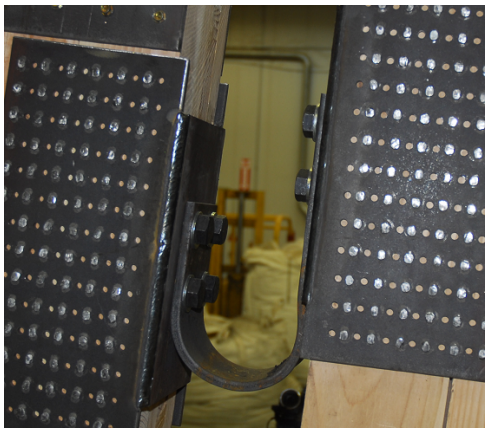

Figure 5.94: Lower UFP Deformation (WDS3) of Specimen 6 During Step 17 (9.4% Drift)

One cycle was run for Step 18 (11.0% drift). All existing damage on both walls increased. Like Cycle 3 of Step 17, when the wall moved to the north (positive direction) it suddenly lost strength but still recentered. However, when coming back to center from the south (negative direction), the wall did not recenter. All damage states were reached throughout the test.

Chapter 6

EXPERIMENTAL DATA ANALYSIS

6.1 Introduction

Data was collected from the various instruments throughout each experiment. This chapter describes how the data was processed and interpreted and presents the results such as the moment versus drift response and specimen stiffness. At the end of this chapter the experimental data is compared to the analytical model presented in Section 3.3. The experimental results are also used to calibrate the numerical model presented in Chapter 7.

6.2 Specimen Summaries

Table 6.1 summarizes the key characteristics for each specimen and shows an illustration indicator that will be used to reference the specimen throughout this chapter.

Table 6.1: Specimen Summaries

Specimen Indicator	Specimen Description
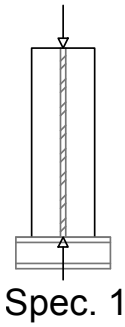	Specimen 1 • Low decompression moment • Low decompression stiffness

Continued on next page

Table 6.1 – Continued from previous page

Specimen Indicator	Specimen Description
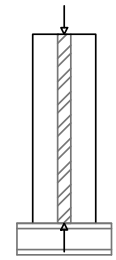 Spec. 2	Specimen 2 • Low decompression moment • High decompression stiffness
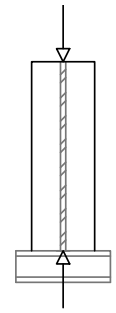 Spec. 3b	Specimen 3a/b • High decompression moment • High decompression stiffness
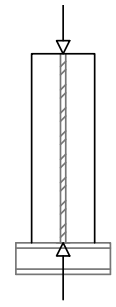 Spec. 3c	Specimen 3c • High decompression moment • High decompression stiffness • Repeat of Specimen 3a, b

Continued on next page

Table 6.1 – Continued from previous page

Specimen Indicator	Specimen Description
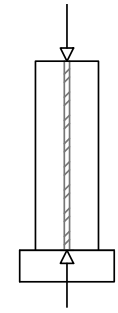 Spec. 4	Specimen 4 • CLT Base • Same bar size and initial prestressing force as Spec. 3a, b, c
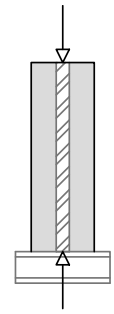 Spec. 5	Specimen 5 • CLT panel with stronger SCL core • Same bar size as Spec. 2 • Same initial prestressing force as Spec. 3a, b, c
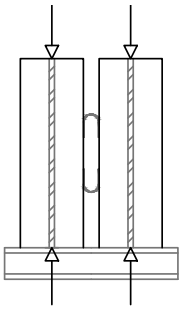 Spec. 6	Specimen 6 • Coupled wall with UFPs • Same bar size and initial prestressing force as Spec. 3a,b,c

6.3 Data Reduction and Corrections

The raw data collected from the DAQ system was decimated and in various ways corrected to compute results. First, initial offsets were removed for all instruments at the point before prestressing of the PT bar. The collected data was then decimated since it was collected at 10 hertz continuously throughout each test. This included data recorded when the actuator was held for test observations at peak displacements or the ends of cycles.

For every test the global top string potentiometer (String Pot. C) varied slightly from the actuator LVDT. This was because the actuator reaction column flexed during testing. Therefore all drift measurements were calculated using the global top string pot instead of the actuator displacement. Since Specimen 6 had two walls and thus two global top string potentiometers (String Pot. B for the north wall and String Pot. C for the south wall), the drift measurements were calculated using an average of both global top string potentiometers and their respective heights. For all specimens, a 7 point running average was applied to the global top string potentiometer data to remove local extraneous spikes.

Since the wall rotated at its base during the test, the actuator load and global top string potentiometer readings were recorded at an angle. A correction factor (Equation 6.1) was computed by using similar triangles (shown in Figure 6.1), the original length and displacement of the actuator ($L_{ACT} + \Delta_{ACT}$), and the String Pot. A (Δ_V) reading (which measured vertical displacement at one end of the actuator). The same procedure was done to correct the top string potentiometer. The length from the wall to the fixed connection point plus the top string potentiometer reading was used instead of the length of the actuator. In both cases it was found the corrected horizontal value was very close to the uncorrected diagonal value.

$$Actuator\ Correction\ Factor = \frac{\sqrt{(L_{ACT} + \Delta_{ACT})^2 - \Delta_V^2}}{L_{ACT} + \Delta_{ACT}} \tag{6.1}$$

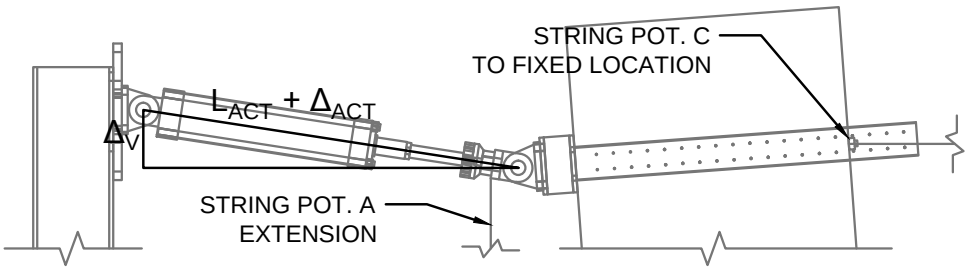

Figure 6.1: Actuator Correction Factor Terms

Specimen 3b had incorrect PT load cell readings because of the curved PT bearing plate (refer to Chapter 5). To fix the load cell readings a new calibration factor was calculated to be applied to the incorrect readings. A portion of the top of Specimen 3b was cut off and, along with the bowed, curved bearing plate and the load cell, placed in a Tinius-Olsen Testing Machine to read loads up to 120 kips. Then the PT load cell with a flat bearing plate was placed in the testing machine also to read loads up to 120 kips. A constant best-fit calibration correction factor to correct the readings from the incorrect curved bearing surface to the correct flat bearing surface was calculated from the two curves, shown in Figure 6.2. To correct the readings, all PT load cell data collected from the Specimen 3b test was multiplied by the constant correction factor.

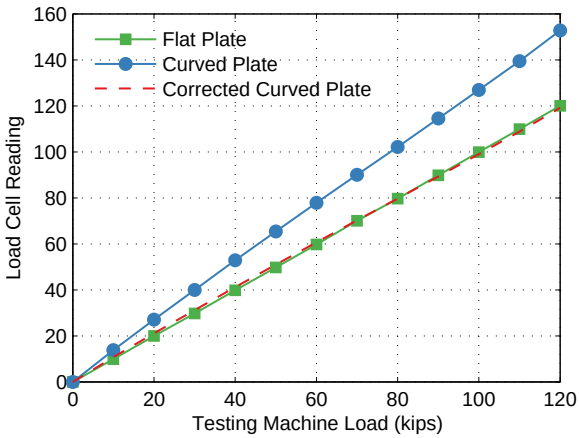

Figure 6.2: Specimen 3b PT Load Cell Correction

For Specimens 3a, 3b, and 3c the wrong calibration factor for the LVDTs was entered into the StrainSmart software. To correct this issue a new calibration factor was computed for each LVDT and the raw data was multiplied by the new correct calibration factor and divided by the old incorrect calibration factor.

During the testing of Specimen 4, the CLT base deformed only directly underneath the CLT wall as shown in Figure 6.3. Since the potentiometers used to measure this CLT base deformation were connected to the CLT wall and CLT base outside of the deformed area, the potentiometer data was unusable to determine the CLT base deformation.



Figure 6.3: Specimen 4 Base Deformation Potentiometers

During the testing of Specimen 6 the PT load cell on the south wall had incorrect readings. The load cell started reading incorrectly during the initial prestressing and caused the PT

bar to be stressed 10 kips too high to 85 kips. In the following data analysis, the strain gauge readings were used to calculate the south wall PT force instead of the load cell readings.

6.4 Strength and Ductility

As described previously the drift was calculated from the global top sting potentiometer (String Pot C.) divided by the height of the string potentiometer. The overturning moment was determined by the actuator load cell multiplied by the actuator height. The overturning moment versus drift response is presented for the single wall specimens in Figure 6.4 and for the coupled wall specimen in Figure 6.5. Ductility measurements are presented in Table 6.2. Ductility was measured by dividing the drift at 20% strength deterioration, θ_{max} by the drift at decompression, θ_{dec}. Certain Specimens did not reach 20% strength deterioration by the end of the test because the actuator ran out of stoke thus the maximum drift experienced was reported for θ_{max}. Strength measurements are presented in Table 6.3. Values are reported for the overturning moment at 2% drift (Step 12), 5% (Step 15), and 9% drift (Step 17). These correspond to a design basis earthquake (DBE), the maximum considered earthquake (MCE), and strength degradation respectively. A ratio of the overturning moment at 9% drift and the maximum overturning moment is used to measure strength degradation.

All Specimens except Specimen 1 exhibited ductile behavior and experienced a slow decline in strength that resulted in a total strength loss between 10% and 25% over the entirety of each test. The specimens tended to start losing strength after the PT bar yielded, but had lost less then 25% of their peak strength at nearly 10% drift.

Specimen 3c had the most asymmetric behavior, reaching a much higher strength to the north (positive drift) compared to the south (negative drift). Because the wall strength is directly related to the PT force, the asymmetrical behavior could be due to the PT bar being placed more toward the north in the specimen causing more PT elongation and thus PT force to the north than the south as shown in PT force versus drift plot (Figure 6.6d). The asymmetrical behavior could also be due to damage occurring at the south end of the wall causing the wall to rock closer to the PT bar which would decrease the moment arm

and cause less PT elongation during negative drifts.

Specimens 2 and 4 had the least amount of strength loss over the loading history. Specimen 2 did not lose strength in the north direction and lost about 16% of its strength in the south direction. Due to the low initial stress of the PT bar, it did not yield until the last cycle of the test. Specimen 4 did not lose strength because of the flexibility of the CLT base. Since the CLT base was more flexible than the wall, the wall caused the CLT base to indent as the specimen was cycled to higher drifts. This did not allow as large of a PT gap to open compared to the specimens with the steel base. The PT bar did not elongate and gain force as quickly and thus the PT bar did not yield.

Specimens 1 and 6 experienced sudden strength losses due to excessive compression damage in the CLT walls. Specimen 1 experienced a large loss of strength in both directions at around 4.5% drift. Specimen 1 lost 50% of its strength in the north direction (positive drift), and 37% of its strength in the south direction (negative drift). The strength loss could be due to the fact that Specimen 1 used Specimen 4's previously tested CLT panels. The panels were visibly undamaged, but could have yielded and experienced internal damage during the Specimen 4 test. It should be noted that Specimen 1 experienced sudden losses in strength at an overturning moment of 3,000 k-in, the value of the maximum overturning moment experienced by Specimen 4.

In the north direction (positive drift) at around 9.0% drift, Specimen 6 experienced a similar loss of strength of 40% as Specimen 1. However Specimen 6 did not experience the same loss in the south direction (negative drift). The CLT damage that caused the losses in Specimen 1 and 6 is most likely due to the inhomogeneous and variable nature of timber as overturning moments and compressive demands were lower than other specimens.

Specimens 2 and 5 reached the highest strength. This is due to both specimens using the larger 1.58 in^2 area PT bar which could reach a higher yield force than the smaller 1.25 in^2 area PT bar used in the other specimens. Specimen 5 reached a slightly higher strength than Specimen 2. This could be due to the fact that Specimen 5 used the stronger SCL core panel.

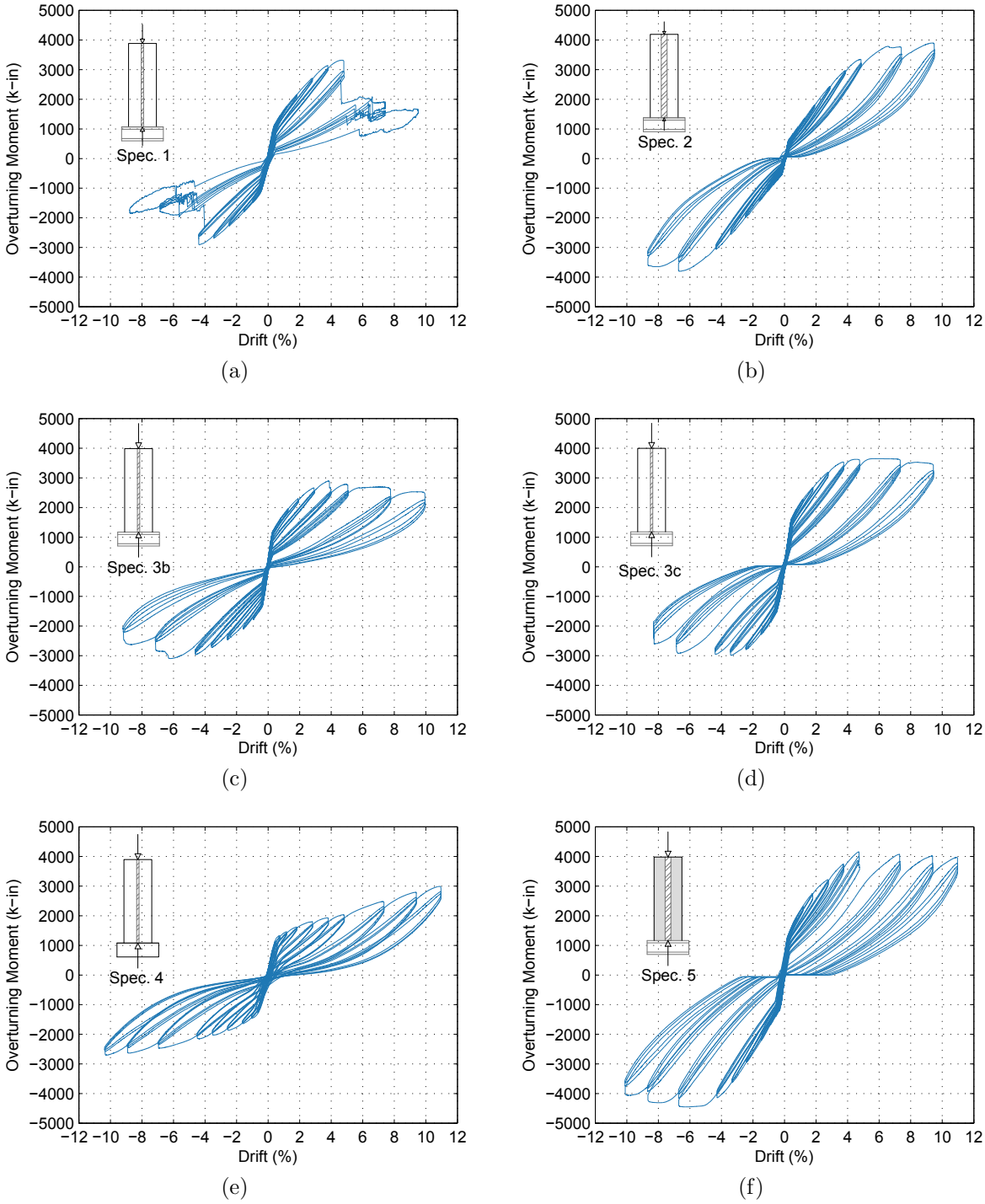

Figure 6.4: (a) Specimen 1, (b) Specimen 2, (c) Specimen 3b, (d) Specimen 3c, (e) Specimen 4, and (f) Specimen 5 Overturning Moment vs. Drift

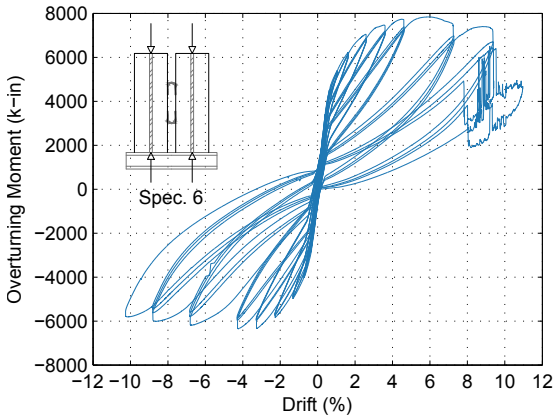

Figure 6.5: Specimen 6 Overturning Moment vs. Drift

Table 6.2: Experimental Ductility Values

Spec.	Dir.	θ_{dec} (%)	θ_{max} (%)	$\frac{\theta_{max}}{\theta_{dec}}$
1	Pos.	0.27	4.80	0.18
	Neg.	-0.39	-4.40	0.11
2	Pos.	0.23	9.50	0.41
	Neg.	-0.17	-8.68	0.51
3b	Pos.	0.35	9.96	0.71
	Neg.	-0.30	-9.20	0.31
3c	Pos.	0.43	9.45	0.22
	Neg.	-0.49	-8.30	0.17
4	Pos.	0.46	10.96	0.24
	Neg.	-0.45	-10.37	0.23
5	Pos.	0.21	10.97	0.53
	Neg.	-0.27	-10.11	0.37
6	Pos.	0.40	9.35	0.24
	Neg.	-0.36	-10.26	0.29

Table 6.3: Experimental Strength Values

Spec.	Dir.	M_{dec} (k-in)	At 2% Drift M_{exp} (k-in)	At 5% Drift M_{exp} (k-in)	At 9% Drift M_{exp} (k-in)	M_{max} (k-in)	$\frac{M@9\%}{M_{max}}$
1	Pos.	915	2163	3275	1638	3320	0.49
	Neg.	-1010	-1800	-2797	-1830	-2910	0.63
2	Pos.	587	1810	3336	3864	3899	0.99
	Neg.	-547	-1440	-3060	-3581	-3804	0.94
3b	Pos.	1166	2237	2757	2470	2898	0.85
	Neg.	-1169	-2102	-2956	-2441	-3096	0.79
3c	Pos.	1610	2670	3594	3429	3651	0.94
	Neg.	-1513	-2283	-2952	-2575	-2989	0.86
4	Pos.	1149	1611	2016	2764	2991	0.92
	Neg.	-1001	-1636	-2133	-2589	-2705	0.96
5	Pos.	1240	2746	4461	3996	4154	0.96
	Neg.	-1138	-2215	-4141	-4221	-4452	0.95
6	Pos.	3395	6229	7694	7217	7838	0.92
	Neg.	-2690	-4917	-6305	-5982	-6348	0.94

6.5 PT Bar Force

One important characteristic of the system is the change in PT force throughout testing. As described above, when the PT bar yields the system experiences its highest strength and the strength stays constant or degrades in subsequent cycles. Figure 6.6 shows the PT force versus drift for the single wall specimens and Figure 6.7 shows the PT force versus drift for the coupled wall specimen. The PT force was measured using the PT load cell and was calculated from the strain gauge readings using a bi-linear stress-strain material model with properties from the PT bar material tests presented in Appendix A. The PT force calculated from the strain gauge readings was fairly close to the load cell readings. The south wall PT load cell in Specimen 6 malfunctioned so only the PT force derived from the strain gauge data is reported. Specimen 3b did not have strain gauges so only the PT load cell reading is reported. Table 6.4 shows the initial PT force and drift at PT yield for each specimen. In addition to maximum PT bar forces, the loss in the PT bar force is important. The PT force loss for each specimen was calculated by comparing the PT force at zero drift of the third cycle of each step to the initial PT force. The percentage of PT force loss is plotted against the peak drift of each step in Figure 6.8. Table 6.4 also shows the percentage of initial PT force lost at the end of the cycles at 0.9% (Step 10), 2% (Step 12), 5% (Step 15), and 9% (Step 17) drift for each specimen.

Throughout each test, permanent deformation at the bottom of the wall, crushing at the top of the wall due to seating of the PT bar, and yielding of the PT bars lead to losses in PT force. Seating occurred because the PT force was transferred through the concentrated PT box area, indenting the softer top of the CLT wall, and allowing the PT bar to shorten. The PT seating loss generally occurred at the beginning of the test before the CLT walls were damaged at the base, and also increased during cycling of the walls.

Specimens 2, 3c and 5 experienced PT bar yielding and lost 100% of the initial PT bar force at zero drift at the end of each test. Prior to bar yielding, these three specimens lost PT force at a similar rate due to CLT damage as shown in Figure 6.8a. Specimen 3c had

the highest initial PT force and the bar yielded at the lowest drift as noted in Figure 6.8a. Specimen 5's PT bar yielded at a larger drift than Specimen 3c and had a large decrease in PT force occurring at a larger drift than Specimen 3c. Specimen 2 had the lowest initial PT bar force and the PT bar yielded at the highest drift. However, Specimen 2 lost PT force quicker than the other specimens. This could be due to the CLT damage or the seating of the PT bar at the top anchorage.

Specimen 1 and Specimen 4 did not experience PT bar yielding. All losses were due to CLT damage and neither specimen had a sharp decrease in PT force. Specimen 4 showed a linear loss in PT force. This is due to the continued indentation of the CLT base that lead to relaxation of the PT bar.

Both walls in Specimen 6 saw similar changes in PT force. The south wall PT bar was initially stressed higher than the north wall PT bar and thus yielded sooner. The south wall PT bar still maintained load at the end of the test and the north wall PT bar did not.

Based on these results, to have the least amount of PT bar loss and adequate strength and energy dissipation at 2% drift, the PT bar initial stress, f_{p0}, should be between 30% and 40% of the ultimate PT bar stress, f_{pu}. All specimens had this initial stress expect for Specimen 2, which was stressed to $0.1f_{pu}$ and lost 28% of the PT bar force by 2% drift. Stressing the PT bar higher than $0.4f_{pu}$ could cause the bar to yield before 4% drift. The PT yielded after 4% drift for all specimens. Note this recommendation depends on the CLT panel aspect ratio, composition, and other factors as well.

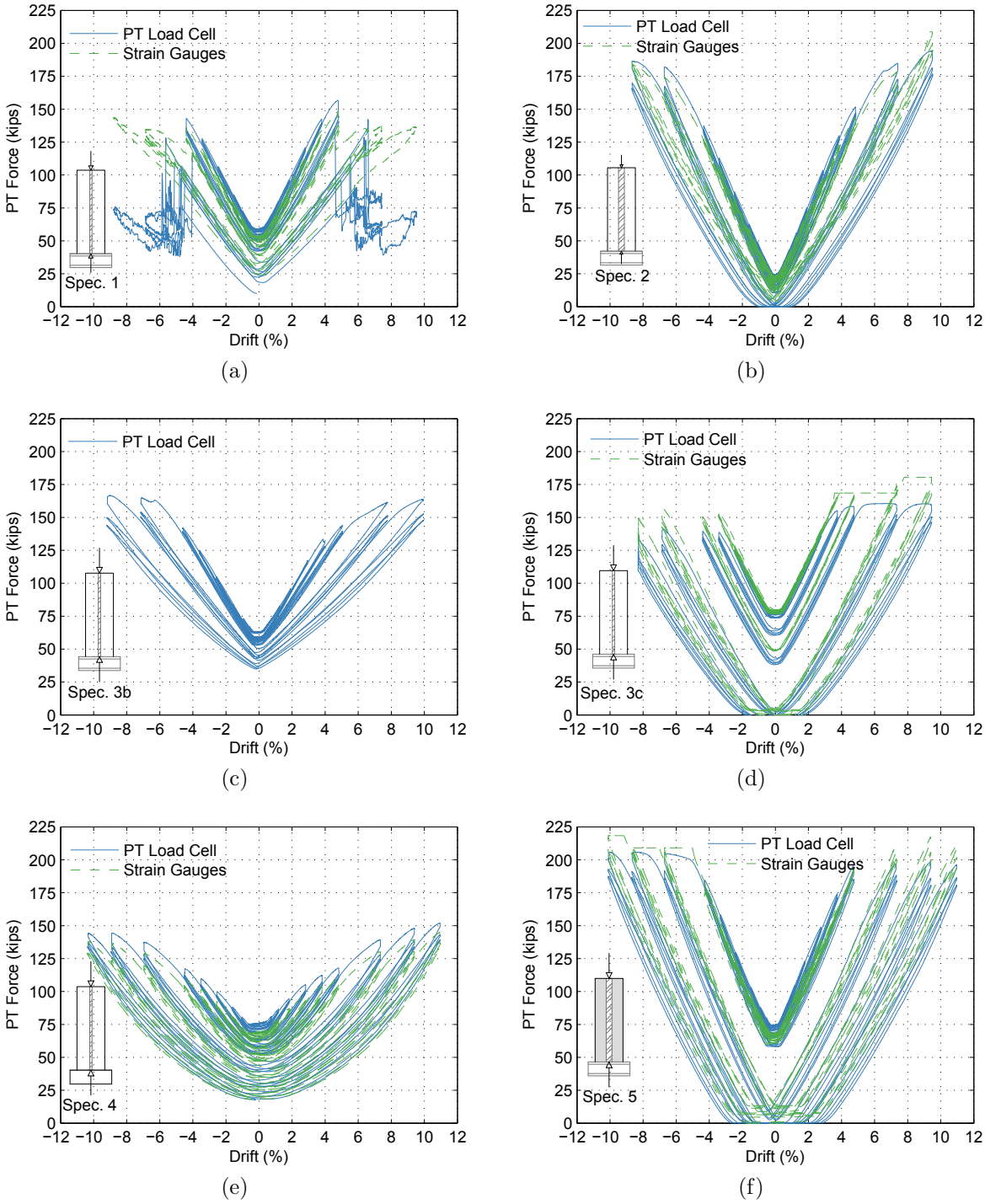

Figure 6.6: (a) Specimen 1, (b) Specimen 2, (c) Specimen 3b, (d) Specimen 3c, (e) Specimen 4, and (f) Specimen 5 PT Force vs. Drift

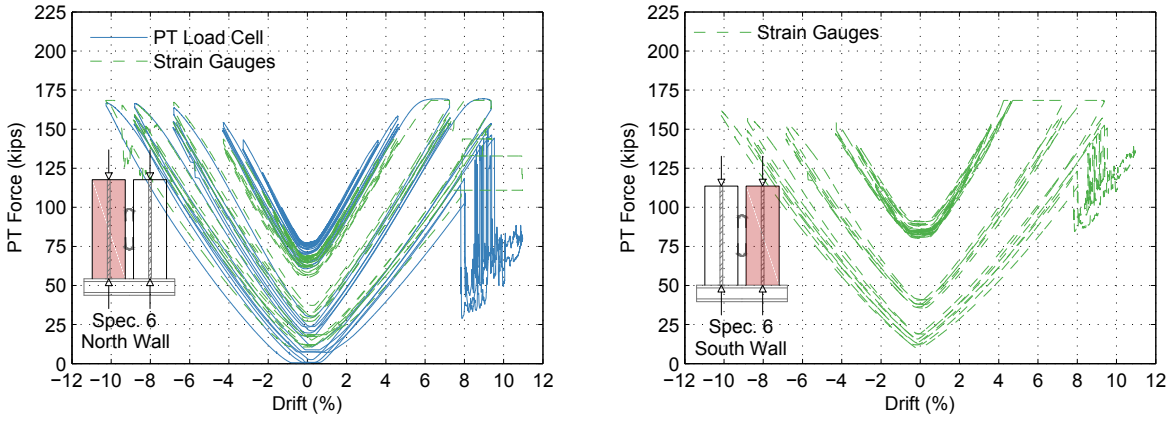

Figure 6.7: Specimen 6 (a) North Wall and (b) South Wall PT Force vs. Drift

Table 6.4: PT Force at Zero Drift After Third Cycles at Indicated Maximum Drifts

Spec.	A_p	f_{p0}	T_0	T_{max}	Drift at	PT Force / Initial PT Force (%) After Max Drifts:			
	(in^2)	(ksi)	$(kips)$	$(kips)$	T_y (%)	0.9%	2.0%	5.0%	9.0%
1	1.25	47	59.0	156.6	N/A	99.1	96.3	71.5	17.3
2	1.58	16	24.5	194.0	8.6	92.4	77.7	42.8	0.0
3b	1.25	50	62.9	166.7	7.7	99.9	92.9	84.3	56.5
3c	1.25	63	78.2	160.5	4.7	99.3	97.2	48.8	0.0
4	1.25	61	75.8	151.9	N/A	96.9	90.5	69.5	36.5
5	1.58	47	74.6	205.8	6.5	98.6	95.1	77.8	0.3
6-NW	1.25	62	77.2	169.5	6.8	99.6	97.9	78.6	0.9
6-SW	1.25	68	85.5	168.3	4.2	99.2	96.6	85.9	15.7

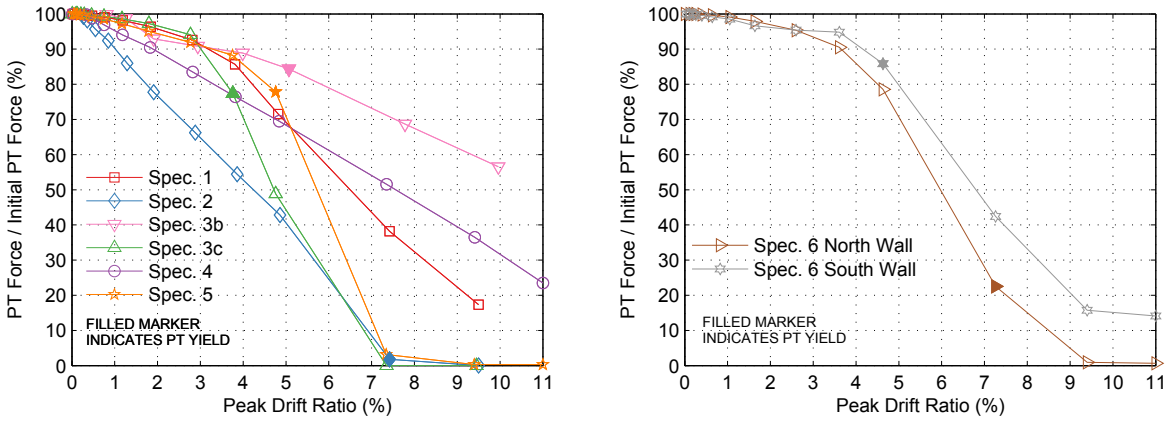

Figure 6.8: (a) Single Wall Specimens and (b) Coupled Wall Specimen PT Force Loss

6.6 Energy Dissipation

Seismic force resisting systems limit force and deformation demands in part through dissipating earthquake input energy. The energy dissipation for each specimen was calculated by summing the area under the force, F, versus displacement, Δ, curve using the trapezoidal rule as shown in Equation 6.2. For the total energy dissipated from the system, the force was taken from the actuator load cell reading and the displacement was taken from the global top string potentiometer reading (String Pot C.). For the energy dissipated from the yielding of PT bar, the force was taken from the PT load cell after the bar was stressed and the displacement was taken to be the PT elongation measured from the PT bar strain gauges multiplied by the PT bar length. The energy dissipated by the CLT damage was calculated as the difference between the total dissipation and the PT bar dissipation.

$$W = \int F d\Delta \approx \sum_{i=2}^{n} \frac{F_i - F_{i-1}}{2}(\Delta_i - \Delta_{i-1}). \tag{6.2}$$

For Specimen 6 (coupled wall), in addition to the PT bar and CLT, the UFP coupling devices dissipated energy. To obtain UFP forces, a force versus displacement curve for

each UFP was estimated by inputting the measured displacement from the UFP string pots (String Pot. F and G) into a calibrated Menegotto-Pinto material model (refer to Chapter 7) using material properties from Appendix A. The energy dissipated from the UFPs was then calculated from the force versus displacement curve using Equation 6.2. The estimated force versus displacement curve for the lower UFP is shown in Figure 6.9. The energy dissipation from the CLT damage for Specimen 6 was calculated as the sum of the PT bar energy dissipation and UFP energy dissipation subtracted from the total energy dissipation.

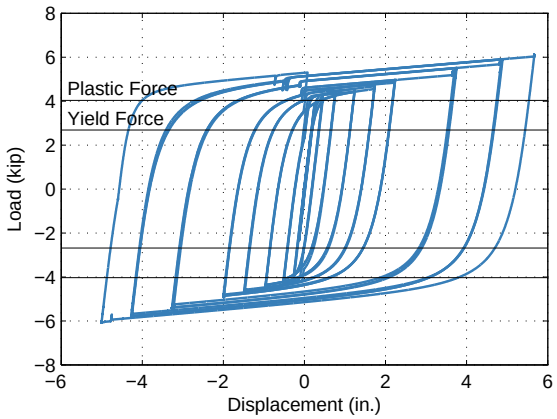

Figure 6.9: Specimen 6 Lower UFP Force versus Displacement

Figure 6.10 shows the energy dissipation for each specimen against the total accumulated drift throughout each test. Table 6.5 shows a summary of the energy dissipated for each specimen at 2% drift (Step 12), 5% drift (Step 15), and the end of each test. In all plots, Specimen 3c is used as a reference for comparison.

In all specimens the total amount of energy dissipated increases when damage to the wall occurs at each new drift step. The first cycle in each step always has the biggest increase in damage and energy dissipated. Where the PT bar yields a sharp increase in total energy dissipated can be seen.

Specimen 1 (Figure 6.10a) used the smaller 1.25 in^2 area PT bar and showed a similar trend as Specimen 3c up to when Specimen 3c's PT bar yielded. Specimen 1's PT bar did not

yield and the energy dissipation did not have the corresponding increase in energy dissipation. Specimen 2 (Figure 6.10b) had the slowest increase in energy dissipation because of the low initial stress in the PT bar and less inelastic deformation of the CLT. Once CLT damage started, Specimen 2 had a similar increase in energy dissipation as the other Specimens. Specimen 3b and 3c (Figure 6.10c) had a similar trend in energy dissipated because both specimens used the smaller 1.25 in^2 area PT bar stressed to a similar amount. The energy dissipation for Specimen 4 (Figure 6.10d) was similar to the other specimens, despite all of the energy dissipation from Specimen 4 being from the deformation of the CLT base. This highlights the deformability of the CLT base loaded perpendicular to grain. Specimen 5 (Figure 6.10e) dissipated the most energy out of all the single wall specimens. This is most likely due to the larger 1.58 in^2 area PT bar used resulting in a higher PT yield force that would be resisted by the larger compression strength of the CLT wall with the SCL core.

Because Specimen 3c used the same bar and initial PT bar force as each wall in Specimen 6, doubling the energy dissipation from Specimen 3c (2xSpecimen 3c) was used as an estimation of the energy dissipation of two walls without UFPs. Specimen 6 (Figure 6.10f) dissipated 50% more energy than 2xSpecimen 3c due to the energy dissipated from the UFPs. This demonstrates the importance of wall configuration and supplemental devices in the seismic performance of rocking walls.

The experimental results show that the PT bar should be stressed initially to at least $0.4f_{pu}$ to achieve good energy dissipation by 2% drift without supplemental devices. As mentioned in the previous section, it should be noted that a PT bar stress initially too high could lead to PT yielding at a low drift which would result in complete loss in PT force and strength of the system. Both the 1.25 in^2 and 1.58 in^2 area bars led to adequate energy dissipation for the system. The high required initial bar stress however highlights the importance of additional energy dissipation devices.

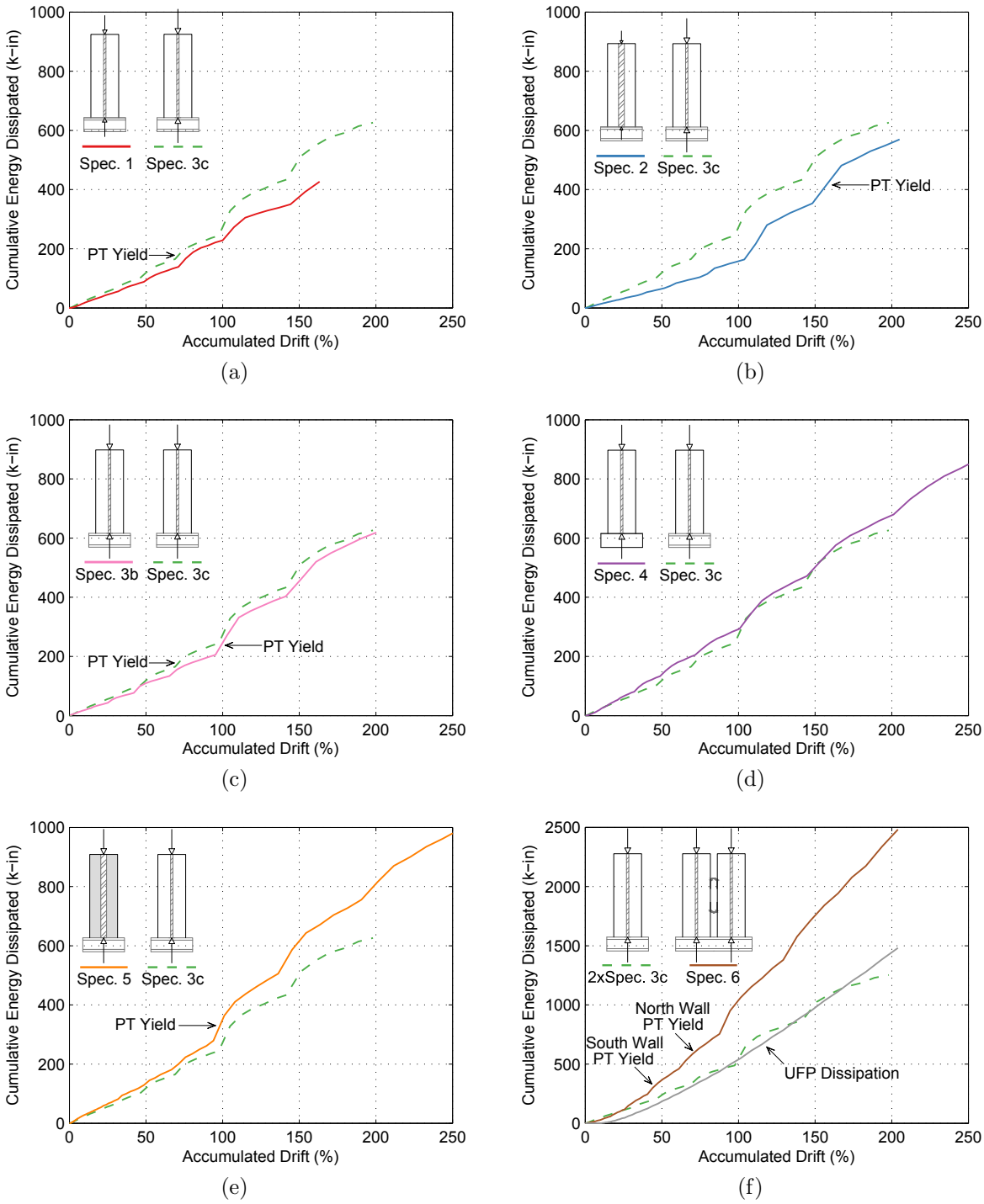

Figure 6.10: (a) Specimen 1, (b) Specimen 2 Cumulative, (c) Specimen 3a/3b, (d) Specimen 4, (e) Specimen 5, and (f) Specimen 6 Energy Dissipation

Table 6.5: Cumulative Energy Dissipation

Spec.	Peak	Cumulative Energy Dissipated (k-in)					
		At 2%	At 5%	At End of Test			
	Drift (%)	Drift	Drift	Total	PT	CLT	UFP
1	9.5	55.8	228	427	0	427	N/A
2	9.5	42.8	164	569	42	527	N/A
3b	10	43.0	205	619	N/A	N/A	N/A
3c	9.5	65.3	244	626	216	410	N/A
4	11	81.0	293	890	0	890	N/A
5	11	75.5	279	992	258	734	N/A
6	10.5	118	755	2482	107	895	1480

6.7 System Stiffness

Characterizing the system stiffness is important for design and modeling of seismic resisting systems. For the rocking CLT wall system, there are three separate stiffness values of interest listed below and shown in Figure 6.11a.

- Initial Stiffness (K_0) - defined as the stiffness before decompression.
- Decompression Stiffness (K_{dec}) - defined as the stiffness after decompression and before recompression as the system moves towards peak drift.
- Recentering Stiffness (K_{rec}) - defined as the stiffness as the system returns toward zero drift and recompression.

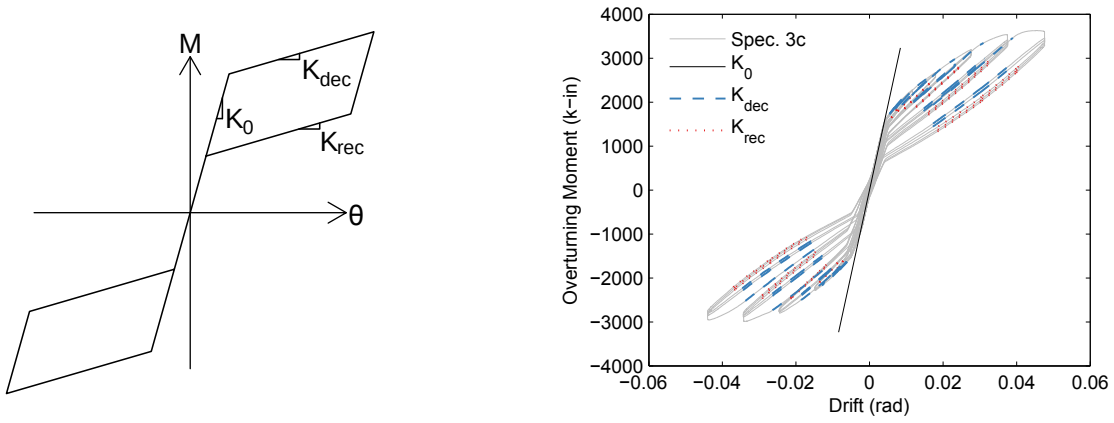

(a) (b)

Figure 6.11: (a) Idealized Flag Shaped Hysteresis and (b) Experimental Overtunring Moment vs. Drift Hysteresis Showing System Stiffness

To calculate experimental stiffness values, the overturning moment was calculated as the actuator load cell reading multiplied by the actuator height and the drift was calculated as the string pot at the top of the Specimen (String Pot. C) divided by the actuator height.

The initial stiffness was calculated from a linear regression of the moment versus drift of the pre-decompression cycles which where when the specimen remained elastic. The slope of this linear regression is reported as $K_{0,exp}$ in Table 6.6. An example of the experimental initial stiffness is shown as a line in Figure 6.11b.

The experimental decompression and recentering stiffnesses were calculated from linear regressions of the overturning moment versus drift for the steps after the specimen reached decompression and after the specimen achieved peak drift. The data points used for the decompression stiffness were after specimen decompression and before specimen recompression or before the specimen starts to return to zero drift. The data points used for the recentering stiffness were after the specimen started to recenter or started to return to zero drift and before complete recompression when the stiffness returned back to the initial stiffness. An example set of the data used for both the decompression and recentering stiffnesses is shown in Figure 6.11b. The experimental decompression stiffness K_{dec} and recentering stiffness K_{rec} are reported in Table 6.6. For each, the value is given for cycles near 0.9% (Step 10), 2% (Step 12), and 5% (Step 15), as well as the average overall.

The initial stiffness values had a significant variation between the tests. Out of the 5-ply specimens, Specimen 2 had the smallest initial stiffness and Specimen 3a/b had the highest initial stiffness. Out of the single wall specimens, Specimen 5 had the highest initial stiffness due to the fact it used a stiffer SCL core for the lower panel. Specimen 5 also had the largest decompression and recentering stiffnesses because of the use of the larger PT bar. As expected, all the single panel decompression and recentering stiffness values were close. Specimen 6 (coupled wall specimen) had more than twice the initial stiffness of the equivalent single wall Specimen 3, most likely due to the UFP coupling devices. The decompression and recentering stiffnesses decreased as CLT damage progressed and PT force was lost. This correlates with the analytical equation for decompression stiffness, Equation 3.33, which states the decompression stiffness is directly related to the PT bar axial stiffness, k_p, and the moment arm length (d) which decreases as CLT damage increases.

Table 6.6: System Stiffness

Spec.	K_0	Cycles at 1% Drift		Cycles at 2% Drift		Cycles at 5% Drift		Test Average	
		K_{dec}	K_{rec}	K_{dec}	K_{rec}	K_{dec}	K_{rec}	K_{dec}	K_{rec}
	$(k\text{-}in/rad)$	$(k\text{-}in/rad)$	$(k\text{-}in/rad)$	$(k\text{-}in/rad)$	$(k\text{-}in/rad)$	$(k\text{-}in/rad)$	$(k\text{-}in/rad)$	$(k\text{-}in/rad)$	$(k\text{-}in/rad)$
1	3.25e5	7.81e4	8.73e4	6.90e4	7.42e4	5.57e4	5.42e4	6.07e4	6.66e4
2	2.60e5	7.52e4	8.29e4	7.62e4	7.90e4	7.13e4	6.85e4	6.39e4	6.58e4
3a	5.37e5	N/A	N/A	N/A	N/A	N/A	N/A	N/A	N/A
3b	3.25e5	8.59e4	9.77e4	7.06e4	7.31e4	5.70e4	5.51e4	7.12e4	7.48e4
3c	3.95e5	9.10e4	1.02e5	7.96e4	8.54e4	6.29e4	6.07e4	6.07e4	6.48e4
4	2.71e5	5.70e4	7.31e4	4.83e4	6.52e4	4.20e4	4.35e4	4.59e4	5.37e4
5	5.65e5	1.08e5	1.21e5	9.38e4	9.63e4	7.83e4	7.58e4	7.85e4	8.11e4
6	1.11e6	3.08e5	4.15e5	2.09e5	2.73e5	1.24e5	1.37e5	1.66e5	2.18e5

6.8 Residual Drift

One of the performance objectives for the performance-based seismic design (PBSD) procedure presented in Chapter 3 is recentering at the 10% in 50 year (10/50) hazard level. The criterion for recentering is a residual drift less than 0.2% which corresponds to the out-of-plumb limits in new construction [ATC, 2009a]. The proposed PBSD procedure limits story drifts to 2% drift at the design-basis earthquake (DBE) which generally corresponds to the 10/50 hazard level. It should be noted that the experiments were not designed according to the PBSD procedure and do not represent a prototype building. They were subjected to displacement controlled histories which are not representative of the dynamic response of buildings in earthquakes. To asses rocking CLT wall recentering capabilities, the residual drift of each specimen was approximated as the drift of the specimen at zero force. This is generally known as the static residual drift and has been shown to be conservative relative to residual drifts for rocking systems from dynamic analysis [Clayton, 2013]. A range of residual drift values for loading in both directions are reported in Table 6.7, more specifically after 2% drift (Step 12), 5% drift (Step 15), and at the end of the test.

After Step 12 (2% drift) all Specimens were able to recenter (i.e. residual drift values less than 0.2% drift). After Step 15 (5% drift) Specimens 5 and 6 were the only specimens which did not recenter. Both specimens failed to recenter in the south direction. However, the residual drifts were only slightly higher than the 0.2% limit. After the end of the each test none of the specimens were able to recenter. Specimen 1 was the closest to recenter with a maximum residual drift of 0.23%. This is because the PT bar did not yield during the testing of Specimen 1. All other tests, except Specimen 4, lost all PT bar force due to PT bar yielding and thus had very high residual drifts at the end of the test. Specimen 4 did not recenter due to damage to the CLT base. The PT bar for Specimen 3c and the south wall of Specimen 6 yielded at Step 15 (5% drift). All other Specimen's PT bars yielded after Step 15. Since all Specimens were close to recentering after 5% drift, the CLT damage that occurred before PT bar yield did not effect the recentering capabilities of the Specimens.

Table 6.7: Residual Drifts

Spec.	Dir.	Residual Drift (%)		
		After 2% Drift Cycles	After 5% Drift Cycles	After End of Test
1	Pos.	0.11	0.16	0.23
	Neg.	-0.05	-0.08	-0.15
2	Pos.	0.09	0.09	1.05
	Neg.	-0.03	-0.08	-1.21
3b	Pos.	0.03	0.04	0.55
	Neg.	-0.08	-0.12	-0.45
3c	Pos.	0.06	0.04	1.66
	Neg.	-.008	-0.13	-2.09
4	Pos.	0.18	0.18	1.75
	Neg.	-0.09	-0.04	0.64
5	Pos.	-0.02	0.07	2.92
	Neg.	-0.17	-0.25	-3.19
6	Pos.	0.10	0.11	0.14
	Neg.	-0.07	-0.24	-3.30

6.9 Elastic and Shear Moduli

The modulus of elasticity (E) and the shear modulus (G) for the CLT panels were estimated by using measurements during the elastic cycles that occurred before wall decompression. The actuator force in conjunction with the inclinometers were used to estimate the modulus of elasticity and the actuator force in conjunction with LVDTs were used to estimate the shear modulus. The moduli were not calculated for Specimens 4 and 6 because both specimens did not have the LVDTs setup to measure shear deformation. Material tests, referenced in Appendix A were performed on a set of CLT specimens cut from test specimens also to determine the modulus of elasticity.

To calculate the modulus of elasticity a linear curvature distribution was assumed as shown in Figure 6.12. Since the rotation is the integral of the curvature, the trapezoidal area in the curvature distribution between the upper ($h2$) and lower ($h1$) inclinometer can be equated to the difference in the upper inclinometer reading (θ_2) and lower inclinometer reading (θ_1) (Equation 6.3). Using the fact that the moment is equal to the curvature multiplied by EI (Equation 6.3), the average moment over the height can be solved for in terms of the change in rotation, EI, and the change in height (Equation 6.6). I is the second moment of inertia about the panel cross-section and defined for a rectangular section in Equation 6.5 where L_w is the base length of the panel and b_w is the panel thickness. It should be noted that the change in rotation divided by the change in height is equal to average curvature.

$$\theta_2 - \theta_1 = \int_{h_1}^{h_2} \phi dh = (\phi_1 + \phi_2)\frac{h_2 - h_1}{2} \tag{6.3}$$

$$M_n = EI\phi_n \tag{6.4}$$

$$I = \frac{1}{2}L_w^3 b_w^2 \tag{6.5}$$

$$\frac{M_1 + M_2}{2} = EI\frac{\theta_2 - \theta_1}{h_2 - h_1} \tag{6.6}$$

Equation 6.6 was plotted for the elastic cycles and is shown for for Specimens 2 in Figure 6.13a and Specimen 3b in Figure 6.13b. The slope of a liner regression was taken as EI for each specimen. The experimental modulus of elasticity is reported in Table 6.8 for all specimens.

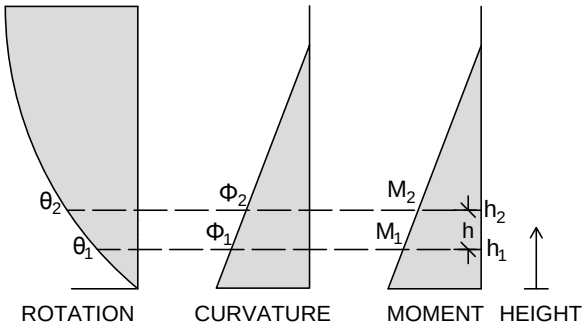

Figure 6.12: Elastic Deformation Calculation Schematic

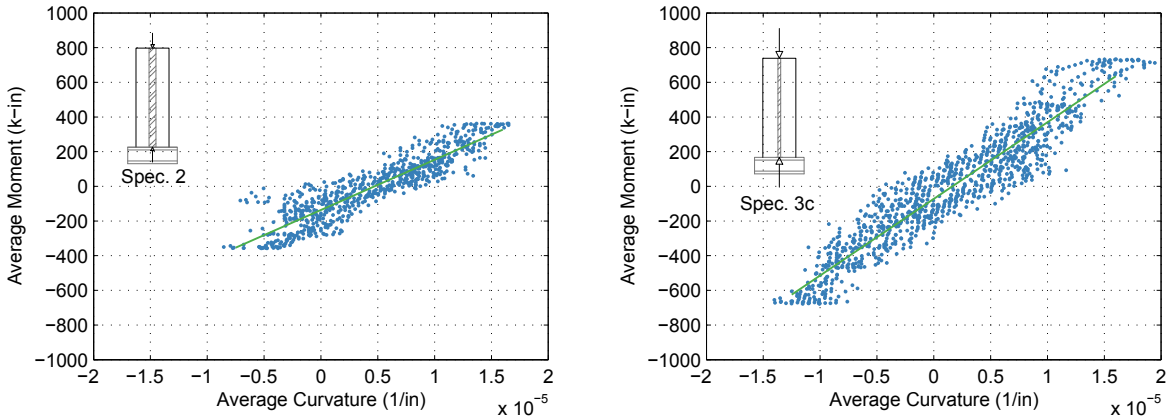

(a) (b)

Figure 6.13: (a) Specimen 2 and (b) Specimen 3c Elastic Deformation

The method used to calculate shear deformation was adapted from Massone and Wallace [2004]. The shear deformation and strain were estimated from LVDT measurements (LVDT-

5 through 8) which were set up vertically and diagonally at the base of the wall. The shear stress was estimated by dividing the actuator load by the panel cross-sectional area.

The element that the shear deformation was calculated from is shown in Figure 6.14. The total lateral displacement $\overline{U}_{Total}$ over the height of the element (h) was calculated using Equation 6.7 where D_{1f} and D_{2f} where the diagonal lengths measured with LVDT-6 and 8, V_1 and V_2, and the change in vertical length measured with LVDT-5 and 7. $\overline{U}_{Total}$ was the sum of the average lateral displacement due to shear ($\overline{U}_s$) and the average lateral displacement due to flexure ($\overline{U}_f$).

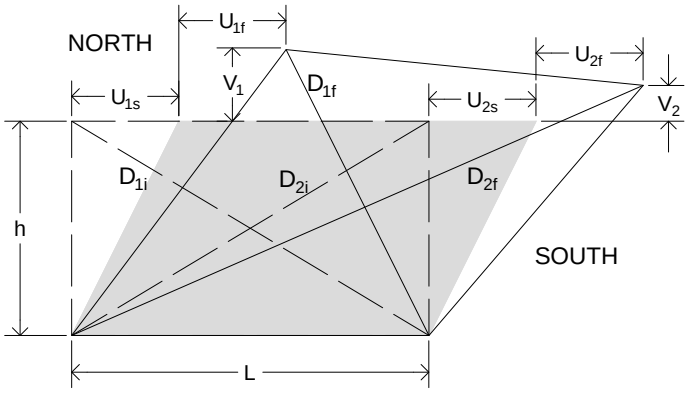

Figure 6.14: Shear Deformation Calculation Schematic

$$\overline{U}_{Total} = \overline{U}_s + \overline{U}_f = \frac{\sqrt{D_{2f}^2 - (h+V_2)^2} - \sqrt{D_{1f}^2 - (h+V_1)^2}}{2} \tag{6.7}$$

It was assumed that the lateral displacement due to flexure was equal on each side of the element such that $U_{f1} = U_{f2} = \overline{U}_f$. Because only two vertical LVDTs were used on each side of the element to measure flexural deformation, the center of curvature and rotation was unknown and must be assumed. Massone and Wallace [2004] suggests that the center of curvature would be at a height of αh where $\alpha = 0.67$. With the estimation of the center of curvature, $\overline{U}_f$ was calculated from Equation 6.8 where θ is the average rotation calculated

from Equation 6.9 and L is the length of the element.

$$\overline{U}_f = \alpha\theta h \tag{6.8}$$

$$\theta = \frac{V_2 - V_1}{L} \tag{6.9}$$

Now that the total lateral displacement and the lateral displacement due to flexure was known, the the average lateral displacement due to shear ($\overline{U}_s$) was calculated by subtracting $\overline{U}_f$ from $\overline{U}_{Total}$ as shown in Equation 6.10. The average shear strain over the element was determined by dividing $\overline{U}_s$ by h as shown in Equation 6.11 and the average shear stress was calculated by dividing the actuator force, V_{Base}, by the shear area, A', shown in Equation 6.12, where k_s is the shape factor taken as $\frac{5}{6}$ for a rectangular cross-section.

$$\overline{U}_s = \overline{U}_{Total} - \overline{U}_f \tag{6.10}$$

$$\gamma = \frac{\overline{U}_s}{h} \tag{6.11}$$

$$\sigma_s = \frac{V_{Base}}{A'} = \frac{V_{Base}}{k_s(A)} \tag{6.12}$$

Shear stress versus shear strain for the elastic cycles are shown for Specimens 2 in Figure 6.15b and Specimen 3c in Figure 6.15b. The shear Modulus (G) was estimated by the slope of a linear regression of the stress versus strain data and is reported in Table 6.8. The values from the material tests and the values listed in the APA [2012] are also listed in Table 6.8 for comparison. Because of instrument reading errors, data from Specimen 5 did not produced meaningful results for the shear modulus.

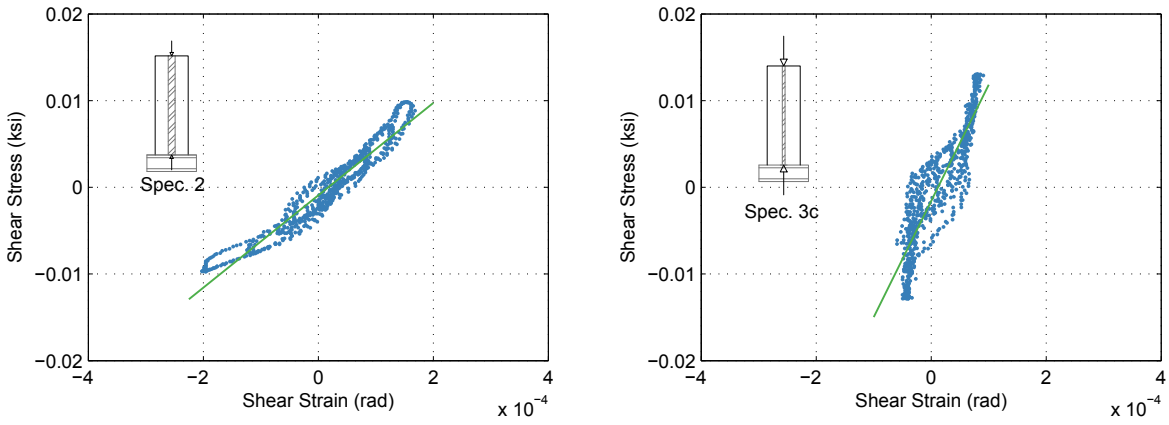

Figure 6.15: (a) Specimen 2 and (b) Specimen 3c Shear Deformation

As expected, since wood is an anisotropic material known to have considerable variation in mechanical properties, the moduli values differed from specimen to specimen. Specimen 5, which had the SCL core panel had a higher elastic modulus than the 5-ply CLT panels used in the other tests. This is in agreement with the higher initial stiffness experienced by Specimen 5 and the higher elastic modulus calculated from the material tests presented in Appendix A. Specimens 1 and 2 had similar elastic and shear moduli. Specimens 3a and 3c had significantly higher elastic and shear moduli values compared to Specimens 1 and 2. This supports the fact that Specimens 3b and 3c had significantly higher initial stiffness values than Specimens 1 and 2 as shown above. Specimens 1 and 2 had similar modului of elasticity to the material tests. The reason for the larger elastic modulus for Specimens 3a and 3b is unknown.

With Specimen 1 and 2 being the closest, all elastic modului from the experiments were higher than the elastic modulus calculated from the material tests. This may be due to that the testing machine head displacement was used to calculate the strains during the material tests, which would cause an overestimation of the strains and cause a higher modulus of elasticity to be calculated from the data. All elastic modului from the experiments were

significantly lower than the recommended values from APA [2012]. This may be due to the CLT panels for the experiments were manufactured in house at WSU instead of a CLT plant.

Table 6.8: Experimental Elastic and Shear Moduli

Spec.	Moment of Inertia I (in^4)	Area A (in^2)	Elastic Modulus E (ksi)	Shear Modulus G (ksi)
1	58555	316	500	46
2	61723	323	470	53
3a/b	61152	320	892	199
3c	61723	323	716	134
5	61909	317	1386	N/A
CLT Material Tests (App. A)	N/A	N/A	441	N/A
APA CLT Standard	N/A	N/A	1600	100

6.10 Neutral Axis and PT Gap Rotation

The neutral axis (NA) location and PT gap rotation are important characteristics that can be used for calibration of analytical and numerical models of rocking walls. The NA location is defined as the location on the rocking wall where the wall loses contact with its bearing surface. The NA depth is defined as the length of wall that is in compression. The PT gap rotation is the rotation angle of the wall at the neutral axis location. The NA location, NA depth, and PT gap rotation are shown in Figure 6.16.

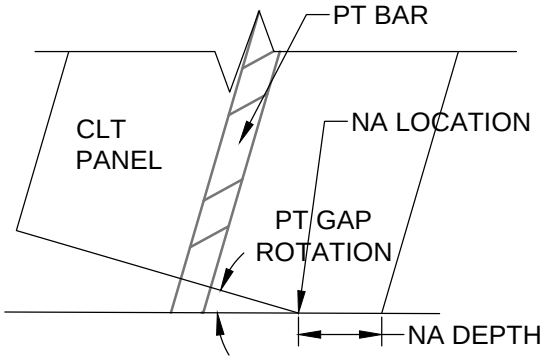

Figure 6.16: Illustration of NA Location, Depth, and PT Gap Rotation in a CLT Rocking Wall

The base displacement potentiometers (LVDT-1, LVDT-2, and DP-1 through DP-5), which were spaced 8 inches apart along the length of the wall, were used to calculate the NA location. The potentiometers were zeroed before each specimen was prestressed. As the wall was prestressed each potentiometer read negative displacement signifying the wall was in compression at that potentiometer location. When the wall decompressed at a potentiometer location, the potentiometer read a zero or positive reading. The NA location was then known to be between two potentiometers, one with a negative (compression) reading and one with a positive (decompression) reading. The NA location was estimated by linearly interpolating between these negative and positive potentiometer readings to find the location where the

reading would theoretically cross zero. The NA depth was then calculated by taking the distance between the NA location and the end of the wall in compression. For positive drifts the north end of the wall was in compression and for negative drifts the south end of the wall was in compression. Figures 6.17a and 6.18a show examples of the NA depth as a percentage of the length of the wall versus drift.

At each base displacement potentiometer that was decompressed (positive reading), the gap rotation was determined by dividing the positive potentiometer reading by the distance from the potentiometer location to the NA location (assuming small angles). The PT gap rotation was then determined to be the average of all the gap rotation calculations at each decompressed potentiometer. Figures 6.17b and 6.18b show examples of PT gap rotation versus drift.

As each specimen decompressed the neutral axis quickly dropped past 50% of the wall length and then leveled out to roughly 20% of the wall length. The NA location must pass the PT bar location, which was at 50% of the wall length, for the PT gap to open. As the PT gap opens, PT is allowed to elongate and increase in force to resist the applied overturning moment.

The PT gap rotation was not equal to the drift indicating the wall was not acting as a rigid body. The difference is most likely due to flexural and shear deformations of the wall. For all specimens there was about a 0.8:1 PT gap rotation to drift ratio.

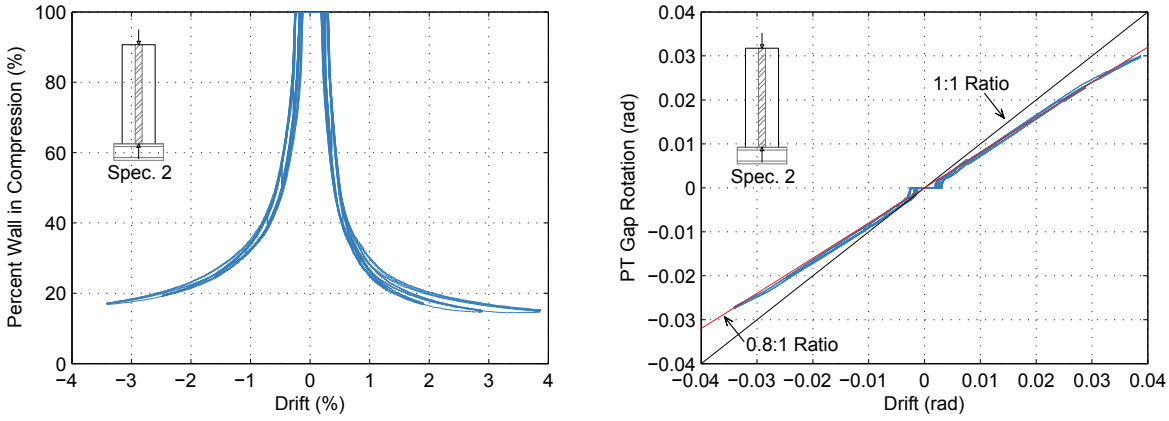

(a) (b)

Figure 6.17: Specimen 2 (a) Neutral Axis Depth and (b) PT Gap Rotation

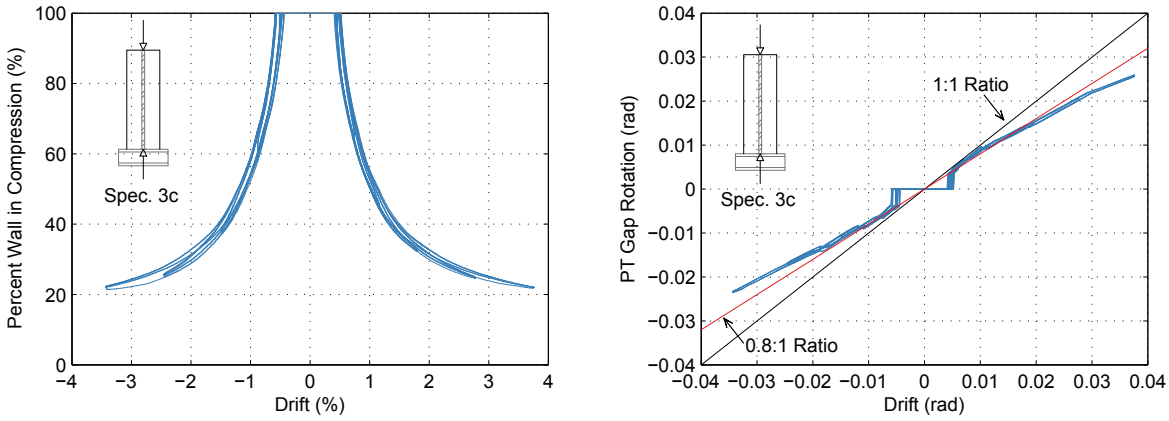

(a) (b)

Figure 6.18: Specimen 3c (a) Neutral Axis Depth and (b) PT Gap Rotation

6.11 Comparison of the Cross-Sectional Analysis Procedure and Experimental Results

Specimens 1, 2, 3b and 3c were modeled using the cross-sectional analysis procedure presented in Section 3.3 and the results were compared to the experimental results presented above. Since the plastic hinge length, l_p, used in the section analysis procedure was unknown, it was calibrated by performing various section analyses in search of the plastic hinge length that best fit the data. The optimal plastic hinge length used for all specimens was determined to be 18 inches. The modulus of elasticity, E, used was 470 ksi and the yield stress, f_y, used 3.4 ksi, both determined from the CLT material tests presented in Appendix A. The modulus of rigidity, G, used was 50 ksi based on the experimental results presented above. Figures 6.19-6.22 show the analytical section analysis results compared with the experimental test results. The overturning moment, PT bar force, neutral axis depth, c, and moment arm length, d, were compared.

For the cross-sectional analyses, equation 3.1 was used to determine the decompression moment. From the experimental data, the moment arm length, d, (presented in Table 6.9) can be calculated using the known decompression moment, M_{dec}, and the initial PT force, T_0. The experimental values for d range from 15 inches to 21 inches. For the cross-sectional analysis procedure a value of 18 inches for the moment arm at decompression, which is equal to the average of the experimental values, was assumed. If a triangular stress distribution for the CLT panel, as shown in Figure 3.12a, and a d of 18 inches is assumed, then the NA depth would be equal to $\frac{3}{8}$ of the wall base length. This corresponds to the wall not decompressing until the NA depth has passed the PT location and the PT has started to elongated.

The PBSD procedure presented in Chapter 3 uses the cross-sectional analysis procedure to determine wall capacities at a limit of 2% story drift. The experimental overturning moment in both directions is compared to the analytical overturning moment at 2% drift in Table 6.10. Overall the experimental and analytical overturning moment values are in good agreement with the cross-sectional analysis being generally conservative. The difference was

less than 10% different except for Specimen 3c in the positive direction which was 12.5% different.

In all cases the analytical procedure overestimated the PT bar force. One possible reason for this is that the cross-sectional analysis procedure did not model CLT damage which would result in PT loss. For all specimens, the neutral axis depth and moment arm length were underestimated. This is most likely due do to the simplified elastic-perfectly plastic constitutive model that was assumed for the CLT material behavior. In reality the CLT material behavior is much more complex.

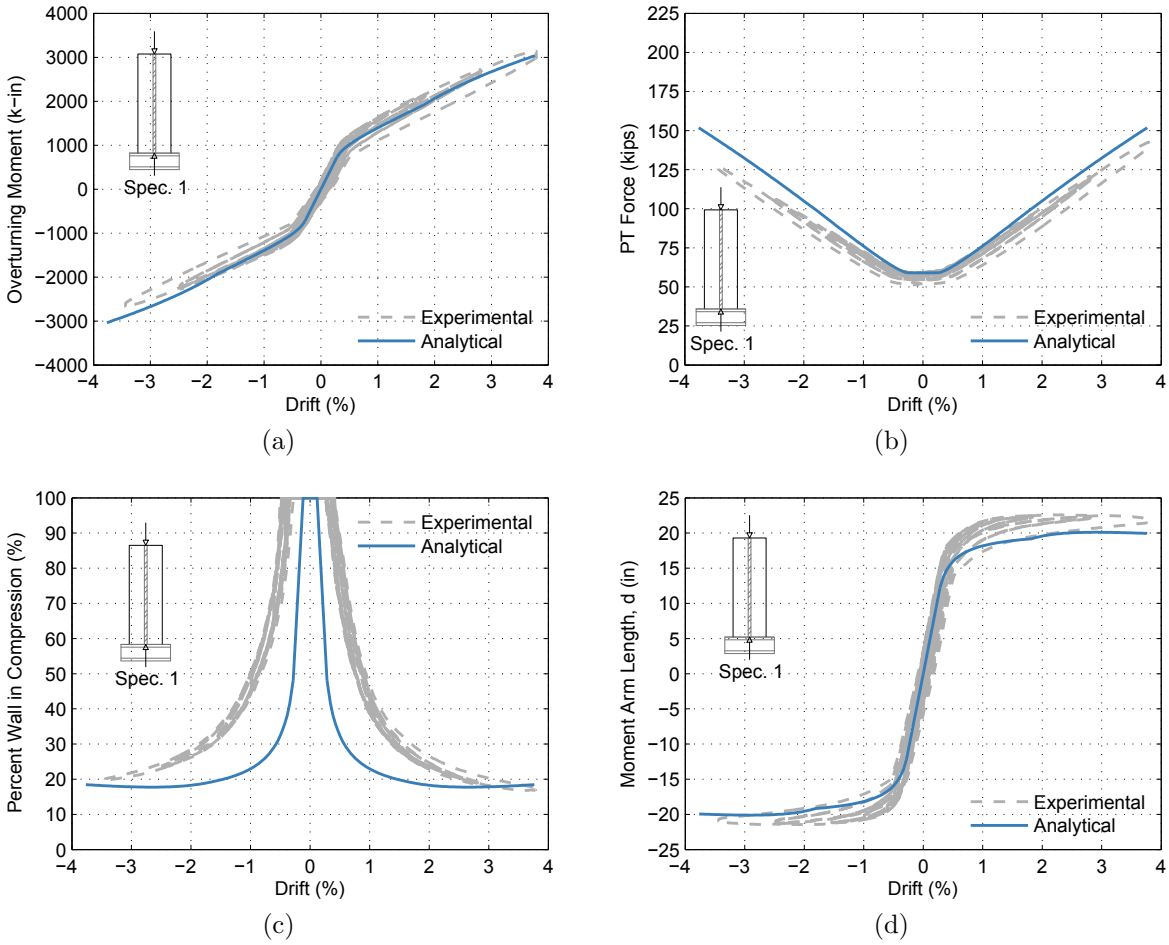

Figure 6.19: Comparison of the (a) Base Shear vs. Drift, (b) PT Force vs. Drift, (c) Neutral Axis Depth, and (d) Couple Arm Length of Specimen 1 from the Cross-Sectional Analysis and Experiments

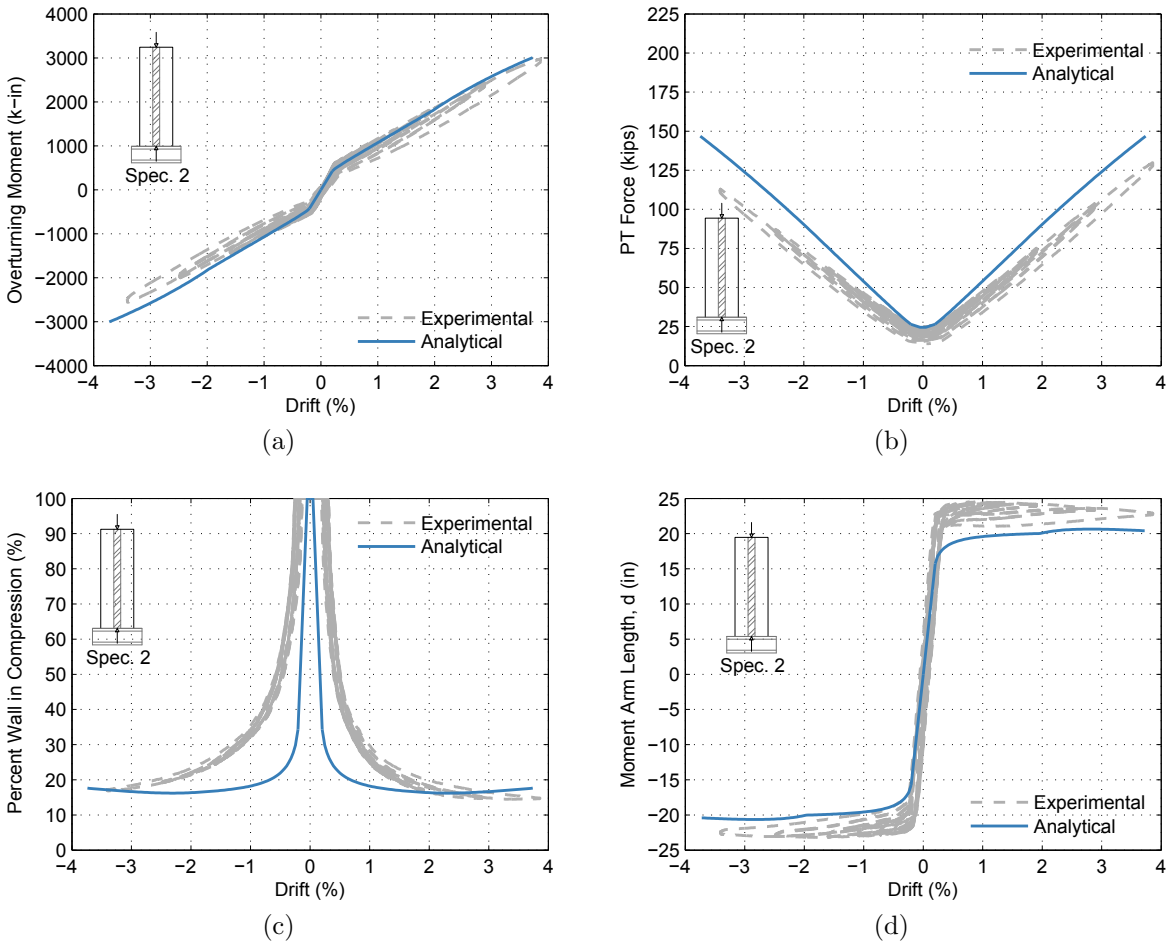

Figure 6.20: Comparison of the (a) Base Shear vs. Drift, (b) PT Force vs. Drift, (c) Neutral Axis Depth, and (d) Couple Arm Length of Specimen 2 from the Cross-Sectional Analysis and Experiments

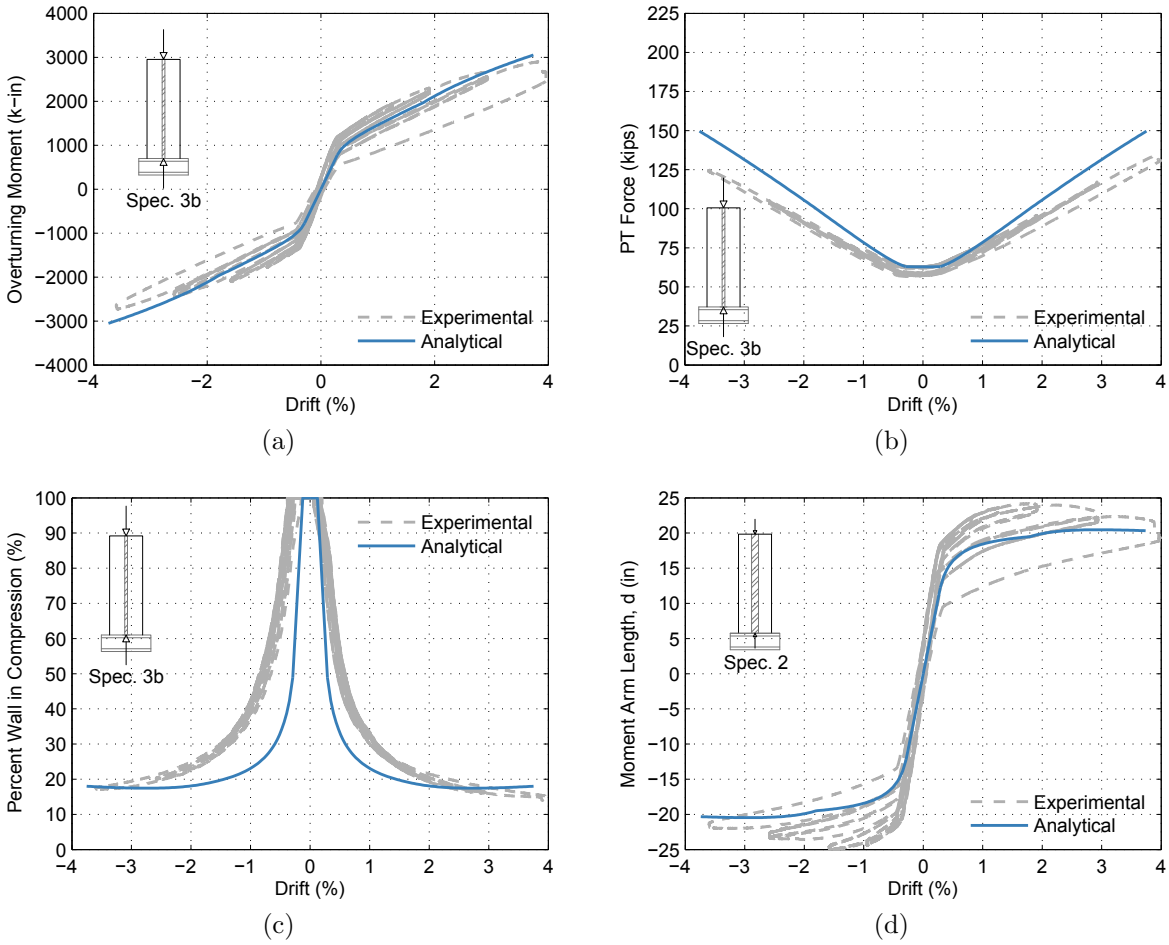

Figure 6.21: Comparison of the (a) Base Shear vs. Drift, (b) PT Force vs. Drift, (c) Neutral Axis Depth, and (d) Couple Arm Length of Specimen 3b from the Cross-Sectional Analysis and Experiments

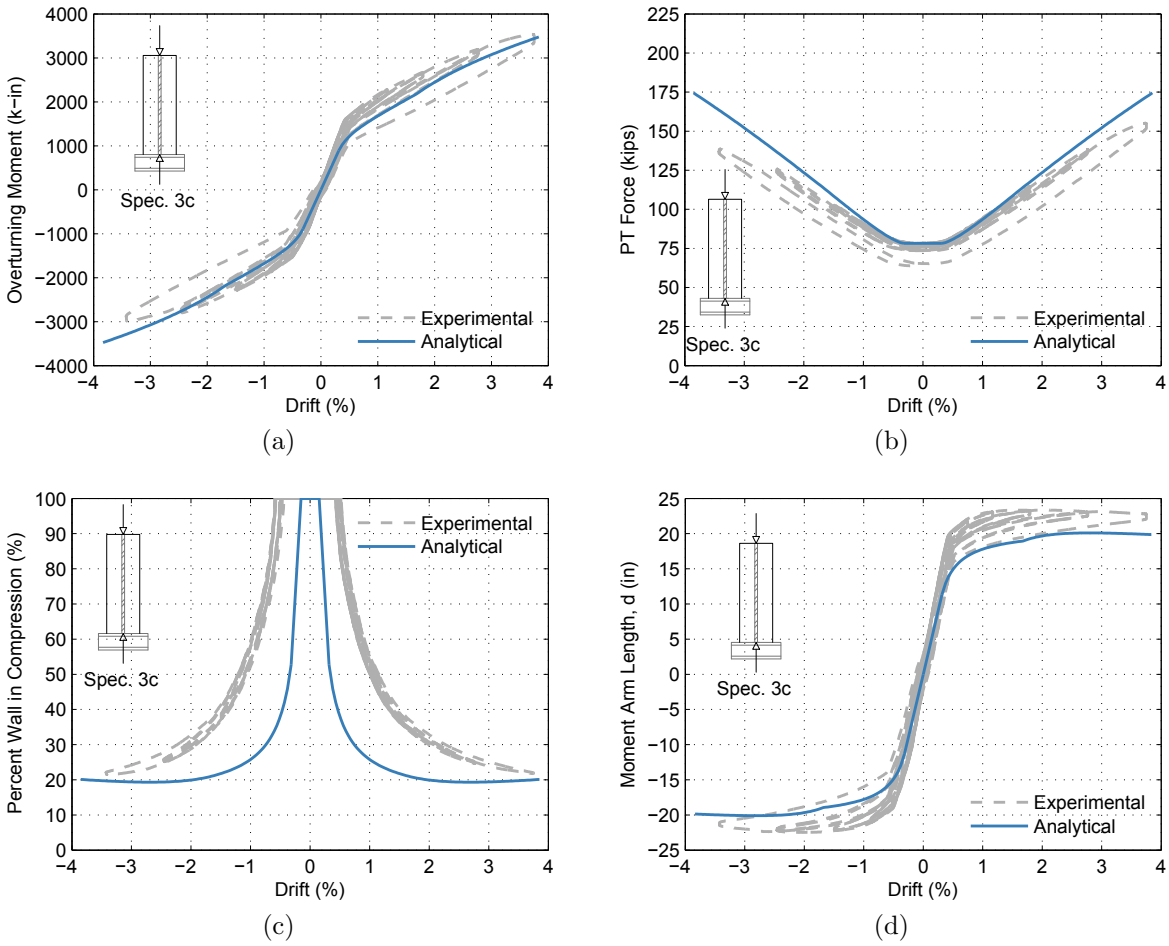

Figure 6.22: Comparison of the (a) Base Shear vs. Drift, (b) PT Force vs. Drift, (c) Neutral Axis Depth, and (d) Couple Arm Length of Specimen 3c from the Cross-Sectional Analysis and Experiments

Table 6.9: Moment Arm Length

Spec.	M_{dec}	T_0	d
	$(k\text{-}in)$	$kips$	in
1	915	59	15.5
2	547	24.5	22.3
3b	1166.4	62.9	18.5
3c	1610	78.2	20.6
4	1149	75.8	15.2
5	1138	74.6	15.3

Table 6.10: Experimental-Analytical Overturning Moment Comparison at 2% Drift

		At 2% Drift		
Spec.	Dir.	M_{th}	M_{exp}	$\frac{M_{th}}{M_{exp}}$
		$(k\text{-}in)$	$(k\text{-}in)$	Difference (%)
1	Pos.	2086	2272	0.92
	Neg.	-2086	-2048	1.02
2	Pos.	1836	1864	0.98
	Neg.	-1836	-1710	1.07
3b	Pos.	2133	2291	0.93
	Neg.	-2133	-2202	0.97
3c	Pos.	2450	2800	0.88
	Neg.	-2450	-2588	0.95

Chapter 7

NUMERICAL MODEL DEVELOPMENT AND APPLICATION

7.1 Introduction

This chapter presents the development of numerical models of individual rocking CLT walls and their application in analyses of buildings using rocking CLT wall systems. These models were calibrated using the experimental results presented in Chapter 6. The modeling techniques were then used to create numerical models of the buildings designed with the performance-based seismic design (PBSD) procedure presented in Chapter 3. The designs were assessed by subjecting each model to a suite of ground motions scaled to the three seismic hazard levels and evaluating the model performance. All numerical modeling was performed in OpenSees [Mazzoni et al., 2009].

7.2 Description of the Rocking CLT Wall Model

The numerical model for a rocking CLT wall consisted of (1) elastic beam-column wall elements, (2) a PT truss element, (3) multispring contact elements, and (4) UFP coupling elements. A schematic of the model used to model the experiments is shown in Figure 7.1. The following description is for the single connection rocking CLT wall model, which was used to simulate the experiments. The model for a wall with rocking connections at the top and bottom (dual PT connection wall) is discussed in the description of the full building model in Section 7.4.

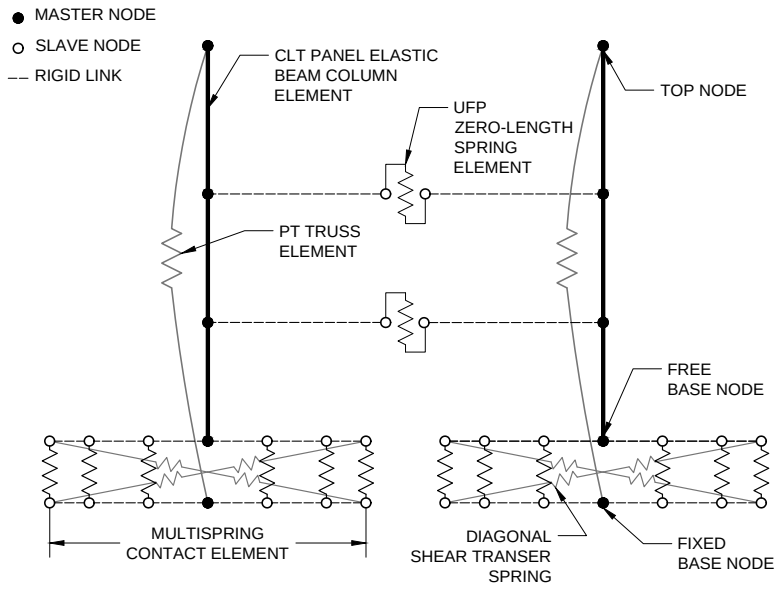

Figure 7.1: Numerical Model for Single Connection Rocking CLT Wall

The PT bar element was modeled as a truss element and connected to the fixed base node and the top control node. A bi-linear hysteretic material model (ElasticPPGap material) was used to model the PT behavior. The material model was limited to not exceed zero positive strain such that the PT bar could not experience compression. An initial strain was applied to the bi-linear material model to simulate the initial prestressing of the PT bar. The initial PT strain was specified such that the PT bar strain would be at the target value after PT force losses due to relaxation of the PT bar after prestressing.

The elastic portion of the CLT wall was modeled with a series of displacement-based elastic beam column elements (ElasticTimoshenkoBeam element) that included axial, flexure, and shear deformations. For the walls without UFP elements, only one element was used that spanned from the free base node to the top wall node. For a coupled wall, the first element spanned from the free base node to a node at the first vertical location of a UFP. The next elements spanned in between each vertical UFP location nodes. The last element

spanned from the last UFP vertical location to the top control node.

The inelastic portion of the CLT wall was modeled with a multispring contact element developed by Spieth et al. [2004]. The multispring contact element consisted of a series of zerolength springs distributed through a Labatto Integration method along a length equal to the base length of the wall. Each top spring node was connected through a rigid link to the free base node and likewise each bottom spring node was connected through a rigid link to the fixed base node.

Each spring was allowed to deform only in the vertical direction and assigned an elastic-perfectly plastic degenerating gap material model (ElasticPPGap material), shown in Figure 7.2 to simulate the CLT compression behavior and wall gap opening discussed in Chapter 3. The material model had an assigned spring stiffness, k_s, and yield strength F_{ys} in the negative (compression) direction and zero stiffness and strength in the positive (tension) direction. An overall contact stiffness, K_s, was determined for the multispring element by dividing the axial stiffness of the CLT panels by a calibrated plastic hinge length from the experiments. Each individual spring stiffness was weighted from the overall contact stiffness using the Labbatto Integration method. Similarly, the yield strength of each spring was determined by weighting the product of CLT panel yield stress and the panel cross-sectional area. To transfer the shear force without inhibiting rocking action, two stiff shear transfer springs were attached diagonally to the outer multispring nodes.

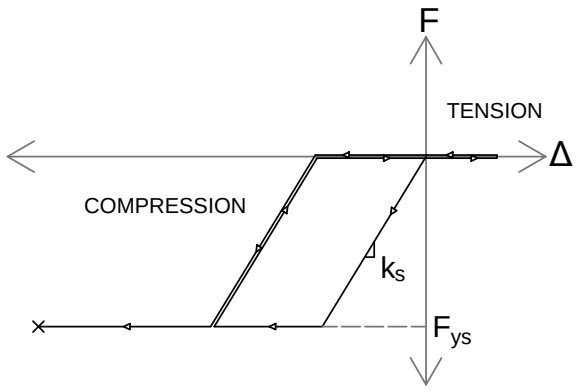

Figure 7.2: Material Model for Mulitspring Contact Element

The UFP coupling devices were modeled using zero-length springs with a Guiffre-Megegotto-Pinto material model with isotropic strain hardening (Steel02 material). Since the UFPs exhibit a shearing force on the CLT walls, the zero-length springs were allowed only to deform in the local vertical direction. The UFP nodes were placed horizontally at the midpoint between two walls and were connected via rigid links to CLT wall nodes at the same vertical positions of the UFPs, such that the UFPs would rotate and deform as the walls rocked.

7.3 Comparison of the Numerical Model and Experimental Results

To calibrate the numerical model, the numerical analysis results for each Specimen were compared to the experimental results presented in Chapter 6. The single connection rocking CLT wall numerical model, in the previous section, was used to model all the experiments presented in Chapter 4 except Specimen 4. Specimen 4 was not modeled because the CLT base deformed and in practice the CLT base would have to be protected from large deformations observed.

The material properties for the PT bars were derived from material tests referenced in Appendix A. The geometric properties for the CLT panel elements were taken from measure-

ments taken before the tests. For all specimens except Specimen 5 (SLC core Specimen), the material properties used for the elastic-beam-column elements that represent the undamaged portions of the CLT wall panels area average values from the experimental data and the CLT material tests (see Appendix A) and are:

- Elastic Modulus, E: 470 ksi
- Shear Modulus, G: 50 ksi
- Compressive Yield Stress, f_y: 3.4 ksi

Since Specimen 5 used the stronger CLT panel with the SCL core, the elastic modulus used was the average of the experimental results and material tests for the CLT panels with SCL cores. Since the shear deformation data collected for Specimen 5 was unusable, the shear modulus was assumed to be that of the 5-ply CLT panels. The material properties used for Specimen 5 are:

- Elastic Modulus, (E): 1114 ksi
- Shear Modulus, (G): 50 ksi
- Compressive Yield Stress (f_y): 4.5 ksi

A contact stiffness, K_s, was calculated for the multispring elements as:

$$K_s = \frac{A_w E_w}{L_p} \tag{7.1}$$

where A_w is the cross-sectional area of the CLT panel, E_w is the elastic modulus of the CLT panel, and L_p is a plastic hinge length. Since the plastic hinge length, L_p, was an unknown value, it was calculated by running various simulations with different plastic hinge lengths

for the Specimens. The results were examined and a plastic hinge length of 8 inches was determined to lead to the most accurate results. A total of 32 springs were used for each multispring element.

Specimen 6 had a coupled wall configuration with UFPs as the coupling devices. Using the analytical equations from Section 3.2.3, the yield stress of the UFPs (determined from the coupon test in Appendix A), and the dimensions of the UFPs, an initial stiffness value and plastic force were calculated for the UFP Guiffre-Menegotto-Pinto material model used in OpenSees. Since the UFPs don't experience significant yielding until they reach their plastic force [Kelly et al., 1972], the plastic force was used for the yield force in the material model. In OpenSees, a zero-length spring element that represented the UFP was subjected to the same UFP protocol as the material test in Appendix A. The results from the UFP material test and the numerical results were in good agreement and are shown in Figure 7.3. The UFP elements in Specimen 6's numerical model were assigned the same material properties derived from the material tests.

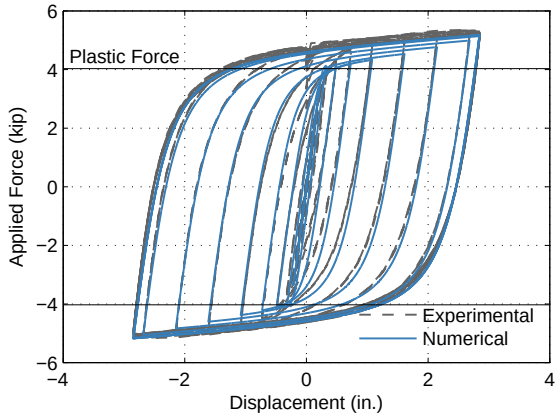

Figure 7.3: Comparison of UFP Material Test and Numerical Model

The analyses of the test specimens were run with a displacement control load protocol assigned to a control node at the location of the actuator. The applied displacement history was equal the history recorded from the top string potentiometer (String Pot. C) during the

tests.

7.3.1 System Strength

Figure 7.4 show the comparison of the moment versus drift response for the experiments and the numerical models. Table 7.1 presents the moment from the numerical models at decompressin, 2% (Step 12), 5% (Step 15), and 9% (Step 17) drift cycles and compares these values with the experimental results.

Overall the moment versus drift responses of the numerical models matched well with the experimental results. All the models showed the similar flag shape hysteresis with similar strength and damage as the experiments. The models predicted the decompression moment with good accuracy with Specimen 2, 3b, and 3c having the largest differences. The maximum moments at 2% had good agreement as well. Specimen 5 in the negative drift direction had the largest difference of 19% between the experiment and numerical model. This may be due to Specimen 5's use of the CLT panel with the SCL core and only one specimen being tested to obtain material properties for this panel type. All other moments from the analyses at 2% drift were within 10% of the experimental values.

Specimen 1 was not able to match the experimental behavior after 5% drift. This is because the numerical model could not simulate the sudden strength loss from CLT damage that Specimen 1 experienced. Similar behavior occurs during the second 9.5% positive drift cycle for Specimen 6.

For Specimen 3c, the maximum strength was underestimated in the positive drift direction and overestimated in the negative drift direction. This is due to the numerical model being unable to replicate the asymmetrical behavior of Specimen 3c discussed in Chapter 6.

At larger drifts the models tended not to match the experimental strength as well. The numerical models generally did not have as much hysteretic area from CLT damage. This may be due to the difficulty in modeling timber because its anisotropic natural causes the behavior to be unpredictable.

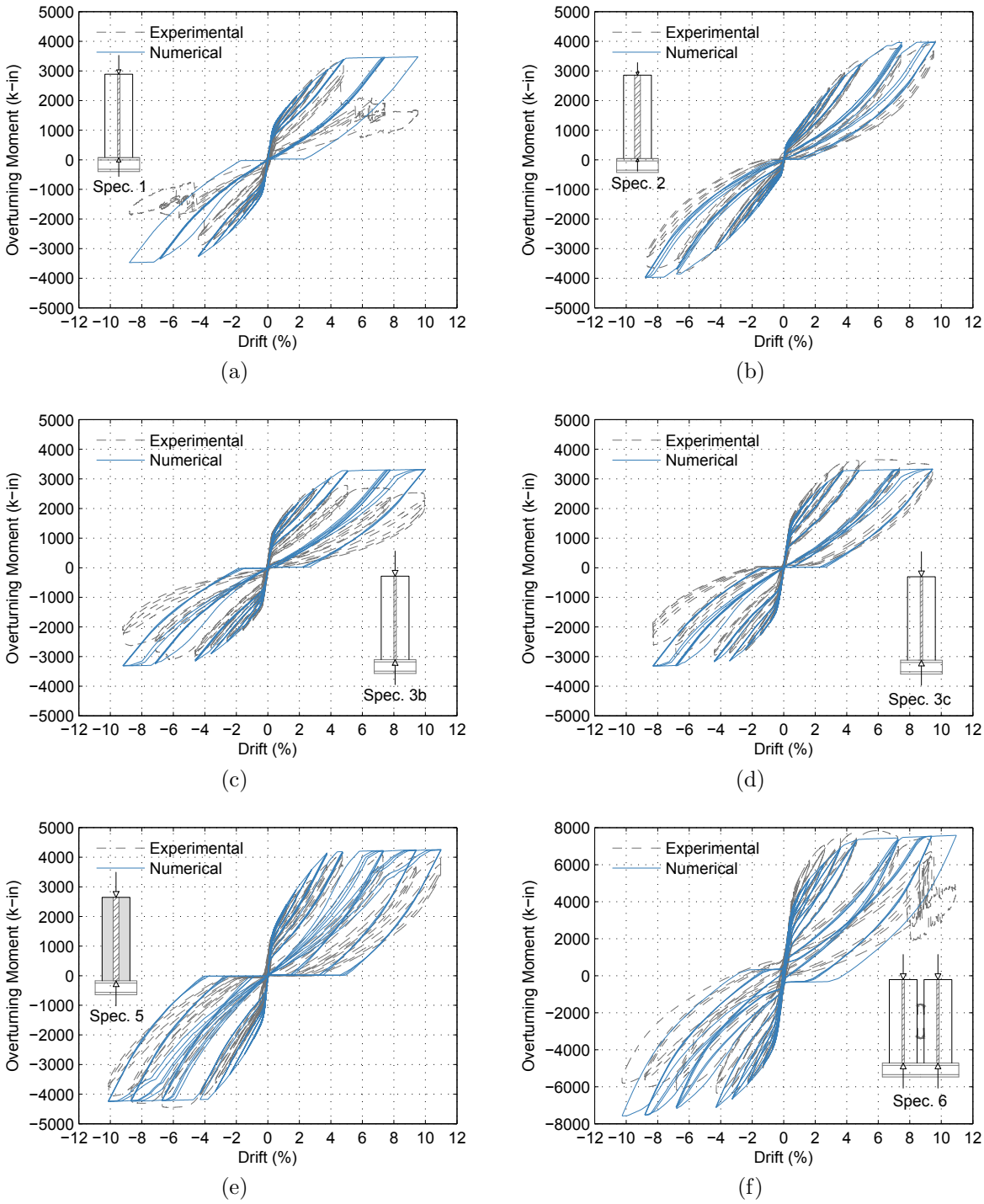

Figure 7.4: Comparison of (a) Specimen 1, (b) Specimen 2, (c) Specimen 3b, (d) Specimen 3c, (e) Specimen 5, and (f) Specimen 6 Overturning Moment vs. Drift from the Numerical Models and Experiments

Table 7.1: Comparison of the Moment Strength from the Numerical Models and Experiments

Spec.	Dir.	$M_{dec,num}$ $(k\text{-}in)$	$\frac{M_{dec,num}}{M_{dec,exp}}$	At 2% Drift M_{num} $(k\text{-}in)$	At 2% Drift $\frac{M_{num}}{M_{exp}}$	At 5% Drift M_{num} $(k\text{-}in)$	At 5% Drift $\frac{M_{num}}{M_{exp}}$	At 9% Drift M_{num} $(k\text{-}in)$	At 9% Drift $\frac{M_{num}}{M_{exp}}$
1	Pos.	971	1.06	2141	0.99	3371	1.03	3470	2.12
	Neg.	-974	0.96	-1974	1.10	-3239	1.16	-3465	1.89
2	Pos.	441	0.75	1772	0.98	3210	0.96	3971	1.03
	Neg.	-420	0.77	-1564	1.08	-3025	0.99	-3967	1.11
3b	Pos.	1039	1.42	2178	0.97	3248	1.18	3315	1.34
	Neg.	-1035	0.89	-2012	0.96	-3126	1.06	-3310	1.36
3c	Pos.	1295	0.80	2417	0.91	3275	0.91	3327	0.97
	Neg.	-1279	0.84	-2248	0.98	-3163	1.07	-3318	1.29
5	Pos.	1223	0.99	2869	1.04	4178	0.94	4225	1.06
	Neg.	-1219	1.07	-2642	1.19	-4173	1.01	-4220	1.00
6	Pos.	3121	0.92	5200	0.83	7240	0.94	7341	1.02
	Neg.	-2792	1.04	-4856	0.99	-7050	1.12	-7351	1.23

7.3.2 System Stiffness

The three numerical system stiffnesses ($K_{0,num}$, $K_{dec,num}$, and $K_{rec,num}$) were calculated in the same manner as the experiments in Chapter 6. Table 7.2 lists and compares the initial stiffnesses (K_0), Table 7.3 lists and compares the decompression stiffnesses (K_{dec}), and Table 7.4 lists and compares the recentering stiffnesses (K_{rec}). The decompression and recentering stiffnesses were compared at 2% (Step 12), 5% (Step 15), and for an average of values for all cycles.

The numerical and experimental initial stiffnesses were fairly close with Specimen 6 having the largest difference. Specimens 3c, 3b, and 5 were the closest to the experiments. The

differences are most likely due to the simplicity of the model and the variability in the mechanical properties of CLT since the initial stiffness is dependent on the elastic and shear stiffnesses of the CLT panels.

The numerical model and experimental decompression stiffnesses were in good agreement for all tests. At the 2% drift cycles, the decompression stiffnesses were close with the exception of Specimen 6. For Specimen 6, this underestimation by the numerical model is shown in Figure 7.4f in the positive drift cycles up to 2% drift. However, after 2% drift, Specimen 6's numerical model decompression stiffness starts to match with the experimental stiffness. At the 5% drift cycles the numerical and experimental decompression stiffnesses had the best agreement, with Specimen 3c having the largest variation of 6.43%.

The numerical model and experimental recentering stiffnesses were also were in good agreement. Like the decompression stiffness, at the 2% drift cycles, Specimen 6 had the largest difference.

Table 7.2: Comparison of the Initial Stiffness from the Numerical Models and Experiments

Spec.	$K_{0,num}$ $(k\text{-}in/rad)$	$\frac{K_{0,num}}{K_{0,exp}}$
1	3.71e5	1.14
2	3.10e5	1.19
3b	3.25e5	1.02
3c	3.85e5	0.98
5	5.78e5	1.02
6	8.20e5	0.74

Table 7.3: Comparison of the Decompression Stiffness from the Numerical Models and Experimentals

Spec.	Cycles at 2% Drift		Cycles at 5% Drift		Overall Average	
	$K_{dec,num}$ $(k\text{-}in/rad)$	$\frac{K_{dec,num}}{K_{dec,exp}}$	$K_{dec,num}$ $(k\text{-}in/rad)$	$\frac{K_{dec,num}}{K_{dec,exp}}$	$K_{dec,num}$ $(k\text{-}in/rad)$	$\frac{K_{dec,num}}{K_{dec,exp}}$
1	6.90e4	1.00	6.09e4	1.09	6.74e4	1.11
2	7.51e4	0.98	6.48e4	0.91	7.04e4	1.10
3b	6.51e4	0.92	5.62e4	0.99	5.62e4	0.79
3c	7.36e4	0.92	6.70e4	1.06	7.21e4	1.19
5	9.98e4	1.06	8.31e4	1.06	8.76e4	1.12
6	1.57e5	0.75	1.22e5	0.99	1.59e5	0.96

Table 7.4: Comparison of the Recentering Stiffness from the Numerical Models and Experiments Comparison

Spec.	Cycles at 2% Drift		Cycles at 5% Drift		Overall Average	
	$K_{rec,num}$ $(k\text{-}in/rad)$	$\frac{K_{rec,num}}{K_{rec,exp}}$	$K_{rec,num}$ $(k\text{-}in/rad)$	$\frac{K_{rec,num}}{K_{rec,exp}}$	$K_{rec,num}$ $(k\text{-}in/rad)$	$\frac{K_{rec,num}}{K_{rec,exp}}$
1	6.99e4	0.94	5.74e4	1.06	6.72e4	1.01
2	7.27e4	0.92	6.05e4	0.88	6.92e4	1.05
3b	6.46e4	0.88	5.23e4	0.95	6.34e4	0.85
3c	7.53e4	0.88	5.68e4	0.94	7.24e4	1.12
5	1.02e5	1.06	8.76e4	1.16	9.47e4	1.17
6	2.17e5	0.80	1.25e5	0.91	2.00e5	0.91

7.3.3 PT Force

Figure 7.5 shows the numerical model and experimental PT force versus drift for the single wall specimens and Figure 7.6 shows the numerical model and experimental PT force versus drift for the coupled wall specimen. Table 7.5 compares the drift when the PT yields for the numerical model and experiments.

The numerical model PT elements generally followed the behavior of the PT bars in the experiments, however there were a few discrepancies. One difference was that the numerical model did not account for the PT relaxation due to seating of the anchorage at the top of the wall. This can be seen in Figures 7.5 and 7.6 for the smaller drift cycles before the PT bar yields. At lower drift cycles, the numerical PT force does not experience as much PT losses compared to the experimental PT force. Because the numerical model did not account for the lower drift PT losses, the PT in the numerical model yielded at lower drifts when compared to the experiments. For Specimens 2, 3c, and 6 the PT bar in the numerical model yielded during the same cycle as in the experiments, but at a lower drift than in the experiments. For Specimens 3b and 5 the PT bar in the numerical model yielded one cycle earlier than in the experiments. For all Specimens, the maximum PT bar force and PT bar stiffness matched well for the numerical model and the experimental results.

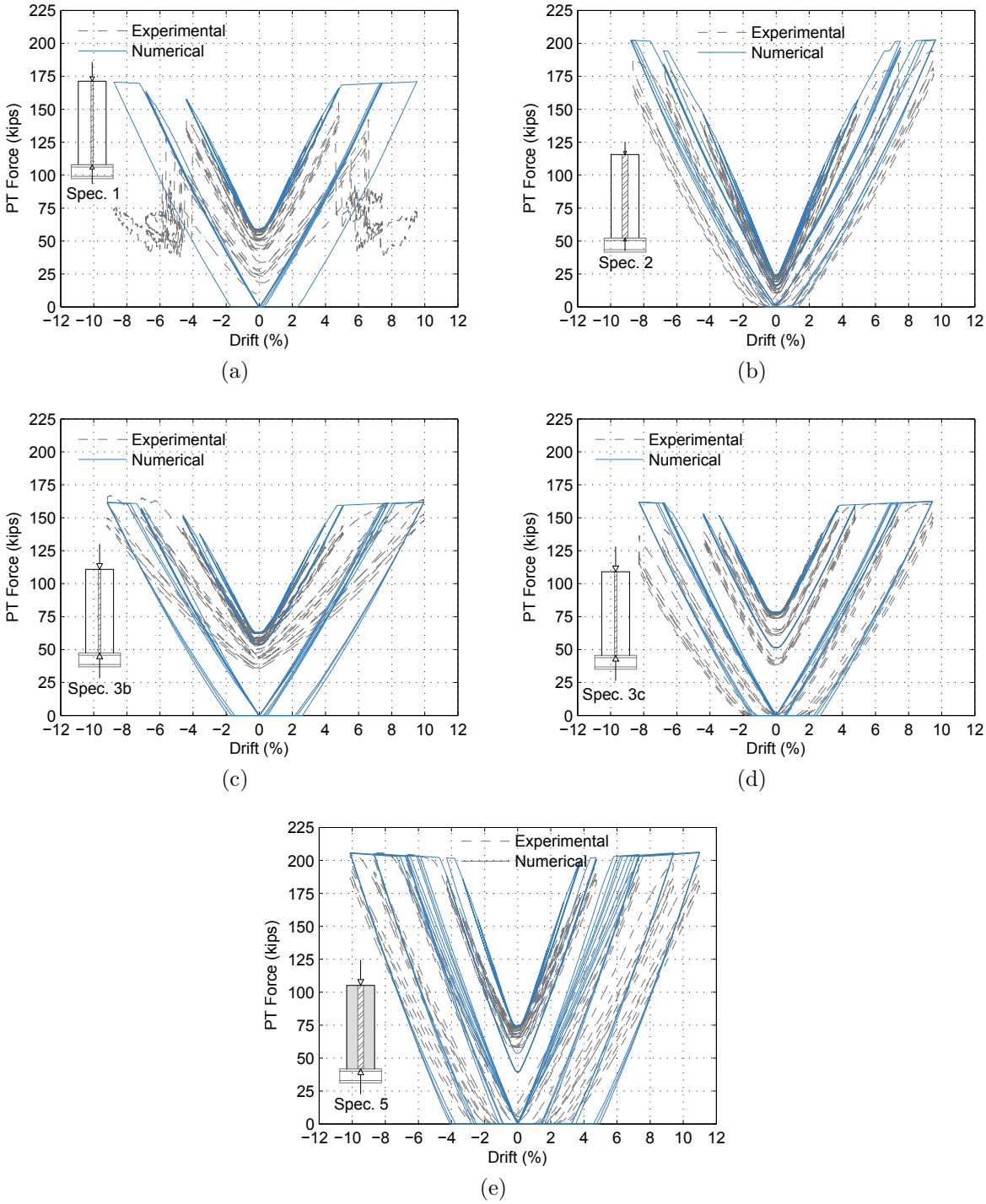

Figure 7.5: Comparison of (a) Specimen 1, (b) Specimen 2, (c) Specimen 3b, (d) Specimen 3c, and (e) Specimen 5 PT Force vs. Drift from the Numerical Models and Experiments

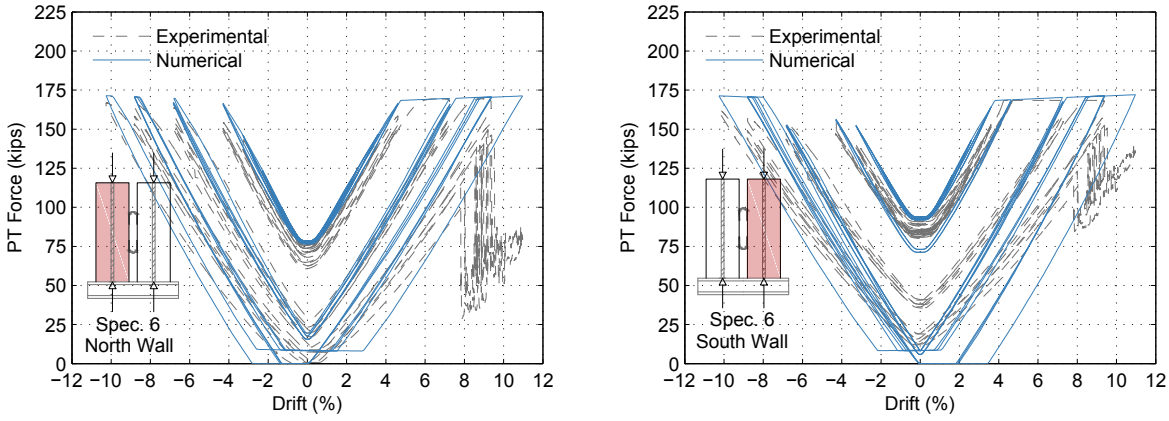

(a) (b)

Figure 7.6: Comparison of Specimen 6 (a) North Wall and (b) South Wall PT Force vs. Drift from the Numerical Models and Experiments

Table 7.5: Comparison of Drift at PT Yield from the Numerical Models and Experiments

	Drift at PT Yield (%)	
Spec.	Numerical	Experimental
1	4.99	N/A
2	7.27	8.60
3b	4.75	7.70
3c	3.81	4.70
5	3.81	6.50
6NW	4.76	6.80
6SW	3.83	4.20

7.3.4 Neutral Axis

The neutral axis (NA) for the numerical models was calculated in a similar manner as the neutral axis location in the experiments. In the numerical model multispring elements, the zero-length springs read a negative value, signifying compression, at the being of the test when the PT element was at it's initial stress. As the displacement history was applied to the load node, one of the edge springs would read a positive value signifying decompression. The NA location was was then known to be between the decompressed spring and the adjacent compressed spring and could be estimated by linearly interpolating between the positive and negative spring displacements to find the location where the displacement would cross zero. As with the experiments, the NA depth was calculated by taking the distance between the NA location and the end of the wall in compression. Figures 7.7 and 7.8 show a comparison of the NA depth versus drift for the numerical models and experimental results.

For all Specimens, the numerical NA depth was underestimated compared to the experimental NA depth. Like the section analysis results presented in Chapter 6, this is most likely due to the simplified elastic-perfectly plastic force-displacement model used to model the inelastic CLT behavior through the multispring elements. The numerical model also predicted wall decompression earlier than the experiments. This may be partly due to the experiments having the furthest potentiometers from the center-line of the wall at 3 inches from the edge of the wall so the decompression at the edge was not captured. For all specimens, at 4% drift the numerical NA depth converged to the experimental NA depth.

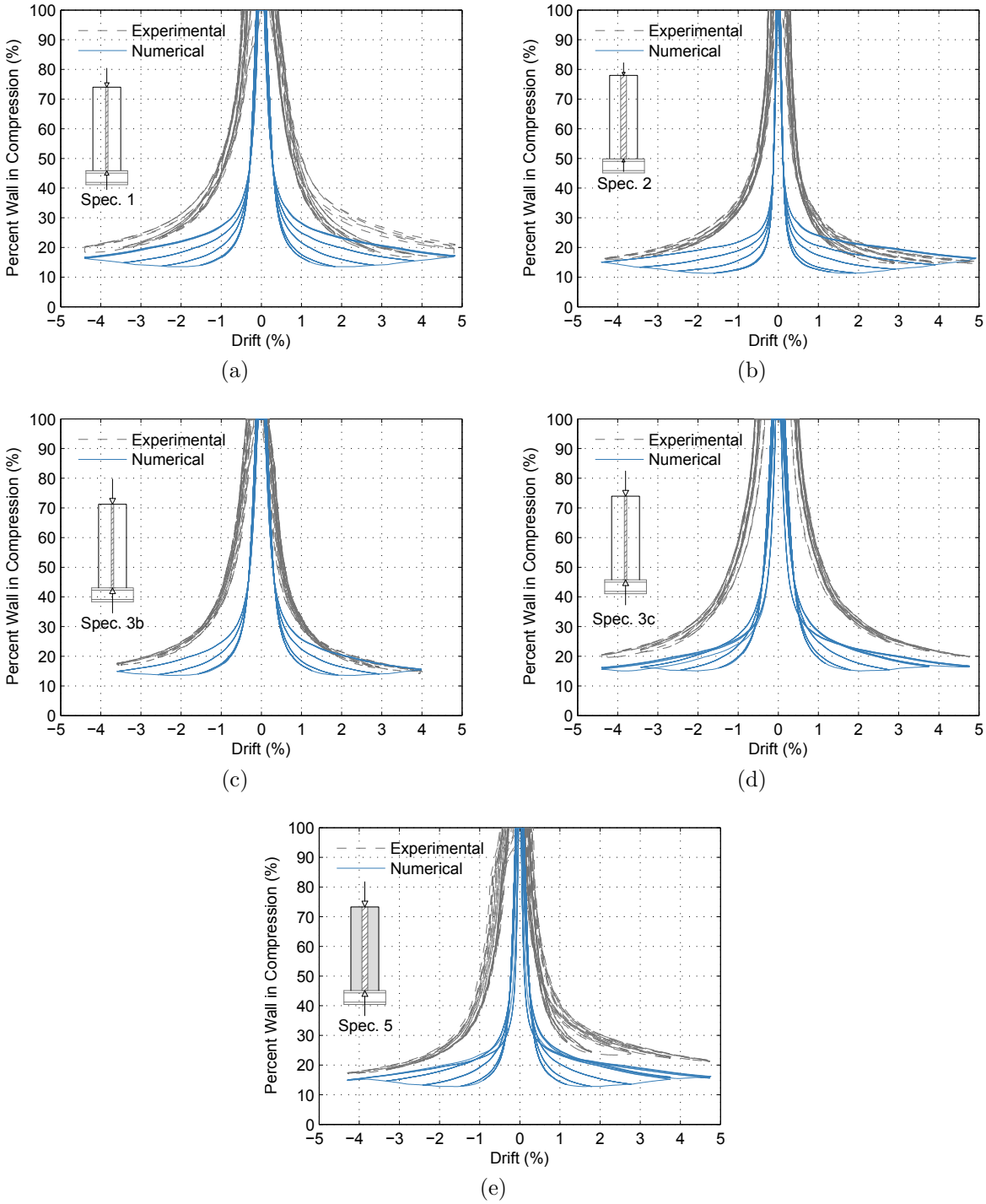

Figure 7.7: Comparison of (a) Specimen 1, (b) Specimen 2, (c) Specimen 3b, (d) Specimen 3c, and (e) Specimen 5 Neutral Axis Depth vs. Drift from the Numerical Models and Experiments

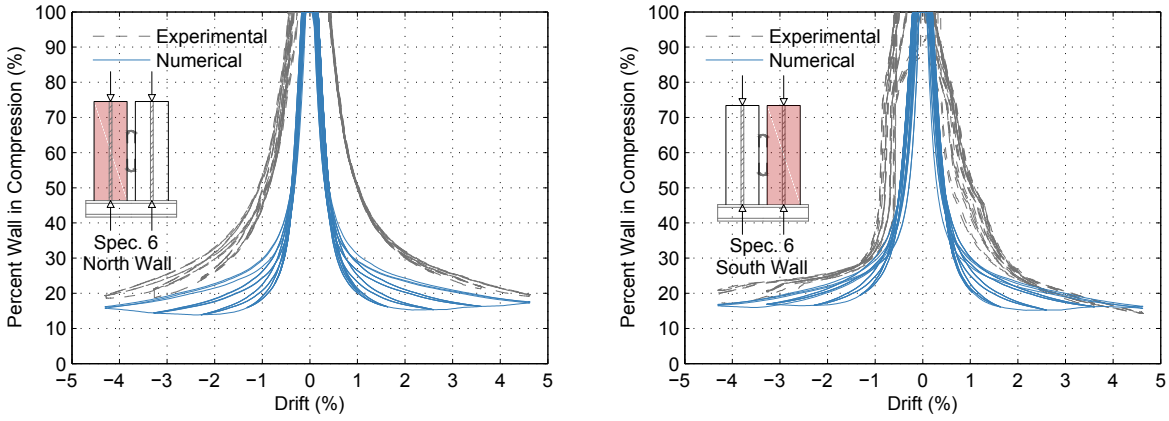

(a) (b)

Figure 7.8: Comparison of Specimen 6 (a) North Wall and (b) South Wall Neutral Axis Depth vs. Drift from the Numerical Models and Experiments

7.3.5 UFPs

Since the UFP relative displacement was measured and the shear force in the UFP was not, the UFP relative displacements were compared and are shown in Figure 7.9 for both the lower and upper UFPs.

Both the lower and upper UFP displacements matched well for the numerical and experimental results. For both UFPs, at large positive drifts the numerical model experienced less displacement compared to the experiments. This may be due to the north wall uplifting more than the south wall because the actuator was connected to the north wall and the actuator load was not transferred evenly to both walls as was in the numerical model. This behavior would cause the UFPs to be displaced more on the north wall. It should be noted that the numerical model UFP displacements should be slightly greater than the experimental UFP displacements because the numerical model UFP nodes were located at the absolute center between the coupled walls instead of at the wall edges where the UFPs were mounted in the experiment. However, this difference in location is small and was not seem in the above numerical-experimental comparison.

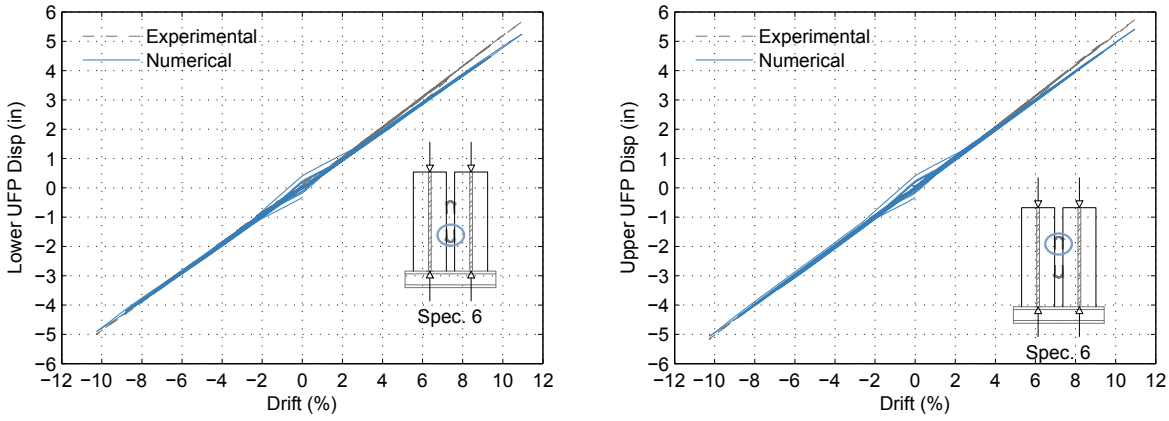

Figure 7.9: Comparison of Specimen 6 (a) Lower UFP and (b) Upper Displacement vs. Drift from the Numerical Models and Experiments

7.4 Application of the Numerical Model

To evaluate the seismic performance of the rocking CLT wall system, numerical models were created for the prototype buildings that were designed in Chapter 3. The building models were subjected to a suite of ground acceleration records that were scaled to represent the three seismic hazard levels used in the design procedure. The results of the nonlinear dynamic analyses were used to evaluate the proposed design procedure.

7.4.1 Description of Building Model

The numerical model for the prototype buildings, shown in Figure 7.10, was two dimensional and represented a line of walls up the building height. Certain stories of the building were designed with rocking CLT walls (rocking stories) while others were designed with hold down walls (hold down stories). Both the dual connection rocking walls and hold down walls (HDWs) were placed in bays by connecting the bottom node of the wall to the floor node below and the top node of the wall to the floor node above. Since all designs used concrete floor diaphragms, the floor nodes were connected with rigid links. Some of the bays did not

have walls because they were not needed or the bay signified a corridor.

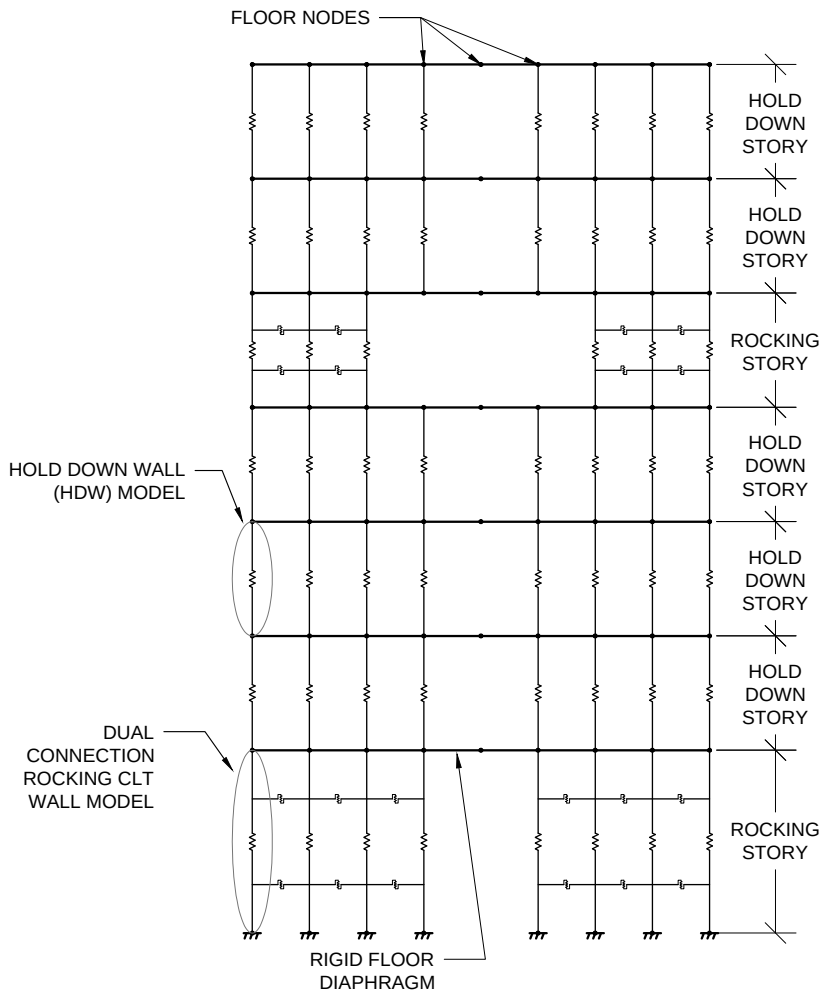

Figure 7.10: Numerical Model for the Prototype Buildings

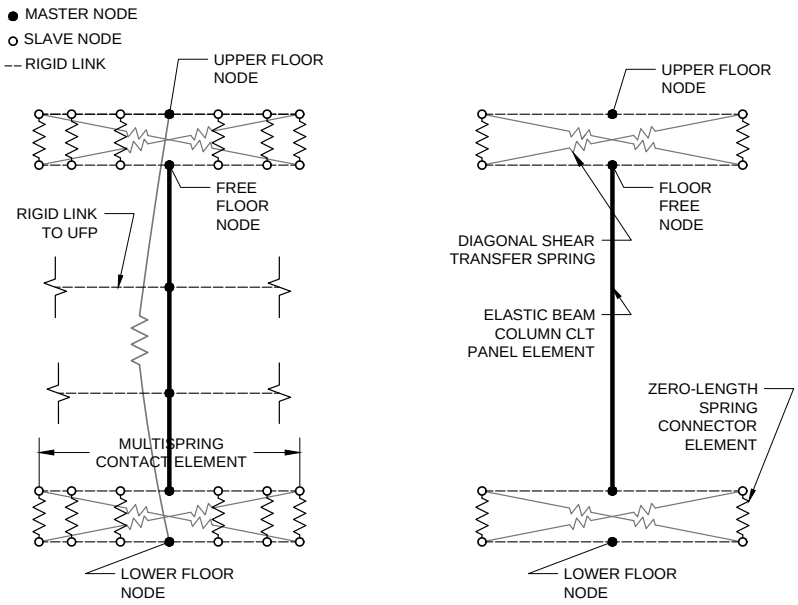

Figure 7.11: Numerical Model for (a) Dual Connection Rocking CLT Wall and (b) Hold Down Wall (HDW)

The dual connection rocking CLT wall, shown in Figure 7.11a, was similar to the single connection rocking wall except it had another multispring contact element to allow for a PT connection at the top of the wall. The HDWs were designed using the procedure outlined in the CLT Handbook [van de Lindt et al., 2013]. The HDW model, shown in Figure 7.11b, consisted of (1) a displacement-based elastic beam column element with axial, flexural, and shear deformations to model the CLT wall panel, (2) zero-length springs to model the hold downs, and (3) diagonal shear transfer springs. The hold down springs used a bi-liner material model (ElasticBilin) that had high stiffness in compression and stiffness equal to the hold downs in tension. The hold downs were rigidly offset from a free node that connected to the CLT wall element.

7.4.2 Wind and Gravity Loads, Seismic Masses, and Damping

Separate analyses were done on each model to determine if any of the rocking walls uplifted under wind loading. The wind loads applied were determined from ASCE [2010]. The Gravity loads ($1.0DL + 0.5LL$) were applied to each floor node equal to the tributary area of the walls beneath. The seismic mass was distributed equally to each node on each floor. Damping was modeled using 2% Rayleigh damping in the first and third modes [Chopra, 2007]. This method created the damping matrix from the stiffness- and mass-proportional damping matrices, where the last committed stiffness matrix was used.

Because of the need for adequate stiffness and strength at the hold down stories, the majority of walls were modeled. A P-Delta column was not used because the tributary gravitational load for each wall was minimal and thus P-Delta effects were minimal. Analyses showed that at 5% drift P-Delta effects would only contribute to 1 to 2% of the total overturning movement.

7.4.3 Analysis Options

During the analyses, the constraint equations were enforced using the OpenSees Lagrange constraint handler object. The OpenSees RCM number object was used to provide mapping between the nodal degrees-of-freedom and the equation numbers using the reverse Cuthill-McKee scheme to order the matrix equations. The UmfPack solver object was used to solve the system of linear equations, and the Newmark integrator object was used to determine the predictive step for time t+dt using the average acceleration method, where the analytical time step, dt, was assumed to be the time step of the inputted ground motion.

The Newton-Raphson solution algorithm with a line search (NewtonLineSearch in OpenSees) was first used to iterate to a converged solution, where the energy increment test (EnergyIncr object in OpenSees) was used to determine convergence within a tolerance of 0.0001. If the solution failed to converge within a set number of iterations, the following steps were taken until the solution converged:

1. The time step, dt, was reduced by a factor of 5.
2. The time step, dt, was reduced by a factor of 10.
3. The time step, dt, was reduced by a factor of 20.
4. The time step, dt, was reduced by a factor of 40.
5. The Newton-Raphson solution algorithm using the initial stiffness in subsequent iterations was used.
6. The Broyden solution algorithm was used.
7. The Krylov-Newton solution algorithm was used.

Using this procedure, convergence was achieved at every time step in the analyses presented later in this chapter. Additional information on the various components of the numerical analysis methods used can be found at the OpenSees wiki (www.opensees.berkeley.edu/wiki) [Mazzoni et al., 2009].

7.4.4 Ground Motion Records

The far-field ground motion record set compiled by ATC [2009b] was used for the nonlinear dynamic analyses of the prototype buildings. All ground motion records in the set were from the Pacific Engineering Research (PEER) Research NGA Ground Motion Database. Table 7.6 summarizes the details of the individual ground motions. The set consisted of 22 earthquake records, each with 2 horizontal components acting perpendicular to one another, making for a total of 44 ground acceleration records.

The spectral accelerations for the three seismic hazard levels, as described in Section 3.4.1, were obtained from the United States Geological Survey (USGS) uniform hazard curves for Seattle, Washington [USGS, 2015]. For each seismic hazard, the ground motions were

individually scaled such that the median of the ground motion's spectral accelerations was as close as possible to the hazard spectral acceleration for a range of periods of to $0.3T$ to $1.5T$, where T is the first natural period of the building. The first mode periods for the building models had a small variance, allowing for a single set of scale factors to be found for all building designs. The hazard spectral acceleration and the median, 16th, and 84th percentiles of the scaled ground motion's spectral accelerations are shown in Figure 7.12 for each hazard level. A free vibration duration equal to $5T$ was added onto each ground motion for computation of residual drifts. Each building model was run with each of the 44 scaled ground acceleration records for the three seismic hazards.

Table 7.6: Ground Motion Details ATC [2009b]

PEER NGA Record No.	Earthquake Name	Year	Mag.	Duration (g)	PGA (sec)	Scale Factor 50/50	10/50	2/50
953	Northridge	1994	6.7	0.52	30.0	0.35	0.95	1.49
960	Northridge	1994	6.7	0.48	20.0	0.37	0.89	1.82
1602	Duzce, Turkey	1999	7.1	0.82	55.9	0.33	0.79	1.45
1787	Hector Mine	1999	7.1	0.34	45.3	0.51	1.02	1.96
169	Imperial Valley	1979	6.5	0.35	99.9	0.55	1.56	2.64
174	Imperial Valley	1979	6.5	0.38	39.0	0.48	1.23	2.01
1111	Kobe, Japan	1995	6.9	0.51	41.0	0.35	0.65	1.56
1116	Kobe, Japan	1995	6.9	0.24	41.0	0.58	1.07	3.33
1158	Kocaeli, Turkey	1999	7.5	0.36	27.2	0.37	1.16	2.27
1148	Kocaeli, Turkey	1999	7.5	0.22	30.0	0.90	1.85	4.59
900	Landers	1992	7.3	0.24	44.0	0.67	1.45	3.25
848	Landers	1992	7.3	0.42	28.0	0.59	1.25	2.21
752	Loma Prieta	1989	6.9	0.53	40.0	0.45	1.11	1.75
767	Loma Prieta	1989	6.9	0.56	40.0	0.35	1.35	1.85
1633	Manjil, Iran	1990	7.4	0.51	53.5	0.24	1.12	2.15
721	Superstition Hills	1987	6.5	0.36	40.0	0.43	1.56	3.55
725	Superstition Hills	1987	6.5	0.45	22.3	0.58	1.12	3.12
829	Cape Mendocino	1992	7.0	0.55	36.0	0.56	1.00	1.67
1244	Chi-Chi, Taiwan	1999	7.6	0.44	90.0	0.25	1.15	2.04
1485	Chi-Chi, Taiwan	1999	7.6	0.51	90.0	0.45	1.12	2.67
68	San Fernando	1971	6.6	0.21	28.0	0.95	1.51	4.75
125	Friuli, Italy	1976	6.5	0.35	36.4	0.65	1.35	3.10

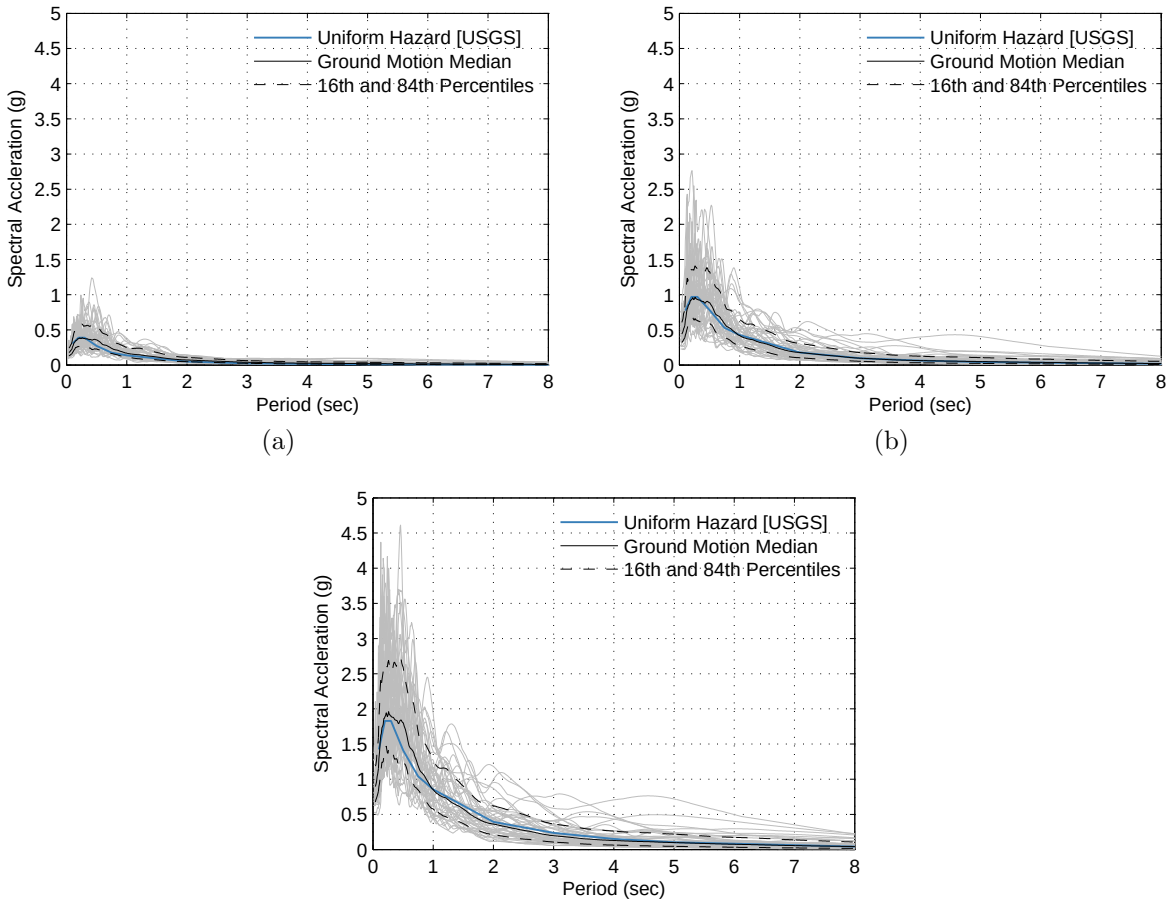

Figure 7.12: Spectral Accelerations for Hazards and Scaled Ground Motions Having a Probability of Exceedence of (a) 50% in 50 Years, (b) 10% in 50 Years, and (c) 2% in 50 Years [USGS, 2015]

7.4.5 Nonlinear Dynamic Analysis Results

Response Histories

Figure 7.13 shows the typical response of the 8-story building with a rocking story at the 5th story under a 10% in 50 year earthquake, which represents an approximation of a DBE. Figure 7.14 shows the typical response of the 14-story building with a rocking story at the 8th story under a 10% in 50 year earthquake. The overall system response, roof displacement versus time, rocking wall story response, and PT force for the walls outer walls in each rocking story normalized by the PT yield force is shown. In the overall response and story response, the stiffness decreases as the walls decompress and energy dissipation can be seen from the UFPs. The overall response does not show a lot of dissipation from the UFPs. This should be considered in modification of the design procedure. For both models the PT force in the outer walls at the first story is asymmetric because of the effect of the global overturning and floor rotation. The system response for both models shows the building recentering after the analyses were complete.

Figures 7.15 and 7.16 show the response of the 8-story building with a rocking story at the 5th story and the 14-story building with a rocking story at 8th story a 2% in 50 year earthquake respectively. For both models, the system response shows a flag shaped hysteresis. The flag shape hysteresis is more prominent in the base shear versus drift response compared to the overturning moment versus drift response. The individual rocking stories show more dissipation than the overall response because these were the stories that had energy dissipation from the CLT panels and the UFP devices. The other stories used hold down walls that remained elastic throughout the analyses. For both models, the ground accelerations were greater in the negative direction and thus some of the PT bars yielded in that direction, though the PT bars still maintained force through the analyses.

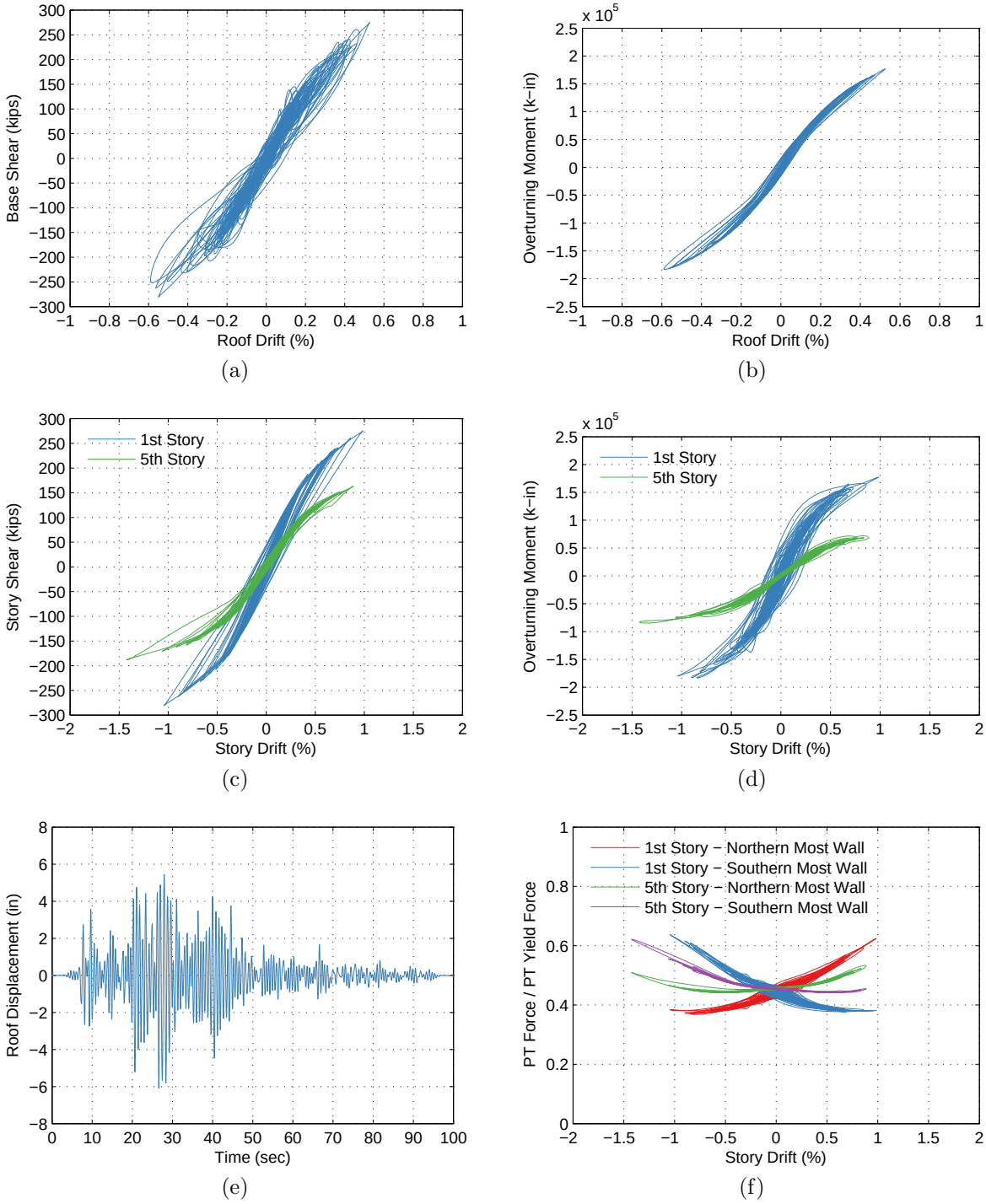

Figure 7.13: (a) Base Shear Response, (b) Overturning Moment Response, (c) Rocking Story Shears, (d) Rocking Story Moments, (e) Roof Displacement History, and (f) Normalized PT Response of Model R8-1.5 Under a 10% in 50 Year Ground Motion (PEER NGA 1148) Representing a DBE

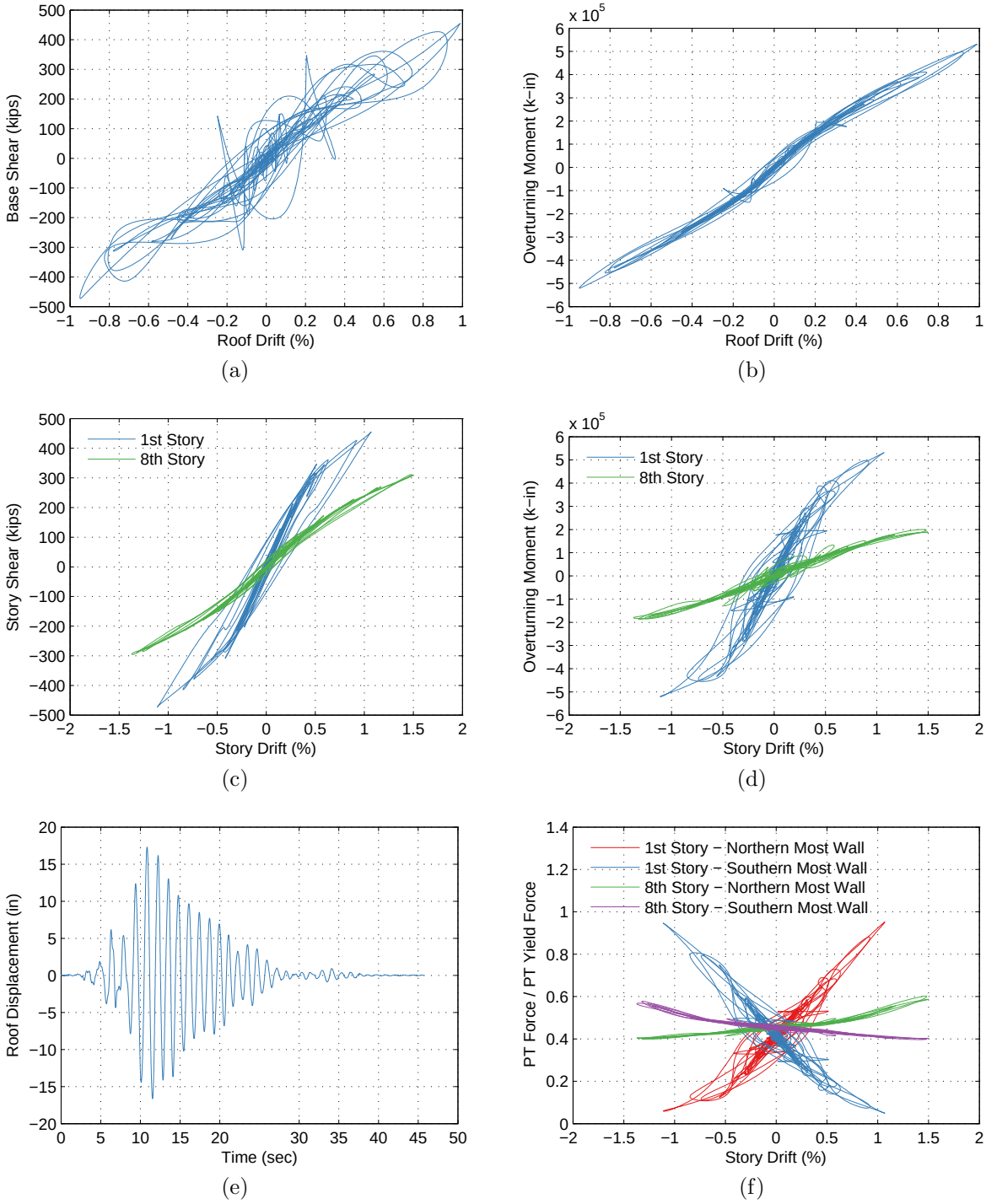

Figure 7.14: (a) Base Shear Response, (b) Overturning Moment Response, (c) Rocking Story Shears, (d) Rocking Story Moments, (e) Roof Displacement History, and (f) Normalized PT Response of Model R14-1.8 Under a 10% in 50 Year Ground Motion (PEER NGA 752) Representing a DBE

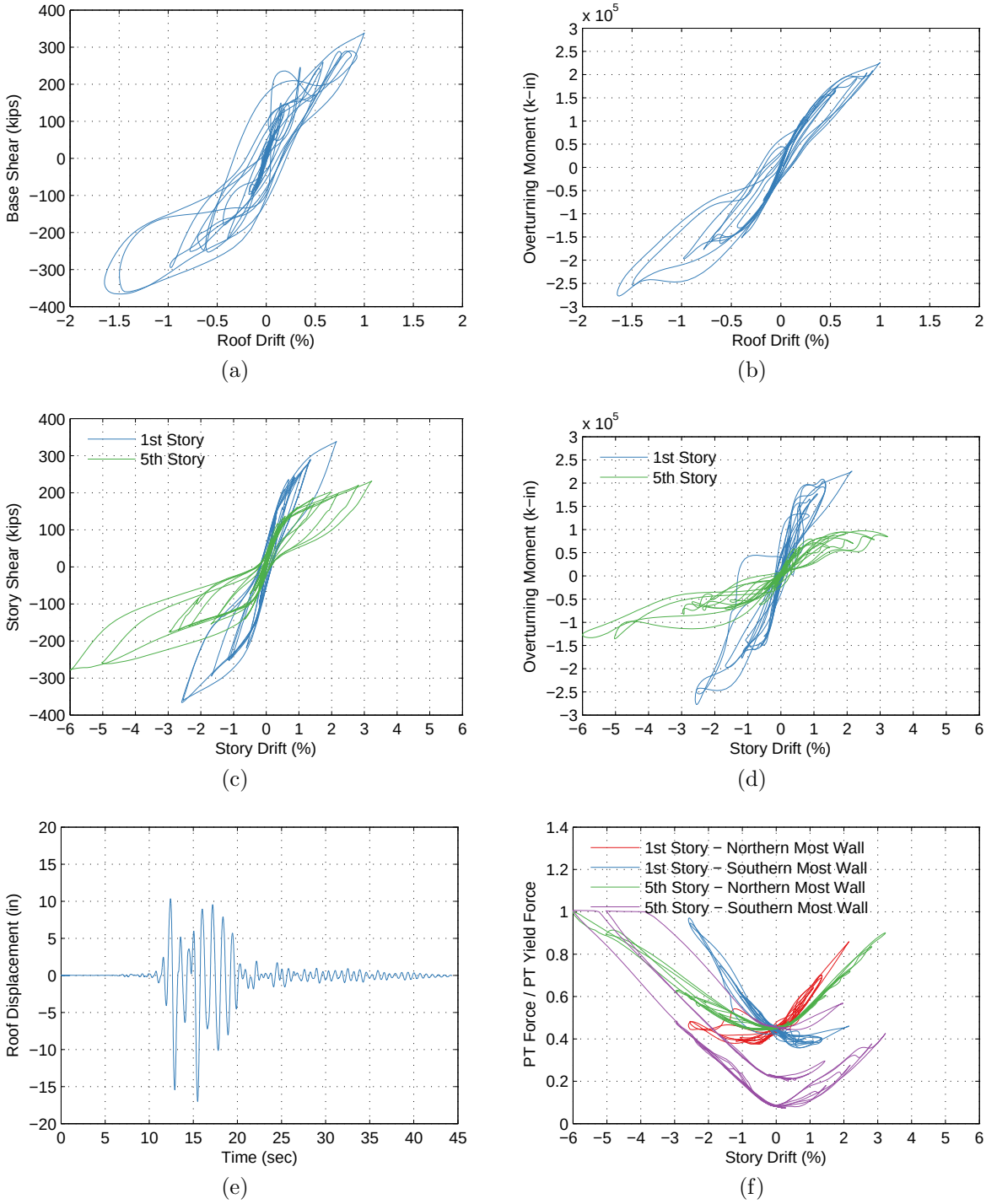

Figure 7.15: (a) Base Shear Response, (b) Overturning Moment Response, (c) Rocking Story Shears, (d) Rocking Story Moments, (e) Roof Displacement History, and (f) Normalized PT Response of Model R8-1.5 Under a 2% in 50 Year Ground Motion (PEER NGA 1111) Representing the MCE

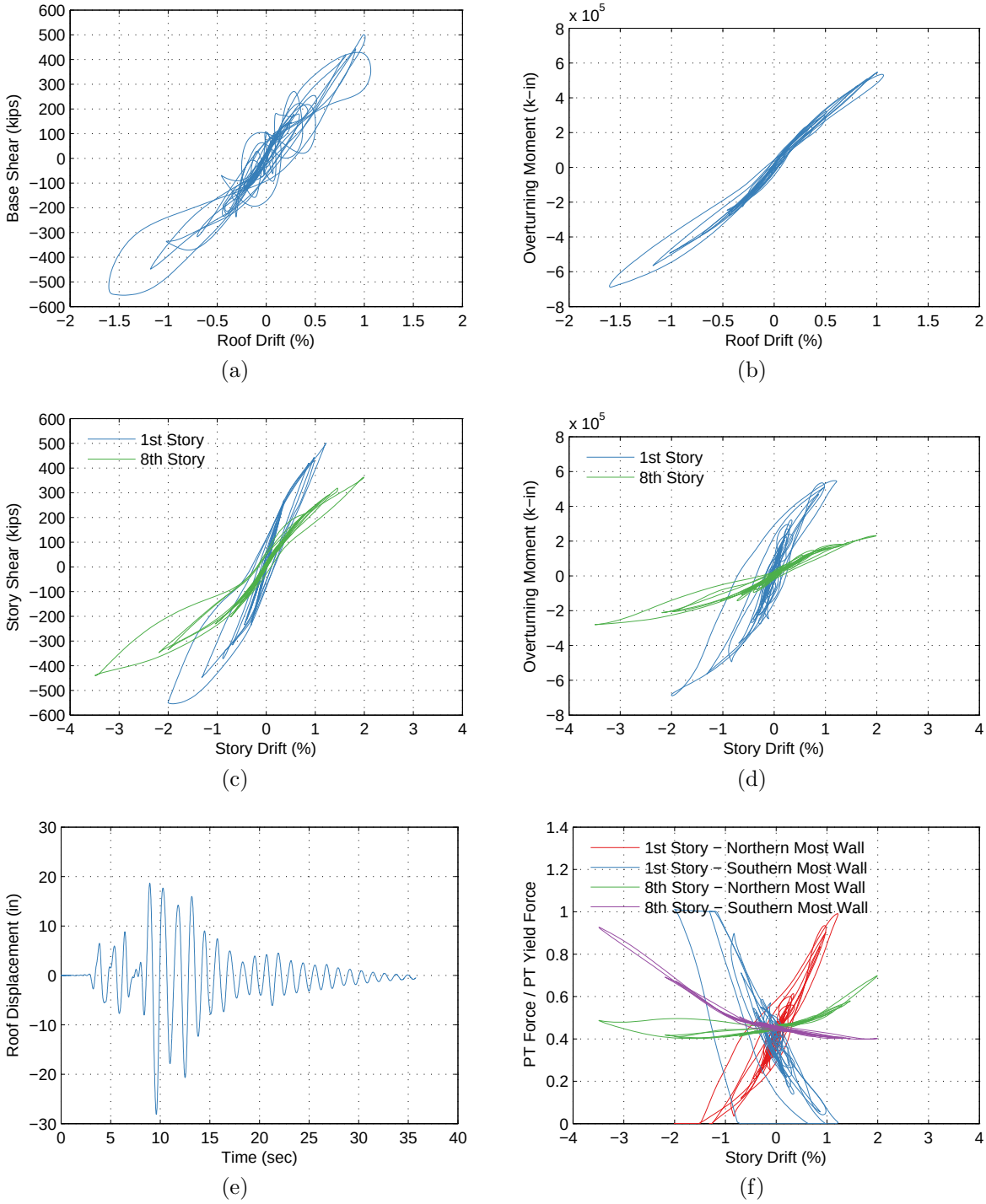

Figure 7.16: (a) Base Shear Response, (b) Overturning Moment Response, (c) Rocking Story Shears, (d) Rocking Story Moments, (e) Roof Displacement History, and (f) Normalized PT Response of Model R14-1.8 Under a 2% in 50 Year Ground Motion (PEER NGA 953) Representing the MCE

Response Parameters

Response parameters were used to evaluate the building performance throughout the analyses. Two drift parameters and five component parameters were chosen. The component parameters were expressed as ratios by comparing the value to a yield criteria explained below. The response parameters evaluated during the dynamic analyses were:

- Peak story drift, $\theta_{s,max}$
- Maximum Residual story drift, θ_{res}
- Maximum UFP force normalized by UFP plastic force, $V_{UFP,max}/F_{UFP,p}$
- Maximum PT bar strain normalized by PT bar yield strain, $\epsilon_{p,max}/\epsilon_{py}$
- Maximum CLT strain normalized by CLT crushing strain, $\epsilon_{CLT,max}/\epsilon_{CLT,u}$
- Maximum CLT displacement normalized by CLT crushing displacement, $\Delta_{CLT,max}/\epsilon_{CLT,u}$
- Maximum hold down connector displacement normalized by the yield displacement of the connector, $\Delta_{conn,max}/\Delta_{conn,y}$

The CLT had two response parameters, one based on a CLT crushing strain and one based on a CLT crushing displacment, because of the uncertainty of CLT crushing. The crushing strain of the CLT was taken to be 0.16 $\frac{in}{in}$ which was the average strain at crushing of the CLT specimens in the material tests in Appendix A. In the numerical models, the CLT strain along a rocking wall cross-section was calculated by dividing each spring in a multispring element by the plastic hinge length. The crushing displacement was taken to be 0.174 inches which was the average displacement at crushing of the CLT specimens in the material tests in Appendix A. In the numerical models, the CLT displacement along a rocking wall cross-section was taken to be the maximum spring negative (compression) displacement. The strain

and displacement in CLT walls in the HDW stories was not accounted for. The connector yield displacement was taken from values in the CLT Handbook [van de Lindt et al., 2013].

Tables 7.7 and 7.8 show the statistical results (median, $mu_{\frac{1}{2}}$, and 84th percentile) for the 8-story and 14-story models respectively for the three hazard levels for the maximum story drift, maximum residual drift, maximum PT Ratio, maximum CLT Ratios, and maximum HD ratio. The median and 84th percentile story and residual drift values for each story are plotted for the 8-story and 14-story models in Figures 7.17- 7.20. The median and 84th percentile component values are plotted for the 8-story and 14-story models in Figures 7.21 and 7.22 respectively. Maximum and residual story drifts were evaluated for each story separately. Maximum UFP ratio, PT ratio, and CLT ratio were evaluated for each rocking story separately and maximum HD ratio was evaluated for each set of the HDW stories between rocking stories. For calculating the statistical results, all the data was fitted to log normal distributions. Note that the model name, as described in Tables 3.2 and 3.3, is given as the number of stories followed by each rocking story number.

The response parameters were used to evaluate compliance with performance objectives associated with the hazard levels (PO 2-PO 4). Tables 7.9 and 7.10 show the number of response criteria that did not meet the specific performance criteria. The maximum story drift limit was 0.5% drift for PO 2, 2% for PO 3, and 8.4% for PO 4. The drift limit for PO 4 was calculated by averaging the drift at specimen failure for each experiment. The residual drift limit was 0.2%. For all ratio parameters, a value greater than one indicated failure. The UFP ratio was used to evaluate PO 2. The PT ratio, CLT ratios, and HD ratio were used to evaluate PO 4.

Table 7.7: Summarized Response Parameters From Nonlinear Analyses for 8-Story Models

		Response	50% in 50 yr		10% in 50 yr		2% in 50 yr	
Model	Story	Parameter	$\mu_{1/2}$	84%	$\mu_{1/2}$	84%	$\mu_{1/2}$	84%
R8-1	1	θ_s	0.26	0.41	0.77	1.36	2.34	4.15
	1	θ_r	0.001	0.003	0.005	0.012	0.014	0.055
	1	V_{UFP}	0.84	1.10	1.12	1.22	1.43	1.71
	1	ϵ_p	0.49	0.52	0.60	0.71	0.93	1.26
	1	ϵ_{CLT}	0.14	0.20	0.37	0.69	1.69	4.41
	1	Δ_{CLT}	0.11	0.14	0.27	0.51	1.24	3.05
	2-8	Δ_{HD}	0.14	0.42	0.54	0.83	0.96	1.20
R8-1.5	1	θ_s	0.24	0.37	0.69	1.19	1.80	3.05
	1	θ_r	0.001	0.004	0.004	0.014	0.012	0.038
	1	V_{UFP}	0.82	1.06	1.11	1.20	1.34	1.54
	1	ϵ_p	0.48	0.51	0.58	0.68	0.82	1.07
	1	ϵ_{CLT}	0.14	0.18	0.33	0.61	1.33	2.62
	1	Δ_{CLT}	0.10	0.13	0.24	0.45	1.16	1.93
	2-4	Δ_{HD}	0.13	0.41	0.49	0.71	0.84	1.03
	5	θ_s	0.30	0.47	0.89	1.49	2.70	4.67
	5	θ_r	0.001	0.005	0.005	0.016	0.009	0.031
	5	V_{UFP}	0.73	1.00	1.09	1.20	1.43	1.71
	5	ϵ_p	0.47	0.49	0.55	0.64	0.86	1.16
	5	ϵ_{CLT}	0.41	0.14	0.30	0.57	1.33	2.88
	5	Δ_{CLT}	0.08	0.10	0.22	0.42	0.98	2.12
	6-8	Δ_{HD}	0.04	0.15	0.19	0.27	0.37	0.48

Table 7.8: Summarized Response Parameters From Nonlinear Analyses for 14-Story Models

		Response	50% in 50 yr		10% in 50 yr		2% in 50 yr	
Model	Story	Parameter	$\mu_{1/2}$	84%	$\mu_{1/2}$	84%	$\mu_{1/2}$	84%
R14-1	1	θ_s	0.16	0.24	0.46	0.84	1.43	3.07
	1	θ_r	0.001	0.004	0.004	0.015	0.021	0.090
	1	V_{UFP}	0.47	0.70	0.93	1.21	1.25	1.48
	1	ϵ_p	0.50	0.54	0.66	0.84	1.21	2.14
	1	ϵ_{CLT}	0.14	0.18	0.26	0.41	1.04	3.50
	1	Δ_{CLT}	0.11	0.13	0.19	0.30	0.76	2.58
	2-14	Δ_{HD}	0.08	0.34	0.46	0.87	0.95	1.37
R14-1.6	1	θ_s	0.16	0.24	0.44	0.79	1.32	2.70
	1	θ_r	0.001	0.003	0.011	0.006	0.013	0.081
	1	V_{UFP}	0.46	0.70	0.93	1.20	1.22	1.43
	1	ϵ_p	0.50	0.54	0.65	0.82	1.12	1.89
	1	ϵ_{CLT}	0.14	0.17	0.26	0.38	0.89	2.73
	1	Δ_{CLT}	0.11	0.13	0.19	0.28	0.66	2.01
	2-5	Δ_{HD}	0.07	0.35	0.45	0.84	0.92	1.32
	6	θ_s	0.24	0.40	0.65	1.11	1.46	2.50
	6	θ_r	0.001	0.006	0.003	0.011	0.018	0.049
	6	V_{UFP}	0.30	0.48	0.70	1.07	1.06	1.25
	6	ϵ_p	0.47	0.48	0.53	0.60	0.74	1.05
	6	ϵ_{CLT}	0.11	0.13	0.19	0.28	0.42	0.85
	6	Δ_{CLT}	0.08	0.10	0.14	0.20	0.31	0.63
	7-14	Δ_{HD}	0.03	0.23	0.30	0.59	0.66	0.93
R14-1.8	1	θ_s	0.16	0.24	0.44	0.79	1.29	2.55
	1	θ_r	0.001	0.004	0.003	0.012	0.015	0.074
	1	V_{UFP}	0.47	0.70	0.93	1.20	1.22	1.40
	1	ϵ_p	0.50	0.54	0.65	0.81	1.10	1.82
	1	ϵ_{CLT}	0.14	0.17	0.26	0.38	0.85	2.49

Continued on next page

Table 7.8 – Continued from previous page

Model	Story	Response Parameter	50% in 50 yr		10% in 50 yr		2% in 50 yr	
			$\mu_{1/2}$	84%	$\mu_{1/2}$	84%	$\mu_{1/2}$	84%
	1	Δ_{CLT}	0.11	0.13	0.19	0.28	0.63	1.83
	2-7	Δ_{HD}	0.08	0.35	0.45	0.84	0.91	1.32
	8	θ_s	0.27	0.44	0.74	1.29	1.89	3.63
	8	θ_r	0.001	0.006	0.004	0.014	0.020	0.071
	8	V_{UFP}	0.38	0.59	0.80	1.13	1.17	1.38
	8	ϵ_p	0.47	0.48	0.52	0.58	0.73	1.01
	8	ϵ_{CLT}	0.10	0.12	0.18	0.30	0.61	1.77
	8	Δ_{CLT}	0.07	0.09	0.14	0.22	0.45	1.30
	9-14	Δ_{HD}	0.02	0.18	0.26	0.52	0.59	0.81
R14-1.10	1	θ_s	0.16	0.24	0.43	0.74	1.02	1.71
	1	θ_r	0.001	0.004	0.003	0.016	0.010	0.047
	1	V_{UFP}	0.47	0.70	0.93	1.18	1.15	1.25
	1	ϵ_p	0.50	0.54	0.64	0.77	0.91	1.24
	1	ϵ_{CLT}	0.14	0.17	0.25	0.35	0.56	1.13
	1	Δ_{CLT}	0.11	0.13	0.18	0.26	0.41	0.83
	2-9	Δ_{HD}	0.07	0.34	0.43	0.78	0.82	1.17
	10	θ_s	0.34	0.56	1.23	2.62	4.86	11.22
	10	θ_r	0.001	0.008	0.006	0.021	0.029	0.094
	10	V_{UFP}	0.62	0.93	1.09	1.36	1.75	2.53
	10	ϵ_p	0.47	0.48	0.61	0.80	1.33	2.63
	10	ϵ_{CLT}	0.13	0.16	0.45	1.16	3.02	10.03
	10	Δ_{CLT}	0.09	0.12	0.33	0.86	2.22	7.38
	11-14	Δ_{HD}	0.02	0.14	0.24	0.44	0.56	0.87

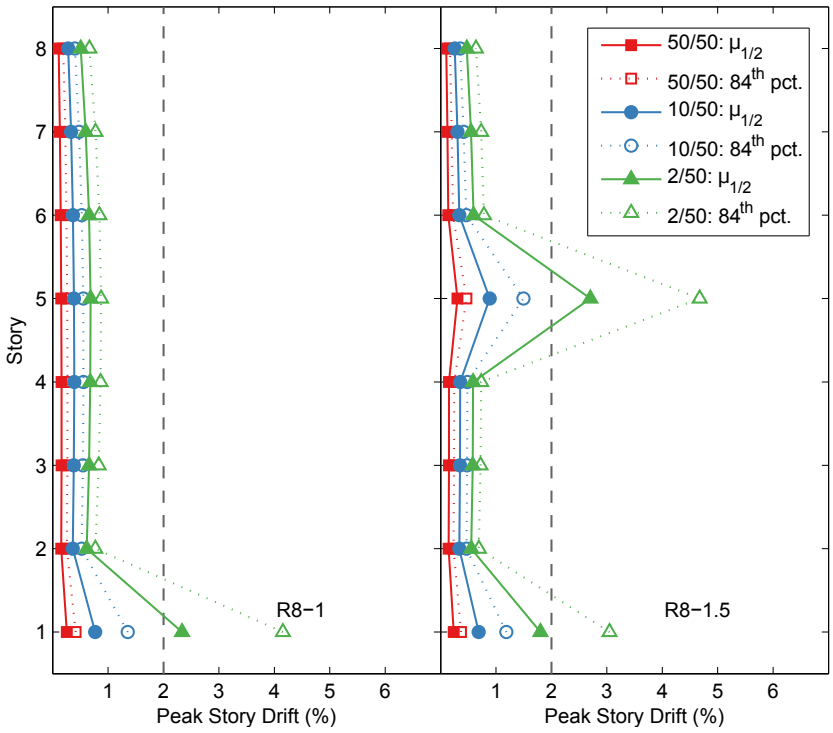

Figure 7.17: Peak Story Drift Median ($\mu_{1/2}$) and 84th Percentile Response for 8-Story Model

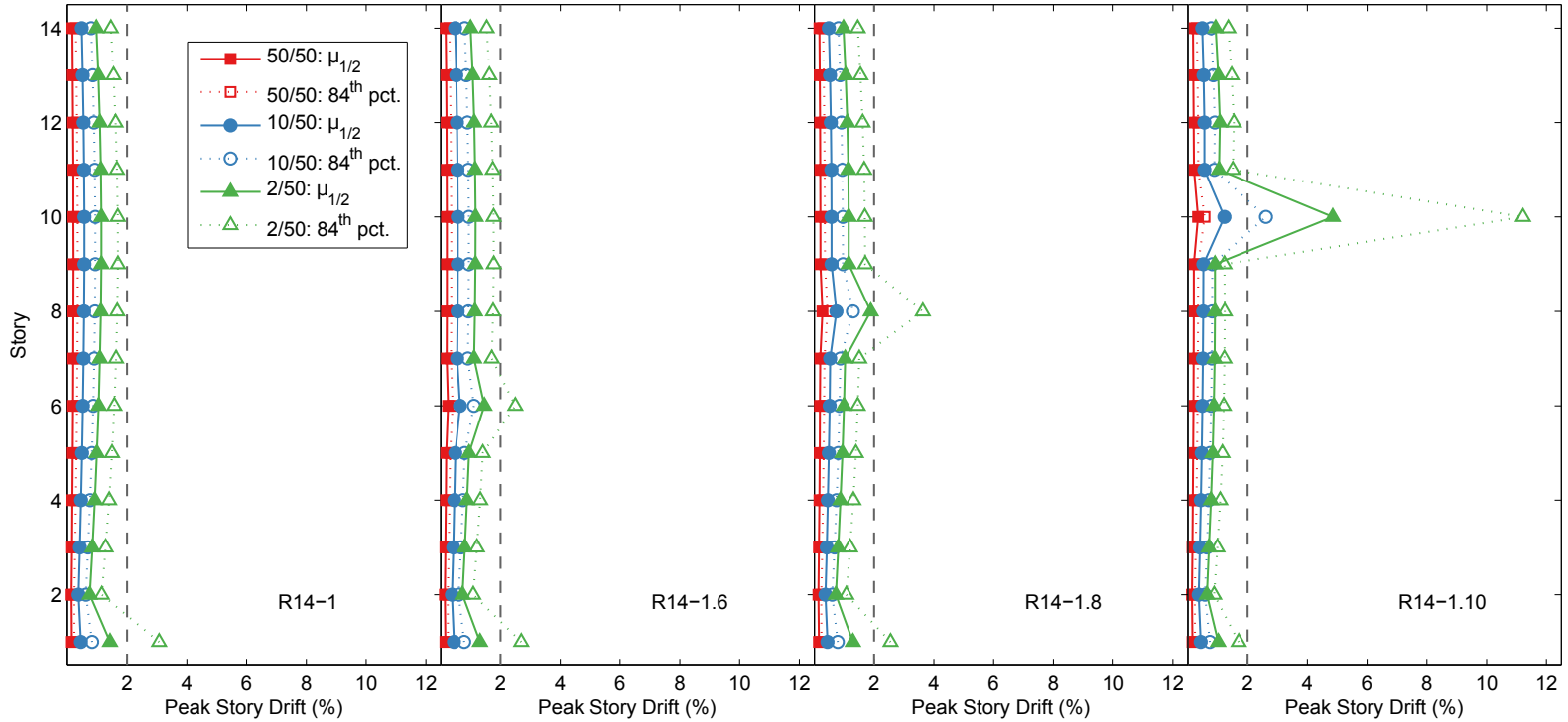

Figure 7.18: Peak Story Drift Median ($\mu_{1/2}$) and 84th Percentile Response for 14-Story Models

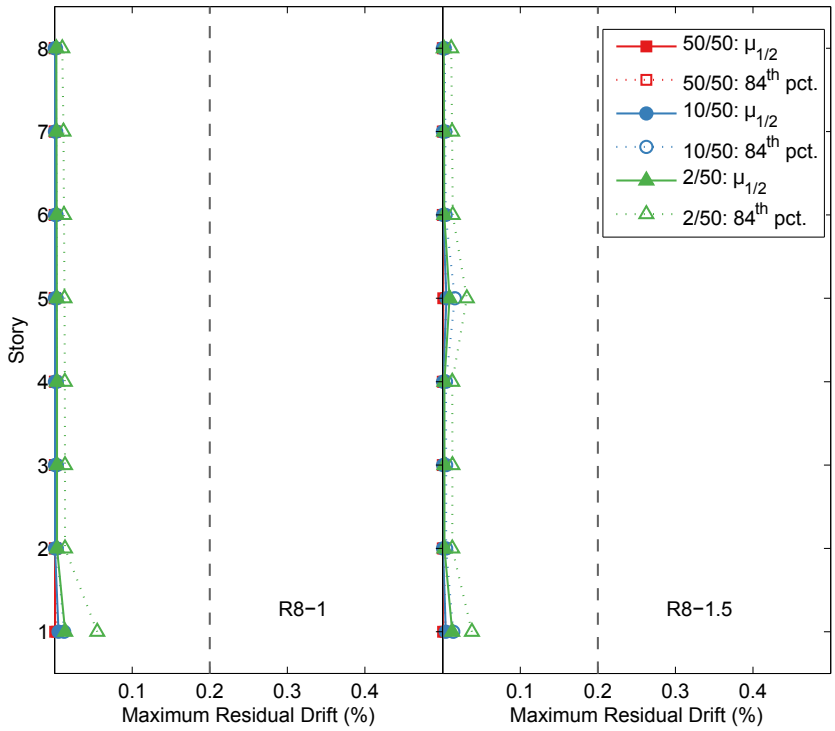

Figure 7.19: Maximum Residual Drift Median ($\mu_{1/2}$) and 84th Percentile Response for 8-Story Model

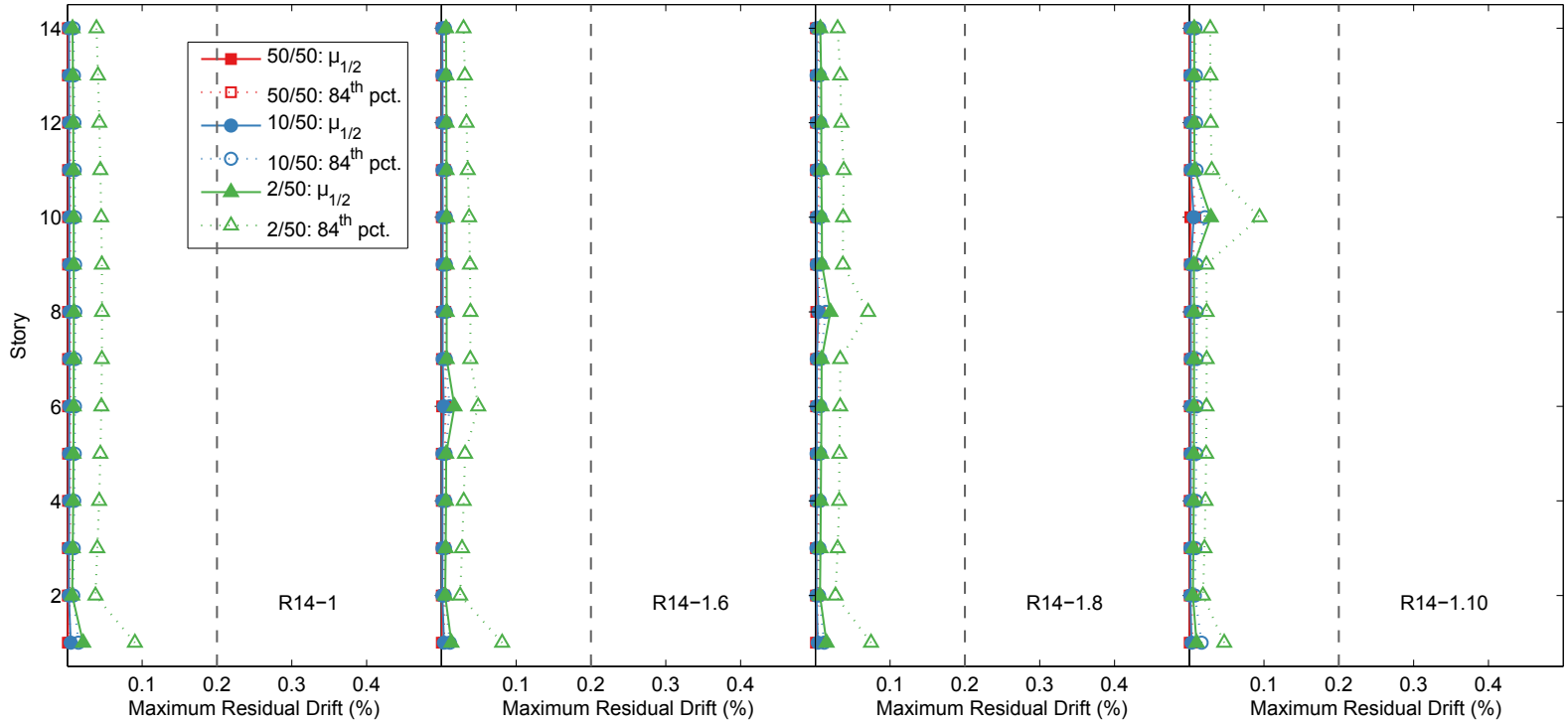

Figure 7.20: Maximum Residual Drift Median ($\mu_{1/2}$) and 84th Percentile Response for 14-Story Models

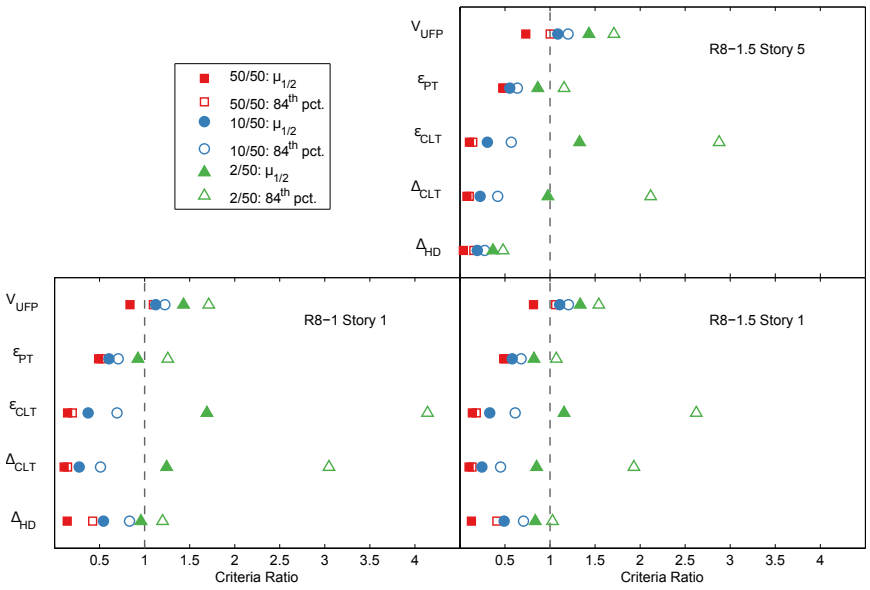

Figure 7.21: Component Criteria Median ($\mu_{1/2}$) and 84th Percentile Response for 8-Story Model

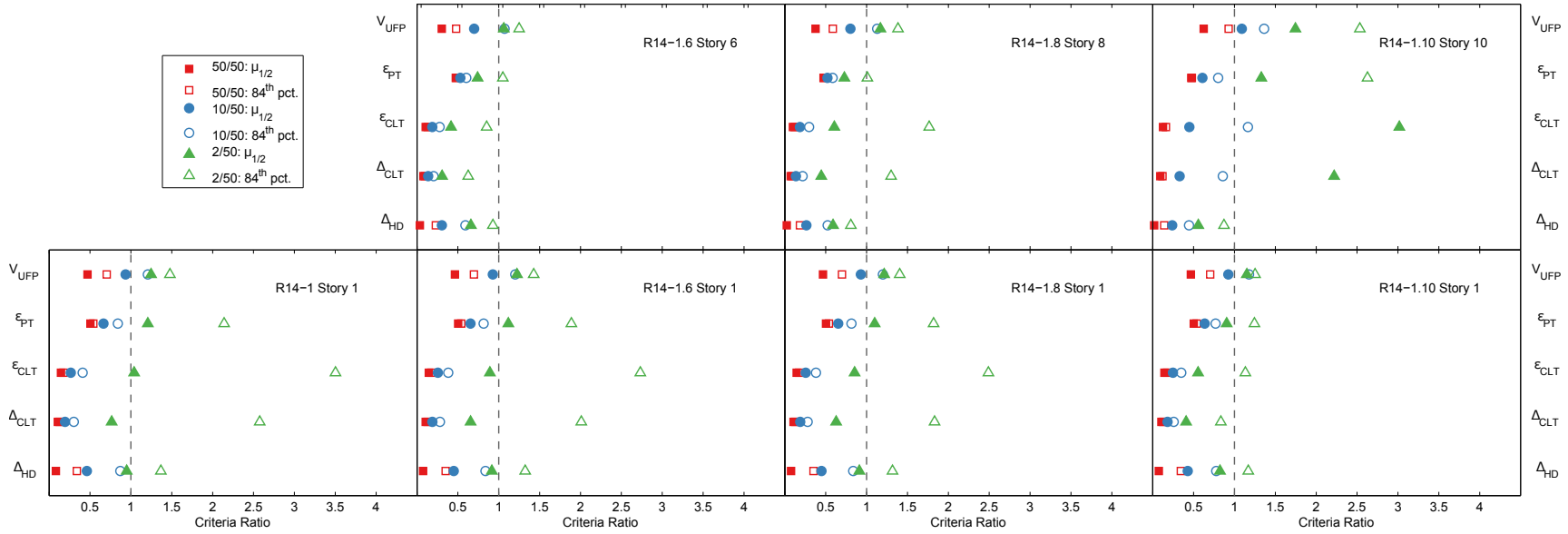

Figure 7.22: Component Criteria Drift Median ($\mu_{1/2}$) and 84th Percentile Response for 14-Story Models

Table 7.9: Number of Analyses Exceeding Yield Criteria for 8-Story Models

Model	Story	Response Criteria	50% in 50 yr	10% in 50 yr	2% in 50 yr
R8-1	1	$N_{\theta_s} > \theta_{lim,s}$	5	1	0
	1	$N_{\theta_r} > 0.2\%$	0	0	0
	1	$N_{V,UFP} > 1$	19	42	44
	1	$N_{\epsilon,p} > 1$	0	0	14
	1	$N_{\epsilon,CLT} > 1$	0	1	29
	1	$N_{\Delta,CLT} > 1$	0	1	25
	1	$N_{\Delta,HD} > 1$	0	1	23
R8-1.5	1	$N_{\theta_s} > \theta_{lim,s}$	2	3	0
	1	$N_{\theta_r} > 0.2\%$	0	0	0
	1	$N_{V,UFP} > 1$	15	42	44
	1	$N_{\epsilon,p} > 1$	0	0	8
	1	$N_{\epsilon,CLT} > 1$	0	3	22
	1	$N_{\Delta,CLT} > 1$	0	3	18
	2-4	$N_{\Delta,HD} > 1$	0	0	9
	5	$N_{\theta_s} > \theta_{lim,s}$	4	5	0
	5	$N_{\theta_r} > 0.2\%$	0	0	0
	5	$N_{V,UFP} > 1$	10	39	44
	5	$N_{\epsilon,p} > 1$	0	0	14
	5	$N_{\epsilon,CLT} > 1$	0	2	28
	5	$N_{\Delta,CLT} > 1$	0	0	20
	6-8	$N_{\Delta,HD} > 1$	0	0	0

Note: 44 analyses were done for each model at each hazard

Table 7.10: Number of Analyses Exceeding Yield Criteria for 14-Story Models

Model	Story	Response Criteria	50% in 50 yr	10% in 50 yr	2% in 50 yr
R14-1	1	$N_{\theta_s} > \theta_{lim,s}$	0	0	0
	1	$N_{\theta_r} > 0.2\%$	0	0	2
	1	$N_{V,UFP} > 1$	0	30	43
	1	$N_{\epsilon,p} > 1$	0	3	22
	1	$N_{\epsilon,CLT} > 1$	0	0	17
	1	$N_{\Delta,CLT} > 1$	0	0	17
	2-14	$N_{\Delta,HD} > 1$	0	5	23
R14-1.6	1	$N_{\theta_s} > \theta_{lim,s}$	0	0	0
	1	$N_{\theta_r} > 0.2\%$	0	0	2
	1	$N_{V,UFP} > 1$	0	28	44
	1	$N_{\epsilon,p} > 1$	0	2	21
	1	$N_{\epsilon,CLT} > 1$	0	0	16
	1	$N_{\Delta,CLT} > 1$	0	0	15
	2-5	$N_{\Delta,HD} > 1$	0	2	20
	6	$N_{\theta_s} > \theta_{lim,s}$	3	0	0
	6	$N_{\theta_r} > 0.2\%$	0	0	0
	6	$N_{V,UFP} > 1$	0	15	39
	6	$N_{\epsilon,p} > 1$	0	0	7
	6	$N_{\epsilon,CLT} > 1$	0	0	4
	6	$N_{\Delta,CLT} > 1$	0	0	2
	7-14	$N_{\Delta,HD} > 1$	0	0	5
R14-1.8	1	$N_{\theta_s} > \theta_{lim,s}$	0	0	0
	1	$N_{\theta_r} > 0.2\%$	0	0	2
	1	$N_{V,UFP} > 1$	0	28	44
	1	$N_{\epsilon,p} > 1$	0	2	21
	1	$N_{\epsilon,CLT} > 1$	0	0	16
	1	$N_{\Delta,CLT} > 1$	0	0	15

Continued on next page

Table 7.10 – Continued from previous page

Model	Story	Response Criteria	50% in 50 yr	10% in 50 yr	2% in 50 yr
	2-7	$N_{\Delta,HD} > 1$	0	2	20
	8	$N_{\theta_s} > \theta_{lim,s}$	5	1	1
	8	$N_{\theta_r} > 0.2\%$	0	0	2
	8	$N_{V,UFP} > 1$	0	19	41
	8	$N_{\epsilon,p} > 1$	0	0	7
	8	$N_{\epsilon,CLT} > 1$	0	0	12
	8	$N_{\Delta,CLT} > 1$	0	0	11
	9-14	$N_{\Delta,HD} > 1$	0	0	0
R14-1.10	1	$N_{\theta_s} > \theta_{lim,s}$	0	0	0
	1	$N_{\theta_r} > 0.2\%$	0	0	0
	1	$N_{V,UFP} > 1$	0	28	44
	1	$N_{\epsilon,p} > 1$	0	0	12
	1	$N_{\epsilon,CLT} > 1$	0	0	8
	1	$N_{\Delta,CLT} > 1$	0	0	6
	2-9	$N_{\Delta,HD} > 1$	0	0	16
	10	$N_{\theta_s} > \theta_{lim,s}$	13	11	15
	10	$N_{\theta_r} > 0.2\%$	0	0	1
	10	$N_{V,UFP} > 1$	6	36	44
	10	$N_{\epsilon,p} > 1$	0	3	23
	10	$N_{\epsilon,CLT} > 1$	0	9	35
	10	$N_{\Delta,CLT} > 1$	0	9	31
	11-14	$N_{\Delta,HD} > 1$	0	0	2

Note: 44 analyses were done for each model at each hazard

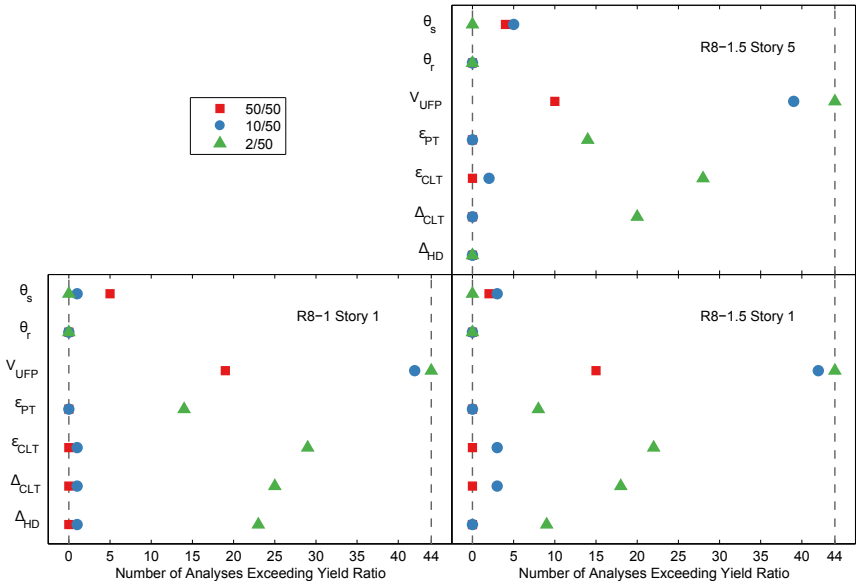

Figure 7.23: Number of Analyses Exceeding Yield Criteria for 8-Story Model

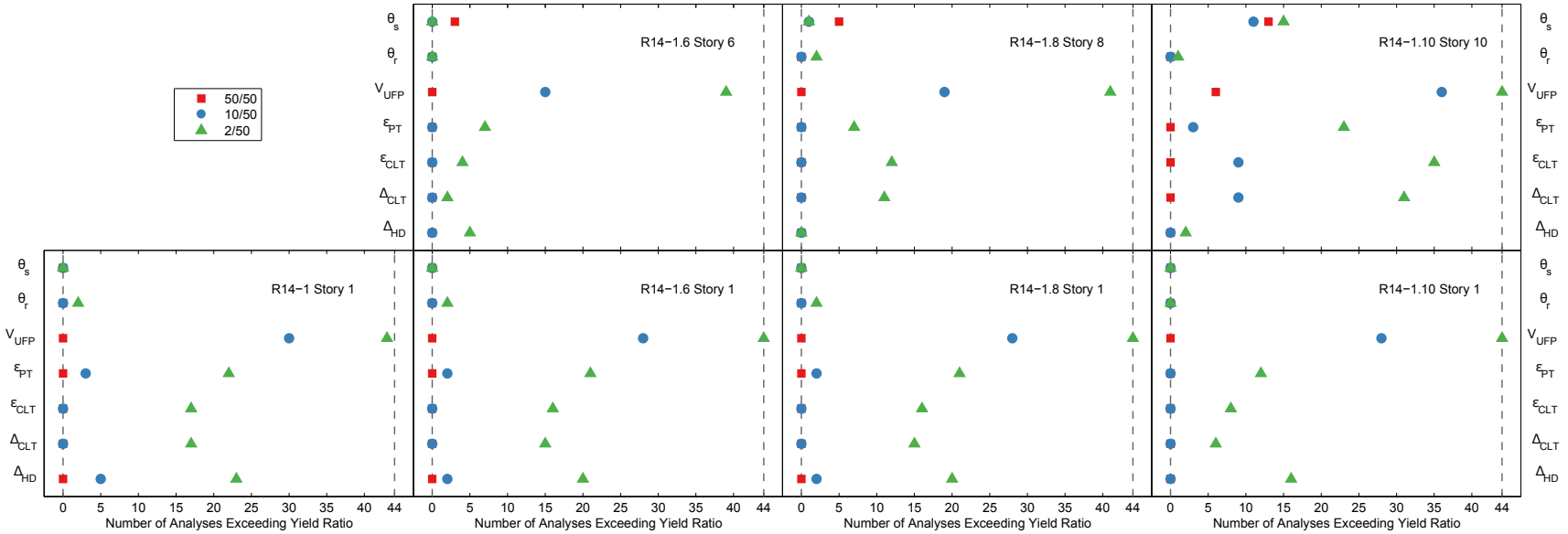

Figure 7.24: Number of Analyses Exceeding Yield Criteria for 14-Story Models

7.5 Evaluation of Design Procedure

Both the 8-story model with the single rocking story at the base (R8-1) and the model with the second rocking story at the 5th story (R8-1.5) performed well and met the performance objectives. The 14-story model with the single rocking story at the base (R14-1), the model with the second rocking story at the 6th story (R14-1.6), the models with the second rocking wall story at the 8th story (R14-1.8) met the performance objectives as well. However, the 14-story model with the rocking wall story at the 10th story (R14-1.11) did not due to the 10th story lacking adequate stiffness. For all designs, under static wind loading, no connection decompression (PO 1) was not observed in any wall.

7.5.1 Evaluation of PO 2

The specific objectives for PO2 were story drifts limited to 0.5% and no repair would be required (all components remain elastic) under a 50% in 50 year event. R8-1 and R8-1.5 was well under the story drift limit as shown in Figure 7.17, however about 40% of the analyses had the UFPs yield in the 50% in 50 year event for each rocking wall story for both models. The 14 story models had similar results to the 8 story model. All the 14 story models met the drift criteria, as shown in Figure 7.18. R14-1.10 was the only model where the UFPs yielded in a 50% in 50 year event. For all 14 story models the 84th percentile value for the UFP ratio was below 1.0.

7.5.2 Evaluation of PO 3

The objectives for PO 3 were story drifts limited to 2%, the PT should remain elastic, the CLT should not crush, the hold downs should remain elastic, and the building should recenter. R8-1 and R8-1.5 reasonably meet this performance objective. As shown in Figure 7.17 the model meet the 2% drift limit. All models recentered, the hold downs remained elastic for all models and only 11% of the models failed the PT and CLT limits as shown in Table 7.9.

R14-1, R14-1.6, and R14-1.8 meet the 2% drift limit for all stories as shown in Figure 7.18. R14-1.6 performed well having only had 5% of the analyses, both at the first story, have the PT yield and no analyses of CLT crushing or hold down yielding as shown in Table 7.10. Similarly R14-1.8 had 7% of the analyses, both at the first story, have the PT yield and no analyses of CLT crushing or hold down yielding at the stories above as shown in Table 7.10. R14-1.10 did not meet the 2% drift limit at the 2nd rocking wall story at story 10. The first story performed well had no analyses of PT yielding, CLT crushing, or hold down yielding above; however story 10 had 14% of the analyses have PT yielding and a 20% of the analyses have CLT crushing. All models were able to recenter and have residual story drifts under 0.2%. For the 14-story models the median UFP ratio value was well under 1.0 which is a concern because the UFPs need to yield in a 10% in 50 year event (which represents the DBE) to adequately dissipated the earthquake input energy. The majority of the UFPs in the 8-story models, which were designed with the same energy dissipation ratio as the 14-story designs, yielded during the 10% in 50 year event. This suggests that the target energy dissipation in the design procedure needs to be modified depending on the height of the building.

7.5.3 Evaluation of PO 4

As shown in Figure 7.17, R8-1 and R8-1.5 meet the collapse drift limit for PO 4 of 8.4% drift. For R8-1.5 none of the analyses surpassed the collapse drift limit for the first story and 7% of the analyses surpassed the collapse drift limit for the 5th story as shown in Table 7.9. A fair amount of the analyses experienced PT yielding with 30% of the analyses experiencing it at the first story and 39% of the analyses experiencing at the 5th story. However the models still maintained enough strength and stiffness to not surpass the drift limit which signifies collapse. This could be due to only the outer wall PT bars yielding and the inner walls not.

As shown in Figure 7.18, R14-1, R14-1.6, and R14-1.8 were able to meet the drift limit for PO 4. Like the R8-1.5 both R14-1.6 and R14-1.8 experienced PT yielding in a substantial

amount of analyses. Both models had about half of the analyses experience PT yielding at the 1st story and 30% experience PT yielding at the 2nd rocking wall story either at the 6th or 8th story. Both R14-1.6 and R14-1.8 were able to maintain enough strength and stiffness to not exceed the collapse drift levels. As shown in Figure 7.18, R14-1.10 was not able to meet the drift limit for PO 4. The 1st floor rocking story has small drifts and no analyses failed, but the 10th floor rocking story had excessive drifts and 40% of the analyses failed.

7.5.4 Placement of the 2nd Rocking Story

The results from the dynamic analyses show that damage is reduced at the base with the inclusion of a second rocking story. Figure 7.17 shows a reduction in the story drifts at the first story with the addition of a second rocking story at mid-height for the 8-story models. As shown in Figure 7.21, for the 8-story models, by placing a rocking story at mid-height, the median and 84th percentile component were all reduced at the base with the largest reduction being in the CLT criteria. The same results can be seen in Figure 7.22 for the 14-story models. As the second rocking story is moved higher up the building more demand on the components lessen at the base story.

The design procedure needs to be modified to supply more stiffness to the second rocking story if it is above mid height. The 14 story models with the rocking story at the 6th and 8th floors meet all the performance objectives while the the 14 story model with the rocking story at the 10th story did not meet PO 3 or PO 4. For all 14 story models, the second rocking story experienced higher drifts than the 1st rocking story. The 14 story models with the rocking story at the 6th and 8th floors show there is more tendency for the PT to yield at the first rocking story when compared with the second rocking story. The 14 story models with the rocking story at the 10th shows a much higher tendency for the PT to yield at the second rocking story when compared with the first rocking story. The reason the design demands are low for higher stories and thus the higher stories are not designed with enough stiffness may be due to the use of the equivalent lateral load procedure [ASCE, 2010] which does not account for increased forces due to higher mode effects.

Chapter 8

SUMMARY AND CONCLUSIONS

8.1 Summary

The purpose of this research was to understand the behavior of a rocking CLT wall system, which uses CLT walls with PT rocking connections and UFP energy dissipation devices, and develop a design procedure for tall wood buildings utilizing the system. The CLT behavior was analyzed through an experimental program and the design procedure was evaluated using the results of a series of nonlinear dynamic response history analyses. This section presents a summary of each topic covered in this thesis.

8.1.1 Rocking CLT wall Behavior

The behavior of the rocking CLT wall can be summarized as:

- Before the PT connection decompresses, the connection acts like a mechanical connector. When the wall reaches it's decompression moment, M_{dec}, the CLT panel starts to rotate and a gap forms, θ_{gap}. The connection and wall have reduced stiffnesses after decompression.

- As the gap opens, the PT bar elongates causing an increase in PT force. The elongation of the PT provides the moment necessary for recentering of the rocking CLT wall.

- The compression stresses in the CLT panel can be approximated as an elastic-perfectly plastic stress-strain distribution. The location of the resultant compression force from the PT force can be solved for by finding the centroid of the stress distribution.

- As the wall rocks, one side of the UFP coupling device will deform vertically relative the other side inducing a force in the UFP. Once the UFP reaches its yield force it will dissipate energy as it is cycled back and force with the rocking of the CLT walls.

8.1.2 Performance Based Seismic Design Procedure

A performance-based seismic design procedure was proposed for tall timber buildings with the rocking CLT wall system. The performance objectives for the proposed design procedure are:

1. No decompression under wind loading
2. No repair following an earthquake with a 50% probability of exceedence in 50 years
3. Repair of the UFPs only and recentering following an earthquake with a 10% probability of exceedence in 50 years
4. Collapse prevention following an earthquake with a 2% probability of exceedence in 50 years

The proposed design procedure is outlined below:

1. Calculate demands
2. Choose location of second rocking story
3. Choose design parameters for rocking stories
4. Calculate the number of walls required for each rocking story
5. Design stories with CLT walls with hold down connections
6. Check limit states

Using the residential archetype building, two 8 story building and four 14 story buildings were designed with the proposed design procedure.

8.1.3 Experimental Program

The rocking CLT wall experimental program can be summarized as:

- Six specimens, five single wall and one coupled wall, were designed and constructed to investigate rocking CLT wall cyclic behavior. A hierarchy of desirable limit states was identified (UFP yielding, CLT panel crushing, PT bar yielding).

- Parameters were varied to investigate their effects of response. The parameters include PT bar area, PT bar initial stress, wall type, base type, and wall configuration.

- The load protocol consisted of sets of three cycles up to 11% drift.

Key results for the tests include:

- The rocking CLT walls had a ductile response.

- As the initial prestress force, f_{p0} is increased, the decompression moment, M_{dec} is also increased and CLT damage will occur sooner.

- A wall with a larger PT bar will have a larger strength capacity and larger decompression stiffness, k_{dec}, compared to a wall with a smaller PT bar and all other parameters equal.

- The loss of PT force due to CLT damage is significant and needs to be addressed in design.

- Using CLT panels with SCL inner cores causes damage to happen at higher drifts when compared to walls with 5-ply CLT panels.

- The CLT floor base, oriented perpendicular to grain, was weaker than the wall and indentation occurred at low drifts and continued through the test. If a CLT floor is to be used in design it must have a reinforcing plate to prevent damage from the rocking action of the CLT walls.

- The PT bar should be stressed between 30 to 40% of the ultimate stress to provide adequate strength, stiffness, and energy dissipation without yielding at low drifts.

- The CLT damage before 5% drift did not effect the recentering of the walls.

- The UFPs provided half of the energy dissipation for the coupled wall specimen.

8.1.4 Numerical Model

A relatively simple numerical model of a rocking CLT wall was developed in the OpenSees framework and was applied to represent the experimental data. The numerical model consisted of:

- An elastic beam column element with axial, flexure, and shear deformations to model the elastic portion of the CLT walls

- A truss element to model the PT bar

- A mulitspring element, which consisted of a series of zero-length springs with a compression only elastic-perfectly plastic material model, to model the inelastic behavior of the CLT wall at the rocking connection

- Zero-length springs with a steel hysteretic material model and connected to the CLT wall elements through rigid links to model the UFP elements

The rocking CLT wall model was combined with a simplified CLT wall model with mechanical connectors to create building models of the prototype designs. The concrete floor diaphragms

were considered rigid and modeled with rigid links. The models were subjected to a suite of 144 ground motions consisting of a set of 44 ground motions each scaled to represent 50% in 50 year, 10% in 50 year, and 2% in 50 year earthquakes.

8.1.5 Results of Dynamic Analyses and Evaluation of Design Procedure

Nonlinear analyses were performed on the models of each of the prototype building designs. The results of the dynamic analyses were used to evaluate the proposed design procedure and are summarized below:

- Both 8 story model and the 14 story model with rocking stories at the 1st 6th and 8th stories were able to meet all the performance objectives.
- The 14 story model with rocking stories at the 10th story did not meet performance objectives 3 or 4.
- The 14 story models with rocking stories at the 6th and 8th stories performed better than the 14 story buildings with rocking stories at the 10th story.
- For both the 8 story and 14 story buildings, even though a substantial amount of cases showed PT yielding, the models were able to maintain enough strength and stiffness to not exceed the collapse drift limit.
- Placing a second rocking story in the building reduced the story drifts and component damage, however the design procedure needs to address the lack of stiffness of the higher rocking stories.

8.2 Conclusions

Tall timber buildings can be designed for regions with high seismic accelerations with the use of single story rocking CLT walls providing system recentering, energy dissipation, and strength. A design procedure was proposed to achieve specified performance objectives at

three different seismic hazard levels. Experimental results found the rocking CLT walls have good qualities for a seismic force resisting system and can meet the proposed performance objectives. Results of the nonlinear dynamic analyses suggest improvements to the design procedure; however the results show that CLT rocking walls are a viable option as a seismic resisting system for tall timber buildings.

8.3 Future Work

Further research is needed for CLT rocking walls to be implemented in tall timber buildings. The following section recommends future research needs for the design procedure, experimental program, and numerical model.

Design Procedure

- The global overturning moment was not accounted for in the design procedure. The numerical analyses show the system overturning moment has a large effect on lower rocking wall stories.
- A method needs to be developed to find the locations of the rocking stories that will reduce demands from higher mode effects.
- A connection to transfer the shear force needs to be designed.
- A design of the gravity system and non-structural components to allow rocking needs to be developed.
- A better method to approximate the required energy dissipation from the UFPs needs to be developed.

Experimental Research

- Different wall aspect ratios need to be considered. In the experiments in this thesis, only one aspect ratio was used.

- The specimen with the CLT base showed the CLT base to be weaker than the CLT panels rocking on it. A new design and experimental needs to be conducted for a reinforced CLT base.

- The experimental results showed that the CLT material properties were variable. An investigation needs to be conducted to better understand the CLT material properties.

- Experiments should be carried out to investigate the addition of a second rocking connection.

Numerical Model

- More prototype building designs with varying heights need to be created and run with the numerical model to better assess the performance objectives.

- Instead of using a bi-linear model for the mechanical connector behavior, a proper hysteretic model needs to be developed for the CLT walls with mechanical connectors.

- The impact of a flexible diaphragm should be investigated. All the models in this thesis used a rigid diaphragm.

REFERENCES

Alig, R. J., Kline, J. D., and Lichtenstein, M. (2004). "Urbanization on the us landscape: looking ahead in the 21st century." *Landscape and Urban Planning*, 69, 219–234.

APA (2012). *Standard for Performance Rated Cross-Laminated Timber, ANSI/APA PRG 320-2012*. APA - The Engineered Wood Association.

ASCE (2010). *Minimum Design Loads for Buildings and Other Structures. ASCE 7-10*. American Society of Civil Engineering.

ATC (2009a). "Guidelines for seismic performance assessment of buildings." *Report No. ATC-58 50% draft*, Applied Technology Council.

ATC (2009b). "Qualification of building seismic performance factors." *Report No. FEMA P-695*, Prepared by the Applied Technology Council for the Federal Emergency Management Agency.

ATC (2012). "Seismic performance assessment of buildings." *Report No. FEMA P-58*, Prepared by the Applied Technology Council for the Federal Emergency Management Agency.

Baird, A., Smith, T., Palermo, A., and Pampanin, S. (2014). "Experimental and numerical study of u-shaped flexural plate (ufp) dissipators." *NZSEE Conference*.

Buchanan, A. H. (1990). "Bending strength of lumber." *Journal of Structural Engineering*, 116(5), 1213–1229.

Ceccotti, A., Sandhass, C., Okabe, M., Yasumura, M., Minowa, C., and Kawai, N. (2013). "Sofie project - 3d shaking table test on a seven-storey full-scale cross-laminated timber building." *Earthquake Engineering and Structural Dynamics*, 42, 2003–2021.

Chopra, A. K. (2007). *Earthquake Dynamics of Structures: Theory and Applications to Earthquake Engineering*. Prentice Hall, Upper Saddle River, New Jersey, 3rd edition.

Christopoulos, C., Filiatrault, A., Uang, C., and Folz, B. (2001). "Post-tensioned energy dissipating connections for moment-resisting steel frames." *Journal of Structural Engineering*, 128(9), 1111–1120.

Clayton, P. M. (2013). "Self-centering steel plate shear walls: Subassembly and full-scale testing." Ph.D. thesis, University of Washington, Seattle, WA.

Eatherton, M., Hajjar, J., Deirerlein, G., Krawinkler, H., Billington, S., and Ma, X. (2008). "Controlled rocking of steel-framed buildings with replaceable energy-dissipating fuses." *14th World Conference on Earthquake Engineering*.

Folz, B. and Filiatrauult, A. (2001). "Cyclic analysis of wood shear walls." *Journal of Structural Engineering*, 127(4), 433–441.

Green, M. C. and Karsh, E. J. (2012). "The case for tall wood buildings." *Report No. 1*, MGB Architecture and Design.

Hasan, M., Roke, D., , and Huang, Q. (2013). "Quantification of higher mode responses for steel self-centering concentrically braced frames." *7th International Structural Engineering and Construction Conference*.

Horvat, D. (2013). "Stability behavoir of cross laminated timber (clt) columns under compressive axial load." M.S. thesis, University of British Columbia, Vancouver, BC.

Iqbal, A., Pampanin, s., Buchanan, A., and Palermo, A. (2007). "Improved seismic performance of lvl post-tensioned walls coupled with ufp devices." *8th Pacific Conference on Earthquake Engineering*.

Karacabeyli, E. and Douglas, B. (2013). *CLT Handbook: Cross-laminated timber*. U.S. Ed. Special Publication-SP-529E. FPInnovations.

Kelly, J. M., Skiner, R. I., and Heine, A. J. (1972). "Mechanisms of energy absorption in special devices for use in earthquake resistant structures." *Bulletin of N. Z. Society for Earthquake Engineering*, 5(3), 63–88.

Kretschmann, D. E. (2013). "Mechanical properties of wood. chapter 5 in wood handbook." *Report No. FPL-GTR-190*, Forest Products Laboratory and U.S. Department of Agriculture.

Kurama, Y., Pessiki, S., Sause, R., and Lu, L. (1999). "Seismic behavior and design of unbonded post-tensioned precast concrete walls." *PCI Journal*, 44(3), 26–39.

Massone, L. M. and Wallace, J. W. (2004). "Load-deformation responses of slender reinforced concrete walls." *ACI Structural Journal*, 101(1), 103–113.

Mazzoni, S., McKenna, F., Scott, M., and Fenves, G. (2009). *Open Systems for Earthquake Engineering Simulation User Command-Language Manual - OpenSees version-2.0*. Pacific Earthquake Engineering Research Center, University of California, Berkeley, Berkely, CA.

Mohammad, M., Gagnon, S., Douglas, B. K., and Podesto, L. (2012). "Introduction to cross laminated timber." *Wood Design Focus*, 22(2), 3–12.

Nakaki, S. D., Stanton, J. F., and Sritharan, S. (1999). "An overview of the PRESSS five-story precast test building." *PCI Journal*, 44(2), 26–39.

Newcombe, M. P., Pampanin, S., Buchanan, A., and Palermo, A. (2008). "Section analysis and cyclic behavior of post-tensioned ductile connections for multi-story timber buildings." *Journal of Earthquake Engineering*, 12, 83–110.

Palermo, A., Pampanin, S., and Buchanan, A. (2006). "Experimental investigations on lvl seismic resistant wall and frame subassemblies." *First European Conference on Earthquake Engineering and Seismology*.

Palermo, A., Pampanin, S., Buchanan, A., and Newcombe, M. (2005). "Seismic design of muli-storey buildings using laminated veneer lumber (lvl)." *NZSEE Conference*.

Pampanin, S., Priestley, M. J. N., and Sritharan, S. (2001). "Analytical modelling of the seismic behaviour of precast concrete frames designed with ductile connections." *Journal of Earthquake Engineering*, 5(3), 329–367.

Pang, W., Rosowsky, D. V., Pei, S., and van de Lindt, J. W. (2010). "Simplified direct displacement design of six-story woodframe building and pretest seismic performance assessment." *Journal of Structural Engineering*, 136(7), 813–825.

Pei, S., van de Lindt, J. W., and Popovski, M. (2013). "Approximate r-factor for cross-laminated timber walls in multistory buildings." *Journal of Architectural Engineering*, 19(4), 245–255.

Pei, S., van de Lindt, J. W., Popovski, M., Berman, J. W., Dolan, J. D., Ricles, J., Sause, R., Blomgren, H., and Rammer, D. R. (2014). "Cross-laminated timber for seismic regions: Progress and challenges for research and implementation." *Journal of Structural Engineering*.

Pollino, M. and Bruneau, M. (2008). "Analytical and experimental investigation of a controlled rocking approach for seismic protection of bridge steel truss piers." *Report No. MCEER-08-0003*, Multidisciplinary Center for Earthquake Engineering Research, State Univ. of New York at Buffalo, Buffalo, N.Y.

Popovski, M., Schneider, J., and Schweinsteiger, M. (2010). "Lateral load resistance of cross-laminated wood panels." *World Conference on Timber Engineering*.

Priestly, M. J. N. (1991). "An overview of presss research program." *PCI Journal*, 36(4), 50–57.

Priestly, M. J. N., Sritharan, S., Conley, J., and S., P. (1999). "Preliminary results and conclusions from the PRESSS five-story precast concrete test building." *PCI Journal*, 44(6), 42–67.

Ricles, J. M., Sause, R., and Garlock, M. M. (2001). "Experimental studies of full-scale post-tensioned steel connections." *Journal of Structural Engineering*, 131(3), 113–121.

Sause, R., Ricles, J. M., Roke, D., Chancellor, N., and Gonner, N. (2010). "Large scale experimental studies of damage-free self-centering concentrically-braced frame under seismic loading." *Structures Congress*.

Seo, C. Y. and Sause, R. (2005). "Ductility demands on self-centering systems under earthquake loading." *ACI Structural Journal*, 102(2), 275–285.

Smith, T., Pampanin, S., Buchanan, A., and Fragiacomo, M. (2008). "Feasibility and detailing of post-tensioned timber buildings for seismic areas." *NZSEE Conference*.

Spieth, H. A., Carr, A. J., Pampanin, S., Murahidy, A. G., and Mander, J. (2004). "Modeling of precast prestressed concrete frame structures with rocking beam-column connections." *Report No. 2004-01*, University of Canterbury. Christchurch, New Zealand.

USGS (2015). "Earthquake Hazards Program, <http://earthquake.usgs.gov/hazards/>.

van de Lindt, J. W., Rammer, D., Popovski, M., Line, P., Pei, S., and Pryor, S. E. (2013). *Lateral Design of Cross-Laminated Timber. Chapter 4 in CLT Handbook: Cross-Laminated Timber*. U.S. Ed. Special Publication-SP-529E. FPInnovations.

Wiebe, L., Christopoulos, C., Tremblay, R., and Leclerc, M. (2013a). "Mechanisms to limit higher mode effect in a controlled rocking steel frame. 1: Concept, modelling, and low-amplitude shake table testing." *Earthquake Engineering and Structural Dynamics*, 42, 1053–1068.

Wiebe, L., Christopoulos, C., Tremblay, R., and Leclerc, M. (2013b). "Mechanisms to limit higher mode effect in a controlled rocking steel frame. 2: Large-amplitude shake table testing." *Earthquake Engineering and Structural Dynamics*, 42, 1069–1086.

Wiedenhoeft, A. (2013). "Structure and function of wood. chapter 3 in wood handbook." *Report No. FPL-GTR-190*, Forest Products Laboratory and U.S. Department of Agriculture.

Appendix A
MATERIAL TESTS

This appendix presents the methods and results for material tests done for the CLT and SCL core panels, PT bars, and UFP coupling devices.

A.1 CLT Panels

Three separate specimen types were tested in compression in three different directions to obtain material properties for the CLT panels. The orientation of the three directions are shown in Figure A.1. The specimens were cut into columns for directions 1 and 3 and cut into cubes for direction 2. For the CLT panels, (10) 3-ply and (2) 5-ply specimens were tested in direction 1, (5) 3-ply and (1) 5-ply were tested in direction 2, and (2) 3-ply and (2) 5-ply specimens were tested in direction 3. For the CLT panels with SCL cores, (1) specimen was tested in each direction. For each specimen, 3 measurements were averaged for the length, width, and depth. The length and width were multiplied to calculate the area.

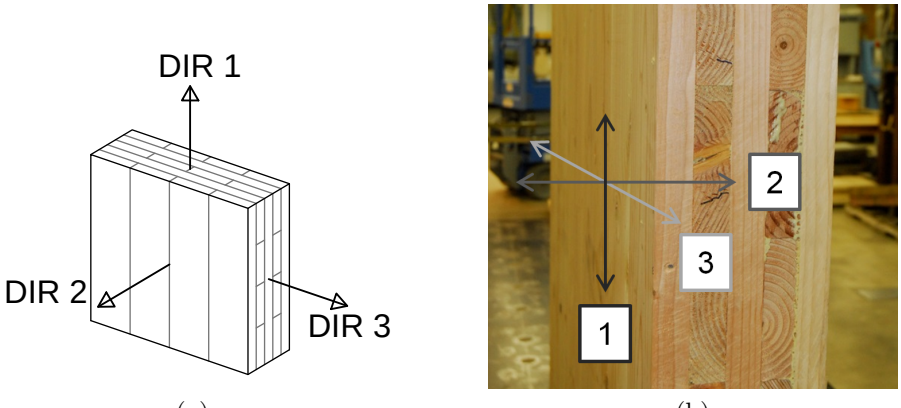

(a) (b)

Figure A.1: (a) Schematic and (b) Photograph Depicting CLT Orientation

The 3-ply specimens were tested in a Tinius-Olsen testing machine shown in Figure A.2a. Both the load reading and testing machine head displacement were recorded by a data acquisition system. The stress was measured by dividing the load reading by the measured cross-sectional area of the specimen. The strain was measured by dividing the testing machine head displacement by the depth of the specimen. An example of a damaged 3-ply specimen is shown in Figure A.2b.

Because of the need of higher capacity, the 5-ply and SCL specimens were tested in a separate higher capacity Tinius-Olsen testing machine as shown in Figure A.3a. Because the higher capacity testing machine did not have a data acquisition system the load reading and testing machine head displacement were measured manually and the softening of the specimens after yield was not captured, thus the max strain values are only reported for the 3-ply material tests. The stress and strain for the 5-ply and SCL specimens were calculated in the same manner as the 3-Ply specimens. An example of a damaged 5-ply specimen is shown in Figure A.3b.

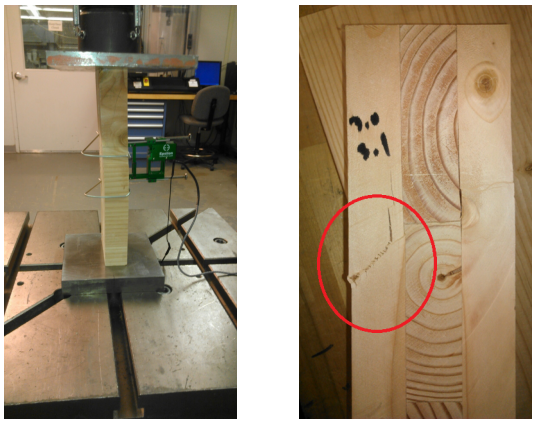

(a) (b)

Figure A.2: Example of (a) 3 Ply Material Test Setup and (b) Damage (Specimen CLT3.1.3)



(a) (b)

Figure A.3: Example of (a) 5 Ply Material Test Setup and (b) Damage (Specimen CLT5.1.1)

The modulus of elasticity, E, was calculated by taking a linear regression of the stress versus strain values after load was applied. The slope of the linear regression was used as E. The yield stress, f_y, was taken as the maximum stress the specimen achieved before it started to lose load. The max strain, ϵ_{max}, was taken as the maximum strain the specimen experienced. The stress verses strain values are shown for each direction in Figure A.4-Figure A.6. The average values for E, f_y, and ϵ_{max} were taken for all the CLT specimens and the SCL core specimens to be used for analysis presented in this thesis and are shown in Table A.1. The test data for all specimens is reported in Table A.2.

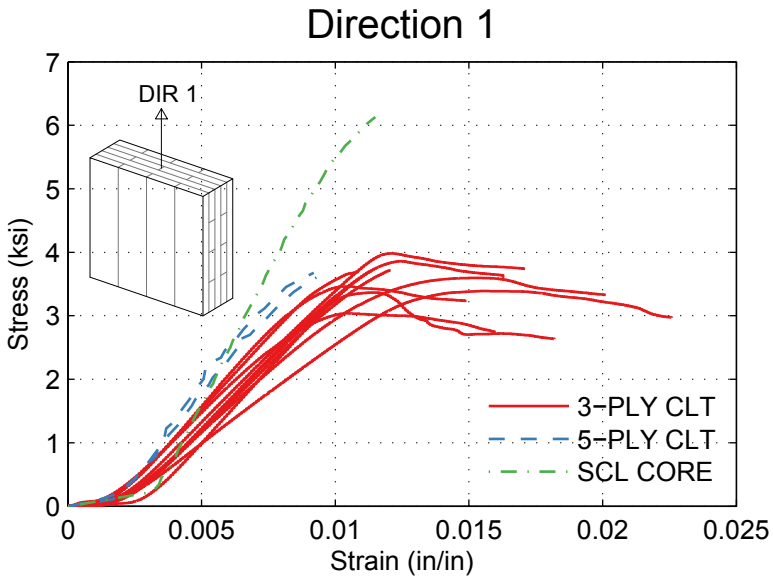

Figure A.4: Stress vs. Strain for CLT Direction 1

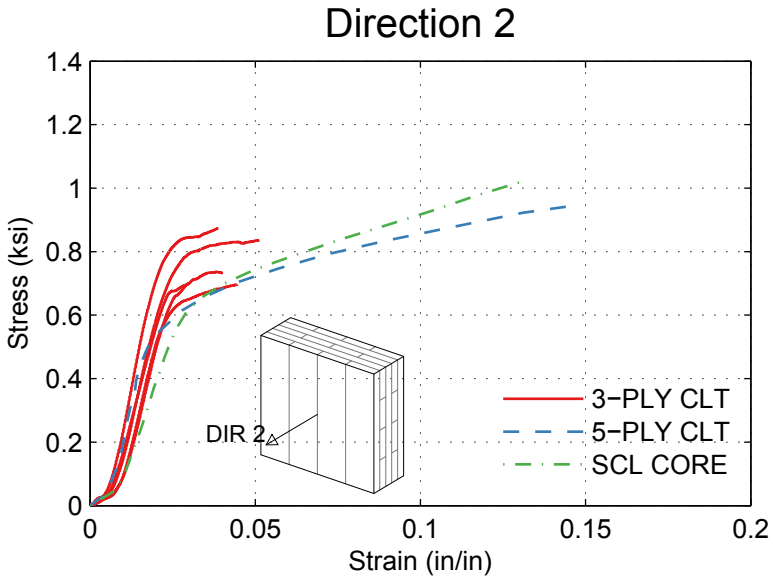

Figure A.5: Stress vs. Strain for CLT Direction 2

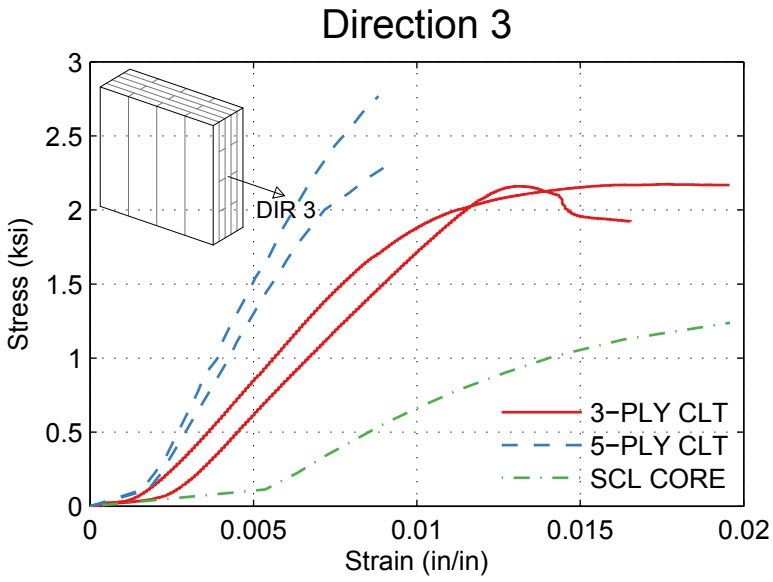

Figure A.6: Stress vs. Strain for CLT Direction 3

Table A.1: CLT and SCL Material Test Averages

Type	Direction	E (ksi)	f_y (ksi)	ϵ_{max} (in/in)	Δ_{max} (in)
CLT	1	441.33	3.60	0.016	0.174
	2	130.61	1.22	0.041	0.151
	3	301.68	2.39	0.018	0.198
SCL	1	842.27	6.20	N/A	N/A
	2	31.00	1.02	N/A	N/A
	3	123.64	1.27	N/A	N/A

Table A.2: CLT and SCL Material Test Results

Spec.	Direction	Area (in^2)	Depth (in)	E (ksi)	f_y (ksi)	ϵ_{max} (in/in)	Δ_{max} (in)
CLT3.1.1	1	4.14	10.94	410.25	3.04	0.016	0.175
CLT3.1.2	1	4.66	10.94	485.61	3.46	0.015	0.163
CLT3.1.3	1	8.25	10.94	312.43	3.39	0.023	0.247
CLT3.1.4	1	7.82	10.94	373.81	3.60	0.020	0.220
CLT3.1.5	1	7.80	10.94	383.94	3.72	0.012	0.132
CLT3.1.6	1	6.76	10.94	424.08	3.98	0.017	0.187
CLT3.1.7	1	7.83	10.94	389.60	3.70	0.011	0.124
CLT3.1.8	1	6.74	10.94	455.85	3.86	0.016	0.178
CLT3.1.9	1	7.85	10.94	437.80	3.69	0.011	0.119
CLT3.1.10	1	6.77	10.94	428.20	3.37	0.018	0.199
CLT5.1.1	1	44.41	20.12	538.24	3.65	N/A	N/A
CLT5.1.2	1	44.90	20.11	656.20	3.76	N/A	N/A
SCL5.1.1	1	44.05	20.26	842.27	6.20	N/A	N/A
CLT3.2.1	2	12.52	3.69	43.02	0.84	0.051	0.189
CLT3.2.2	2	11.77	3.69	52.01	0.87	0.039	0.143
CLT3.2.3	2	12.57	3.69	42.23	0.70	0.044	0.164
CLT3.2.4	2	12.54	3.69	35.52	0.70	0.030	0.110
CLT3.2.5	2	12.74	3.69	36.92	0.74	0.040	0.147
CLT5.2.1	2	45.53	6.68	48.38	0.94	N/A	N/A
SCL5.2.1	2	42.96	6.57	31.00	1.02	N/A	N/A
CLT3.3.1	3	12.03	10.94	237.01	2.17	0.020	0.214
CLT3.3.2	3	12.46	10.94	230.91	2.16	0.017	0.181
CLT5.3.1	3	44.98	20.22	374.69	2.36	N/A	N/A
CLT5.3.2	3	45.16	20.29	437.11	2.84	N/A	N/A
SCL5.3.1	3	44.40	20.33	123.64	1.27	N/A	N/A

A.2 PT Bars

Two different diameter PT bars (1.25 inch and 1.375 inch) were used for experimental testing. To obtain material properties, three coupons per bar type, measuring about 50 inches in length, were tested to failure in a tensile testing machine. The stress verses strain plots for all coupons are shown in Figure A.7. The average values for the modulus of elasticity, E, yield stress, f_y, and ultimate stress, f_u used for analysis are reported in Table A.3 and the results for all the tests are shown in Table A.4.

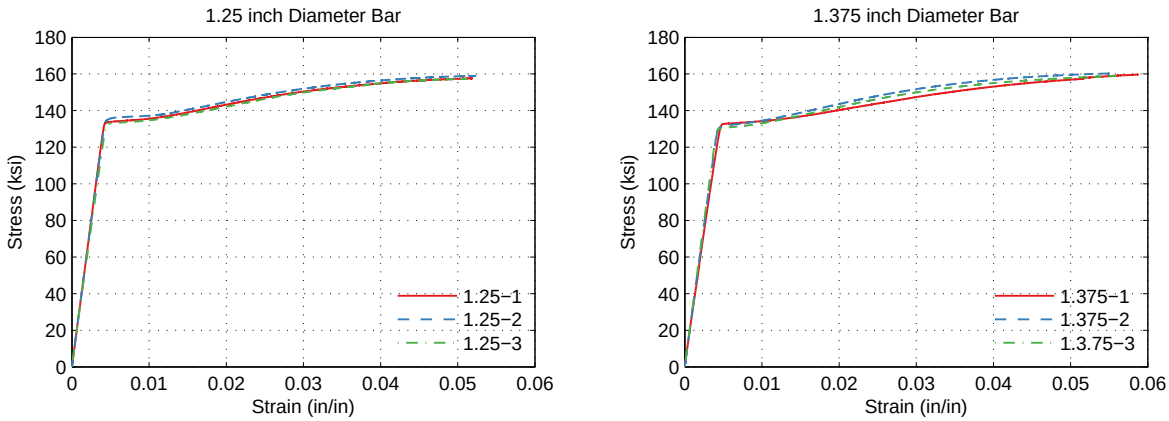

Figure A.7: (a) 1.25 in Diameter and (b) 1.375 in Diameter PT Bar Stress vs. Strain

Table A.3: PT Bar Material Test Averages

Diameter (in)	Area (in^2)	E (ksi)	f_y (ksi)	f_u (ksi)
1.25	1.25	31835	134.7	158.2
1.375	1.58	32023	132.1	159.9

Table A.4: PT Bar Material Test Results

Spec.	Diameter (in)	Area (in^2)	Length (in)	E (ksi)	f_y (ksi)	f_u (ksi)
1.25-1	1.25	1.25	52	31984	134.3	157.8
1.25-2	1.25	1.25	51.5	31398	136.4	159.0
1.25-3	1.25	1.25	52.25	32123	133.4	157.6
1.375-1	1.375	1.58	50	32723	133.1	159.9
1.375-2	1.375	1.58	49.5	31071	132.3	160.9
1.375-3	1.375	1.58	50	32275	131.0	159.0

A.3 UFPs

A total of four UFPs were fabricated for testing. Two were used for Specimen 6 (coupled wall) and two were tested to obtain material properties. The UFPs were fabricated by bending a 4 inch wide by $\frac{3}{8}$ inch thick plate to the desired $4\frac{1}{16}$ inch diameter (see Figure 3.7a).

A testing apparatus, shown in Figure A.8, was built to test the UFPs in a 100 kip MTS testing machine equipped to run a cyclic procedure. To ensure only shear and no moment was applied to the UFPs, two were tested in conjunction with each other. The measured force was assumed to be equal in both UFPs. The UFPs were connected together with a 1 inch thick steel load plate that was attached to the testing machine actuator with hydraulic grips. The other sides of the UFPs were attached to a box made of $\frac{3}{4}$ inch steel plates with $\frac{1}{2}$ stiffeners and braces. The box was attached via hydraulic grips to the testing machine and stayed fixed throughout the test. To connect the UFPs to the testing apparatus $\frac{3}{4}$ inch diameter bolts were tightened to slip critical to ensure the bolts would not slip during testing. A LVDT was attached to the fixed boxed and measured the displacement of the load plate. The LVDT displacements were compared to the actuator displacement and were very close. The load was measured from the actuator load cell. The load protocol, shown in

Table A.5, was created from estimated displacements for Specimen 6. Each step consisted of three cycles that reached the step displacement in tension and compression. The last step was set to be 3 inches because that was the max stroke of the actuator. The UFP was cycled 10 tens instead of 3 at the last step.

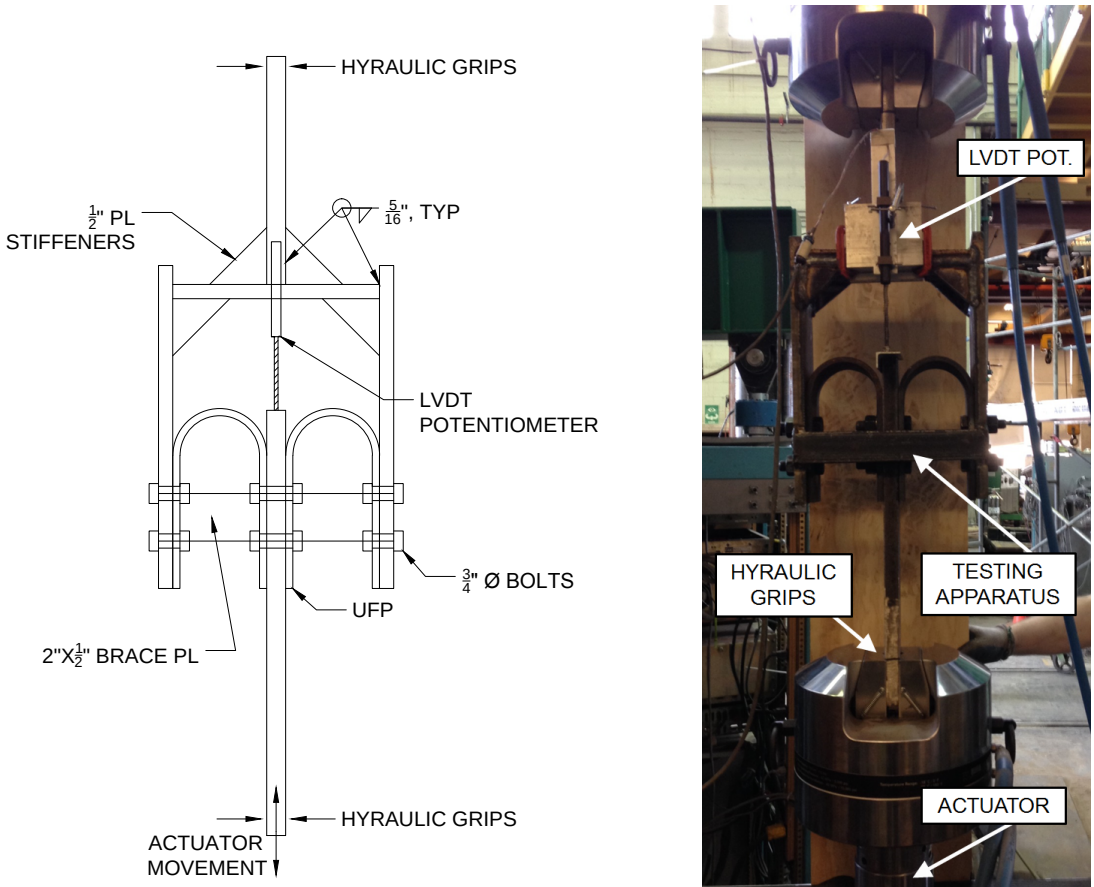

(a) (b)

Figure A.8: (a) UFP Testing Apparatus Schematic and (b) Photograph

Table A.5: UFP Material Test Load Protocol

Step	1	2	3	4	5	6	7	8
Disp. (in)	0.0168	0.024	0.036	0.048	0.072	0.096	0.144	0.192
Step	9	10	11	12	13	14	15	16
Disp. (in)	0.288	0.432	0.648	0.96	1.44	1.92	2.4	3.0

The applied force verses displacement for a single UFP is shown in Figure A.9. The load for a single UFP was calculated as half of the total actuator force since the loading was symmetrical each UFP was assumed to have experienced the same load throughout the test.

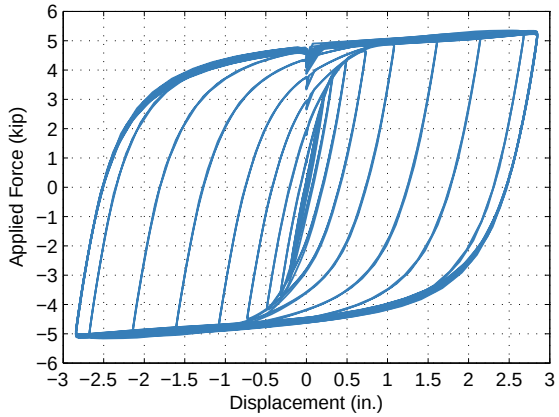

Figure A.9: UFP Experimental Force verses Displacement

A coupon was cut from one of the UFPs to test for the stress-strain properties. The stress verses strain results are shown in Figure A.10. The coupon, shown in Figure A.11 was cut to have a 1 inch gauge length and conformed to ASTM A370-14. The material properties were:

- Yield Stress, f_y: 60 ksi
- Ultimate Stress, f_u: 86 ksi

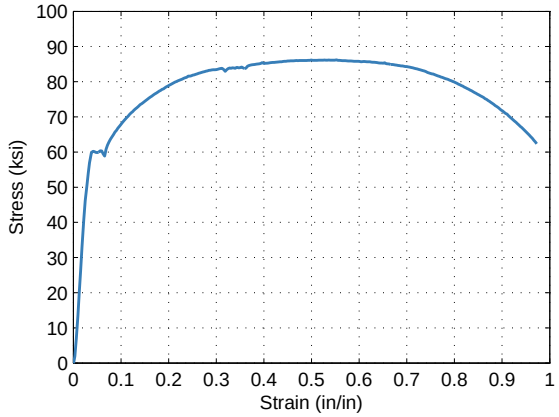

Figure A.10: UFP Coupon Stress verses Strain

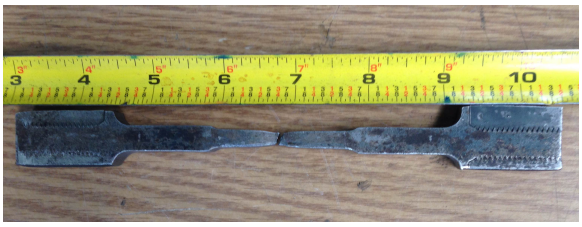

Figure A.11: Tested UFP Coupon

Appendix B

EXAMPLE DESIGN CALCULATIONS

B.1 Introduction

This section provides example calculations for the rocking CLT walls at the first story of the R8-1.5 prototype which uses the Residential Archetype. The member sizes used in this example are those of the final design as presented in Table3.2.

B.2 Calculate Demands

A total seismic weight of 330 kips was determined for each floor resulting in a total weight of 2640 kips. The total height of the 8-story building was 86 feet (16 foot first story and 10 foot stories for the rest of the stories) A building period of 0.56 seconds was calculated using the simplified period calculation from ASCE [2010]. The spectral acceleration of the 10% in 50 year uniform hazard curve for Seattle, WA [USGS, 2015] for the building period is 0.72 g. The seismic base shear is calculated with an R of 6 as:

$$V_{Base} = (2640\ kips)(0.72\ g) = 317\ kips$$

The seismic story shears are determined using the ELF method and the wind story shears are deterimined using the methods outlined in ASCE 7-10 Chapter 27 [ASCE, 2010], resulting in the following overturing moment demands:

$$M_E = 234052 \ k\text{-}in$$

$$M_W = 94654 \ k\text{-}in$$

B.3 Select Design Parameters

The following design parameters were chosen:

- $L_w = 54$ in
- $b_w = 6.75$ in (5-ply CLT panel)
- $h_w = 192$ in
- $A_p = 1.58$ in^2
- $L_p = 480$ in
- $f_{p0} = 0.4 f_{pu} = 60$ ksi
- $D_u = 3$ in
- $b_u = 5$ in
- $t_u = 0.5$ in

B.4 Calculate Required Number of Walls

Using the cross-sectional analysis procedure, a capacity of M = 7839 k-in was determined for a single wall. The reuqired number of walls is:

$$n_w = \frac{234052\ k\text{-}in}{7839\ k\text{-}in} = 30\ walls$$

Use 5 walls per line (6 total wall lines). Create 2 sets of 3 coupled walls, one set at the north end and one set at the south end.

B.5 Calculate Required Number of UFPS

Aim for a energy dissipation ratio of 30%. The tributary weight of a single wall is 30 kips. The decompression moment is calculated as follows:

$$M_{dec} = (W + T_0)\, d = (30\ kips + 95\ kips)\left(\frac{3}{4}\right)(54\ in) = 5054\ k\text{-}in$$

The UFP plastic force is:

$$F_p = \frac{(50\ ksi)(5\ in)(0.5\ in)^2}{(2)(3\ in)} = 10.4\ kips$$

The moment due to the UFP is:

$$M_{UFP} = (10.4\ kips)(54/2\ in) = 563\ k\text{-}in$$

Try using 8 UFPs to couple two walls together. Calcualte the energy dissipation ratio for one set: (Since one set has 3 walls, it will have 16 UFPs)

$$\beta = \frac{16(563\ k\text{-}in)}{(2)(3)(5054\ k\text{-}in)} = 0.30$$

B.6 Design Hold Downs for Stories 2-7

Using the cross-sectional analysis procedure, the capacity of the rocking CLT walls for the entire first story at 4% drift is 1382 kips. For the hold down stories, use 10 walls per wall line (50 total) that are 60 inches long and 120 inches tall. Place hold downs at each corner of both sides of each wall (8 total per wall). Use a hold down yield force of 14 kips. The smallest gravity load is 18.75 kips per wall (at the 7th story). The total hold down capacity is calculated as follows:

$$V = \left(\frac{(18.75\ kips)(30\ in) + (4)(14\ kips)(60\ in)}{120\ in} \right) (10\ walls)(5\ lines) = 1634\ kips$$

B.7 Check Limit States

The walls need to be checked against decompression under wind loading. Since there are 30 walls, the overturning moment from the wind load per wall is 3155 k-in which is less than the decompression moment of 5054 kips.

The PT bar and CLT must not crush at 4% drift. This can be checked by finding the PT force and CLT strain for a single wall at 4% drift using the cross-sectional analysis procedure. At 4% drift:

- $T = 190\ kips < T_y = 201\ kips$
- $\epsilon_{CLT} = 0.013\ \frac{in}{in} < \epsilon_c = 0.016\ \frac{in}{in}$

Design is complete.